





This is to certify that the  
dissertation entitled

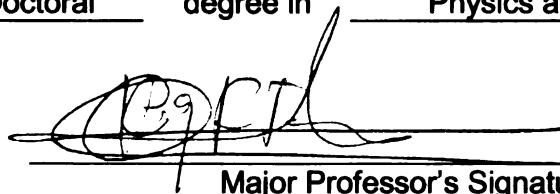
THE  $^{150}\text{Sm}(t, ^3\text{He})^{150}\text{Pm}^*$  AND  $^{150}\text{Nd}(^3\text{He}, t)^{150}\text{Pm}^*$  REACTIONS  
AND APPLICATIONS FOR  $2\nu$  and  $0\nu$  DOUBLE BETA DECAY

presented by

Carol Jeanne Guess

has been accepted towards fulfillment  
of the requirements for the

Doctoral degree in Physics and Astronomy



Major Professor's Signature

28 July 2010

Date



**PLACE IN RETURN BOX** to remove this checkout from your record.  
**TO AVOID FINES** return on or before date due.  
**MAY BE RECALLED** with earlier due date if requested.

DATE DUE	DATE DUE	DATE DUE



THE  $^{150}\text{Sm}(t, ^3\text{He})^{150}\text{Pm}^*$  AND  $^{150}\text{Nd}(^3\text{He}, t)^{150}\text{Pm}^*$  REACTIONS AND  
APPLICATIONS FOR  $2\nu$  AND  $0\nu$  DOUBLE BETA DECAY

By

Carol Jeanne Guess

A DISSERTATION

Submitted to  
Michigan State University  
in partial fulfillment of the requirements  
for the degree of

DOCTOR OF PHILOSOPHY

Physics and Astronomy

2010



## ABSTRACT

### THE $^{150}\text{Sm}(t, ^3\text{He})^{150}\text{Pm}^*$ AND $^{150}\text{Nd}(^3\text{He}, t)^{150}\text{Pm}^*$ REACTIONS AND APPLICATIONS FOR $2\nu$ AND $0\nu$ DOUBLE BETA DECAY

By

Carol Jeanne Guess

In models of  $2\nu\beta\beta$  and  $0\nu\beta\beta$  decay, the transition is described as proceeding through “virtual” states of the intermediate nucleus. Knowledge of the location and population strength of these levels is crucial for constraining the nuclear matrix elements of the transition. Charge-exchange (CE) experiments at intermediate energies can be used to extract the Gamow-Teller strength for both legs of this transition, as well as additional information on dipole and quadrupole excitations. The  $\beta\beta$  decay of  $^{150}\text{Nd}$  to  $^{150}\text{Sm}$  was probed in two experiments:  $^{150}\text{Nd}(^3\text{He}, t)^{150}\text{Pm}^*$  at RCNP, Osaka, Japan, and  $^{150}\text{Sm}(t, ^3\text{He})^{150}\text{Pm}^*$  at NSCL/MSU, East Lansing, Michigan, USA. Gamow-Teller strength distributions and dipole and quadrupole cross section distributions have been extracted using multipole decomposition techniques, including a strong GT state in  $^{150}\text{Pm}$  at 0.11 MeV. Applying the extracted Gamow-Teller strength from both experiments in this region, the single-state dominance hypothesis predicts a  $2\nu\beta\beta$  decay half life of  $10.0 \pm 3.7 \times 10^{18}$  years. This is a reasonable result, but the presence of other low-lying Gamow-Teller strength requires further investigation using QRPA or other theoretical techniques. The extracted strength distributions should constrain the nuclear matrix elements for both  $2\nu\beta\beta$  and  $0\nu\beta\beta$  decay. In addition, an excess of Gamow-Teller strength in the  $^{150}\text{Sm}(t, ^3\text{He})$  experiment is attributed to the population of the IVSGMR. Data are compared with deformed QRPA calculations from V. Rodin.



Copyright by  
CAROL JEANNE GUESS  
2010



*To Victor and Lois Guess,  
who have always supported and encouraged  
my interest in science.*

## ACKNOWLEDGMENTS

No thesis is completed in a vacuum, even in a field like nuclear physics where vacuum systems are a part of life. There are many people who have contributed to the experiments described here and to the thesis itself.

First, I'd like to thank my adviser, Dr. Remco G.T. Zegers. I knew upon my arrival at the cyclotron that any professor carrying a mug depicting the Muppets Statler and Waldorf would be an interesting person to talk to, and I was not disappointed. He puts an amazing amount of time into his research students and is always ready to listen and give comments and suggestions. I appreciate his deep knowledge of physics, patience with students as we learn (and forget, and learn again), and attention to details that others overlook. His sense of humor, informal manner, and perceptive questions help to make the charge-exchange group an invigorating environment in which to learn physics. All chapters of this thesis were drastically improved due to Remco's insistence on reading things again and again until they were completely correct and well-organized.

Drs. Alex Brown, Alexandra Gade, Wayne Repko, and Stuart Tessmer agreed to serve on my guidance committee. I thank them for their assistance over the last few years and for helpful comments on this thesis.

I have benefited from many friendships with the members of the CE group over the last 5 years. Though the group members have changed, we have a convivial atmosphere and I've benefited from interacting with all of you. Sam Austin's persistent questions during group meetings have been very valuable, as has Daniel Bazin's knowledge of the S800 spectrometer. Arthur, Yoshi, George, and Masako have been postdocs in our group and were always willing to answer my questions. Meredith and Wes have done previous triton beam experiments and their experiences were invaluable in the planning process for my ( $t, {}^3\text{He}$ ) experiment and helping me get on my feet with the PAW code. Wes has given me many detailed explanations of CE



phenomena, and I appreciate his insights. Rhiannon has been very supportive and always has constructive criticism when I need it, and was very helpful while locating interview clothes. Her policy of eating anything that I cook or bake has been very entertaining. Amanda is the perfect source for a completely logical viewpoint when I need to bounce ideas off of someone, and I appreciate her sense of humor and generosity. Jenna has boundless enthusiasm and attention to detail no matter what she is working on, even when grading papers and working out the minutiae of an electronics diagram. Shawna's tendency to ask the first question is inspirational. Thanks for taking so many midnight shifts. I hope we can work together again soon.

The other graduate students at the cyclotron have been unfailingly friendly and helpful, and I appreciate the good conversations I have had with many of you. Many thanks go to my amazing office-mates. Despite having five people in the office, we have always managed to get along. I'll miss the interesting conversations and good food that occur so frequently in the office.

The cyclotron staff and my collaborators at NSCL and RCNP were very helpful during planning and execution of my two experiments. Thank you for the explanations, help with design and setup, great beam tunes, and for coming in to fix the beam line magnets at 4 am. H. Fujita, and T. Adachi were invaluable while setting up the  $^{150}\text{Nd}(^3\text{He},t)$  experiment, and I also appreciate insightful discussions with Y. Fujita, H. Ejiri, M. Fujiwara, D. Frekers, and J. Thies. J. Yurkon and N. Verhanovitz made the  $^{150}\text{Sm}$  target, and J. Honke designed the target frames. Daniel, Mauricio, and Remco ensured that the dispersion-matching was correct. H. Sakai and S. Noji allowed us to use their  $^{13}\text{C}$  target for calibrations.

Vadim Rodin has answered many questions about his QRPA calculations. Any mistakes in my descriptions of his work are mine.

The National Science Foundation and the Joint Institute for Nuclear Astrophysics provided the funds for my graduate career, bought my targets, sent me to Japan twice,

and gave me money to present at conferences.

The Capital Area District Library and the Curious Book Shop have helped to keep me sane.

When I arrived at the cyclotron after receiving a music minor, I hoped to stay active in the music community. The Grand Canonical Ensemble has been a source of bad physics jokes, laughter, and friendship over the last five years and a wonderful break from nuclear physics. I miss singing with you already.

Many thanks go out to Amanda, Megan, Ania, and Dan for fun and eventually productive homework sessions. Somehow, we always managed to get work done, even when it was delayed by spherical jousting horses, quantum mechanics Pac-Man, pumpkin carving, and discussions about stuff completely unrelated to physics. Ania, I'll miss our food trades.

My friends in Dinner Club have shared so many meals of delicious food, good wines, piñatas, plays, poetry, and friendship. Thanks to Kim, Erin, Neil, Ana, and Catherine and those who have come to our meetings from time to time. I look forward to future meetings in our separate states and countries.

Johanna and John have been extremely helpful during beam time, big exams, and stretches of concentrated writing. Thank you for the extra dishes and cat care.

Victor and Lois Guess were very understanding about my lack of visits home, even though I lived a 2-hour drive away from them. Mom and Dad, thank you.

Neil, thank you for all of your encouragement, love, and support.

# TABLE OF CONTENTS

<b>List of Figures</b>	x
<b>List of Tables</b>	xiv
<b>1 Introduction</b>	<b>1</b>
1.1 Motivation	1
1.2 Organization	3
<b>2 Double Beta Decay</b>	<b>4</b>
2.1 $2\nu$ and $0\nu$ Double Beta Decay	4
2.1.1 Introduction	4
2.1.2 Implications	6
2.2 Detection Challenges	7
2.2.1 Detection Methods	7
2.2.2 Detectors for $^{150}\text{Nd}$ $\beta\beta$ decay	10
2.3 Nuclear Matrix Elements	11
2.3.1 Half-Life Calculation	11
2.3.2 The Shell Model Approach	15
2.3.3 QRPA	16
2.3.4 Constraining NMEs with charge-exchange experiments	18
<b>3 Charge-Exchange Reactions</b>	<b>21</b>
3.1 Introduction to Charge-Exchange Reactions	21
3.2 Reaction Theory	26
3.2.1 DWBA	26
3.2.2 One-body transition densities	28
3.2.3 The nucleon-nucleon interaction	29
3.2.4 FOLD	32
3.2.5 DWHI	33
3.2.6 The unit cross section and B(GT)	34
3.3 Giant Resonances	35
<b>4 <math>^{150}\text{Nd}(^3\text{He},t)^{150}\text{Pm}^*</math> at RCNP</b>	<b>42</b>
4.1 RCNP Experimental Setup and Procedure	42
4.1.1 Beam preparation and tuning	42
4.2 Calibrations	52
4.2.1 Sieve Slit Calibrations	52
4.2.2 Beam rate Calibration and Cross Section Calculation	54
4.3 Analysis of Data	55

# TABLE OF CONTENTS

<b>List of Figures</b> . . . . .	x
<b>List of Tables</b> . . . . .	xiv
<b>1 Introduction</b> . . . . .	<b>1</b>
1.1 Motivation . . . . .	1
1.2 Organization . . . . .	3
<b>2 Double Beta Decay</b> . . . . .	<b>4</b>
2.1 $2\nu$ and $0\nu$ Double Beta Decay . . . . .	4
2.1.1 Introduction . . . . .	4
2.1.2 Implications . . . . .	6
2.2 Detection Challenges . . . . .	7
2.2.1 Detection Methods . . . . .	7
2.2.2 Detectors for $^{150}\text{Nd}$ $\beta\beta$ decay . . . . .	10
2.3 Nuclear Matrix Elements . . . . .	11
2.3.1 Half-Life Calculation . . . . .	11
2.3.2 The Shell Model Approach . . . . .	15
2.3.3 QRPA . . . . .	16
2.3.4 Constraining NMEs with charge-exchange experiments . . . . .	18
<b>3 Charge-Exchange Reactions</b> . . . . .	<b>21</b>
3.1 Introduction to Charge-Exchange Reactions . . . . .	21
3.2 Reaction Theory . . . . .	26
3.2.1 DWBA . . . . .	26
3.2.2 One-body transition densities . . . . .	28
3.2.3 The nucleon-nucleon interaction . . . . .	29
3.2.4 FOLD . . . . .	32
3.2.5 DWHI . . . . .	33
3.2.6 The unit cross section and B(GT) . . . . .	34
3.3 Giant Resonances . . . . .	35
<b>4 <math>^{150}\text{Nd}(^3\text{He},t)^{150}\text{Pm}^*</math> at RCNP</b> . . . . .	<b>42</b>
4.1 RCNP Experimental Setup and Procedure . . . . .	42
4.1.1 Beam preparation and tuning . . . . .	42
4.2 Calibrations . . . . .	52
4.2.1 Sieve Slit Calibrations . . . . .	52
4.2.2 Beam rate Calibration and Cross Section Calculation . . . . .	54
4.3 Analysis of Data . . . . .	55

4.3.1	FOLD calculations for $^{150}\text{Nd}(^3\text{He},t)$ . . . . .	58
4.3.2	The Optical Potential and the IAS . . . . .	58
4.3.3	Multipole Decomposition Analysis . . . . .	61
4.3.4	Resonance fits . . . . .	65
4.3.5	Extrapolation to $q=0$ . . . . .	77
4.3.6	Calculation of the Gamow-Teller strength . . . . .	79
4.3.7	Other Multipole Excitations . . . . .	81
4.4	Comparison with Theory . . . . .	88
4.4.1	Cross sections and Giant Resonances . . . . .	88
4.4.2	QRPA calculations . . . . .	90
<b>5</b>	<b><math>^{150}\text{Sm}(t,^3\text{He})^{150}\text{Pm}^*</math> at the NSCL . . . . .</b>	<b>95</b>
5.1	Experimental Setup and Procedure . . . . .	95
5.1.1	Production of a Triton Beam . . . . .	95
5.1.2	The S800 Focal Plane . . . . .	100
5.2	Calibrations . . . . .	102
5.2.1	CRDC Mask Calibrations . . . . .	102
5.2.2	Beam Rate Calibration . . . . .	102
5.2.3	Calculation of the Excitation Energy of $^{150}\text{Pm}$ . . . . .	104
5.2.4	Acceptance Corrections . . . . .	106
5.2.5	Background and Hydrogen Subtraction . . . . .	109
5.2.6	Calculation of the Cross Section . . . . .	112
5.3	Data Analysis . . . . .	115
5.3.1	FOLD calculations . . . . .	115
5.3.2	Multipole Decomposition . . . . .	118
5.3.3	Extrapolation to $q=0$ . . . . .	123
5.3.4	Calculation of the Gamow-Teller strength . . . . .	123
5.3.5	Other Multipole Excitations . . . . .	129
5.4	Comparison with Theory . . . . .	139
5.4.1	$\Delta L=0$ Cross sections and the IVSGMR . . . . .	139
5.4.2	QRPA calculations . . . . .	140
<b>6</b>	<b>Application to <math>2\nu\beta\beta</math> decay . . . . .</b>	<b>145</b>
6.1	Low-lying states and the SSD hypothesis . . . . .	145
6.2	Calculating the $2\nu\beta\beta$ decay half life in the SSD . . . . .	146
<b>7</b>	<b>Conclusions and Outlook . . . . .</b>	<b>149</b>
	<b>Bibliography . . . . .</b>	<b>152</b>



## LIST OF FIGURES

Images in this dissertation are presented in color

2.1	The two methods of double beta decay, 2-neutrino and 0-neutrino. . .	5
2.2	Neutrino mixing and two possible arrangements of the hierarchy. . . .	7
2.3	Simulation of the $\beta\beta$ decay summed electron spectrum in a direct counting experiment. . . . .	9
2.4	A SuperNemo module . . . . .	11
2.5	Prototype of DCBA. . . . .	12
2.6	The SNO detector. . . . .	13
2.7	Population of intermediate states in $^{150}\text{Pm}$ with charge-exchange re- actions. . . . .	19
3.1	Schematic of charge-exchange on a subset of the chart of nuclides. . .	24
3.2	Isospin in charge-exchange reactions. . . . .	25
3.3	Pauli blocking in charge-exchange reactions. . . . .	25
3.4	Operator strengths for the $\sigma\tau$ and $\tau$ t-matrices. . . . .	31
3.5	The Fermi and Gamow-Teller unit cross sections as a function of A. .	36
3.6	Giant Resonances . . . . .	38

## LIST OF FIGURES

Images in this dissertation are presented in color

2.1	The two methods of double beta decay, 2-neutrino and 0-neutrino. . .	5
2.2	Neutrino mixing and two possible arrangements of the hierarchy. . . .	7
2.3	Simulation of the $\beta\beta$ decay summed electron spectrum in a direct counting experiment. . . . .	9
2.4	A SuperNemo module . . . . .	11
2.5	Prototype of DCBA. . . . .	12
2.6	The SNO detector. . . . .	13
2.7	Population of intermediate states in $^{150}\text{Pm}$ with charge-exchange reactions. . . . .	19
3.1	Schematic of charge-exchange on a subset of the chart of nuclides. . .	24
3.2	Isospin in charge-exchange reactions. . . . .	25
3.3	Pauli blocking in charge-exchange reactions. . . . .	25
3.4	Operator strengths for the $\sigma\tau$ and $\tau$ t-matrices. . . . .	31
3.5	The Fermi and Gamow-Teller unit cross sections as a function of A. .	36
3.6	Giant Resonances . . . . .	38

3.7	IVSGMR schematic for $^{150}\text{Nd} \rightarrow ^{150}\text{Pm}$ . . . . .	40
3.8	IVSGMR schematic for $^{150}\text{Sm} \rightarrow ^{150}\text{Pm}$ . . . . .	41
4.1	The WS beamline at RCNP. . . . .	44
4.2	Ion optical modes for high-resolution spectrometers . . . . .	45
4.3	Dispersion-matched beam image at the target of the Grand Raiden spectrometer. . . . .	46
4.4	The $^{150}\text{Nd}$ targets . . . . .	47
4.5	The Grand Raiden Spectrometer . . . . .	48
4.6	PID for the Grand Raiden . . . . .	49
4.7	Angular acceptance of the Grand Raiden . . . . .	50
4.8	Elastic scattering on $^{150}\text{Nd}$ . . . . .	51
4.9	Images of the sieve-slit as measured in the focal plane of the Grand Raiden spectrometer. . . . .	53
4.10	Reconstructed sieve slit spectrum after the determination of raytracing parameters. . . . .	54
4.11	Cross sections for the $^{150}\text{Nd}(^3\text{He,t})$ experiment . . . . .	56
4.12	Cross sections from 0-2 MeV for the $^{150}\text{Nd}(^3\text{He,t})$ experiment. . . . .	57
4.13	Angular distributions from $^{150}\text{Nd}(^3\text{He,t})$ as calculated with FOLD. . . . .	59
4.14	The angular distribution of the optical potential compared to the IAS . . . . .	60
4.15	Multipole decomposition of the first two peaks in $^{150}\text{Pm}$ . . . . .	63
4.16	Multipole decomposition of the 5-6 MeV excitation energy bin. . . . .	64
4.17	Multipole decomposition summary for each half-degree angular bin. . . . .	66
4.17	<i>cont.</i> Multipole decomposition summary for each half-degree angular bin. . . . .	67

4.17 <i>cont.</i> Multipole decomposition summary for each half-degree angular bin. . . . .	68
4.17 <i>cont.</i> Multipole decomposition summary for each half-degree angular bin. . . . .	69
4.18 Resonance fit to the excitation energy spectrum. . . . .	72
4.19 Angular distributions of the giant resonances. . . . .	78
4.20 Ratio of the cross section at $\theta=0^\circ$ and 0 linear momentum transfer to that of 0 linear momentum transfer, as calculated in DWBA. . . . .	80
4.21 GT strength from the MDA . . . . .	81
4.22 Low-lying GT strength from the MDA . . . . .	84
4.23 Dipole cross sections from the MDA . . . . .	85
4.24 Quadrupole cross sections from the MDA . . . . .	85
4.25 QRPA calculations for $^{150}\text{Nd}(^3\text{He},t)$ . . . . .	91
4.26 Gamow-Teller strength in $^{150}\text{Pm}$ via $^{150}\text{Nd}(^3\text{He},t)$ . . . . .	93
4.27 Dipole cross sections and strength in $^{150}\text{Pm}$ via $^{150}\text{Nd}(^3\text{He},t)$ . . . .	94
5.1 Schematic of the Coupled Cyclotron Facility and the S800 Spectrograph	96
5.2 Dispersion-matched triton beam image at the target of the S800 spectrometer. . . . .	98
5.3 The $^{150}\text{Sm}$ target . . . . .	99
5.4 Layout of the CRDCs in the focal plane of the S800 spectrometer . .	100
5.5 Ytac spectrum . . . . .	105
5.6 PID at the S800 focal plane . . . . .	107
5.7 Background subtraction for $^{150}\text{Sm}(t,^3\text{He})$ . . . . .	110
5.8 Hydrogen subtraction for $^{150}\text{Sm}(t,^3\text{He})$ . . . . .	111

5.9	Cross sections for the $^{150}\text{Sm}(t,^3\text{He})$ experiment (300 keV bins)	113
5.10	Cross sections for the $^{150}\text{Sm}(t,^3\text{He})$ experiment (1 MeV bins)	114
5.11	Angular distributions from $^{150}\text{Sm}(t,^3\text{He})$ as calculated with FOLD, at $Q=0$ .	116
5.12	Angular distributions from $^{150}\text{Sm}(t,^3\text{He})$ as calculated with FOLD, at $Q=20$ .	117
5.13	MDA for the 0-1 MeV excitation energy bin	119
5.14	MDA for the 20-21 MeV excitation energy bin	120
5.15	MDA for the 0-0.3 MeV excitation energy bin	121
5.16	MDA for the 0.1-0.2 MeV excitation energy bin	122
5.17	Multipole decomposition summary for each angular bin.	124
5.18	Multipole decomposition summary for each angular bin (0-6 MeV).	127
5.19	Ratio of the cross section at $\theta=0^\circ$ and 0 linear momentum transfer to that of 0 linear momentum transfer, as calculated in DWBA.	130
5.20	Extracted GT strength, 0-26 MeV	132
5.21	Extracted GT strength, 0-6 MeV	134
5.22	Extracted $\Delta L=1$ cross section, 0-26 MeV	135
5.23	Extracted $\Delta L=2$ cross section, 0-26 MeV	138
5.24	Raw QRPA calculations for $^{150}\text{Sm}(t,^3\text{He})$	141
5.25	Gamow-Teller strength in $^{150}\text{Pm}$ via $^{150}\text{Sm}(t,^3\text{He})$	143
5.26	Dipole cross sections in $^{150}\text{Pm}$ via $^{150}\text{Sm}(t,^3\text{He})$	144
6.1	B(GT) strength in $^{150}\text{Pm}$ at low energies	147



## LIST OF TABLES

2.1	Half-life values for $\beta\beta$ decay. . . . .	10
3.1	Charge-exchange excitations and their quantum numbers . . . . .	22
3.2	Giant resonances . . . . .	39
4.1	Parameters of the Grand Raiden Spectrometer . . . . .	48
4.2	Optical potentials for the elastic scattering data and the angular distribution of the IAS. . . . .	61
4.3	Parameters used in calculating the quasi-free curve. . . . .	77
4.4	Gamow-Teller strengths from resonance fits. . . . .	80
4.5	Gamow-Teller strength distribution from the MDA, 0-30 MeV . . . .	82
4.6	Gamow-Teller strength distribution from low-lying states, 0-2 MeV. .	83
4.7	Dipole cross sections from the MDA, 0-30 MeV . . . . .	86
4.8	Quadrupole cross sections from the MDA, 0-30 MeV . . . . .	87
4.9	Dipole cross sections from giant resonance fits. . . . .	88
4.10	Quadrupole cross sections from giant resonance fits. . . . .	88
4.11	Exhaustion of the full normal mode strength for $\Delta L=0$ . . . . .	89
4.12	Exhaustion of normal mode strength for $\Delta L=1$ . . . . .	90
4.13	Exhaustion of normal mode strength for $\Delta L=2$ . . . . .	90

4.14	Values of $\beta_2$ , $g_{pp}$ , and $g_{ph}$ as adopted in the QRPA calculations. . . .	90
5.1	Parameters of the S800 Spectrometer . . . . .	101
5.2	Important S800 parameters in the analysis of the $^{150}\text{Sm}(t, ^3\text{He})$ experiment . . . . .	103
5.3	Parameters for the $^{150}\text{Sm}(t, ^3\text{He})$ missing mass calculation . . . . .	108
5.4	Gamow-Teller strength distribution from the MDA, 0-26 MeV . . . .	131
5.5	Gamow-Teller strength distribution from the MDA, 0-6 MeV . . . .	133
5.6	$\Delta L=1$ cross sections from the MDA, 0-26 MeV . . . . .	136
5.7	$\Delta L=2$ cross sections from the MDA, 0-26 MeV . . . . .	137
6.1	Calculation of the $2\nu\beta\beta$ decay matrix element assuming single-state dominance . . . . .	147

# Chapter 1

## Introduction

### 1.1 Motivation

Double beta decay is currently the focus of a great deal of interest from within the physics community.  $2\nu\beta\beta$  decay occurs when two neutrinos and two electrons are simultaneously emitted from a nucleus. This process occurs only when other decay methods are forbidden, and the half-lives associated with it are extremely long (greater than  $10^{17}$  years). Much of the interest in  $\beta\beta$  decay is centered around the second possible mode, which is  $0\nu\beta\beta$  decay. The emission of two electrons without two neutrinos would violate the Standard Model, breaking the conservation of lepton number, and would prove that neutrinos are Majorana rather than Dirac in nature. A Majorana neutrino is its own antiparticle. Half life values for the  $0\nu$  mode of decay are several orders of magnitude higher than the  $2\nu$  mode and  $0\nu$  events could easily be overshadowed by  $2\nu$  events, so successful detection of this  $0\nu$  mode would be a major experimental feat. If the measurement is exact enough, it should be possible to extract the Majorana neutrino mass from the half life.

$\beta\beta$  emitters tend to be heavy nuclei, which makes them hard to model. Theorists working on this problem must model the location and strength of an enormous number

of states, and little to no data exists to constrain these models for several nuclei. The decay of  $^{150}\text{Nd}$  to  $^{150}\text{Sm}$  (through  $^{150}\text{Pm}$ ) is one of these cases. A quantity called a nuclear matrix element contains the physics of two simultaneous beta decays, from  $^{150}\text{Nd}$  to  $^{150}\text{Pm}$  and then to  $^{150}\text{Sm}$ , and this quantity must be known with an error less than 20% to design the experiments that measure the decay half life and then to successfully extract the neutrino mass from a half life measurement [1]. Knowing the location of the levels in the intermediate nucleus, as well as how strongly they may be populated, can place constraints on the models used to describe  $\beta\beta$  decay.

Charge-exchange experiments are an excellent tool for this, since they allow us to measure the location and strength of Gamow-Teller, Fermi, dipole, and quadrupole transitions along the same paths taken by beta decay. A charge-exchange reaction is characterized by a change in isospin ( $\Delta T$ ) of 1. When performed at intermediate energies (energies between 100 and 500 MeV/u), the reaction can be modeled as a single-step process and Gamow-Teller transitions are preferentially excited.

This thesis describes two charge-exchange experiments designed to constrain the nuclear matrix elements for the  $\beta\beta$  decay of  $^{150}\text{Nd}$  to  $^{150}\text{Sm}$ . Both populate excited states in  $^{150}\text{Pm}$ . The first experiment,  $^{150}\text{Nd}(^3\text{He},t)$ , took place at RCNP (Osaka, Japan) with a primary  $^3\text{He}$  beam. The second experiment was  $^{150}\text{Sm}(t,^3\text{He})$  and took place at the NSCL (East Lansing, Michigan, USA) with a secondary triton beam. Gamow-Teller strengths were extracted from both experiments, along with information on dipole and quadrupole strengths and the population of several giant resonances. The results of these two experiments will be immediately useful for  $\beta\beta$  decay theorists and for several experiments that are planned to directly search for  $0\nu\beta\beta$  decay signals [2, 3, 4] from  $^{150}\text{Nd}$ .

## 1.2 Organization

This work is divided into chapters by topic. Double beta decay is introduced in Chapter 2, followed by an introduction to charge-exchange reaction theory in Chapter 3. Chapters 4 and 5 discuss the two experiments and make up the bulk of this work. Chapter 6 briefly ties the two experiments together, and Chapter 7 summarizes the findings of both experiments and provides an outlook for similar experiments and future charge-exchange techniques.



# Chapter 2

## Double Beta Decay

### 2.1 $2\nu$ and $0\nu$ Double Beta Decay

#### 2.1.1 Introduction

Fermi introduced his theory of beta ( $\beta$ ) decay in 1934 [5, 6]. One year later, half lives for two-neutrino double-beta decay ( $2\nu\beta\beta$ ) were first calculated by M. Goeppert-Mayer [7]. She correctly predicted half lives to be on the order of  $10^{17}$  years or more. Four years later, M. Furry built upon this work by also considering zero-neutrino double beta decay ( $0\nu\beta\beta$ ) [8], which was possible only using Majorana symmetry concepts, a departure from Fermi's Dirac model. While double electron capture [9] has also been considered, much of the subsequent experimental and theoretical focus has been on  $2\nu\beta\beta$  and  $0\nu\beta\beta$  decays. Figure 2.1 shows a schematic of both types of decay.  $2\nu\beta\beta$  decay is modeled as two simultaneous  $\beta$  decays, making it a second-order weak interaction within the standard model.  $2\nu\beta\beta$  decay:

$$N(A, Z) \rightarrow N(A, Z + 2) + 2e^{-} + 2\bar{\nu}_e \quad (2\beta_{2\nu}^{-}) \quad (2.1)$$

$$N(A, Z) \rightarrow N(A, Z - 2) + 2e^{+} + 2\nu_e \quad (2\beta_{2\nu}^{+}) \quad (2.2)$$

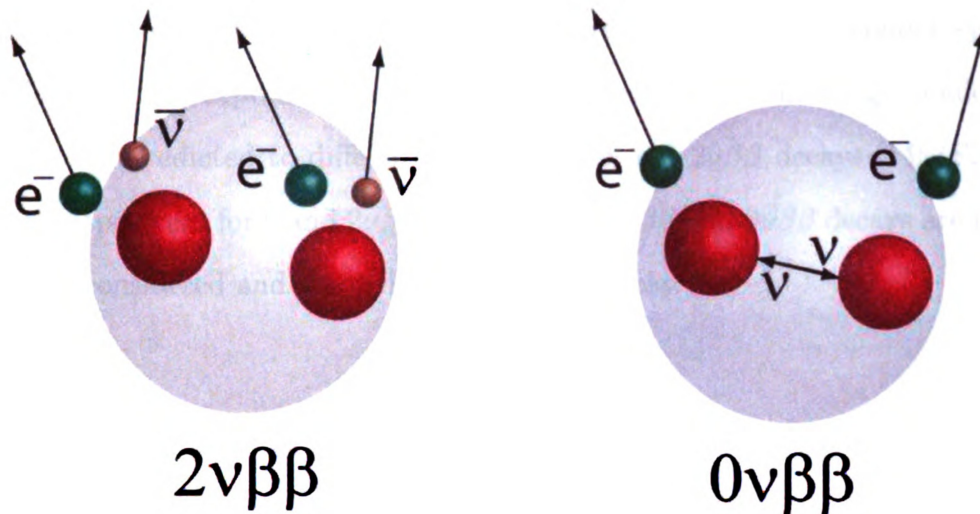


Figure 2.1: The two methods of double beta decay, 2-neutrino and 0-neutrino.

is permitted in the standard model, while  $0\nu\beta\beta$  decay

$$N(A, Z) \rightarrow N(A, Z + 2) + 2e^- \quad (2\beta_{0\nu}^-) \quad (2.3)$$

$$N(A, Z) \rightarrow N(A, Z - 2) + 2e^+ \quad (2\beta_{0\nu}^+) \quad (2.4)$$

would require physics beyond the standard model.  $\beta\beta$  half lives are between  $10^{17}$  to  $10^{26}$  years, and  $\beta\beta$  decay is only observed in situations where single- $\beta$  decay and other decay modes are forbidden. This can have two causes: extremely high angular momentum transfer between mother and daughter (e.g.  $^{48}\text{Ca}$ ), or parent nuclei where decay to the  $\beta$  daughter has a positive Q value and decay to the  $\beta\beta$  daughter a negative Q value. All  $\beta\beta$  mother and daughter nuclei have ground state  $J^\pi$  of  $0^+$ , and decay from ground state to ground state is more common than that to excited states, because the phase space is reduced in decay to excited states [10, 11]. Currently, decay to excited states has only been measured in  $^{100}\text{Mo}$  and  $^{150}\text{Nd}$  (see [12] and references within). Some exotic models predict other causes and variants of  $\beta\beta$

decay, such as the simultaneous emission of a Majoran  $\chi$  particle, which is a hypothetical Goldstone boson associated with the breaking of lepton number symmetry [13]. However, the experimental spectrum of summed electron energy would have a shape that is predicted to differ from both  $0\nu\beta\beta$  and  $2\nu\beta\beta$  decays [14] (Figure 2.3 shows this spectrum for 0 and  $2\nu\beta\beta$  decay only).  $2\nu\beta\beta$  and  $0\nu\beta\beta$  decays are the most frequently considered and studied modes for  $\beta\beta$  decay.

## 2.1.2 Implications

Signatures of neutrino oscillation were first seen in atmospheric neutrinos during the Super-Kamiokande experiment [15] and were confirmed by the SNO experiment [16]. The scientific community then turned to questions of the absolute mass scale, how the flavors change, the nature of the mass hierarchy, and whether neutrinos are their own antiparticle. Neutrino flavor eigenstates and mass eigenstates are linked through the Pontecorvo-Maki-Nakagawa-Sakata (PMNS) unitary mixing matrix:

$$\begin{pmatrix} \nu_e \\ \nu_\mu \\ \nu_\tau \end{pmatrix} = \begin{pmatrix} U_{e1} & U_{e2} & U_{e3} \\ U_{\mu1} & U_{\mu2} & U_{\mu3} \\ U_{\tau1} & U_{\tau2} & U_{\tau3} \end{pmatrix} \begin{pmatrix} \nu_1 \\ \nu_2 \\ \nu_3 \end{pmatrix} \quad (2.5)$$

where  $e$ ,  $\mu$ , and  $\tau$  are flavor eigenstates and 1, 2, and 3 are mass eigenstates. The  $U_{\alpha i}$  matrix elements contain the neutrino mixing angles and three charge-parity (CP) violating phases (one Dirac phase and two Majorana phases, none of which have been determined yet). Neither the absolute scale nor the hierarchy of mass eigenstates is well known. Oscillation experiments were able to determine the squared differences between squares of mass eigenstates, but not their order. Figure 2.2 shows the two options for the neutrino hierarchy. Successful detection of neutrinoless double  $\beta$  decay would allow bounds to be placed on the absolute mass scale and hierarchy [17] if

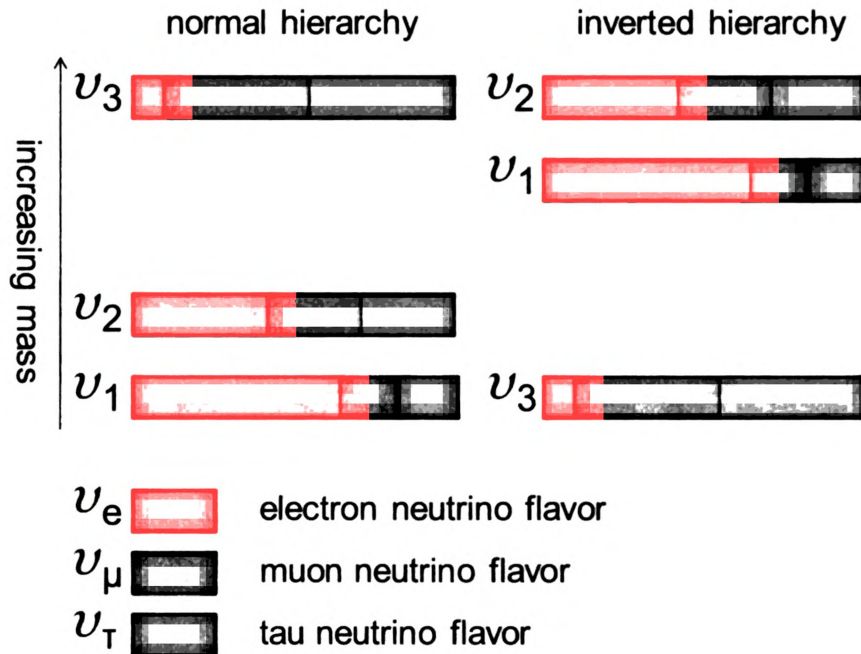


Figure 2.2: Two possible configurations of the neutrino mixing and hierarchy. If combined with improved measurements of the neutrino mixing angles and the mass squared differences, a successful measurement of double beta decay can constrain the absolute mass scale and hierarchy.

the mass squared differences and mixing angles are also known [18]. An observation of  $0\nu\beta\beta$  decay would break the conservation of lepton number and also immediately confirm that neutrinos are their own antiparticle (Majorana) rather than being two distinct particles (Dirac). An unprecedented number of experiments are being developed to measure this decay.

## 2.2 Detection Challenges

### 2.2.1 Detection Methods

There are three techniques used to detect evidence of  $\beta\beta$  decay: geochemical, radiochemical, and direct detection. In geochemical experiments, samples of very old ore are carefully analyzed for the presence of  $\beta\beta$  emitters and their daughters. Since this method looks only at the presence of past decays, it measures a total rate for com-

bined  $2\nu\beta\beta$  and  $0\nu\beta\beta$  decays [19]. In radiochemical studies, a 40-50 year old sealed sample containing a  $\beta\beta$  emitter is chemically purified and analyzed for evidence of  $\beta\beta$  decay [20, 21]. Like geochemical analysis, this method is sensitive to a total decay rate. The two methods have been used to set lower limits on the half lives of three isotopes.

The most common method of measuring  $\beta\beta$  decay half lives is that of direct counting experiments. In this method, a large quantity of an isotope is placed in a low-background environment and decay electrons analyzed. Many experiments take place underground and are built from extremely low-background material. Direct counting experiments can distinguish between the two decay methods.  $2\nu\beta\beta$  decay gives off a total of four particles: two electrons/positrons and two neutrinos/antineutrinos. Some of the decay energy is lost to the neutrinos, so the total decay energy of the electrons is therefore a continuous distribution. In  $0\nu\beta\beta$  decay (without emission of a Majoran  $\chi$ ), the neutrino is reabsorbed, and the sum of the two decay electrons must equal the total Q value for the reaction. Poor experimental energy resolution can lead to the tail of the  $2\nu\beta\beta$  decay overpowering a small  $0\nu\beta\beta$  decay signal, so accurate models of the detector response and simulated  $2\nu\beta\beta$  signal are important. Figure 2.3 shows a schematic for the a total  $\beta\beta$  decay electron energy spectrum.

A plethora of experimental techniques exist for direct detection experiments. The CANDLES [22] project searches for the decay of  $^{48}\text{Ca}$  using  $\text{CF}_2(\text{Eu})$  scintillators. CARVEL [23] is a competing experiment using  $^{48}\text{CaWO}_4$  crystals with an expected sensitivity of .04-.09 eV. CUORE (a larger version of CUORICINO) [24] uses bolometers to detect thermal energy from electrons emitted by the decay of  $^{128,130}\text{Te}$ . COBRA, made of cadmium-zinc-telluride (CZT) detectors, contains five  $\beta\beta$ - emitters and four  $\beta\beta+$  emitters [14]. MAJORANA [25] is constructed of segmented Ge detectors enriched in  $^{76}\text{Ge}$ , and together with GERDA [26] ( $^{76}\text{Ge}$  diodes) it will test the controversial claim for  $0\nu\beta\beta$  decay detection made by the HEIDELBERG-MOSCOW

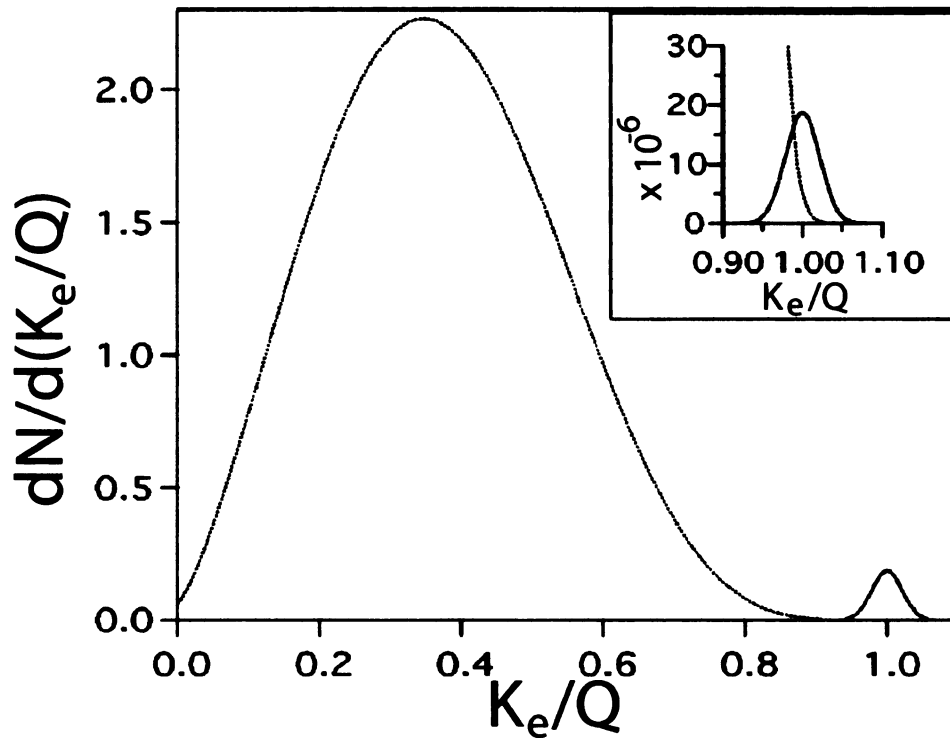


Figure 2.3: Simulation of the  $\beta\beta$  decay summed electron spectrum in a direct counting experiment, taken from reference [18].  $K_e$  is the electron kinetic energy and  $Q$  is the  $Q$  value. The  $0\nu\beta\beta$  events fall at  $K_e=Q=1$ , while the  $2\nu\beta\beta$  events have a wider energy distribution. In the inset, the size of the  $0\nu\beta\beta$  decay spectrum is normalized to  $10^{-6}$  of the  $2\nu\beta\beta$  decay amplitude. Detector energy resolutions of 5% are folded into the simulation. (see text)



Isotope	Q value (MeV)	$Z^2Q^5$	$G^{2\nu}(1/y)$ ([30])	$T^{1/2}$ (y) ([12, 31])
$^{48}\text{Ca}$	4.274	$5.7 \times 10^5$	$4.0 \times 10^{-17}$	$4.4^{+0.6}_{-0.5} \times 10^{19}$
$^{76}\text{Ge}$	2.039	$3.6 \times 10^4$	$1.3 \times 10^{-19}$	$1.5 \pm 0.1 \times 10^{21}$
$^{82}\text{Se}$	2.995	$2.8 \times 10^5$	$4.3 \times 10^{-18}$	$0.92 \pm 0.07 \times 10^{20}$
$^{96}\text{Zr}$	3.347	$6.7 \times 10^5$	$1.8 \times 10^{-17}$	$2.3 \pm 0.2 \times 10^{19}$
$^{100}\text{Mo}$	3.035	$4.5 \times 10^5$	$8.9 \times 10^{-18}$	$7.1 \pm 0.4 \times 10^{18}$
$^{116}\text{Cd}$	2.004	$7.4 \times 10^4$	$7.4 \times 10^{-18}$	$2.8 \pm 0.2 \times 10^{19}$
$^{124}\text{Sn}$	2.287	$1.6 \times 10^5$	$1.5 \times 10^{-18}$	$\geq 1.0 \pm 0.2 \times 10^{17}$
$^{128}\text{Te}$	0.865	$1.3 \times 10^3$	$8.5 \times 10^{-22}$	$1.9 \pm 0.4 \times 10^{24}$
$^{130}\text{Te}$	2.530	$2.8 \times 10^5$	$4.8 \times 10^{-18}$	$6.8^{+1.2}_{-1.1} \times 10^{20}$
$^{136}\text{Xe}$	2.468	$2.7 \times 10^5$	$4.9 \times 10^{-18}$	$\geq 8.1 \times 10^{20}$
$^{150}\text{Nd}$	3.368	$1.6 \times 10^6$	$1.2 \times 10^{-16}$	$8.2 \pm 0.9 \times 10^{18}$

Table 2.1: Recommended half-life values for  $\beta\beta$ -emitters. Q values are from NNDC.

experiment [27]. EXO [28] uses liquid xenon calorimeters to detect the  $\beta\beta$  decay of  $^{136}\text{Xe}$ . MOON [29] is a tracking calorimeter device that looks for the decay of  $^{100}\text{Mo}$ . Several more experiments are either planned or have completed their run, using some combination of these techniques. Table 2.1 lists the most recent recommended values for some double-beta half lives.

### 2.2.2 Detectors for $^{150}\text{Nd}$ $\beta\beta$ decay

In the case of  $\beta\beta$  decay from  $^{150}\text{Nd}$ , there are three high-sensitivity direct counting experiments planned: SuperNemo [32], DCBA [33], and SNO+ [4]. DCBA is a magnetic tracking chamber that will be able to trace three-dimensional electron paths. The detector is still in development, but it should be able to distinguish a neutrino mass as low as 0.1 to 0.5 eV. See Figure 2.5 for a picture of the prototype. SuperNemo is the successor to NEMOIII, which contained small slices of several different  $\beta\beta$  emitters. SuperNEMO is a calorimetry-based experiment and will look at either  $^{82}\text{Se}$  or  $^{150}\text{Nd}$  in more detail. Sensitivity is expected to be around 70 meV.

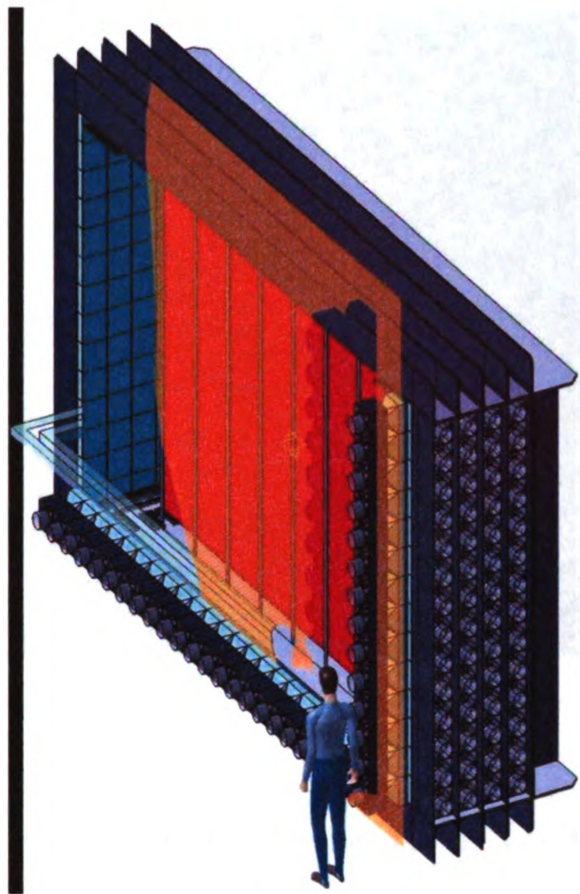


Figure 2.4: One module of the SuperNemo detector. Picture credit: [2].

Figure 2.4 shows a single SuperNEMO module. SNO+ is a successor to the SNO neutrino oscillation experiment, where the heavy water neutrino detector has been drained and will be replaced with Nd-loaded liquid scintillator. This detector aims for a sensitivity of around 100 meV [34]. A schematic of SNO+ is shown in Figure 2.6.

## 2.3 Nuclear Matrix Elements

### 2.3.1 Half-Life Calculation

$^{150}\text{Nd}$  is a popular choice of nucleus because it has a short  $2\nu\beta\beta$  decay half life and is expected to also have a short half life for  $0\nu\beta\beta$  decay. In order to accurately predict

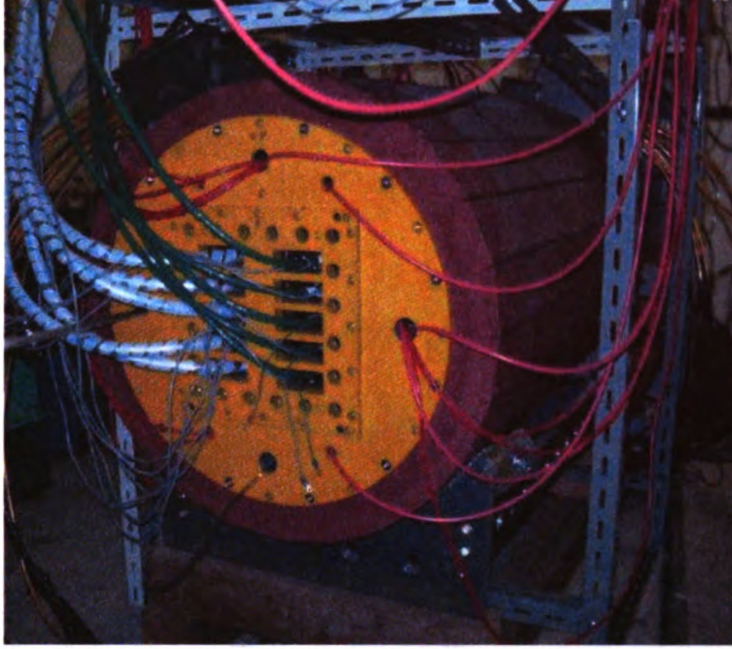


Figure 2.5: A prototype of the DCBA detector. Image taken from [3].

what direct detection experiments might see, all parameters of the half life equation must be well known. The  $2\nu\beta\beta$  decay half life is

$$[T_{1/2}^{2\nu}(0^+ \rightarrow 0^+)]^{-1} = G^{2\nu}(E_0, Z)|M_{GT}^{2\nu}|^2 \quad (2.6)$$

where  $G^{2\nu}$  is a phase space factor and is proportional to  $Z^2Q^5$ . It can be calculated exactly, and  $^{150}\text{Nd}$  has the highest value of this quantity.  $Z^2Q^5$  and  $G^{2\nu}$  values for  $\beta\beta$ -nuclei are shown in Table 2.1.  $M^{2\nu}$  can be represented by a double Gamow-Teller matrix element: a sum over the  $1^+$  states in the intermediate nucleus.

$$M_{GT}^{2\nu} = \sum_j \frac{\langle 0_f^+ \| \sigma\tau \| 1_j^+ \rangle \langle 1_j^+ \| \sigma\tau \| 0_i^+ \rangle}{E_j + Q_{\beta\beta/2} - E_0} \quad (2.7)$$

The double Gamow-Teller matrix element is the combination of Gamow-Teller matrix elements for each leg of the decay and comes from second-order perturbation theory. Chapter 3 will discuss the  $\sigma\tau$  (Gamow-Teller) operator in greater detail. In the



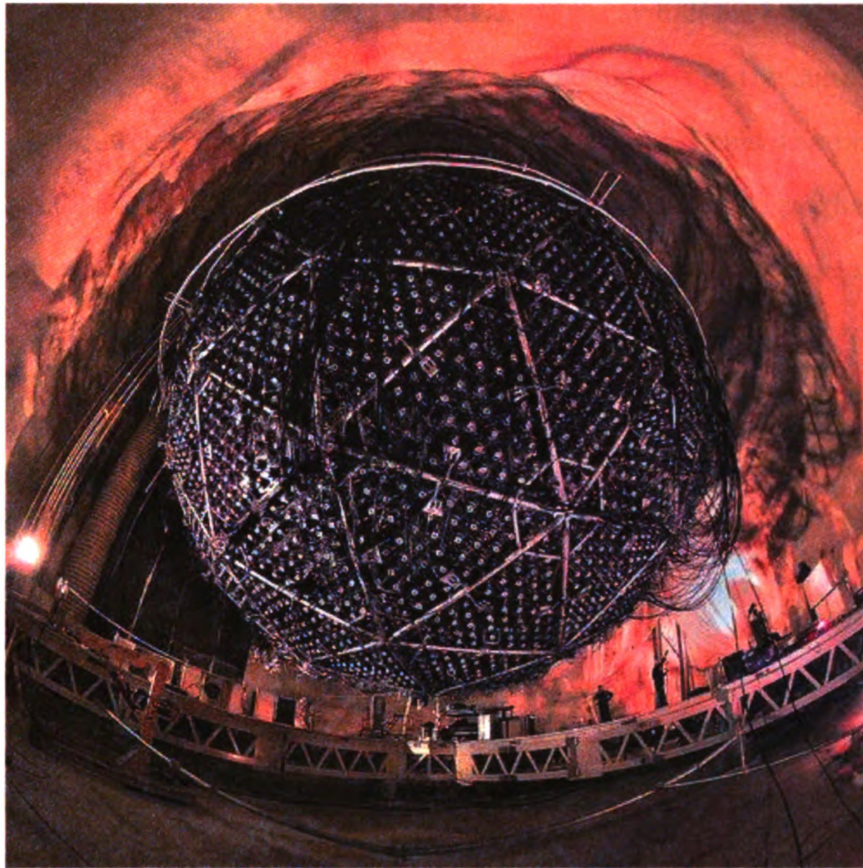


Figure 2.6: The SNO detector. SNO+ will feature the same acrylic vessel, but will be held down with a series of ropes to offset the density difference between liquid scintillator and water. Photo credit: Lawrence Berkeley National Lab (Roy Kaltschmidt, photographer)

denominator,  $E_0$  is the energy of the initial ground state,  $Q_{\beta\beta}$  is the Q value for  $\beta\beta$  decay, and  $E_j$  is the energy of the intermediate state. Contributions from the various states may interfere either constructively or destructively, so theory must be used to calculate the relative phases. Because of this, experimental information about transitions in each leg can constrain but not replace theory. Since the phase space factor  $G_\nu^2$  is well known (see Table 2.1) and the  $2\nu\beta\beta$  decay half life has been measured experimentally [35, 36], theorists can check their calculations of the summed nuclear matrix elements directly. Abad *et al.* [37] first hypothesized that the presence of a single low-lying state in the intermediate nucleus was sufficient to predict the  $2\nu\beta\beta$  decay half life. The idea of single-state dominance (SSD) has become a significant question in the field. It seems to apply to some nuclei but not to others, and it is not known whether higher-lying states simply do not contribute to the total matrix element or whether their contributions cancel [38]. Dvornický *et al.* [39] recently proposed that single-state dominance would not be realized in the decay of  $^{150}\text{Nd}$  unless a low-lying  $1^+$  state were measured in  $^{150}\text{Pm}$ , thinking higher-state dominance (HSD) to be more likely.

The  $0\nu$  mode of decay is much more complicated than the  $2\nu$  mode. A neutrino reabsorbed in  $0\nu\beta\beta$  decay can have a very large virtual excitation energy in the intermediate nucleus with an associated momentum transfer around 50-100 MeV/c [14], because the interaction occurs at a very short range. Therefore, the  $0\nu\beta\beta$  decay process can go through any intermediate state rather than just  $1^+$  states. The half life equation is

$$[T_{1/2}^{0\nu}(0^+ \rightarrow 0^+)]^{-1} = G^{0\nu}(E_0, Z) |M_{GT}^{0\nu} + M_T^{0\nu} + \frac{g_V^2}{g_A^2} M_F^{0\nu}|^2 \langle m_{\beta\beta} \rangle^2 \quad (2.8)$$

where  $G^{0\nu}$  is known [30]. Matrix elements for Gamow-Teller ( $M_{GT}^{0\nu}$ ), Fermi ( $M_F^{0\nu}$ ), and tensor ( $M_T^{0\nu}$ ) transitions must be calculated. The final term is the effective

Majorana neutrino mass:

$$m_{\beta\beta} = \sum_{k=1}^3 U_{ek}^2 m_k \quad (2.9)$$

where  $U$  is the unitary neutrino mixing matrix from section 2.1.2 and  $m$  is the neutrino mass eigenstate. Accurate half life calculations are important when planning direct decay experiments, but if a positive signal of neutrinoless  $\beta\beta$  decay is found, half life must be known to an error of 15-20% to allow for the extraction of the Majorana neutrino mass [1] with high enough precision to discern the correct neutrino mass scale and hierarchy [40]. This requires additional work on the nuclear matrix elements (NMEs).

### 2.3.2 The Shell Model Approach

The large-scale shell model can be used to calculate the nuclear matrix elements of  $\beta\beta$  emitters.  $2\nu\beta\beta$  decay in  $^{48}\text{Ca}$  can be calculated without any truncations to the pf model space [41]. Recently, Horoi *et al.* have extended this effort to the calculation of  $^{48}\text{Ca}$ 's  $0\nu\beta\beta$  decay matrix elements [42], though they assumed that negative parity states in the intermediate nucleus could safely be neglected. Unfortunately, the prohibitively large model spaces required for heavier nuclei restrict the reach of the shell model and do not allow for full calculations of these nuclei within complete model spaces. Caurier *et al.* did  $0\nu\beta\beta$  decay calculations in limited model spaces for  $^{76}\text{Ge}$  and  $^{82}\text{Se}$  when only considering the ground-state-to-ground-state transition [43]. The Interacting Shell Model has recently allowed for  $0\nu\beta\beta$  decay calculations in masses up to 136 [44], but these calculations (as well as many QRPA calculations) rely on the closure approximation. Since the  $0\nu\beta\beta$  decay calculation is so complex, attempts have been made to reduce the dependence of the calculated nuclear matrix elements on extensive knowledge of the intermediate nucleus. The closure approximation [45] collapses the sum over intermediate virtual states to a single matrix element

and approximates the difference in their excitation energies as an average energy. The rationalization for this approach is that the virtual neutrino's high momentum (100 MeV) drowns out the smaller differences in nuclear excitation energy [46]. Errors from using the closure approximation are estimated to be approximately 10% [47], but this is still a concern when the matrix elements overall need to be known to 15-20%. More accurate calculations are certainly desirable.

$^{150}\text{Nd}$  is both heavy and deformed, and shell model calculations are not yet available even if the closure approximation is applied, although work on the projected shell model may produce results in the future [48]. Calculations in the Interacting Boson Model can provide another tool to calculate  $\beta\beta$  decay matrix elements [49].

### 2.3.3 QRPA

The QRPA (quasiparticle random phase approximation) is based on the RPA (random phase approximation) method of calculation. Quasiparticles are fermions constructed from particles and holes via a canonical Bogoliubov transformation. The addition of quasiparticles to the RPA reproduces ground state pairing correlations more closely than with particles alone [50]. A full discussion on techniques for solving the QRPA equations will not be presented here. (See references [46, 51, 50, 52].) However, I will give a brief overview of recent developments in the field that are of importance to nuclear matrix element calculations for  $\beta\beta$  decay.

The QRPA model was developed to accurately describe collective states, such as giant resonances. In the words of reference [46], "...in the QRPA and RQRPA (relativistic QRPA) one can include essentially unlimited set of single-particle states ... but only a limited subset of configurations (iterations of the particlehole, respectively two-quasiparticle configurations), in contrast to the nuclear shell model where the opposite is true."

Two important variants of QRPA are the pnQRPA (proton-neutron QRPA) and

cQRPA (continuum QRPA). The pnQRPA [53, 54] was developed to model  $\beta$  decay and Gamow-Teller excitations in nuclei, and is now one of the most popular techniques for calculating  $\beta$  decay nuclear matrix elements. Particle-particle and particle-hole residual interactions are required [55]. The cQRPA [56, 57, 58] allows for the consideration of particle-unbound states and the study of widths and decay properties of isovector giant resonances (see section 3.3).

$2\nu\beta\beta$  decay calculations in the pnQRPA and cQRPA are very sensitive to the chosen values of the parameter  $g_{pp}$ . This parameter represents the strength of the particle-particle part of the proton-neutron two-body interaction [54, 59]. It is determined by the ratio of the particle-particle and particle-hole interaction strengths [60], and should be on the order of 1. A successful reproduction of the  $2\nu\beta\beta$  decay half life is often used to check the feasibility of the more difficult  $0\nu\beta\beta$  decay calculation. There are two main ways to determine the value of  $g_{pp}$ : one can fit it to matrix elements derived from experimental data on the  $2\nu\beta\beta$  decay half-life [61], or one can use information from single  $\beta$  decay [62]. Most calculations use the first method, but increased use of charge-exchange experiments to constrain nuclear matrix elements may change this. The QRPA's sensitivity to  $g_{pp}$  is a cause for concern [42], but using available data from single- and  $2\nu\beta\beta$  decay should constrain the term enough that calculations for  $0\nu\beta\beta$  decay can be successfully performed.

Large deformations in some  $\beta\beta$  emitters ( $^{76}\text{Ge}$ ,  $^{150}\text{Nd}$ ) have posed a serious challenge to theorists [63, 64]. Deformation differences between the mother and daughter nuclei are thought to decrease the  $\beta\beta$  decay nuclear matrix elements because of reduced overlap in their wavefunctions [65, 66] in comparison to transitions from one spherical nucleus to another. Introducing deformations into the QRPA calculations changes both the location and the shape of Gamow-Teller strengths in the intermediate nucleus. Information on these intermediate states is necessary for accurate calculations of the nuclear matrix elements, and this can be done with the use of



charge-exchange experiments.

The group of Vadim Rodin (University of Tübingen) has provided new QRPA calculations for the Gamow-Teller and dipole strengths in  $^{150}\text{Pm}$  from both  $^{150}\text{Nd}$  and  $^{150}\text{Sm}$ . These results will be presented and compared with experiment in Chapters 4, 5, and 6.

### 2.3.4 Constraining NMEs with charge-exchange experiments

Intermediate-energy charge-exchange experiments (see Chapter 3) can be used to preferentially populate Gamow-Teller transitions in the intermediate nucleus between the  $\beta\beta$  mother and daughter. Transitions in the  $\beta+$  direction may take place using the (n.p), (d, $^2\text{He}$ ), (t, $^3\text{He}$ ), or ( $^7\text{Li}$ , $^7\text{Be}$ ) reactions, and transitions in the  $\beta-$  direction may use the (p,n) or ( $^3\text{He}$ ,t) reactions.

Since all  $\beta\beta$  mothers and daughters have a ground state  $J^\pi$  of  $0^+$ , the Gamow-Teller transitions ( $\Delta L=0, \Delta S=1$ ) go to  $1^+$  states.  $2\nu\beta\beta$  decay should proceed largely through  $1^+$  states, and knowledge of the exact location and the strengths with these states are populated is important for accurate nuclear matrix element calculations. Charge-exchange experiments will also populate other multipoles, such as dipole and quadrupole transitions, which are significant in calculations of  $0\nu\beta\beta$  decay matrix elements [61]. Figure 2.7 shows the population of intermediate states in  $^{150}\text{Pm}$  via charge-exchange reactions on  $^{150}\text{Nd}$  and  $^{150}\text{Sm}$ .

A collaborative effort is underway to systematically measure charge-exchange transitions in  $\beta\beta$  decay nuclei. Older (p,n) and (n,p) data sets are being augmented by new data, and this approach allows for Gamow-Teller contributions to be measured up to high excitation energy.  $^{48}\text{Ca}(\text{p,n})$  and  $^{48}\text{Ti}(\text{n,p})$  were recently re-measured by Yako *et al.* [67]. Unfortunately, (n,p) measurements suffer from poor ( $\sim 1$  MeV) energy resolution, which makes spectroscopy of low-lying states very challenging. Use of more complex probes (such as (t, $^3\text{He}$ ) and (d, $^2\text{He}$ )) has brought (n,p)-direction reso-

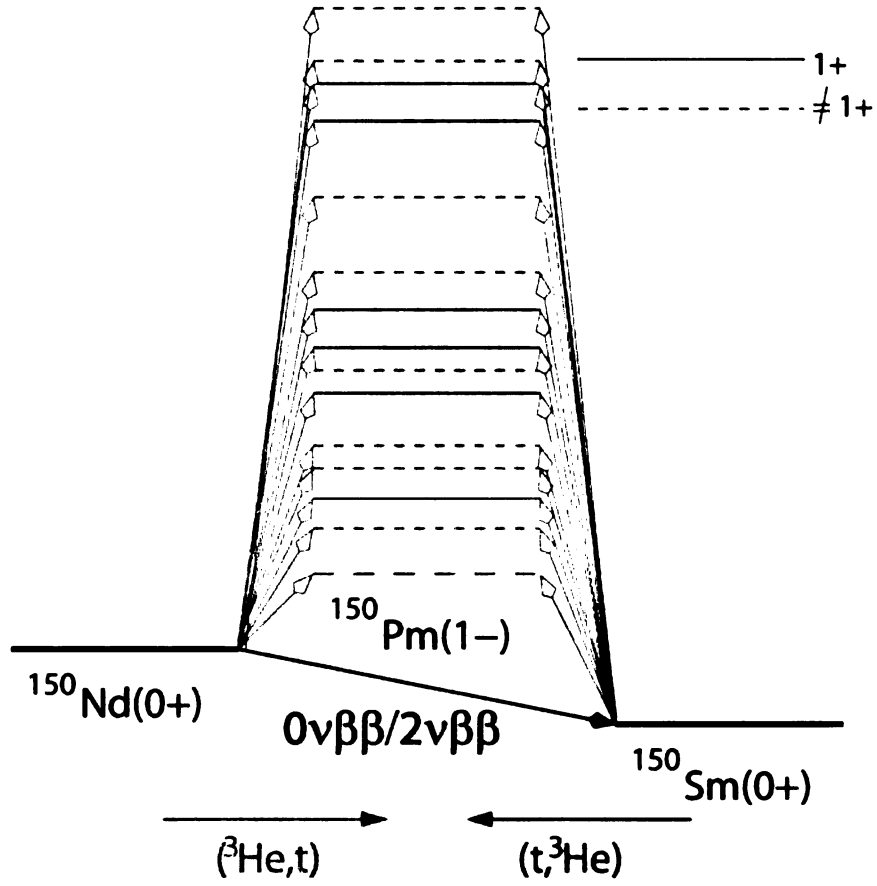


Figure 2.7: Population of intermediate states in  $^{150}\text{Pm}$  via the  $(t, {}^3\text{He})$  and  $({}^3\text{He}, t)$  charge-exchange reactions. This figure is a schematic, and levels shown do not correspond to the location of actual levels. Figure by R.G.T. Zegers.

lutions down to 110-300 keV. In the (p,n) direction, high-resolution beams of  $^3\text{He}$  are regularly produced at RCNP, and ( $^3\text{He,t}$ ) experiments can achieve a 20-40 keV resolution. Recent measurements include  $^{96}\text{Mo}(\text{d},^2\text{He})$  [68],  $^{76}\text{Se}(\text{d},^2\text{He})$  [69],  $^{64}\text{Zn}(\text{d},^2\text{He})$  [70],  $^{100}\text{Mo}(^3\text{He,t})$  and  $^{116}\text{Cd}(^3\text{He,t})$  [71],  $^{48}\text{Ti}(\text{d},^2\text{He})$  [72], and  $^{48}\text{Ca}(^3\text{He,t})$  [73]. Data on several more nuclei exist but have not yet been published. The measurements of  $^{150}\text{Nd}(^3\text{He,t})$  and  $^{150}\text{Pm}(\text{t},^3\text{He})$  described in this document are the first such measurements to address the  $\beta\beta$  decay of  $^{150}\text{Nd}$ .

# Chapter 3

## Charge-Exchange Reactions

### 3.1 Introduction to Charge-Exchange Reactions

Extensive programs in charge-exchange (CE) reactions have been developed in the last half century (see [74, 75] and references therein) to probe the spin-isospin response of nuclei. Charge-exchange reactions are characterized by an isospin transfer ( $\Delta T$ ) of 1, and can excite a number of different transitions. Table 3.1 provides a partial list. In hadronic charge-exchange, a proton (neutron) transitions into a neutron (proton). The process can be modeled by the exchange of  $\pi$  (and other) mesons between the projectile and the target, where the projectile may consist of a single nucleon or be a composite probe. Pion charge-exchange has also been used as a probe [76], but will not be discussed in any detail here. Although charge-exchange is mediated by the strong interaction and  $\beta$  decay by the weak interaction, the same final and initial states are populated. The Fermi and Gamow-Teller transitions correspond to the two types of allowed  $\beta$  decay, and the other transitions correspond to various types of forbidden  $\beta$  decays. In a  $\beta$  decay experiment, states may be seen in an excitation energy region from 0 MeV up to the Q value of the reaction, but higher-lying states will not be accessible. Charge-exchange reactions allow for the excitation of higher-

$\Delta\mathbf{L}$	$\Delta\mathbf{S}$	$\hbar\omega$	$0^+ \rightarrow J^\pi$
0	0	0	$0^+$ Fermi
0	1	0	$1^+$ Gamow-Teller
1	0	1	$1^-$ dipole
1	1	1	$(0,1,2)^-$ spin-dipole
2	0	0,2	$2^+$ quadrupole
2	1	0,2	$(1,2,3)^+$ spin-quadrupole
3	0	1,3	$3^-$ octupole
3	1	1,3	$(2,3,4)^-$ spin-octupole
4	0	0,2,4	$4^+$ hexadecapole

Table 3.1: Charge-exchange excitations and their quantum numbers. All have  $\Delta T=1$ . A  $0^+$  ground state is assumed. The  $\hbar\omega$  column refers to a transition between major oscillator shells (i.e. a  $\Delta\hbar\omega=1$  could represent a transition between the sd- and pf-shells).

lying states and give a complementary description of the spin-isospin response of a nucleus.

Gamow-Teller (GT) strength is represented by  $B(\text{GT})$ . The GT transition is mediated by the  $\sigma\tau$  operator. If the general forms of a CE particle-hole operator are

$$O^{\lambda\tau} = \sum_j r_j^\lambda Y_\lambda(\hat{r}_j) t_{\pm j} \quad (3.1)$$

for no-isovector spin-flip transitions and

$$O^{\lambda\sigma\tau} = \sum_j r_j^\lambda [Y_\lambda(\hat{r}_j) \otimes \vec{\sigma}_j]_{J\pi} t_{\pm j} \quad (3.2)$$

for isovector spin-flip transitions, setting  $\lambda$  to 0 results in the Fermi and GT operators from  $\beta$ -decay:

$$\sum_j t_{\pm j} \quad \text{and} \quad \sum_j \vec{\sigma}_j t_{\pm j} \quad [77]. \quad (3.3)$$

$\lambda$  corresponds to  $\Delta L + \Delta n$ , where  $\Delta n$  is the change in major oscillator shell.

Equation 3.4 gives the relationship between  $B(GT)$  and the  $\sigma\tau$  operator in  $\beta$ -decay.  $\psi_I$  and  $\psi_F$  are the initial and final nuclear states, and  $g_A$  is the axial-vector coupling constant of the weak interaction.

$$B(GT)_{\pm} = \frac{1}{2J+1} \left| \sum_j \langle \psi_F || \sigma_j \tau_j^{\pm} || \psi_I \rangle \right|^2 \quad (3.4)$$

In 1963, Ikeda *et al.* [78] developed a non-energy-weighted sum rule for the total amount of GT strength that should be seen in CE transitions from a given nucleus. Ikeda's model-independent sum rule is

$$S(\beta^{-}) - S(\beta^{+}) = 3(N - Z). \quad (3.5)$$

Fermi strength has a similar sum rule:

$$S(\beta^{-}) - S(\beta^{+}) = N - Z. \quad (3.6)$$

The GT sum rule provides a useful upper limit on the amount of strength an experimentalist is likely to see, although in most cases only 50-60% of the expected sum rule strength can be accounted for (for an example, see reference [79]). This is known as the quenching problem [80, 81, 82, 83], and will be discussed in Chapters 4 and 5. Sum rules also exist for higher multipole excitations (see reference [77] for examples).

A charge-exchange reaction can go in either of two directions:  $\Delta T_z = \pm 1$ .  $\Delta T_z = +1$  corresponds to an (n,p)-type reaction, which goes diagonally down and to the right on a chart of nuclides.  $\Delta T_z = -1$  corresponds to a (p,n)-type reaction, which goes diagonally up and to the left on a chart of nuclides. Figure 3.1 shows both types superimposed upon a small section of the chart of nuclides of relevance for this thesis. Figure 3.2 shows a more thorough picture of isospin in CE reactions. The target nucleus has  $T_z = (N-Z)/2$ . For a (p,n)-type transition, a  $T_0$  ground state in the target

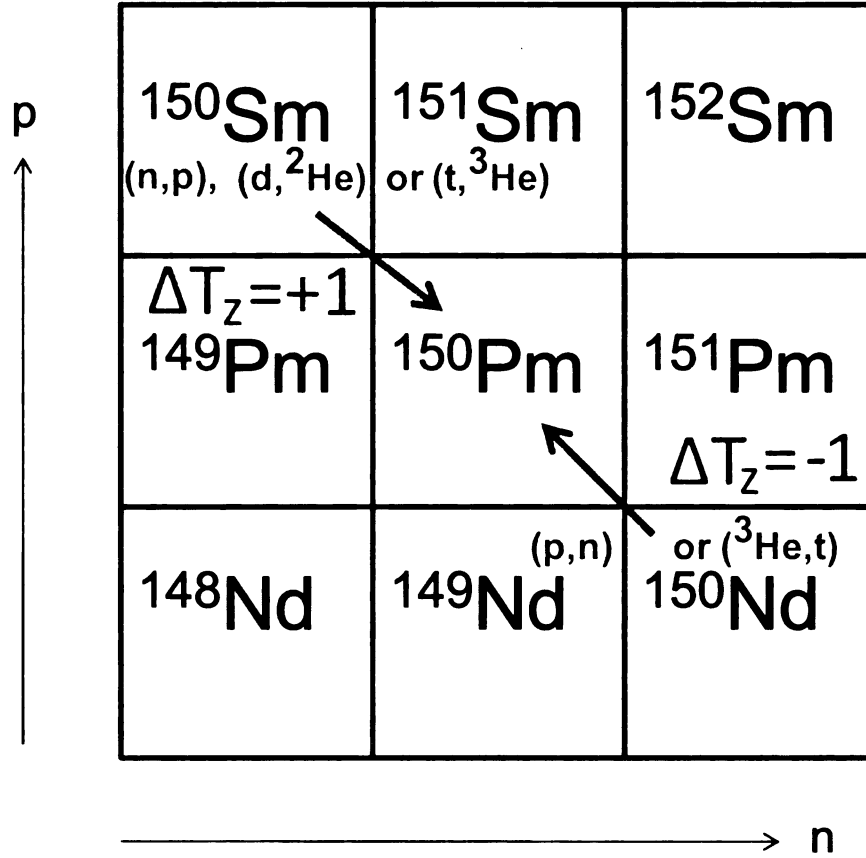


Figure 3.1: Schematic of charge-exchange on a subset of the chart of nuclides. Nuclei of interest ( $^{150}\text{Nd}, \text{Pm}, \text{Sm}$ ) are shown. The transition from  $^{150}\text{Sm}$  to  $^{150}\text{Pm}$  represents an isospin change of  $\Delta T_z = +1$ , and the transition from  $^{150}\text{Nd}$  to  $^{150}\text{Pm}$  represents an isospin change of  $\Delta T_z = -1$ .

has an analogue  $T=T_0$  state (the Isobaric Analogue State) in the residual. In general, a (p,n) transition can populate  $T_0+1$ ,  $T_0$ , and  $T_0-1$  states in the residual nucleus. In an (n,p)-type transition, the residual has a minimum isospin of  $T=T_0+1$ , so only states with isospin of  $T_0+1$  can be populated.

Figure 3.3 shows the microscopic picture of CE reactions as excitations of proton-holes/neutron-particles ( $\Delta T_z = +1$ ) and neutron-holes/proton-particles ( $\Delta T_z = -1$ ). In medium-to-heavy stable nuclei with a significant neutron/proton asymmetry, the neutron single-particle orbits are filled above the proton Fermi level. Pauli blocking constrains the single-particle orbits involved in a transition: excitations of 1p-1h components in the same oscillator shell are hindered in the (n,p) direction.

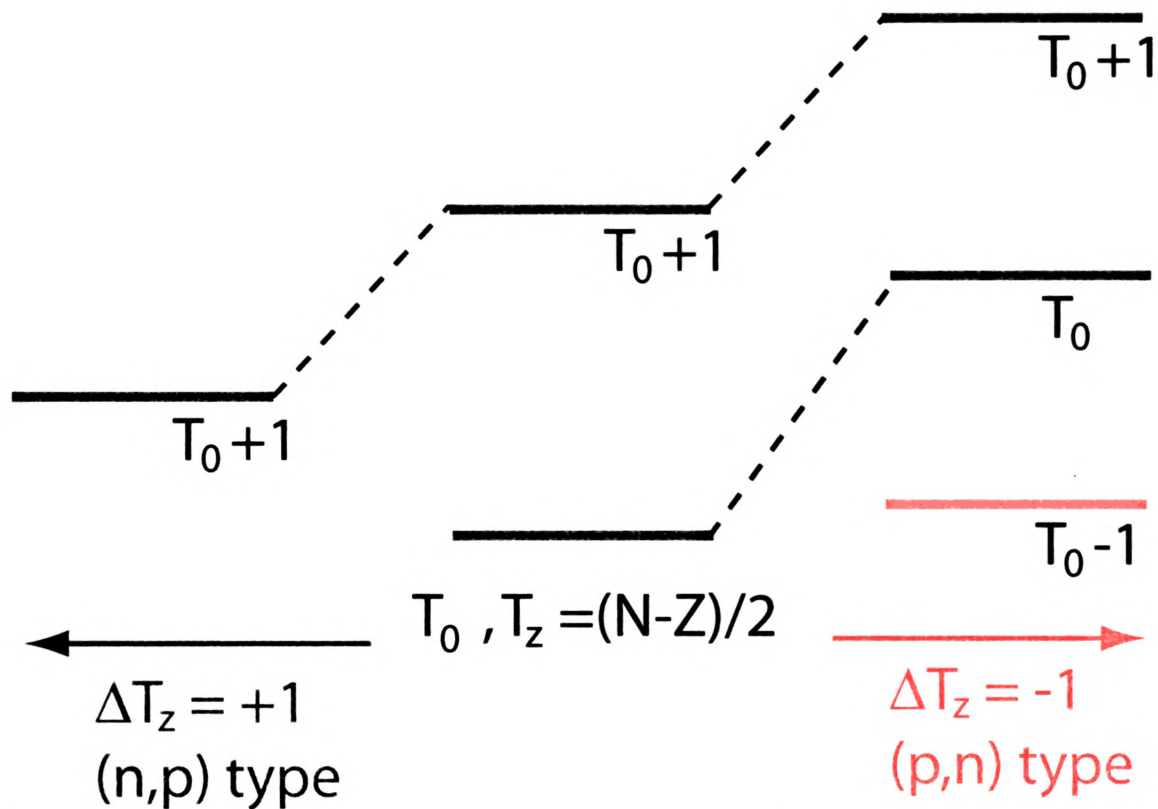


Figure 3.2: Isospin symmetry in charge-exchange reactions. States of like isospin (analogue states) are shown in like colors. In the (p,n) direction, the IAS is populated from a  $T_0$  to  $T_0$  transition, but no such transition can occur in the (n,p) direction.

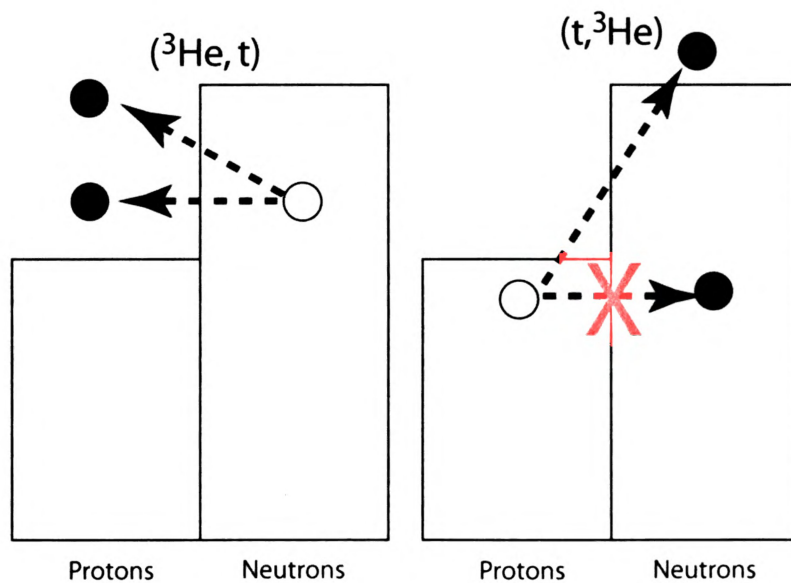


Figure 3.3: Pauli blocking is strong for the  $(t, ^3\text{He})$  reaction and reduces transition strengths, but is not as significant in the  $(^3\text{He}, t)$  direction.



## 3.2 Reaction Theory

Cross section calculations in this thesis are performed using DWBA (Distorted Wave Born Approximation) methods with the code FOLD [84]. The incoming and outgoing waves are distorted by the nuclear mean field of the target. An effective potential ( $V_{eff}$ ) describes the interaction between nuclei in the target and the projectile. The cross section can be determined from the square of the amplitude of the outgoing spherical wave. A T-matrix represents the transition between final and initial states.

Input from single-particle wave functions, one-body transition densities (OBTDs), the nucleon-nucleon interaction, and optical potentials result in calculated angular distributions for each type of charge-exchange transition listed in Table 3.1. These angular distributions are then compared to data. Absolute Gamow-Teller and Fermi strengths are calculated with the help of a phenomenological unit cross section.

### 3.2.1 DWBA

The scattering potential ( $V$ ) is separated into two pieces: the distorting potential from the nuclear mean field ( $U_1$ ) plus a residual interaction ( $U_2$ ) containing the physics of interest. The Schrödinger equation is then

$$(E - T - U_1 - U_2)\psi = 0 \quad (3.7)$$

and the wavefunction may be written as a partial Lippmann-Schwinger equation

$$\psi = \phi + \hat{G}_0^+(U_1 + U_2)\psi, \quad (3.8)$$

where  $\phi$  is the homogeneous solution to the Schrödinger equation and  $\hat{G}_0^+$  is a Green's function equal to  $(E - T)^{-1}$ . The resulting T-matrix is

$$T^{tot} = -\frac{2\mu}{\hbar^2 k} \langle \phi^- | V | \psi \rangle. \quad (3.9)$$

When  $V$  is expanded into  $U_1 + U_2$ , the expression for the T-matrix can be simplified to

$$-\frac{\hbar^2 k}{2\mu} T^{tot} = T^{U_1} + T^{U_2} = \langle \phi^- | U_1 | \chi \rangle + \langle \chi^- | U_2 | \psi \rangle, \quad (3.10)$$

where  $\chi$  is  $\phi$  after being distorted by the mean field of the nucleus:

$$\chi = \phi + \hat{G}_0^+ U_1 \chi. \quad (3.11)$$

Expanding  $\chi$  into a series yields the Born Series

$$T^{U_2} = -\frac{2\mu}{\hbar^2 k} \langle (\chi + \chi U_2 \hat{G}_1^+ + \dots) | U_2 | \chi \rangle, \quad (3.12)$$

where  $\hat{G}_1^+$  is equal to  $(E - T - U_1)^{-1}$ .  $T^{U_1}$  can be ignored, since  $U_1$  does not connect the initial and final states. The T matrix for DWBA calculations is then

$$T^{DWBA} = -\frac{2\mu}{\hbar^2 k} \langle \chi^- | U_2 | \chi \rangle. \quad (3.13)$$

(Notation and equation sequence largely taken from reference [85].) In many cases, the Born series is truncated at the first term, and this approximation is known as a first order Distorted Wave Born Approximation (DWBA). The reaction cross section is proportional to the square of the T-matrix element governing the transition between initial and final states

$$\frac{d\sigma}{d\Omega} = \left( \frac{\mu}{2\pi\hbar^2} \right)^2 \frac{k_f}{k_i} |T_{fi}|^2. \quad (3.14)$$

When  $U_1$  of the DWBA is a central optical potential,  $T^{U_1}$  is 0 and  $T^{U_2} = T_{fi}$ .

$$T_{fi} = T^{U_2} = -\frac{2\mu}{\hbar^2 k} \langle \chi | U_2 | \chi \rangle. \quad (3.15)$$

DWBA calculations in this work were carried out using the FOLD code. FOLD [84] is a three-part program for charge-exchange reaction calculations originally developed by J. Cook and J.A. Carr in 1988. The three separate sections of this code are called WSAW, FOLD, and DWHI.

WSAW uses numerical methods to solve for single-particle radial wave functions of relevance to the DWBA calculation. A Wood-Saxon potential is used to represent the volume section of the total potential, and Coulomb and spin-orbit potentials are also taken into account. The input of WSAW consists of binding energies and shell model quantum numbers for single-particle orbits. Output wave function files are then read into the FOLD code along with other input parameters.

### 3.2.2 One-body transition densities

Wave functions from WSAW are single-particle wave functions. The DWBA nuclear structure input for each calculation involves a combination of 1p-1h transitions between single-particle orbits.

The relative weight of each 1p-1h transition is given by its OBTD. OBTDs contain information on the overlap between the final and initial nuclear states [51] and must be calculated for both the projectile/ejectile and the target/residual systems. A nuclear structure code (often a shell model code like OXBASH [86] or NuShellX [87]) calculates the importance of each single-particle transition, calculates phase factors, incorporates all of the necessary angular momentum coefficients, and returns

an OBTD. The OBTD formula in an isospin framework is

$$OBT D(f i k_{\alpha} k_{\beta} \lambda \Delta T) = \frac{\langle f T \parallel [a_{k_{\alpha}}^{\dagger} \otimes \tilde{a}_{k_{\beta}}]^{\lambda, \Delta T} \parallel i T' \rangle}{\sqrt{(2\lambda + 1)(2\Delta T + 1)}} \quad [88] \quad (3.16)$$

where  $a^{\dagger}$  and  $\tilde{a}$  are single-particle creation and annihilation operators,  $f$  and  $i$  represents the final and initial quantum numbers,  $\lambda$  is the rank of the operator,  $k_{\alpha, \beta}$  are final and initial isospin states, and  $\Delta T$  is the change in isospin.

$^{150}\text{Nd}$  and  $^{150}\text{Sm}$  are too heavy to calculate the OBTDs in the shell model because the model space is too large. A normal modes formalism [89] is used instead. Normal modes are the most coherent superposition of 1-particle 1-hole states for a particular operator in a given particle-hole basis. They exhaust full (non-energy-weighted) sum rule strengths and give a set of OBTDs for each type of transition associated with the operator  $O^{\lambda\sigma\tau}$ . However, the downside of this method is that no information is provided on the strength distribution as a function of excitation energy.

The following bases were used in calculations in this thesis:  $^{150}\text{Sm} (^{150}\text{Pm})(^{150}\text{Nd})$  was assumed to have 32 (31)(30) protons (4 (3)(2) in the 2p 3/2 shell) and 88 (89)(90) neutrons (6 (7)(8) in the 1h 9/2 shell). The neutron space included the 1h 11/2 level for the  $^{150}\text{Sm} \rightarrow ^{150}\text{Pm}$  calculation to allow for GT transitions — without this modification, Pauli blocking would prevent all GT transitions. To accommodate all of the transitions relevant for this work, the model space was allowed to include orbits up through 1i 11/2.

### 3.2.3 The nucleon-nucleon interaction

The free nucleon-nucleon interaction  $V_{12}$  takes the form

$$V_{12} = V^C(r_{12}) + V^{LS}(r_{12}) \vec{L} \cdot \vec{S} + V^T(r_{12}) S_{12}. \quad (3.17)$$

where  $V^C$  is the central potential,  $V^{LS}$  is the spin-orbit potential,  $V^T$  is a tensor potential, and 1 and 2 refer to the two interacting nucleons.  $\vec{L} \cdot \vec{S}$  is the spin-orbit operator and  $S_{12}$  is the tensor operator. In their 1981 paper, Love and Franey [90, 91, 92] determine  $V_{12}$  with the use of a large body of nucleon-nucleon scattering data. They decompose  $V^C(r)$ ,  $V^{LS}(r)$ , and  $V^T(r)$  in terms of Yukawa potentials with the form  $\frac{e^{-x}}{x}$ , chosen for their similarity to the one-pion exchange potential (OPEP). The three potentials become

$$\begin{aligned} V^C(r) &= \sum_{i=1}^{N_C} V_i^C Y\left(\frac{r}{R_i}\right) \\ V^{LS}(r) &= \sum_{i=1}^{N_{LS}} V_i^{LS} Y\left(\frac{r}{R_i}\right) \\ V^T(r) &= \sum_{i=1}^{N_T} V_i^T r^2 Y\left(\frac{r}{R_i}\right). \end{aligned} \tag{3.18}$$

These sums run over Yukawa potentials with different ranges that reflect the ranges of the  $\pi$ ,  $\rho$ , and  $2\pi$  meson exchange. The result of Love and Franey's work was a set of effective nucleon-nucleon t-matrix interaction strengths applicable to a wide variety of nucleon-nucleus scattering techniques, such as (p,p') and (p,n). While the full effective interaction has many terms, the ones important for charge exchange are

$$\begin{aligned} V_{eff} = \sum_{ij} & \left( V_{\tau}^C Y\left(\frac{r_{ij}}{R_{\tau}}\right) + V_{\sigma\tau}^C Y\left(\frac{r_{ij}}{R_{\sigma\tau}}\right) (\hat{\sigma}_i \cdot \hat{\sigma}_j) + V_{\tau}^{LS} Y\left(\frac{r_{ij}}{R_{LS\tau}}\right) L \cdot S \right. \\ & \left. + V_{\tau}^T r_{ij}^2 Y\left(\frac{r_{ij}}{R_{T\tau}}\right) S_{ij} \right) (\hat{\tau}_i \cdot \hat{\tau}_j) \quad [93]. \end{aligned} \tag{3.19}$$

(The sum over i and j runs over all nucleons in the projectile and target.) Love and Franey showed that the  $\sigma\tau$  component is preferentially excited at energies above 100 MeV/u and below 500 MeV/u, where the  $\tau$  contribution is at a minimum (see

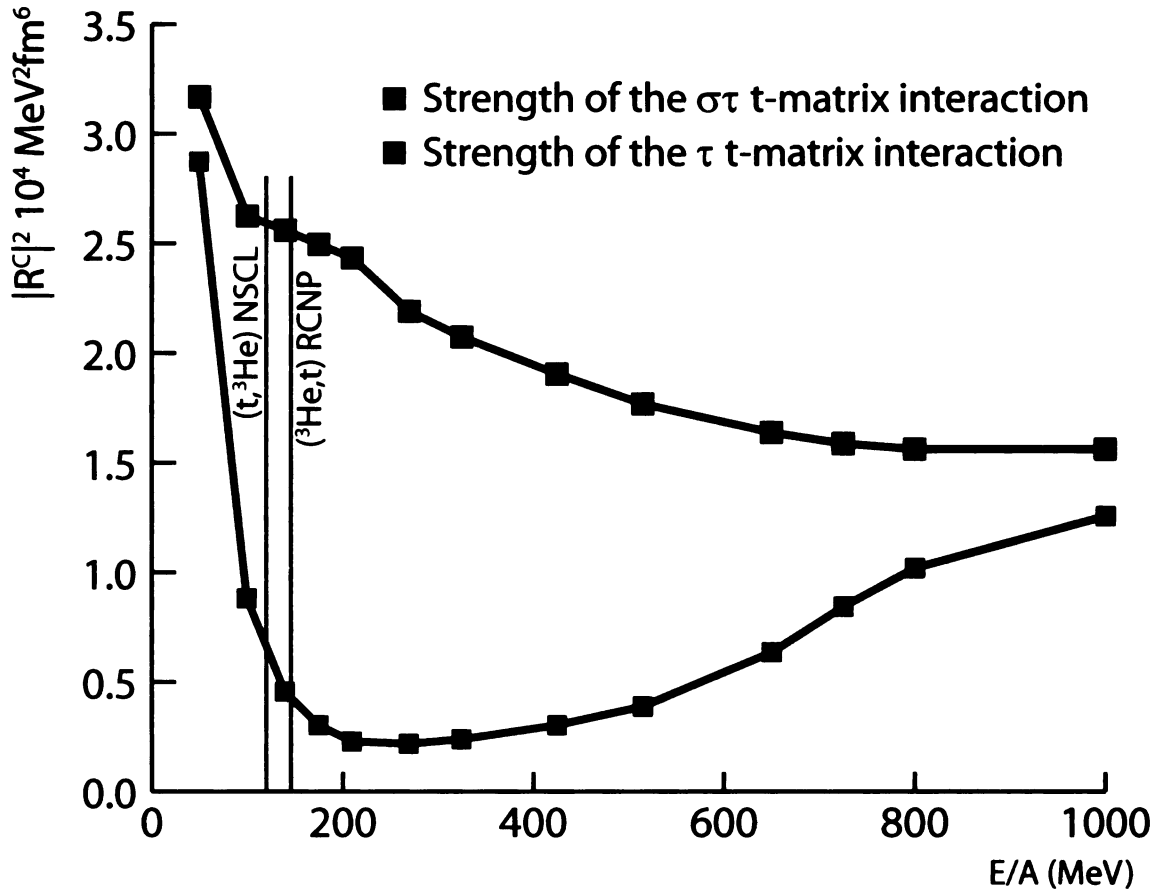


Figure 3.4: Relative operator strengths for the  $\sigma\tau$  and  $\tau$  t-matrices, from reference [91]. The  $\sigma\tau$  t-matrix is significantly stronger than the  $\tau$  t-matrix at energies above 100 MeV/u, which allows charge-exchange experiments to preferentially populate  $\sigma\tau$  transitions over  $\tau$  ones. Values come from reference [91].

Figure 3.4). In addition to the dominance of the  $\sigma\tau$  term above 100 MeV, this energy regime also features decreased contributions from multi-step processes and decreased distortion effects from the central isoscalar potential. Near zero momentum transfer, the  $LS\tau$  term is so small it is negligible (it is also taken out of FOLD calculations). Contributions from the  $T\tau$  interaction are small, but must be taken into account for non-zero momentum transfer as they create amplitudes that interference with amplitudes mediated by  $V_{\sigma\tau}$ .

A two-body interaction between nucleons is represented by “direct” and “exchange” terms. The exchange term represents amplitudes due to processes where

a nucleon in the target is struck and ejected and the projectile nucleon is captured [77]. The exchange term contains non-local effects, which makes it much more difficult to calculate. A short-range (no-recoil) approximation is often used [90] to deal with the exchange terms, although it is known to underestimate the destructive exchange contributions for reactions involving complex probes like  $(t, {}^3\text{He})$  and  $({}^3\text{He}, t)$  [94, 95].

### 3.2.4 FOLD

The Love-Franey interaction is an effective nucleon-nucleon interaction, but CE with complex probes involves a nucleus-nucleus interaction. In order to calculate the correct T-matrix, the effective nucleon-nucleon interaction must be double-folded (integrated) over the transition densities of the projectile/ejectile and target/residual systems to create a form factor:

$$F(r) = U_2(r) = \langle \alpha_e \alpha_r | V_{eff}(r) | \alpha_t \alpha_p \rangle, \quad (3.20)$$

where  $\alpha_{e,r,t,p}$  represent the ejectile, residual, target, and projectile wavefunctions, respectively. The FOLD code carries out the double-folding procedure and produces this form factor.

Each type of transition requires its own FOLD input file. For the  ${}^{150}\text{Nd}$  and  ${}^{150}\text{Sm}$  experiments, the use of normal-mode OBTDs means that only one form factor is available for each type of  $J^\pi$  transition. (If QRPA or shell model transition densities were available, form factors for many states of the same  $J^\pi$  could be calculated.) Depending on the excitation, several form factors might have to be calculated: these correspond to different units of angular momentum transfer between the target and the projectile. Contributions to the cross section from each form factor are then added. As an example, in a GT transition the relative change in total angular momentum is  $\Delta J=1$  ( $\Delta L=0$ ,  $\Delta S=1$ ) for both the projectile/ejectile and target/residual

systems. The relative angular momentum transfer can be calculated from that in the projectile and target

$$J_R = J_P + J_T. \quad (3.21)$$

In this case,  $J_P=1$  and  $J_T=1$ , so  $J_R$  can be either 0 or 2 (1 is forbidden due to parity conservation). A form factor is calculated for each  $J_R$ .

Calculations were done for all of the multipoles listed in Table 3.1 using OBTDs from NORMOD (with the exception of octupole transitions, where only the 3- spin-flip octupole was calculated).

### 3.2.5 DWHI

As mentioned in section 3.2, the incoming and outgoing particles are represented by plane and spherical waves distorted by the optical potential. DWBA calculations account for this effect. Form factors are integrated with the distorted waves to calculate the T-matrix

$$T = \langle \chi_f | F(r) | \chi_i \rangle, \quad (3.22)$$

which is then used in Equation 3.14 to calculate the cross section.

A common way to determine optical potential parameters is to take elastic scattering data with the same experimental setup used for the experiment you wish to apply it to — using the same projectile, the same target, and the same beam energy. Optical potentials are fit to the cross sections from this elastic scattering data. Programs such as ECIS (used here) [96] or SFRESCO [97] are used. Real and imaginary Wood-Saxon functions (volume, radius, and diffuseness parameters) are used as the base for the fit, and the complexity of the fit can increase if extra functions are included to account for surface or spin-orbit potentials. As DWHI is set up to handle only volume-type optical potentials, these extra functions were not used.

In many cases, optical potentials are not available: they may be very difficult



to measure, or it may be almost impossible to get beam time to do the measurement. Fit parameters are then extrapolated from known potentials. Some efforts have been made to establish global potentials from simultaneous analysis of many elastic scattering experiments. For the two experiments discussed in this work, the  $^{150}\text{Nd}(^3\text{He},^3\text{He})$  optical potential was measured following the  $^{150}\text{Nd}(^3\text{He},t)$  experiment. A measurement of the  $^{150}\text{Sm}(t,t)$  reaction was not feasible, so the  $^{150}\text{Nd}$  optical potential from was scaled by 85% for the  $^{150}\text{Sm}(t,^3\text{He})$  experiment (following reference [98]). This is a purely phenomenological solution and has been employed in other  $(t,^3\text{He})$  experiments. More details of the optical potential measurement will be discussed in section 4.3.2.

### 3.2.6 The unit cross section and B(GT)

Taddeucci *et al.* found a quantitative description [99] of the proportionality between the Fermi and Gamow-Teller cross sections and beta decay:

$$\left. \frac{d\sigma}{d\Omega} \right|_{q=0} = K N |J_\tau|^2 B(F) = \hat{\sigma}_F B(F), \quad (3.23)$$

$$\left. \frac{d\sigma}{d\Omega} \right|_{q=0} = K N |J_{\sigma\tau}|^2 B(GT) = \hat{\sigma}_{GT} B(GT) \quad [99], \quad (3.24)$$

where  $\hat{\sigma}_F$  and  $\hat{\sigma}_{GT}$  are phenomenological unit cross sections.  $N$  is a distortion factor (the ratio of distorted to plane waves, and here the transformation to  $q=0$  has been included)

$$N = \frac{\sigma^{DW}(q=0)}{\sigma^{PW}(q=0)} \quad [99, 100], \quad (3.25)$$

$K$  is a kinematical factor that includes the momenta ( $k_i$  and  $k_f$ ) and reduced energies ( $E_i$  and  $E_f$ ) for both the entrance and exit channels

$$K = \frac{E_i E_f}{(h^2 c^2 \pi)^2} \frac{k_f}{k_i}, \quad (3.26)$$

and  $J_{\sigma\tau}$  (or  $J_\tau$ ) is the volume integral of the corresponding effective interaction (see equation 3.19). In his derivation, one of Taddeucci's assumptions was that the Eikonal approximation was valid — both the projectile and ejectile trajectories are well-represented by straight lines and the beam energies are much higher than the excitation energy. These conditions are satisfied for CE experiments at  $E > 100$  MeV/u and  $q \approx 0$ . The Eikonal approximation comes into play because its use allows the different components of the T-matrix to be factorized into a nuclear structure and a nuclear reaction part [101, 99]. While the factorization is only exact in the plane wave approximation [101], experiments have shown that it also works well for distorted waves in  $\Delta L = 0$  transitions [99, 95].

The proportionality of Equation 3.24 can be checked using GT strengths obtained from beta decay experiments [102]. The unit cross section for both Fermi and Gamow-Teller transitions are simple functions of the mass number  $A$  [99]. Figure 3.5 shows this dependence for the ( $^3\text{He}, t$ ) reaction [95]. Where there are differences in the calculated and measured unit cross sections, interference between  $V_{\sigma\tau}^C$  and  $V_\tau^T$  is thought to partially explain this difference. One example is the case of  $^{58}\text{Ni}$ , where removing contributions from the tensor interaction (based on theory) restored the proportionality of Equation 3.24 and brought the data point back to the phenomenological curve [103].

### 3.3 Giant Resonances

In a macroscopic picture, giant resonances are defined as a density oscillation of proton-neutron nuclear fluid. The two fluids form overlapping spheres in the nucleus. Density oscillations of these spheres can fall into one of two categories: isoscalar, if the two fluids move in phase, or isovector, if they move out of phase. Isovector resonances are further separated by whether particles with opposite spins move in or

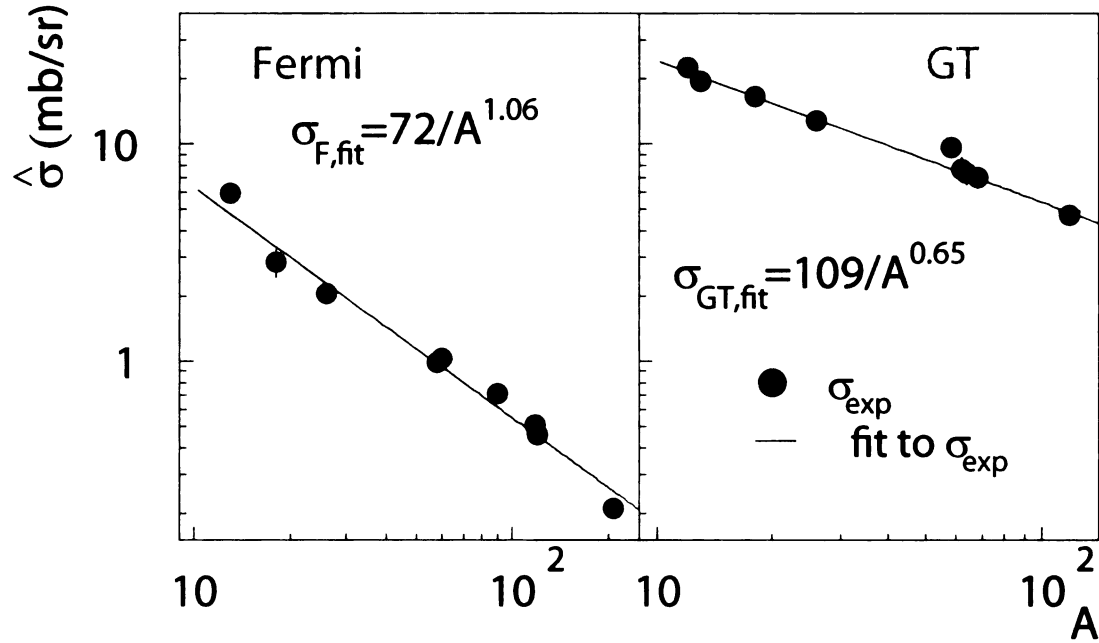


Figure 3.5: To the left, the Fermi unit cross section as a function of mass number for  $({}^3\text{He}, t)$  data taken at 420 MeV. At the right, the dependence of the Gamow-Teller unit cross section as a function of mass number for  $({}^3\text{He}, t)$  data taken at 420 MeV. The data point completely off of the fit line corresponds to the case of  ${}^{58}\text{Ni}$ , and the difference is due to the interference of  $V_{\tau}^T$  with  $V_{\sigma\tau}^C$  [103]. Both figures are adapted from reference [95].

out of phase. Those resonances with a spin dependence are known as isovector spin giant resonances (represented by an extra S in the abbreviation). Figure 3.6 shows the oscillatory modes for several giant resonances.

A microscopic picture of giant resonances may be constructed by considering a coherent superposition of many particle-hole excitations. If a large number of particle-hole pairs are excited (collective excitations), single-particle characteristics are washed out [77].

The amount of collective motion present may be observed by comparing the total multipole strength seen with that predicted by a sum rule. Examples include the Fermi and Gamow-Teller sum rules mentioned in section 3.1. A general expression for the non-energy-weighted sum rule (NEWSR) for transitions with multipolarity  $\lambda \geq 1$  is

$$S_{-}^{\lambda J} - S_{+}^{\lambda J} = \frac{2J+1}{2\pi} (N \langle r_n^{2\lambda} \rangle - Z \langle r_p^{2\lambda} \rangle) \quad [104]. \quad (3.27)$$

Spin transfer is ignored in this equation. Giant resonances are defined to fulfill over 50% of the relevant NEWSR [77].

Table 3.2 provides the quantum numbers, approximate centroid, and excitation energy for monopole, dipole, and quadrupole giant resonances. The resonances are categorized based on angular momentum, spin, and isospin transfer. The single asterisks of Figure 3.6 indicate that the spin polarizations of the IVSGMR, IVSGDR, and the IVSGQR can be drawn in two different ways. For example, in the IVSGMR you can have protons with spin up and neutrons with spin down or protons with spin down and neutrons with spin up.

Isovector giant resonances have three isospin components in the ( ${}^3\text{He}, t$ ) direction. The total strength will be split between  $T_0+1$ ,  $T_0$ , and  $T_0-1$  isospin levels. The relative population strengths of each level is dependent on the isospin of the target nucleus. The strength of the  $T_0+1$  level is weighted with a factor of  $\frac{1}{(T_0+1)(2T_0+1)}$ .

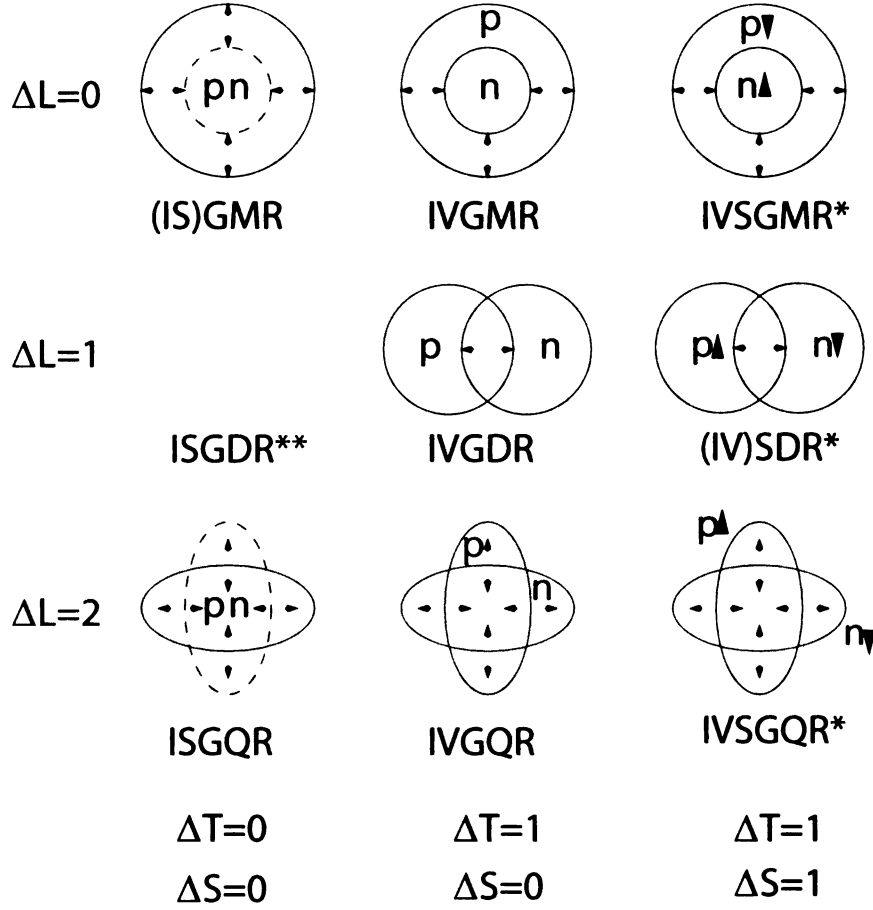


Figure 3.6: Giant resonance modes from Table 3.2. p and n represent protons and neutrons, and the small triangles indicate spin. Arrows show the proton and neutron directions of motion. Single asterisks denote resonances for which more than one accurate picture can be drawn: the spin polarization of protons and neutrons can be either spin up or spin down. The double asterisk by the ISGDR indicates that this is a second-order resonance. Neither this figure nor Table 3.2 is meant to be exhaustive; higher-order resonances exist but will not be discussed in this work. See [77] for more detailed information. The figure was modified from [105].

Resonance name	$\Delta L$	$\Delta S$	$\Delta T$	$E_X$ (MeV)
ISGMR	0	0	0	$80A^{-1/3}$
IVGMR	0	0	1	$59.2A^{-1/6}$
IVSGMR	0	1	1	*
ISGDR	1	0	0	$120A^{-1/3}$
IVGDR	1	0	1	$31.2A^{-1/3} + 20.6A^{-1/6}$
IVSGDR	1	1	1	*
ISGQR	2	0	0	$64.7A^{-1/3}$ (heavy nuclei) )
IVGQR	2	0	1	$130A^{-1/3}$
IVSGQR	2	1	1	*

Table 3.2: Isoscalar and isovector giant resonances, from [77]. IS stands for isoscalar, IV for isovector, and IVS for isovector-spin. Likewise, GMR stands for giant monopole resonance, GDR for giant dipole resonance, and GQR for giant quadrupole resonance. The excitation energy given is approximate and based on the hydrodynamic model, and may be changed by significant deformation. See Figure 3.6 for a drawing of the various modes. \* The IVSGDR and IVSGQR have three spin components (the middle resonance will have an excitation energy similar to the no-spin-flip resonance of the same type), while the IVSGMR has one spin component. All resonances in the (p,n) direction also have three isospin components, but one is preferentially populated (see text for more details).

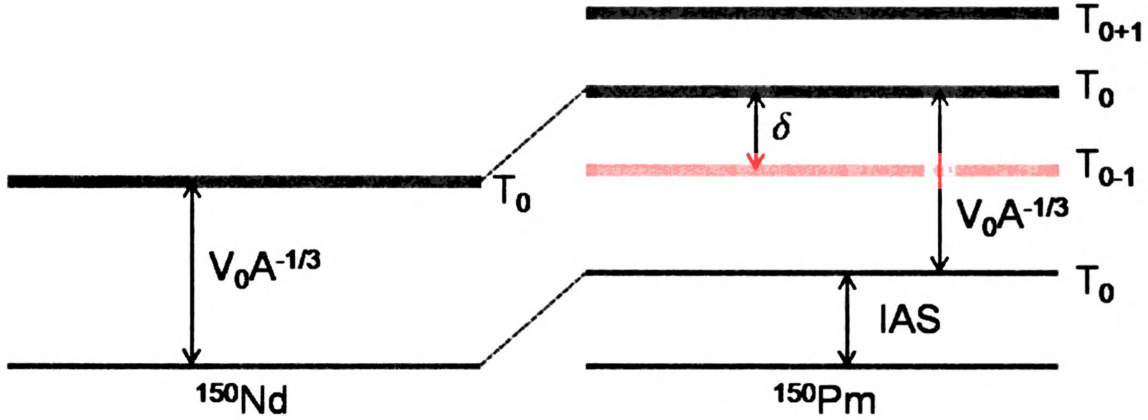


Figure 3.7: IVSGMR schematic for  $^{150}\text{Nd} \rightarrow ^{150}\text{Pm}$ . Monopole excitations are represented by very thick lines, and isobaric analogue levels in  $^{150}\text{Nd}$  and  $^{150}\text{Pm}$  are connected by thin dotted lines.

the  $T_0$  level with a factor of  $\frac{1}{T_0+1}$ , and the  $T_0-1$  level with a factor of  $\frac{2T_0-1}{2T_0+1}$ . For the  $^{150}\text{Nd}(^3\text{He},t)^{150}\text{Pm}$  case (the target isospin is 15), these correspond to values of 0.002, 0.0625, and 0.9355, so we expect the  $T_0-1$  resonance to dominate. In the  $(t,^3\text{He})$  direction, all of the strength goes into the  $T_0+1$  isospin component because it is the only one that can be populated. The IVSGMR has only one spin component, but the IVSGDR and IVSGQR resonances have three spin components on top of their isospin components: from a  $0^+$  ground state,  $0^-$ ,  $1^-$ , and  $2^-$  states can be populated through the IVSGDR, and  $1^+$ ,  $2^+$ , and  $3^+$  states through the IVSGQR.

For example, let's examine the population of the IVSGMR in  $^{150}\text{Pm}$  as excited from  $^{150}\text{Nd}$  and  $^{150}\text{Sm}$ . In the  $(^3\text{He},t)$  direction, Bohr and Mottelson [106] predict that the  $(T_0-1)$  IVSGMR can be found at an energy of  $\delta=(T_0+1)V_1A^{-1}$  lower than the  $T_0$  monopole resonance:

$$E_x^{IVSGMR} = V_0A^{-1/3} + E_x^{IAS}(T) - \delta \quad (3.28)$$

where  $V_0$  is around 155 and  $V_1$  is 55 [107, 105]. This equation predicts a resonance centroid of 37.5 MeV. Figure 3.7 shows the relevant schematic.

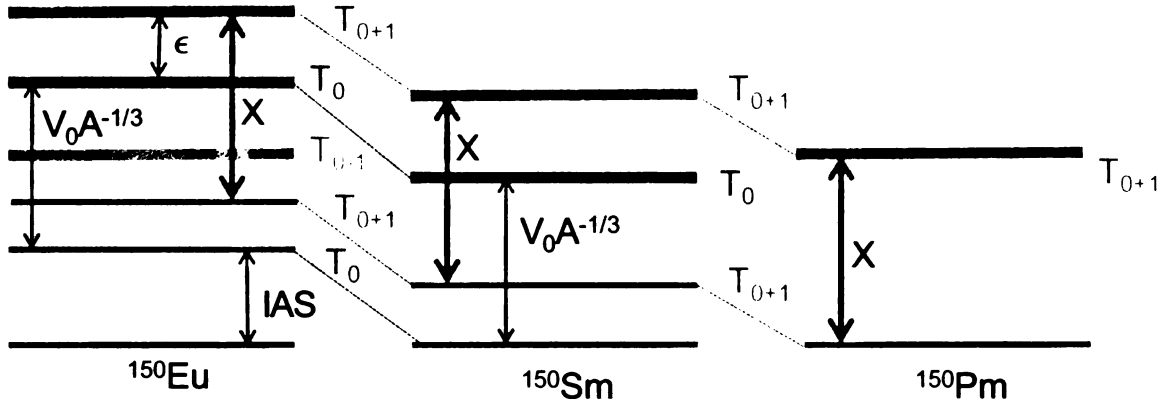


Figure 3.8: IVSGMR schematic for  $^{150}\text{Sm} \rightarrow ^{150}\text{Pm}$ . Monopole excitations are represented by very thick lines, and isobaric analogue levels are connected by dotted lines. Differences in excitation energy between analogue levels are close to the Coulomb displacement. The excitation energy of the IVSGMR in  $^{150}\text{Pm}$  is represented by the quantity  $X$ , which has isobaric analogues in both  $^{150}\text{Sm}$  and  $^{150}\text{Eu}$ .

The situation in the  $(t, ^3\text{He})$  direction is more complicated. Figure 3.8 shows this situation. There are no other quantities in the residual nucleus with which to calculate the excitation energy, but the analogue state in  $^{150}\text{Eu}$  can be calculated and that excitation energy can then be extrapolated back to  $^{150}\text{Pm}$  based on isospin symmetry. The excitation energy in  $^{150}\text{Eu}$  is  $\epsilon = (T_0)V_1A^{-1}$  above the  $T_0$  monopole resonance, and the excitation energy in  $^{150}\text{Pm}$  can be found by subtracting twice the energy of the Coulomb displacement from the  $^{150}\text{Eu}$  value.

$$E_x^{IVSGMR}(^{150}\text{Pm}) = V_0A^{-1/3} + E_x^{IAS}(T)(\text{in } ^{150}\text{Eu}) + \epsilon - 2V_C \quad (3.29)$$

and

$$\Delta V_C = 0.7046 \frac{2Z+1}{A^{1/3}} \left(1 - \frac{0.76}{Z^{2/3}}\right). \quad (3.30)$$

For values of  $V_C = 16.5$  MeV and  $\epsilon = 4.77$  MeV, the  $E_x^{IVSGMR}$  in  $^{150}\text{Pm}$  is predicted to be around 15 MeV.

Centroids of the dipole and quadrupole resonances can be calculated in a similar fashion.



# Chapter 4

## $^{150}\text{Nd}(^3\text{He},t)^{150}\text{Pm}^*$ at RCNP

### 4.1 RCNP Experimental Setup and Procedure

#### 4.1.1 Beam preparation and tuning

The Research Center for Nuclear Physics (RCNP) in Osaka, Japan, has a well-developed program of experiments with intermediate-energy  $^3\text{He}^{2+}$  beams. The AVF and the Ring cyclotrons are coupled to accelerate a beam of  $^3\text{He}$  nuclei to 420 MeV and achieve beam intensities of up to  $5 \times 10^{10}$  particles per second. The faint-beam method is used to check dispersion-matched tuning [108, 109] in the WS beam line [110, 111] (see Figure 4.1 for the WS floorplan). Excitation energy resolutions of 20-40 keV can be achieved.

The Grand Raiden Spectrometer [112] (see Figure 4.5) is used to analyze the momentum of tritons from  $(^3\text{He},t)$  experiments taking place at RCNP. It contains three dipole magnets, two quadrupoles, one sextupole, and one multipole magnet. The multipole magnet can produce dipole, quadrupole, octupole, sextupole, and decapole fields to correct for aberrations in the ion optics. One magnet, the DSR (dipole magnet for spin rotation), is meant for polarized beam experiments and was not used in this work. The Grand Raiden focal plane contains two sets of Multi-Wire Drift

Chambers (MWDCs), which were used to collect position and angle information. Each MWDC has two planes of anode wires in between its three cathode planes: the X layer has wires perpendicular to the “medium plane” of the spectrometer and the U plane has wires at a  $48.19^\circ$  angle [112] with respect to that plane. “Potential” wires are charged to create a uniform electrical potential [113], and “sense” wires are grounded and detect ionization electrons. Cathode voltages were set to -5.6 kV and potential wire voltages were set to -0.3 kV. The MWDCs were filled with a mixture of 71.4% argon, 28.6% isobutane, and a very small amount of isopropyl alcohol [113, 114]. Drift times from the four sets of anode wires give position resolutions around  $300\mu\text{m}$  in each plane. A set of two 10mm-thick plastic scintillators placed behind the drift chambers is used to measure energy loss and time-of-flight information for each hit, and the first scintillator triggers the data acquisition system and serves as the start of the time of flight measurement. The cyclotron RF provides the stop signal. A 1 mm aluminum plate placed between the scintillators improves the particle identification (PID) by increasing the energy lost in the second scintillator (see Figure 4.6). For more information on the parameters of the Grand Raiden, see Table 4.1. Event rates were such that the data acquisition live time during the experiment was 96%.

One of the primary considerations in planning a charge-exchange experiment is to optimize the measured energy resolution of the ejectile, which (in combination with angular resolution) determines the excitation energy resolution in the residual. This is accomplished by carefully considering the type of probe and target thickness, but use of dispersion-matched rather than focused beam optics prior to the target can increase the resolution by up to a factor of 3 (for a  $^3\text{He}$  beam at RCNP — the increase is closer to a factor of 5 for the tritium beam at the NSCL). Dispersion-matching techniques were employed for both the  $^{150}\text{Nd}(^3\text{He},t)$  and  $^{150}\text{Sm}(t,^3\text{He})$  experiments (see Chapter 5). The beam is momentum-dispersed on the target to match the dispersion of the spectrometer, and the spectrometer then focuses the beam

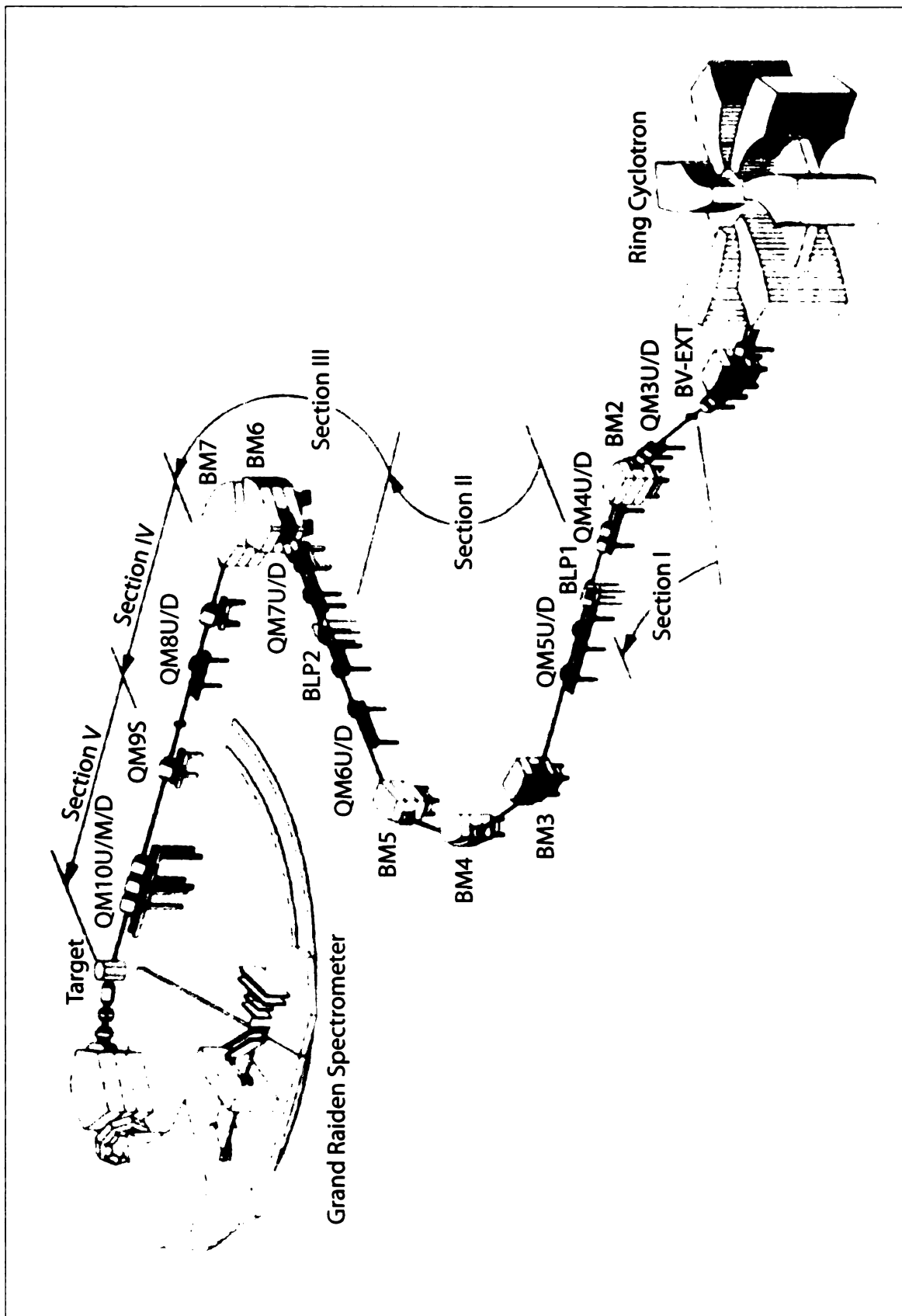


Figure 4.1: The WS beamline at RCNP. Figure taken from reference [111].

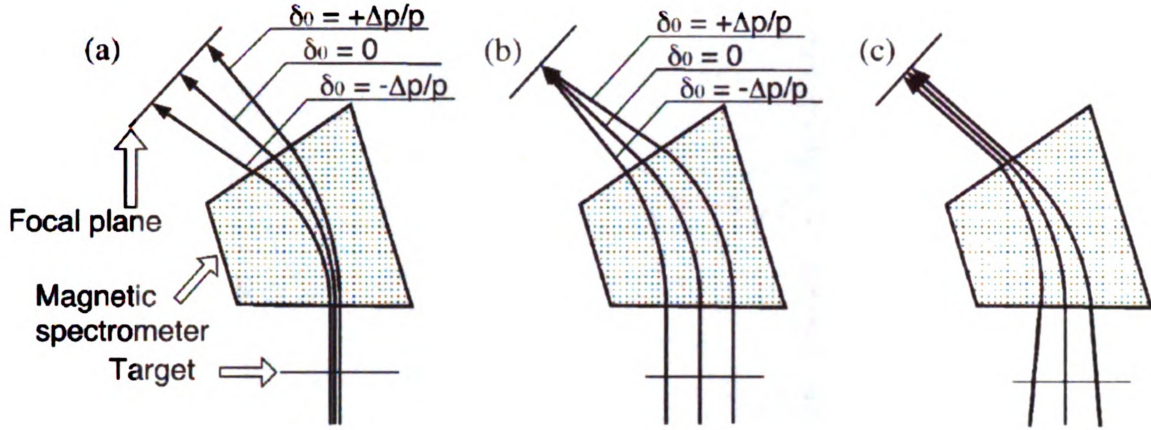


Figure 4.2: Ion optical modes for high-resolution spectrometers. The beam trajectories represent different incoming momenta. a) shows focus mode, which focuses the beam at the target and disperses the ejectiles throughout the focal plane. b) shows dispersion-matched mode with lateral dispersion-matching only. The momentum-dispersed beam hits the target and creates a large beam spot in the dispersive direction, but the ejectiles have different angles coming into the focal plane. c) shows a dispersion-matched mode with both lateral and angular dispersion-matching. The ambiguity in the ejectile angle at the focal plane is considerably reduced. The figure is taken from reference [109].

at a single point in the focal plane. In a lateral dispersion-matched tune, the beam coming into the target area is focused along the spectrometer's non-dispersive axis and momentum-dispersed along the spectrometer's dispersive axis. This produces a long, thin beam spot. The lateral dispersion-matching technique can result in angular ambiguities [109] in the dispersive direction unless angular dispersion matching is also applied. In this process, the beam line is tuned so that tracks incident at different angles to the target have the same angle in the focal plane [110]. Both types of dispersion-matching were used in the  $^{150}\text{Nd}(^3\text{He},t)$  experiment. Figure 4.2 shows the beam optics for focus matching, lateral dispersion-matching, and simultaneous lateral and angular dispersion-matching. Figure 4.3 shows an image of the beam spot from the  $^{150}\text{Nd}(^3\text{He},t)$  experiment.

The faint beam method is used to tune the dispersion-matching. In this method, an attenuated beam is sent directly into the spectrometer without hitting a target



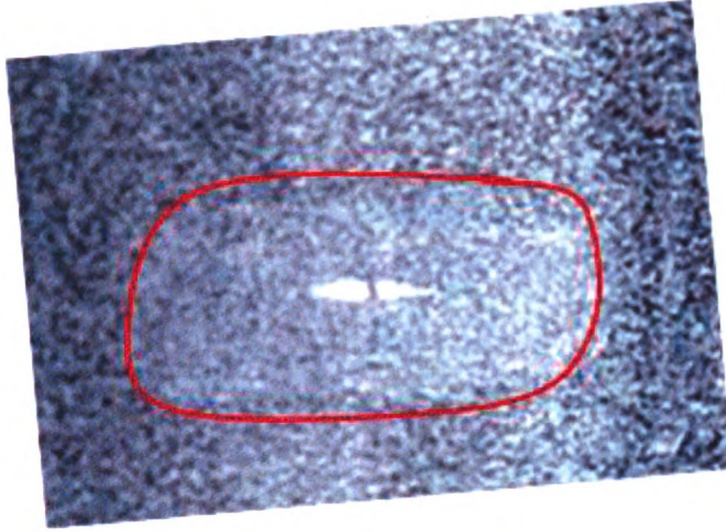


Figure 4.3: Dispersion-matched beam image at the target of the Grand Raiden [112] spectrometer. The viewer dimensions are circled in red. Targets are around 2 cm by 2 cm or slightly smaller, and the beam spot is a bit less than 1 cm long.

foil. The dispersion of the beam can then be fine-tuned by optimizing the image in the focal plane, and the absence of a target foil ensures that the measured resolution is intrinsic to the beam rather than energy straggling in a target. Four target foils were used to aid in the beam tuning in the  $^{150}\text{Nd}$  experiment: a ZnS viewer,  $^{27}\text{Al}$  to check energy resolution, and  $^{197}\text{Au}$  and  $^{13}\text{C}$  to optimize the angular calibrations. Once tuning was complete, strong Gamow-Teller transitions from a  $^{nat}\text{Mg}$  target were used to calibrate the triton momentum.

Nd foils oxidize quickly, so a special container was used to keep the foils in vacuum during the transfer from a glove box to the target chamber. Both foils were made from  $^{150}\text{Nd}$  enriched to 96% purity (see Figure 4.4). They were thin and self-supporting, with thicknesses of  $1\text{ mg/cm}^2$  and  $2\text{ mg/cm}^2$ . Excellent beam tuning and thin foils allowed us to achieve an energy resolution of 32 keV FWHM. The difference in energy loss between the  $^3\text{He}^{++}$  particles and tritons in the target is 8 keV (as calculated in LISE++ [115]), and does not limit the resolution.

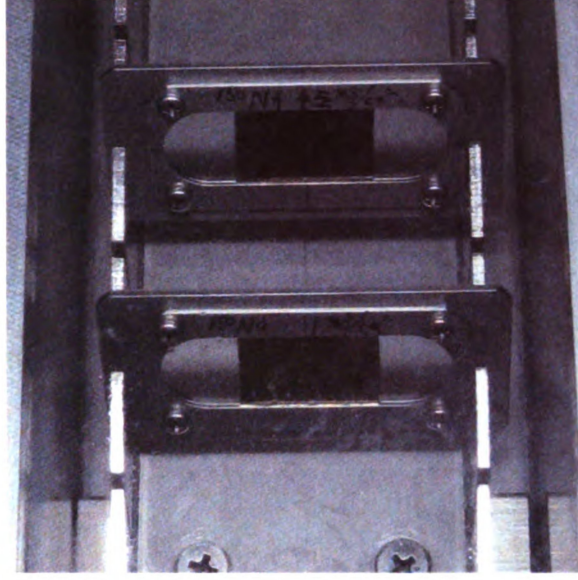


Figure 4.4: The  $^{150}\text{Nd}$  targets used in the experiment,  $1 \text{ mg/cm}^2$  and  $2 \text{ mg/cm}^2$ .

To optimize the angular resolution, an optical technique called “over-focus mode” was used [108]. The ion optics of the Grand Raiden are such that the non-dispersive angular magnification between target and focal plane is 0.17 [114] in focused mode. A large non-dispersive angle at the target ( $\Theta_{ta}$ ) corresponds to a small non-dispersive angle ( $\Theta_{fp}$ ) in the focal plane in focus mode, which, for a given angular resolution in the focal plane, makes it difficult to reconstruct  $\Theta_{ta}$  with good precision. To improve this situation, the field of the Q1 quadrupole magnet is changed to place the non-dispersive optical focus outside of the focal plane, producing a large  $y_{fp}$  (non-dispersive position at the focal plane) that is directly proportional to  $\Theta_{ta}$  and has a small relative error. The proportionality changes as a function of  $x_{fp}$ .

When centered around  $0^\circ$ , the Grand Raiden can accept particles in the ranges of  $0$ - $2^\circ$ . To increase the angular range available for this experiment, the spectrometer was rotated to take data at  $\Theta_{hor}=2.5^\circ$  and  $\Theta_{hor}=4^\circ$ . Figure 4.7 shows the Grand Raiden’s angular acceptances for the three data sets. Each rectangle represents an angular range of  $\pm 20 \text{ mrad}$  horizontally and  $\pm 40 \text{ mrad}$  vertically, for a total solid angle of  $3.2 \text{ msr}$ . After the  $^{150}\text{Nd}(^3\text{He,t})$  data was taken, one day was allocated for



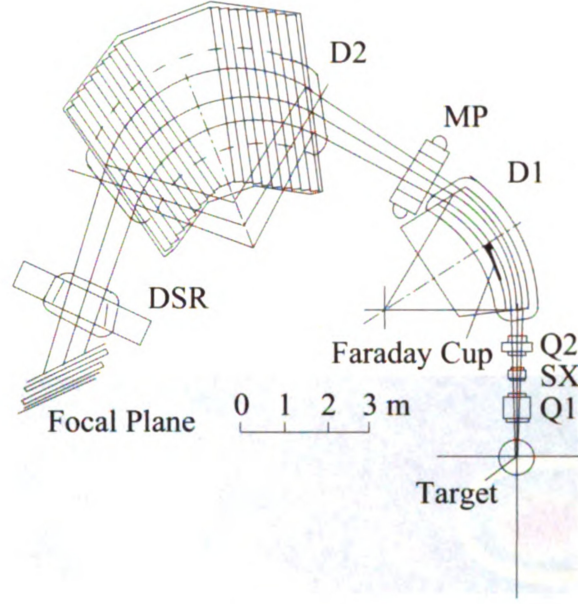


Figure 4.5: Schematic of the Grand Raiden Spectrometer. Image from Ref. [113].

Parameter	Value
momentum resolution ( $\Delta p/p$ )	$2.7 \times 10^{-5}$
energy resolution ( $\Delta E/E$ )	$4.5 \times 10^{-5}$
position resolution	300 $\mu\text{m}$ (both horizontal and vertical)
maximum $B\rho$	5.4 Tm
maximum B (D1 and D2)	1.8 T
maximum magnetic gradient (Q1)	0.13 T/cm
maximum magnetic gradient (Q2)	0.033 T/cm
momentum range	5%
focal plane tilt	$45^\circ$
mean orbit radius	3m
total deflection angle	$162^\circ$
angular range	$-5$ to $90^\circ$
horizontal magnification ( $x \rightarrow x$ )	-0.417
vertical magnification ( $y \rightarrow y$ )	5.98
maximum momentum dispersion	15.45 m
horizontal acceptance angle	$\pm 20$ mr
vertical acceptance angle	$\pm 40$ mr (in over-focus mode)
solid angle	5.6 msr (3.2 in over-focus mode)
weight	600 tons

Table 4.1: Parameters of the Grand Raiden Spectrometer

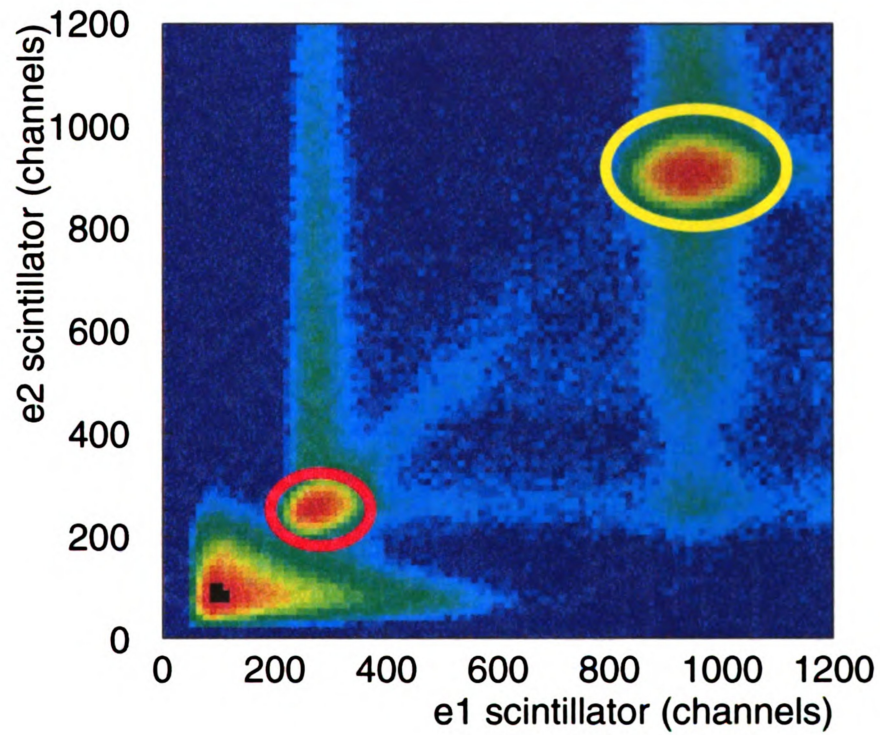


Figure 4.6: Particle identification from the plastic scintillator signals at the Grand Raiden focal plane. Tritons are circled in red, and the charge state is circled in yellow. Particles clustered near channel 0 in both axes are due to cosmic rays and other noise in the scintillators. These events are not associated with reconstructed tracks in the MWDCs.



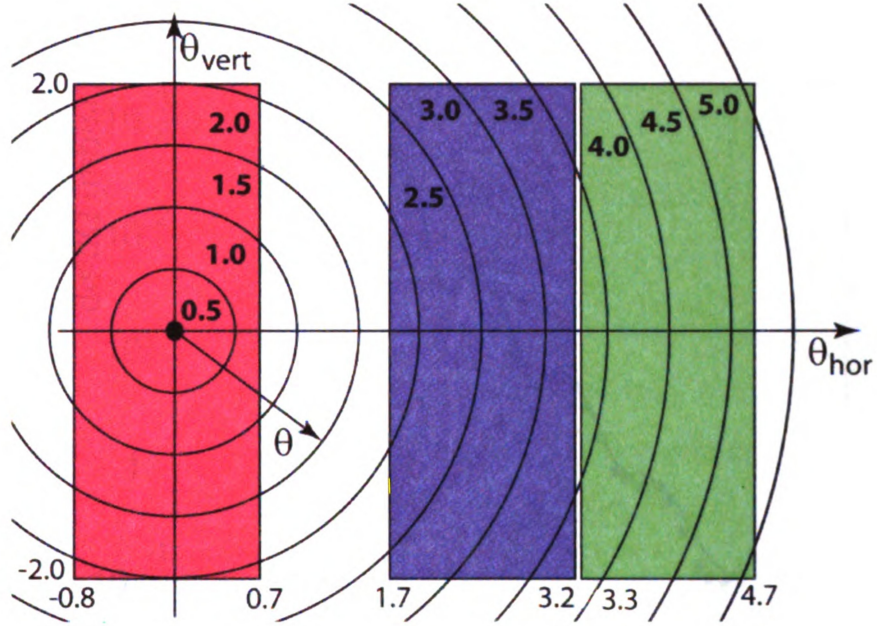


Figure 4.7: The angular acceptance of the Grand Raiden Spectrometer for the three angular settings used. The scattering angle, as measured from the beam axis, is shown with circles for 0.5-degree angular bins. Three rectangles represent the angular coverage accessible when the spectrometer is rotated around its pivot point. Red: angular acceptance for 0-degree measurements. Blue: angular acceptance for 2.5 degree measurements. Green: angular acceptance for 4-degree measurements. In areas where two angle settings overlap, the measurement with best statistics and most complete coverage of the angular range is used, as indicated by the numerical label.

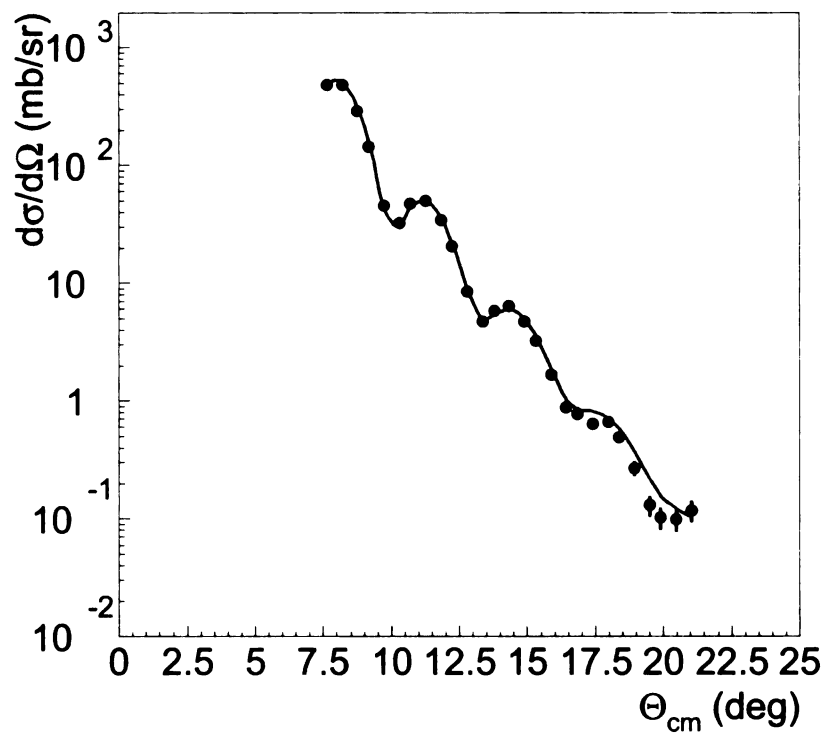


Figure 4.8: Elastic scattering on  $^{150}\text{Nd}$ , including an ECIS fit from which the optical potential was extracted. The fit shown was used in all FOLD calculations. See section 4.3.2 for further details.

a ( $^3\text{He}, ^3\text{He}$ ) elastic scattering measurement. Twenty-seven data points were taken at angles between 8 and 21 degrees in the center of mass. The angular distribution of the cross section was fit with the code ECIS [96] as shown in Figure 4.8, resulting in an optical potential that will be discussed in section 4.3.2.

## 4.2 Calibrations

### 4.2.1 Sieve Slit Calibrations

Field maps that provide detailed information on distribution and strength of the magnetic field emanating from a magnet do not exist with sufficient precision for the elements of the Grand Raiden Spectrometer to use them for the purpose of particle track reconstruction. However, the ability to ion-optically ray-trace particles from the focal plane back to the target is important for any experiment. The solution is to perform a sieve-slit measurement. A block with a distinctive hole pattern is inserted into the beam line  $\sim 60$  cm behind the target and data is taken. Polynomials dependent on  $x_{fp}$ ,  $y_{fp}$ , and  $\Theta_{horizontal}^{fp}$  are then found to reconstruct  $\Theta_{horizontal}^{ta}$  and  $\Theta_{vertical}^{ta}$  based on the hole pattern in the sieve slit. These polynomials go up to the 6<sup>th</sup> order. The sieve slit is then removed from the beam line and the polynomials are used to reconstruct target angles for the rest of the data. See Figures 4.9 and 4.10 for more details on this procedure.

In this experiment, the triton energies were calibrated from known states in  $^{24,25,26}\text{Mg}$ . Strong states in the  $^{nat}\text{Mg}$  data were matched to known values of the excitation energy to extract a relationship between the triton energy and the dispersive position and angle in the focal plane, and this relationship was then applied to the  $^{150}\text{Nd}$  data. A second correction accounted for the difference in recoil energy as a function of scattering angle between the  $^{nat}\text{Mg}$  and  $^{150}\text{Nd}$ . Differences in energy losses for different targets were calculated using LISE++ [115] and accounted for as

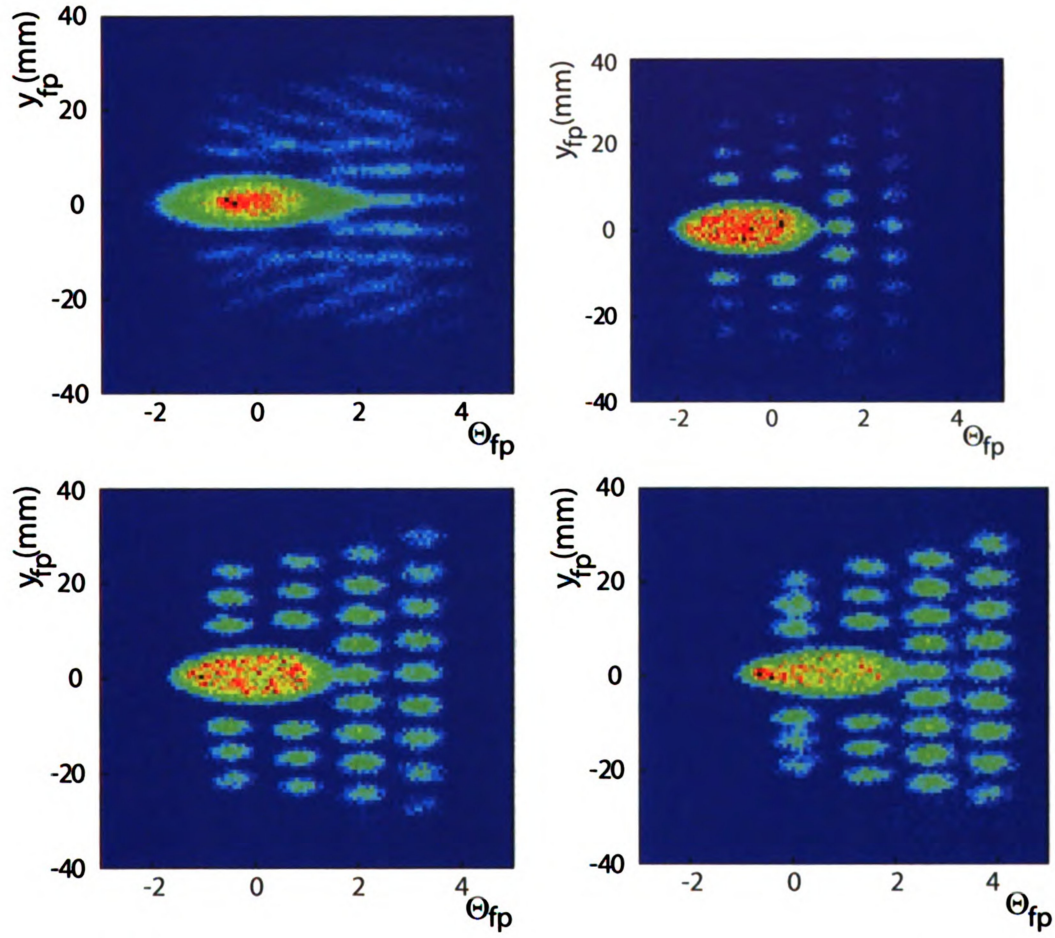


Figure 4.9: Images of the sieve-slit as measured in the focal plane of the Grand Raiden spectrometer. The axes are  $y_{fp}$  versus  $\theta_{fp}$  for four situations: (top left) no cuts on  $x$ , (top right)  $x$  between -100mm and 100mm, (bottom left)  $x$  between 100mm and 300mm, and (bottom right)  $x$  between 300mm and 500mm.

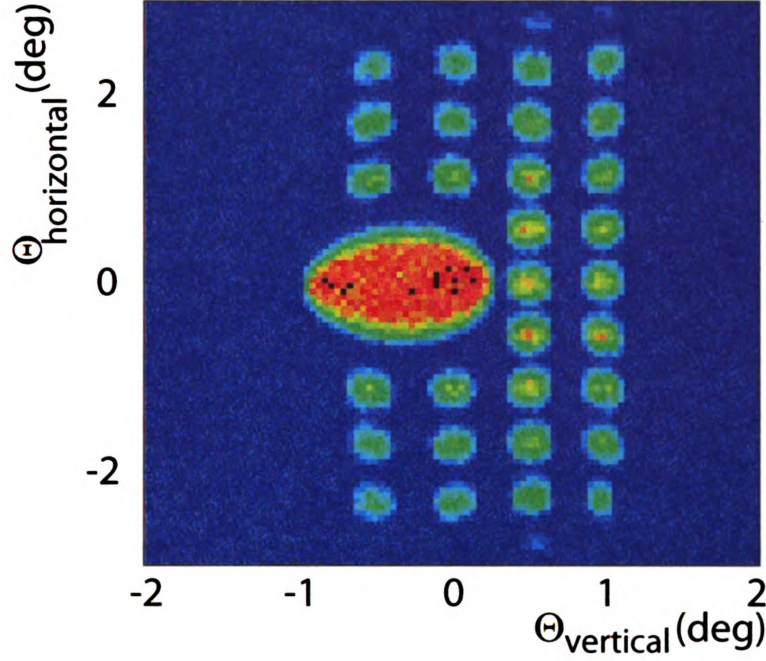


Figure 4.10: Reconstructed sieve slit spectrum after the determination of raytracing parameters (dispersive angle vs. non-dispersive angle at the target)

well. Run-dependent shifts (due to small changes in beam parameters) in the focal plane angles and the beam energy over the course of the experiment were monitored and corrected for so that all of the data could be viewed at once with optimal angular and energy resolution. The energy resolution was 33 keV FWHM. The angular resolution of the laboratory scattering angle was  $0.42^\circ$ , which is based on the angular widths of the  $^3\text{He}^+$  charge state as observed in the focal plane.

#### 4.2.2 Beam rate Calibration and Cross Section Calculation

Beam line polarimeters (BLPs) at two stations were used to cross-check the Faraday cups used to integrate the beam charge at different angular settings. In each BLP, two plastic scintillator detectors at  $48^\circ$  and  $17^\circ$  were placed around a retractable  $14\mu\text{m}$   $\text{CH}_2$  foil in the beam line. The incident beam undergoes elastic scattering on the protons in the  $\text{CH}_2$ , and this yield can then be used to cross-calibrate Faraday cups



for the ( $^3\text{He},t$ ) measurements. Three different Faraday cups were used to measure the beam rate: the  $0^\circ$  cup was inside the D1 dipole, the  $2^\circ$  cup is by the Q1 quadrupole, and  $4^\circ$  cup is inside the scattering chamber (see Figure 4.5). No rescaling had to be applied. Cross sections were calculated with the equation

$$\frac{d\sigma}{d\Omega} = \frac{Y}{N_b N_t \epsilon_1 \epsilon_2 d\Omega}. \quad (4.1)$$

where  $Y$  is the total number of counts in an angular bin,  $N_b$  is the number of nuclei in the beam,  $N_t$  is the number of nuclei in the target,  $d\Omega$  is the opening angle,  $\epsilon_1$  corrects for the lifetime of the data acquisition system (DAQ) (which was around 96%), and  $\epsilon_2$  corrects for the target purity (also 96%).

### 4.3 Analysis of Data

Data for the three angular settings of the Grand Raiden were merged. The laboratory angular range of  $0$ - $5^\circ$  was sliced into ten half-degree bins, as shown in Figure 4.7. Figure 4.11 shows the excitation energy spectrum of  $^{150}\text{Pm}$  for every other angular bin. Shape changes occur as a function of angle due to the angular distributions of the isobaric analogue state (IAS, at 14.35 MeV), Gamow-Teller resonance (GTR, centered at 15.25 MeV), and the spin-dipole resonance (SDR or IVSGDR, centered at 22.8 MeV). The non-spin-flip giant resonances (IVGMR and IVGDR) are very small and do not contribute significantly to the spectrum. The peak due to the IAS exceeds the y-axis scale in Figure 4.11 and peaks at 0.43 mb/sr/5keV (at  $0^\circ$ ). A strong, forward-peaked discrete state is visible at 0.11 MeV, and a weaker pair of dipole states is present near 1.6 MeV (both are easier to see in Figure 4.12).

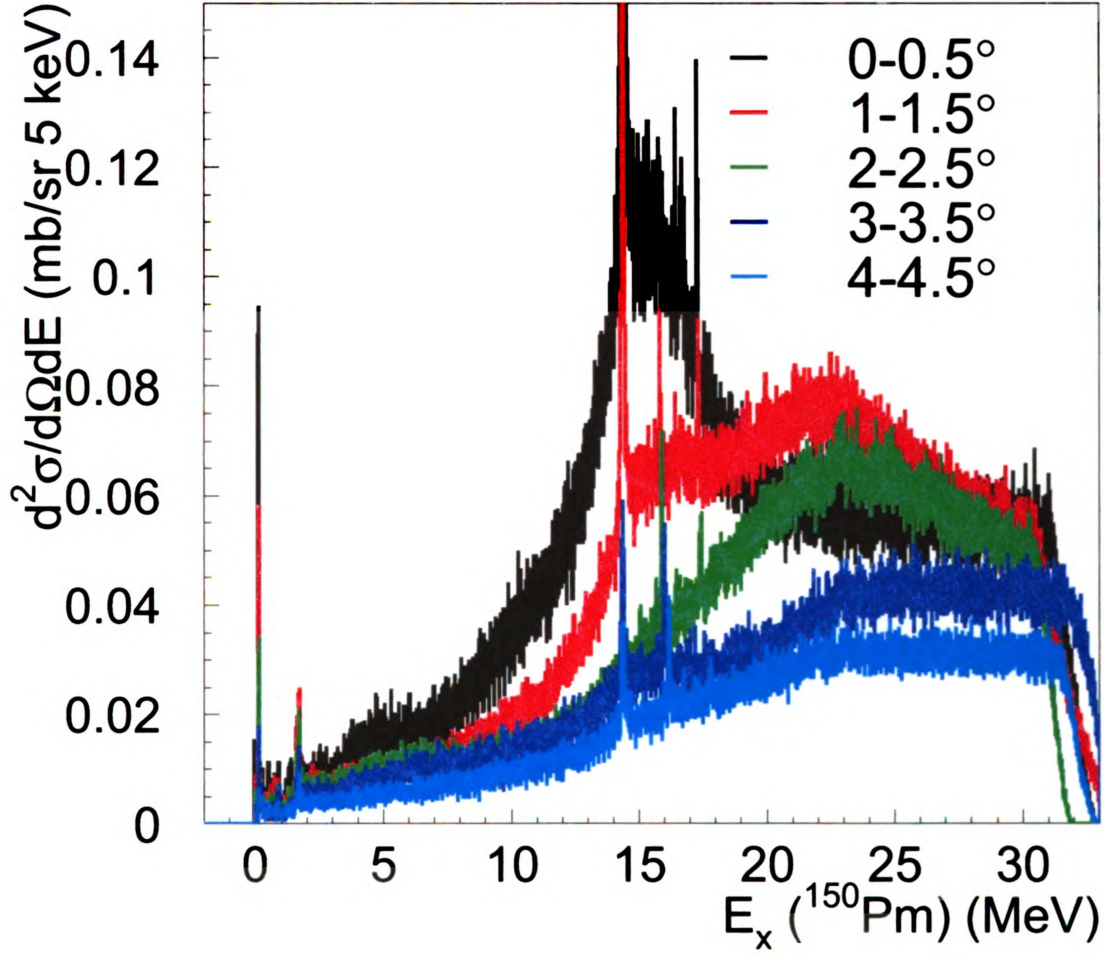


Figure 4.11: Cross sections for the  $^{150}\text{Nd}(^3\text{He},t)$  experiment: every other  $0.5^\circ$ -wide angular bin is shown. The IAS, GTR, and IVSGDR (respectively) are located near 14 MeV, 15 MeV, and 22 MeV. The IAS and GTR are strongest at forward angles, while the IVSGDR is strongest around  $1.5^\circ$ . Slight contamination from  $^{16}\text{O}$  causes the peaks at 16 and 17.5 MeV. Angles are in the laboratory frame.

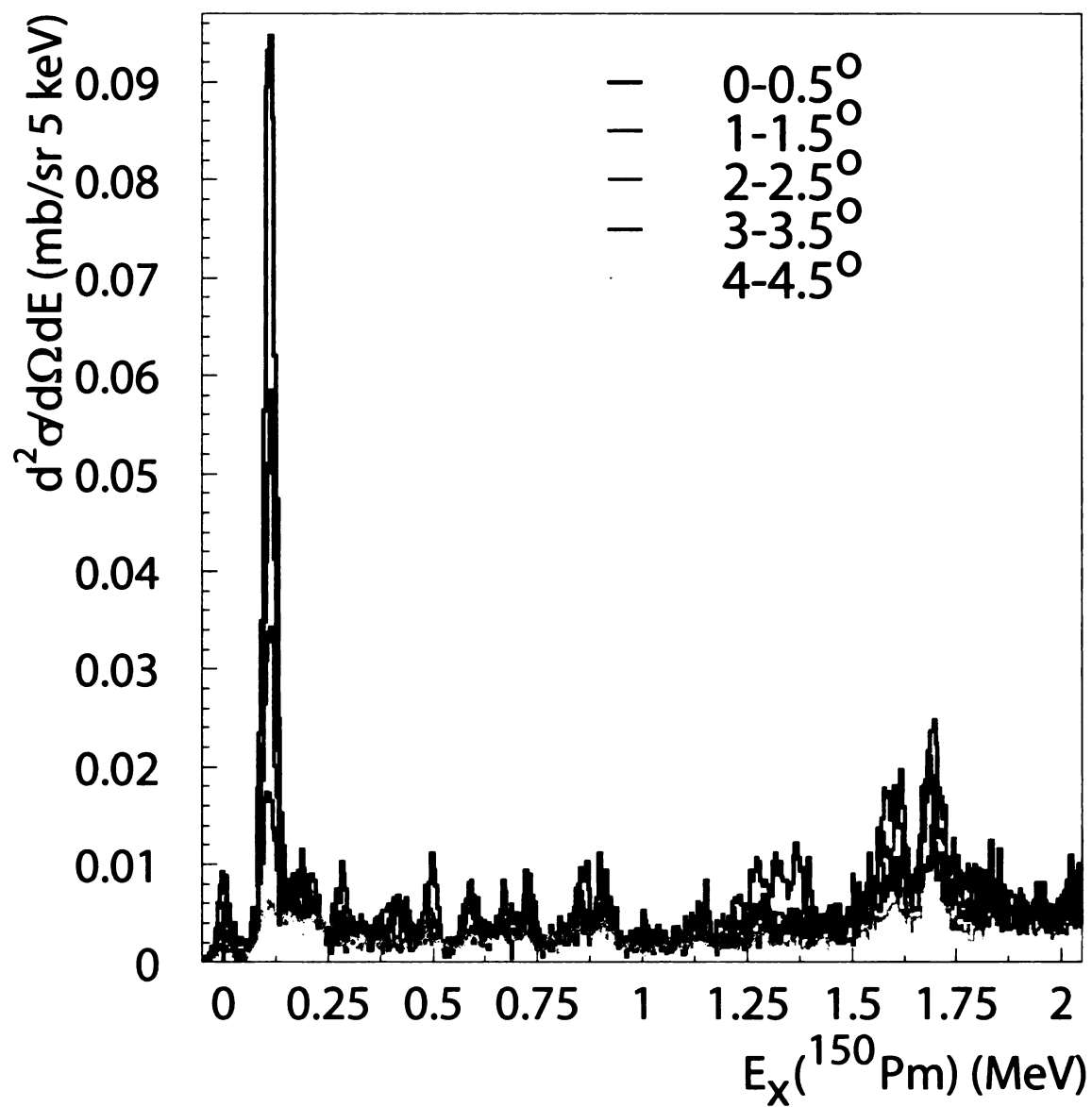


Figure 4.12: Cross sections from 0-2 MeV for the  $^{150}\text{Nd}(^3\text{He},t)$  experiment. Angles are in the laboratory frame.



### 4.3.1 FOLD calculations for $^{150}\text{Nd}(^3\text{He},t)$

As described in Chapter 3, the FOLD code can be used to calculate angular distributions for charge-exchange differential cross sections. Figure 4.13 shows the five shapes representing  $\Delta L = 0, 1, 2, 3$ , and 4. In general,  $\Delta L + \Delta S = \Delta J$ .  $\Delta L=0$  strength corresponds to a Fermi or Gamow-Teller transition ( $J^\pi = 0^+$  or  $1^+$  respectively) or their  $2\hbar\omega$  overmodes (the IVGMR and IVSGMR) and peaks near  $0^\circ$ .  $\Delta L=1$  is a dipole transition, with a  $\Delta J^\pi$  of either  $0^-$ ,  $1^-$ , or  $2^-$ , and peaks around  $1.5^\circ$ .  $\Delta L=2$  is a quadrupole transition, and  $\Delta L=3$  (octupole) and  $\Delta L=4$  (hexadecapole) transitions are also used. For a complete list of the relevant quantum numbers, refer to Table 3.1. All of the relevant  $J^\pi$  transitions up through  $4^+$  are represented by combinations of these five shapes. For example, the  $J^\pi=2^-$  case is a combination of  $\Delta L=1$  and 3 with  $\Delta S=1$ . Transitions with  $\Delta L > 4$  are not included in the analysis, because the angular distributions peak beyond  $5^\circ$  in the center of mass and data was taken in the range of  $0-5^\circ$ . The population of transitions with high  $\Delta L$  values is reduced near  $q=0$ , and contributions from these transitions (with  $\Delta L > 4$ ) are effectively absorbed into  $\Delta L=3$  and 4.

### 4.3.2 The Optical Potential and the IAS

As mentioned at the end of Section 4.1.1, optical potential parameters were fit to elastic scattering data using the code ECIS [96]. The first optical potential tried (potential 1 of Table 4.2) was an extrapolation of parameters obtained from elastic scattering on other targets (such as  $^{90}\text{Zr}$  and  $^{208}\text{Pb}$ ). This potential produced a cross section that had a magnitude 60% higher than the IAS seen in the data. This is consistent with what has been seen for other targets, but in this case the calculated angular distribution for the IAS did not match the data. A second set of optical model parameters (potential 2 in Table 4.2) was deduced from a fit to the elastic

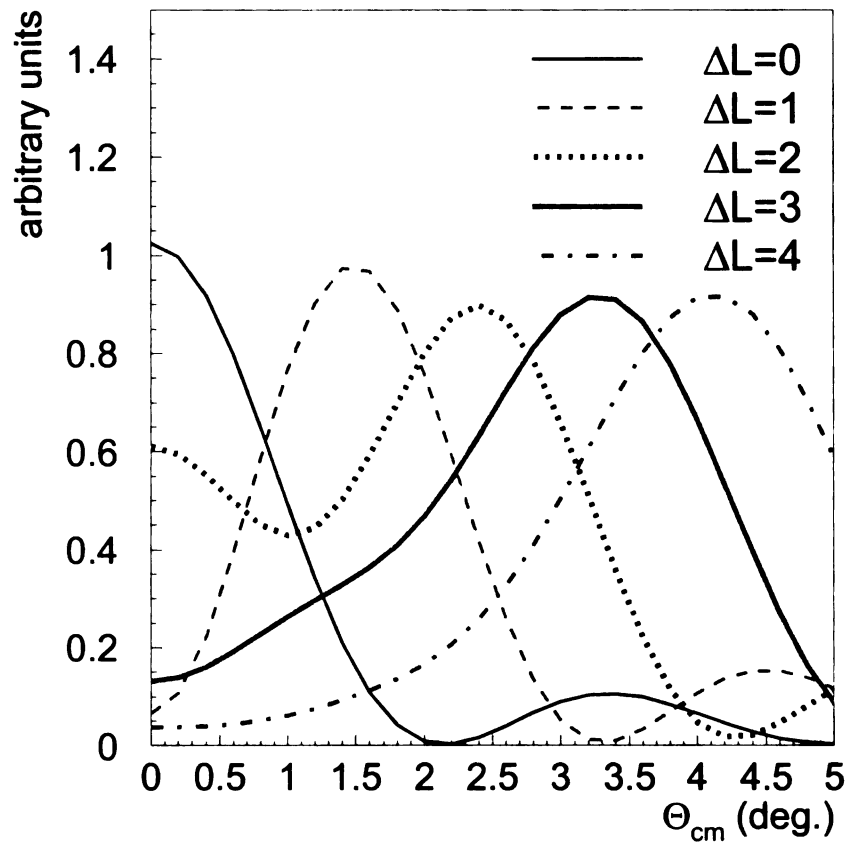


Figure 4.13: Angular distributions from  $^{150}\text{Nd}(^3\text{He},t)$  as calculated with FOLD. Relative scaling of the distributions is arbitrary and chosen solely to better display the function shape.

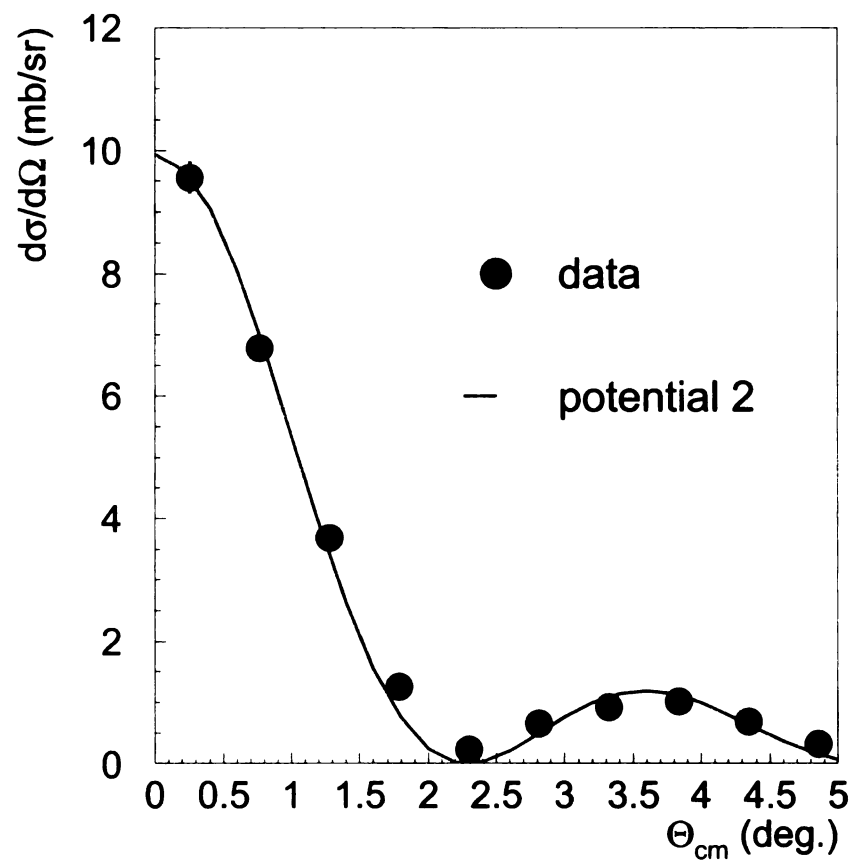


Figure 4.14: The angular distribution of the optical potential compared to the IAS. Table 4.2 contains the parameters for potential 2.

Potential	V	r	a	W	$r_w$	$r_a$
1	31.79	1.34	0.83	36.4	0.94	1.28
2	58.57	1.134	1.032	66.7	1.0925	0.94

Table 4.2: Optical potentials for the elastic scattering data and the angular distribution of the IAS. Potential 1 was the standard potential at the beginning of the iterative process and fit neither the elastic scattering data or the IAS. Potential 2 was chosen for use in DWHI calculations because it was a reasonable fit to both.

scattering data in Figure 4.8. When this potential was scaled and applied to the IAS, the location of maxima and minima were well reproduced (see Figure 4.14). This set of optical model parameters was used in the rest of the analysis, since the main purpose of the calculated angular distribution is to provide input for a multipole decomposition analysis. While the  $W$  (imaginary volume term) is unusually large in potential 2, lower values of  $W$  could not reproduce the elastic scattering curve. This may be because of  $^{150}\text{Nd}$ 's deformation, or it may be a sign that the functional form of the optical potential should include other components, such as surface or spin-orbit terms. Given the limited angular coverage of the elastic scattering measurement and the absence of polarization observables, it was not possible to perform a fit to a more complicated optical potential.

### 4.3.3 Multipole Decomposition Analysis

The  $^{150}\text{Nd}(^3\text{He},t)$  data was analyzed with two separate methods. The first method is a multipole decomposition analysis (MDA)[116]. Since  $^{150}\text{Pm}$ 's level density is high (it is a heavy odd-odd nucleus), a peak-by-peak analysis is impossible, even at low energies. Instead, the spectrum is split up into 1 MeV bins, and the angular distribution of the measured cross section is fit with a linear combination of the calculated cross sections from DWBA. Angular distributions for each discernable peak in the region of 0-2 MeV were fit in a similar fashion. In the following equation

for a multipole decomposition,  $\sigma_i$  represents the calculated angular distribution from Figure 4.13 for  $\Delta L=i$  and the capital letters represent the fit parameters.

$$\sigma_{tot} = A * \sigma_1 + B * \sigma_2 + C * \sigma_3 + D * \sigma_4 + E * \sigma_5 \quad (4.2)$$

In the  $^{150}\text{Nd}$  analysis, five functions were used in the multipole decomposition, representing  $\Delta L=0,1,2,3$ , and 4. Contributions from certain  $\Delta L$  values were consistent with 0 for some angular bins.

As shown in Figure 4.15 (top), transitions to the ground state peak around  $1.5^\circ$ , which implies it is dominated by dipole ( $\Delta L=1$ ) contributions. A significant  $\Delta L=3$  contribution is also observed. Unless two states exist at energies too close to separate, this fit indicates that the ground state may have a  $J^\pi$  of  $2^-$ . Barrette *et al.* [117] studied the decay of  $^{150}\text{Pm}$  to  $^{150}\text{Sm}$  and give a tentative  $J^\pi$  of  $1^-$  or  $1^+$  to this level, but this is based entirely on arguments that no states of high spin in  $^{150}\text{Sm}$  were observed to be directly fed by the  $^{150}\text{Pm}$  ground state decay. However, a large number of levels from that experiment were not placed in a level scheme, and their evidence for a  $J$  of 1 is incomplete. The MDA from the current experiment shows that  $J^\pi$  contributions of  $2^-$  or  $1^-+3^-$  (in the case of two inseparable states) are possible, but  $1^+$  is ruled out. Since we don't have OBTDs for individual transitions, we cannot fully exclude the possibility that this is a  $1^-$  state with an angular distribution that has been modified due to the influence of the  $T\tau$  interaction.

A very strong state at 0.11 MeV (see the bottom of Figure 4.15) peaks at 0 degrees and decreases in strength at higher angles, which is a sign of a sizable  $\Delta L=0$  (GT) component. There are  $\Delta L=1$  and 2 contributions to this angular distribution, but it is dominated by  $\Delta L=0$  contributions. The extracted  $\Delta L=0$  cross section is  $0.565 \pm 0.085$  mb/sr. The  $\Delta L=2$  contribution may be from the GT transition, and both the  $\Delta L=1$  and 2 components may be indicative of a second state at the same excitation

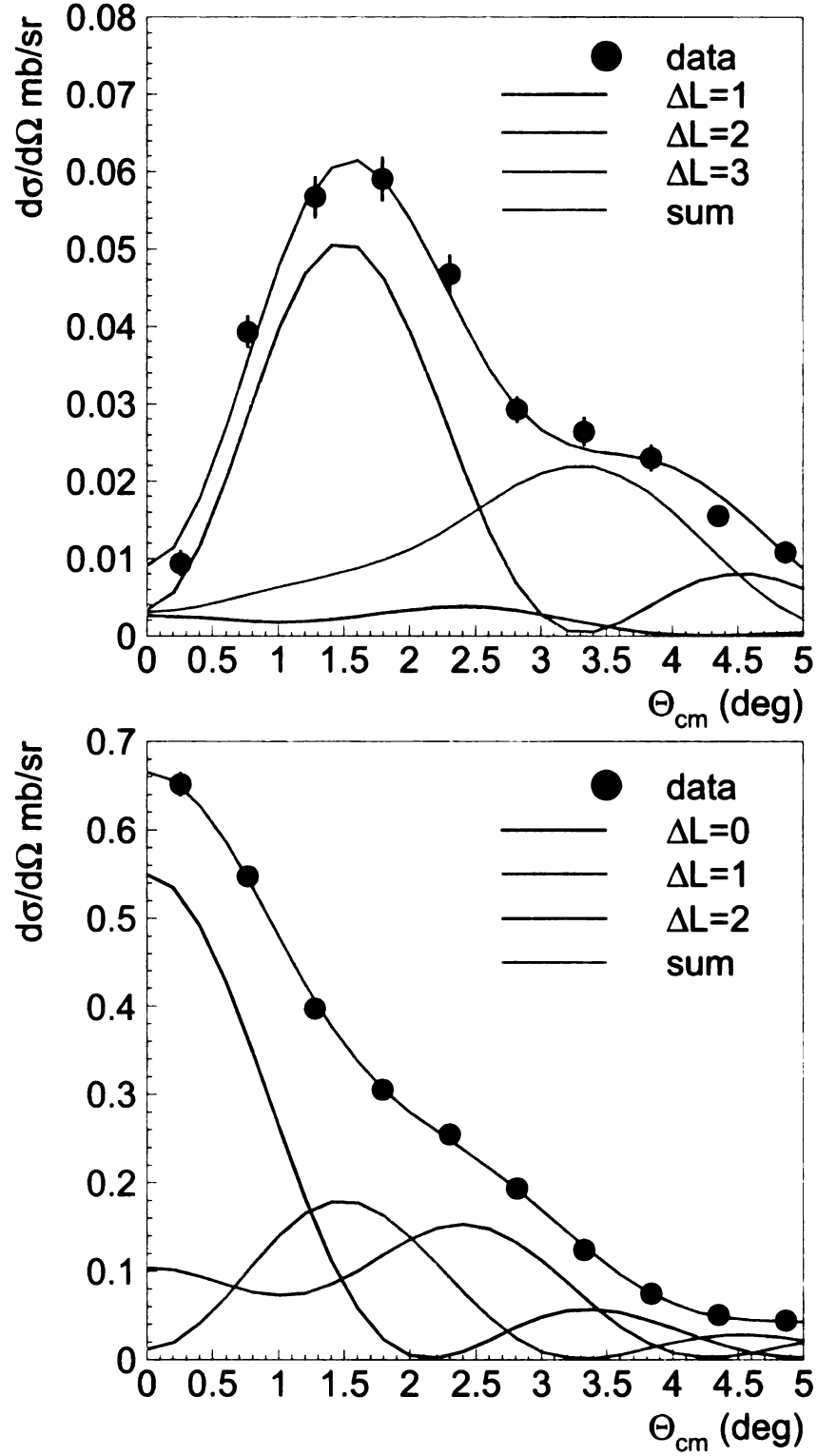


Figure 4.15: Multipole decomposition of the first two single peaks in  $^{150}\text{Pm}$ : the ground state and the first excited state. The differential cross section for each peak is fitted to a linear combination of angular distributions associated with different units of angular momentum transfer.

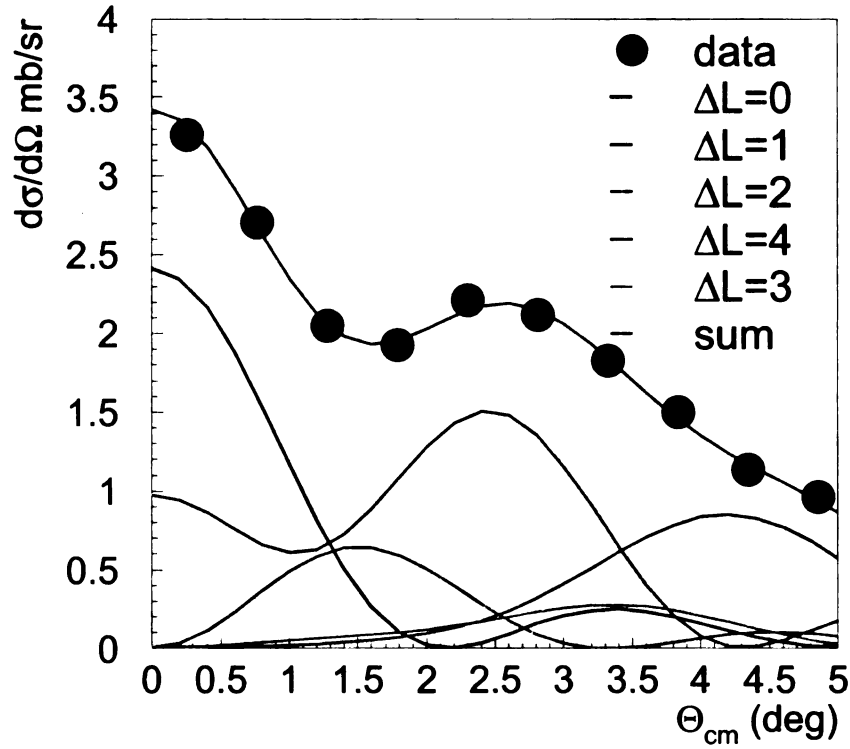


Figure 4.16: Multipole decomposition of the 5-6 MeV excitation energy bin. The  $\Delta L=0,2$  components are strongest.

energy or the presence of small states nearby. Other states below 2 MeV that could be identified were analyzed in the same fashion. They are all much weaker than the 0.11 MeV state. Some states, such as the three peaks near 1.3 MeV, can be modeled well as  $\Delta L=0$  states, and others, such as the two peaks near 1.63 MeV, as  $\Delta L=1$  states.

After dividing the excitation energy spectrum into 1 MeV energy bins, angular distributions were created and MDA fits were performed for the entire energy range of the experiment (0-30 MeV). Figure 4.16 gives an example for the 5-6 MeV energy bin. Results from the MDA for each energy bin can be combined to show the excitation energy distribution of different types of transition strengths. Figure 4.17 shows the results for all angles and excitation energies. The Gamow-Teller resonance peaks around 15 MeV, along with some strength at 5 and 10 MeV, but the long tail at higher excitation energies may come from the spin-flip giant monopole resonance (IVSGMR)

and/or high-lying GT strength associated with coupling to 2p-2h configurations [77]. As noted in Chapter 3, the resonance centroid of the IVSGMR is expected to be around 37 MeV. In a similar experiment on  $^{120}\text{Sn}$ , low-lying  $\Delta L=0$  strength was attributed to “core polarization spin-flip” ( $j = l \pm \frac{1}{2} \rightarrow j = l \pm \frac{1}{2}$ ) and “back spin flip” ( $j = l - \frac{1}{2} \rightarrow j = l + \frac{1}{2}$ ) [118, 119] modes. The strength at 5 and 10 MeV is likely due to the same types of contributions. These peaks are referred to as pygmy resonances [120, 58]. The spin-dipole resonance dominates between 1.5 and 2°. No resonance structures are seen (or expected) for  $\Delta L=2,3$ , and 4. Giant resonances associated with these  $\Delta L$  values are expected to peak at higher excitation energies. Information from the  $\Delta L=3,4$  distributions may represent higher multipoles as well, as noted in Section 4.3.1.

#### 4.3.4 Resonance fits

A second method of analyzing the  $^{150}\text{Nd}$  data was that of resonance fits. The goal of this method is to completely reproduce the spectrum with a combination of (resonance) base functions. Many studies of nuclear giant resonances have been done in this manner [77], and the location of some resonances (such as the IAS, GTR, and the IVSGDR) is quite well-known. The IAS and GTR both peak around 15 MeV. While the IVSGDR has three components ( $0^-$ ,  $1^-$ , and  $2^-$ ), they are not distinguishable from one another in the data because they overlap and have the same  $\Delta L$  value and angular distribution. Instead, the summed strength peaks around 22 MeV. The IVGDR occurs around the same excitation energy, but it is much smaller in magnitude than the IVSGDR (around a factor of 1/30). To model the entire excitation energy spectrum, one should include the GTR, IAS, IVSGDR, the fragmented GT strength at 5 and 10 MeV, and a function for quasi-free (QF) processes.

Quasi-free charge exchange can occur when the  $^3\text{He}$  projectile interacts with a single neutron in the target in such a way that the rest of the nucleus can be considered



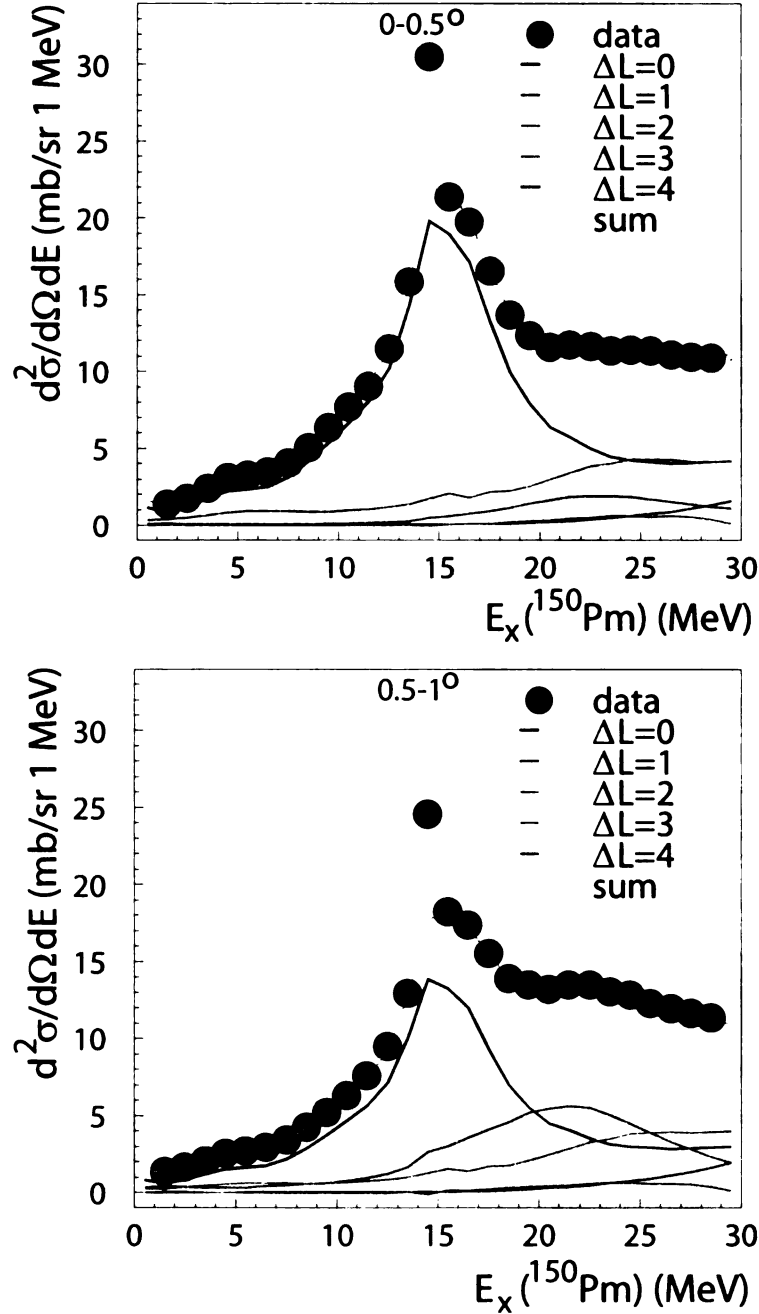


Figure 4.17: Multipole decomposition summary for each  $0.5^\circ$  angular bin. The IAS was removed from the fit, causing the visible discontinuities around 14 MeV in excitation energy, and the  $^{16}\text{O}$  impurity causes a second discontinuity around 16 MeV. The GT resonance dominates the spectrum between  $0-0.5^\circ$ , but rapidly diminishes and is replaced by the IVSGDR at  $1.5-2^\circ$ . Higher multipoles (or quasifree processes) take over at higher angular bins.

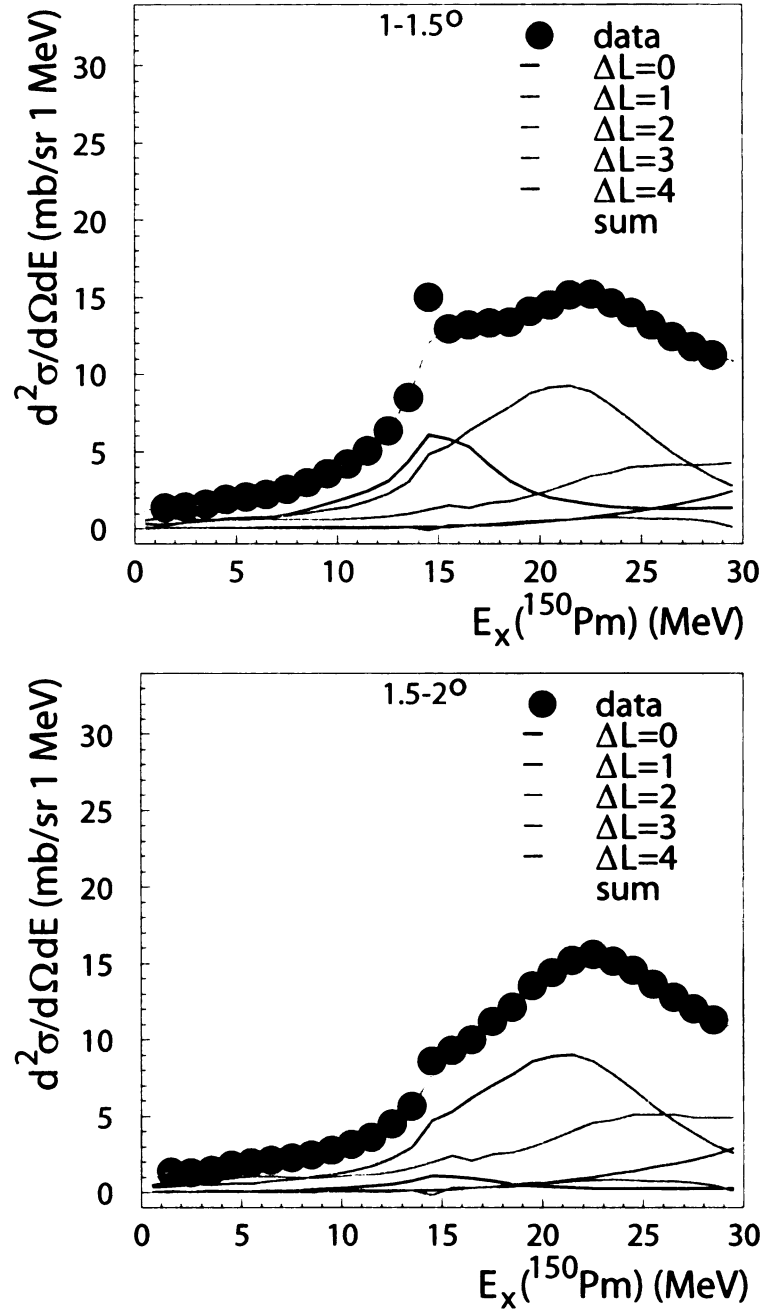


Figure 4.17: Multipole decomposition summary for each  $0.5^\circ$  angular bin. The IAS was removed from the fit, causing the visible discontinuities around 14 MeV in excitation energy, and the  $^{16}\text{O}$  impurity causes a second discontinuity around 16 MeV. The GT resonance dominates the spectrum between  $0-0.5^\circ$ , but rapidly diminishes and is replaced by the IVSGDR at  $1.5-2^\circ$ . Higher multipoles (or quasifree processes) take over at higher angular bins.

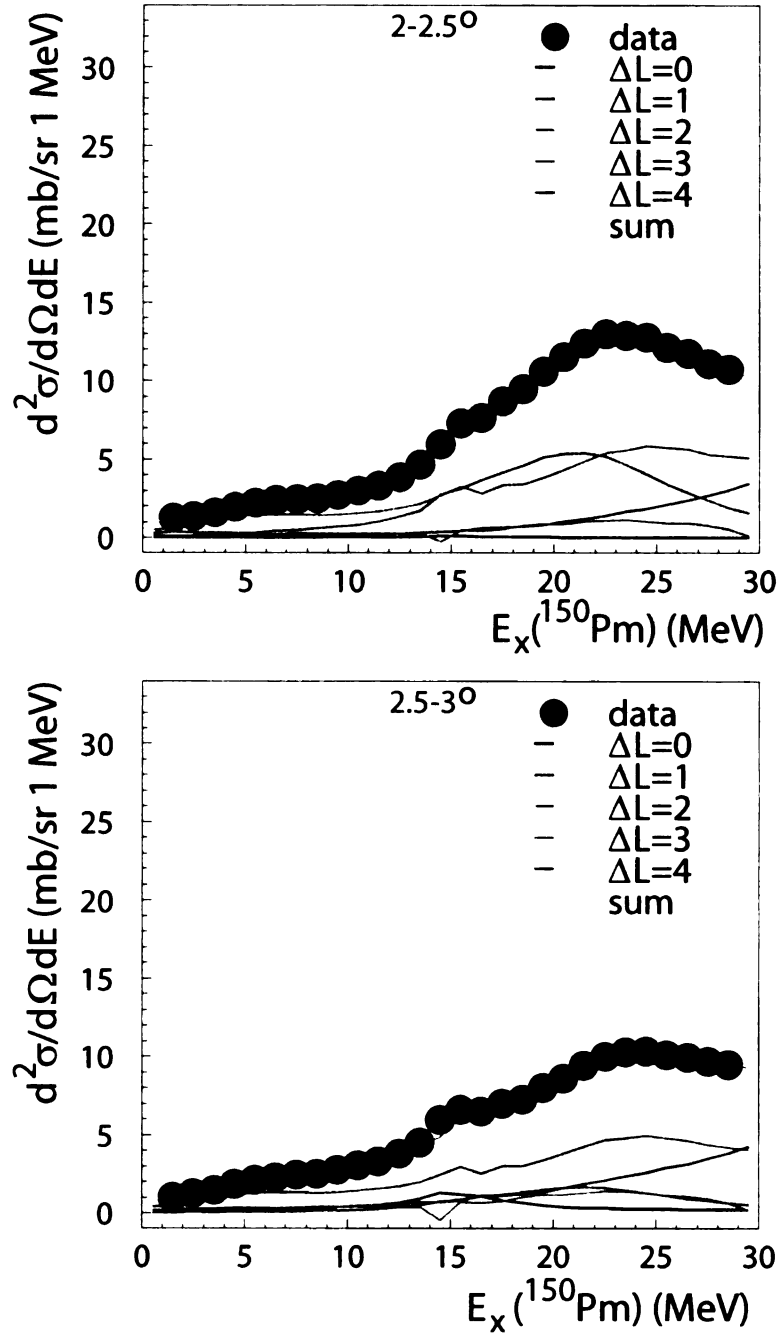


Figure 4.17: Multipole decomposition summary for each  $0.5^\circ$  angular bin. The IAS was removed from the fit, causing the visible discontinuities around 14 MeV in excitation energy, and the  $^{16}\text{O}$  impurity causes a second discontinuity around 16 MeV. The GT resonance dominates the spectrum between  $0-0.5^\circ$ , but rapidly diminishes and is replaced by the IVSGDR at  $1.5-2^\circ$ . Higher multipoles (or quasifree processes) take over at higher angular bins.

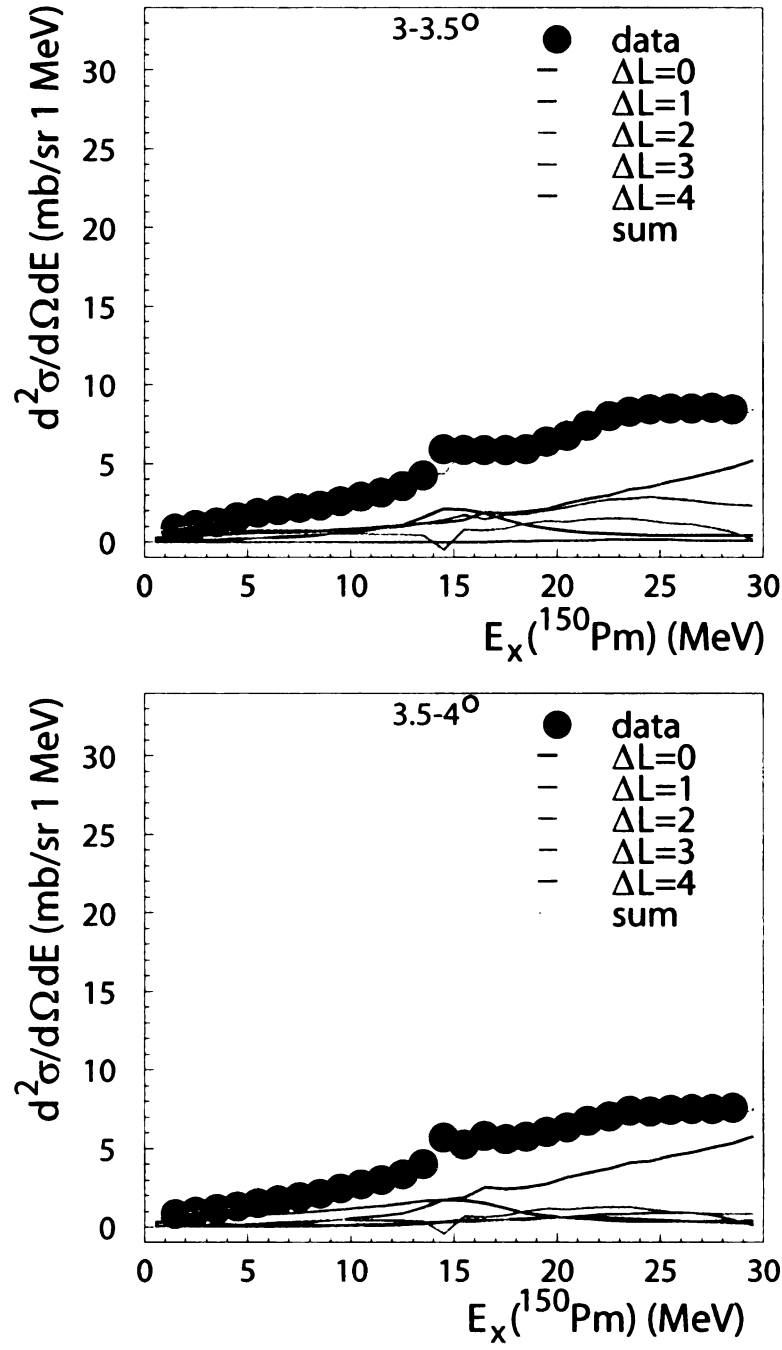


Figure 4.17: Multipole decomposition summary for each  $0.5^\circ$  angular bin. The IAS was removed from the fit, causing the visible discontinuities around 14 MeV in excitation energy, and the  $^{16}\text{O}$  impurity causes a second discontinuity around 16 MeV. The GT resonance dominates the spectrum between  $0-0.5^\circ$ , but rapidly diminishes and is replaced by the IVSGDR at  $1.5-2^\circ$ . Higher multipoles (or quasifree processes) take over at higher angular bins.

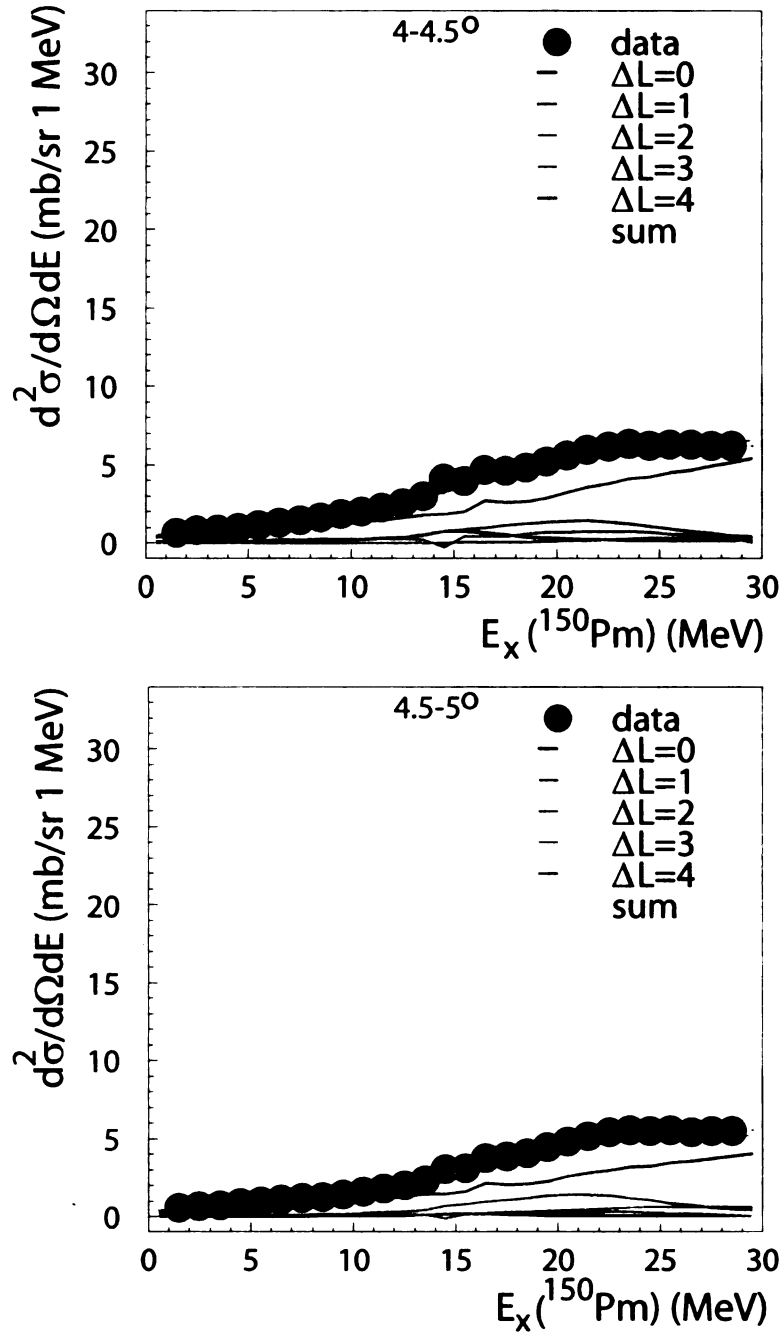


Figure 4.17: *cont.* Multipole decomposition summary for each half-degree angular bin. The IAS was removed from the fit, causing the visible discontinuities around 14 MeV in excitation energy, and the  $^{16}\text{O}$  impurity causes a second discontinuity around 16 MeV. The GT resonance dominates the spectrum between  $0-0.5^\circ$ , but rapidly diminishes and is replaced by the IVSGDR at  $1.5-2^\circ$ . Higher multipoles (or quasifree processes) take over at higher angular bins.

a spectator and the neutron a free particle except for its binding energy. The neutron is transformed into a proton and “knocked out,” which requires the process to take place only above the proton separation energy. As the energy transferred to the residual gets higher, neutrons in deeper shells (with greater binding energy) can be removed. Superimposing the energy of the knocked-out protons results in the characteristic QF shape (see Figure 4.18). In this work, the QF contribution was modeled with Erell’s [76] semi-phenomenological function

$$\frac{d^2\sigma}{dEd\Omega} = N \frac{1 - e^{[(Et_{gs} - x - E_0)/T]}}{1 + [(Et_{gs} - x - E_{qf})/W]^2} \quad (4.3)$$

initially developed for pion charge-exchange. This function has since been applied to ( $^3\text{He}, t$ ) [118, 119] and other types of CE experiments. Three parameters are fit:  $N$  is an overall normalization factor different for each angular bin,  $W$  represents the Fermi motion of the nucleon within the nucleus, and  $T$  is a temperature parameter.  $E_0$  is the energy at which the QF curve crosses the  $x$  (excitation energy) axis. The exponential represents the effects of Pauli blocking. The remaining parameters are described or derived from values in Table 4.3.

The GTR and IVSGDR are represented by Gaussians, because using Lorentzians creates non-physical long tails. The IAS was modeled with a Lorentzian. In addition to the quasi-free curve, two small Gaussian functions (G5 and G10) were added to the fit near 5 MeV and 10 MeV to represent the pygmy GT resonances and other low-lying strength. With these six functions, an 18-parameter fit was performed using MINUIT [121]. Figure 4.18 shows the result for all ten angular bins.

The fit resonances were integrated for each angular bin to produce an angular distribution. These were then decomposed into  $\Delta L$  components with the functions used in the MDA (see Figure 4.13). Comparisons between the two methods could then be made (see Figure 4.19). As expected, the function labeled IAS was entirely

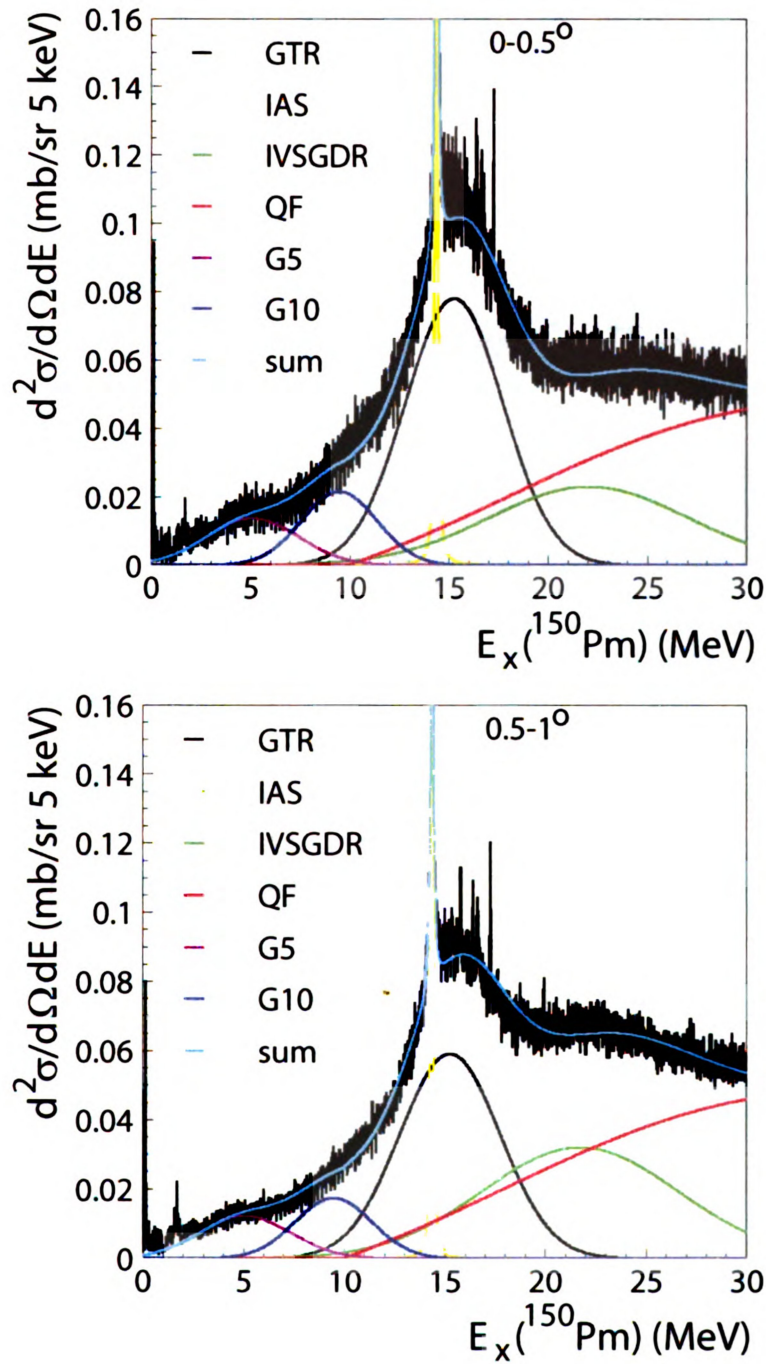


Figure 4.18: Resonance fit to the excitation energy spectrum. The sum of the six fit functions reproduces the original shape of the data.

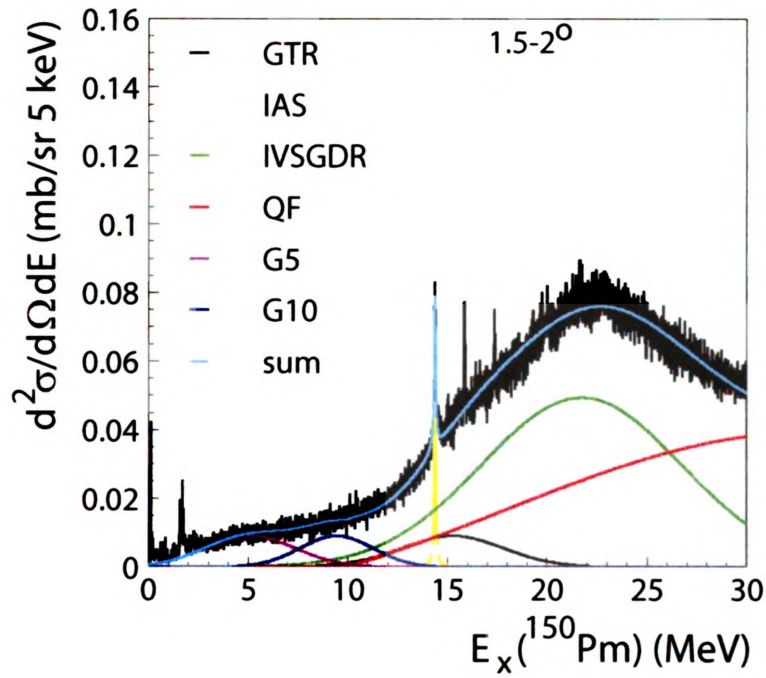
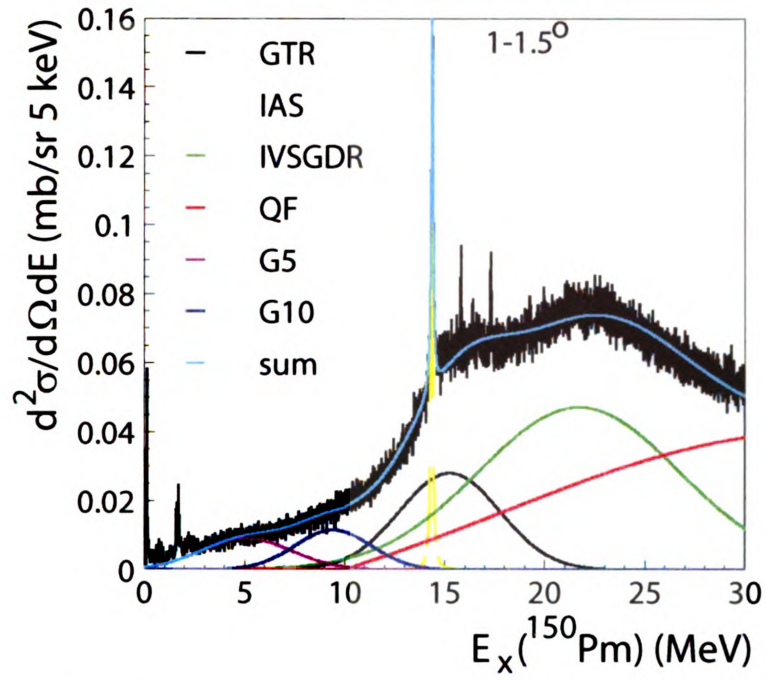


Figure 4.18: *cont.* Resonance fit to the excitation energy spectrum. The sum of the six fit functions reproduces the original shape of the data.



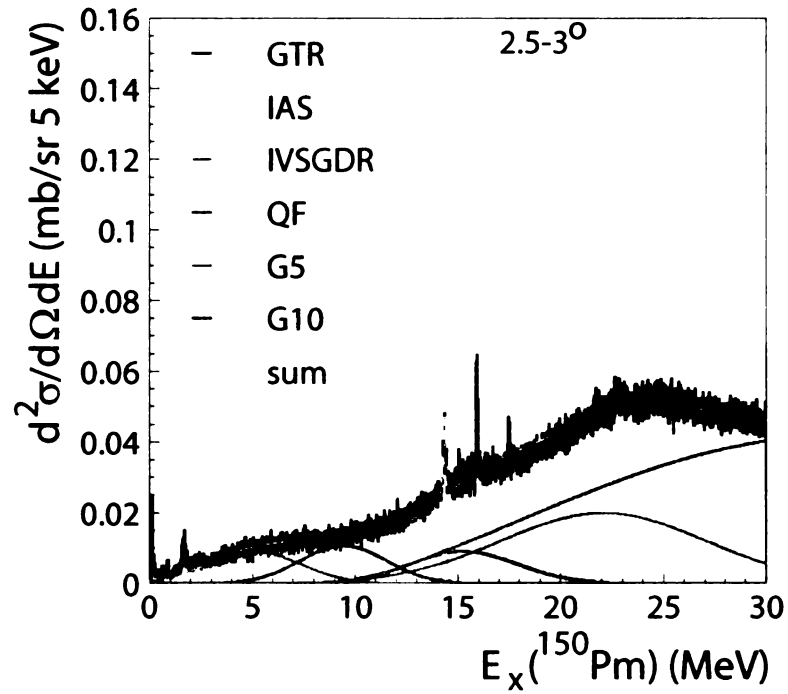
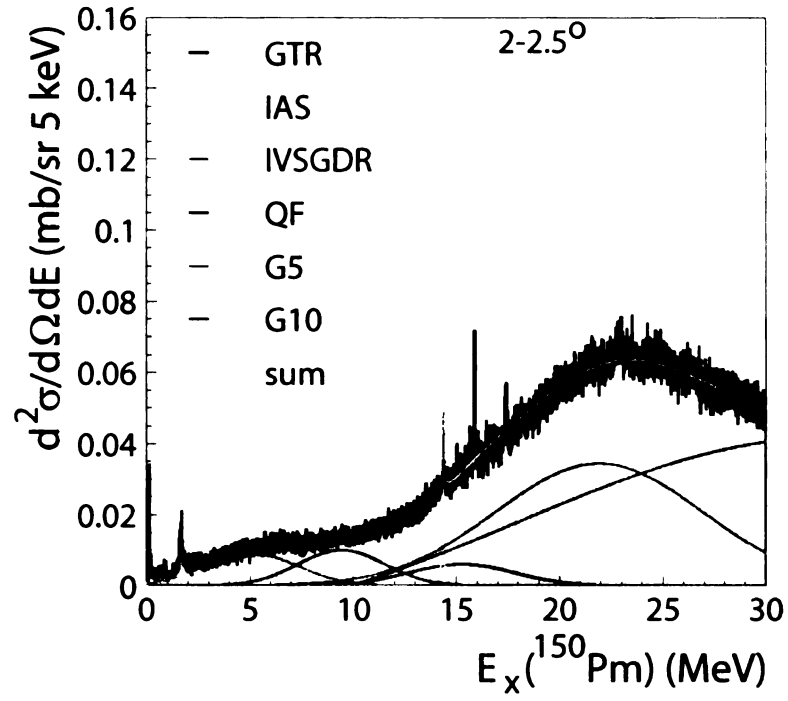


Figure 4.18: *cont.* Resonance fit to the excitation energy spectrum. The sum of the six fit functions reproduces the original shape of the data.

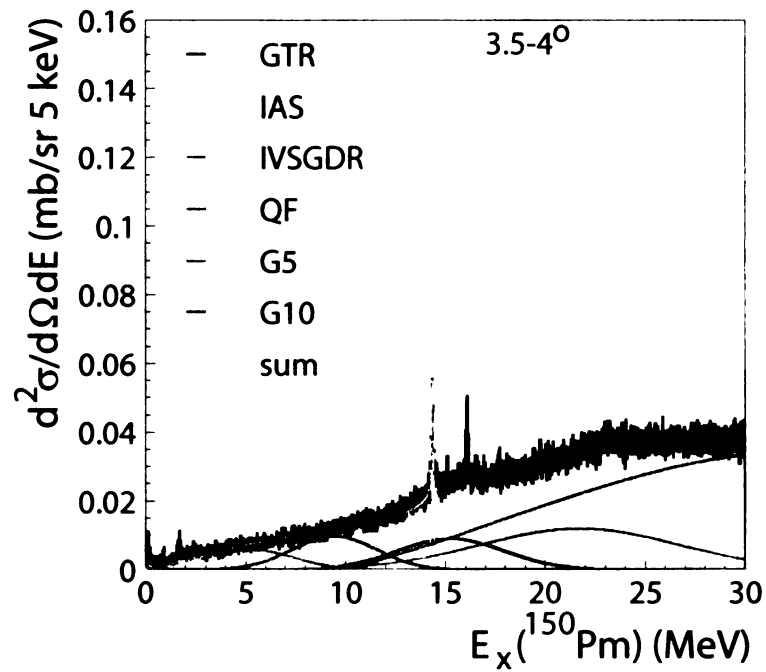
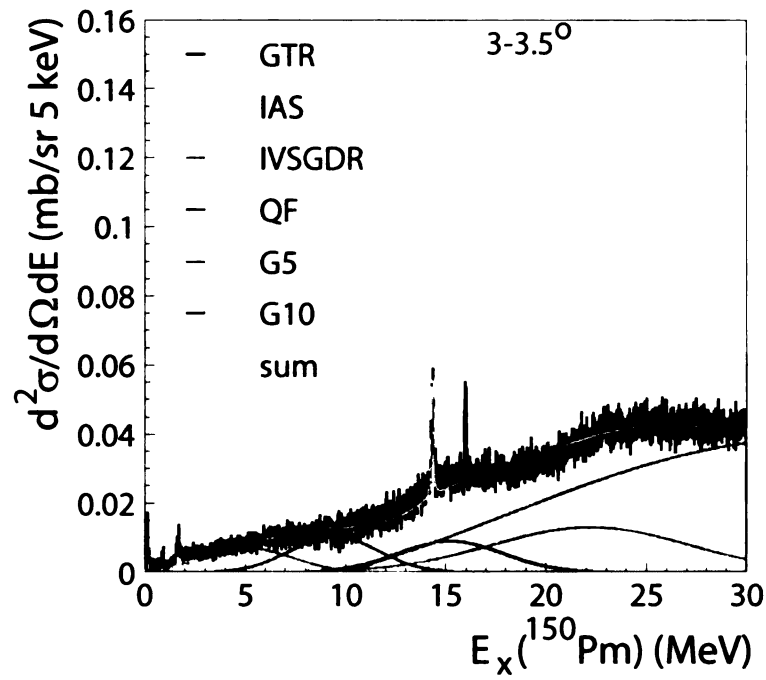


Figure 4.18: *cont.* Resonance fit to the excitation energy spectrum. The sum of the six fit functions reproduces the original shape of the data.

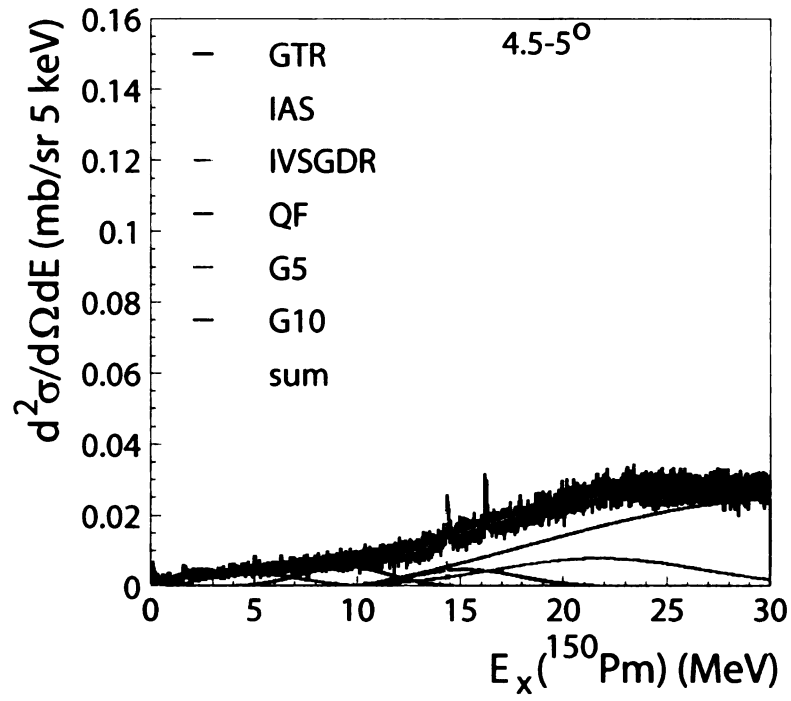
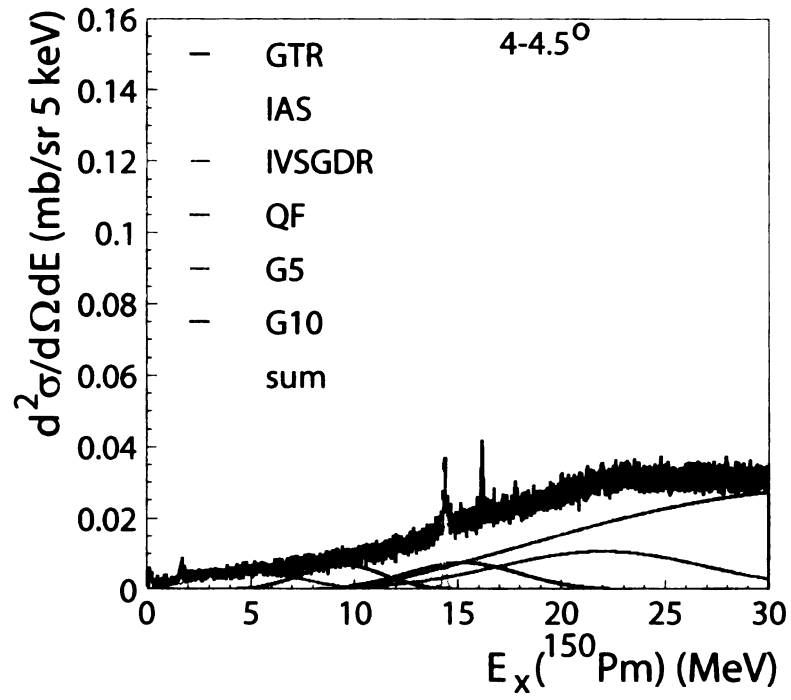


Figure 4.18: *cont.* Resonance fit to the excitation energy spectrum. The sum of the six fit functions reproduces the original shape of the data.

Parameter name	Definition/Method of Calculation	Value
N	normalization, fit	fit
Q	Q value for $^{150}\text{Nd}(^3\text{He},t)$	0.105 MeV
nQ	Q value for $n(^3\text{He},t)p$ at 420 MeV	0.764 MeV
$E_{proj}$	energy of the incoming $^3\text{He}$	420 MeV
$E_{t\ free}$	energy of the free triton, $E_{proj} + nQ$	420.764 MeV
$E_{t\ gs}$	ground state energy of the triton, $E_{proj} - Q$	419.895 MeV
$S_p$	proton separation energy for $^{150}\text{Nd}$	9.922 MeV
$B_{coul}$	Coulomb barrier for the proton	12 MeV
$E_{xn}$	excitation energy of the neutron hole state, from [105]	2 MeV
$E_{qf}$	quasi-free energy, $E_{t\ free} - (S_p + E_{xn} + B_{coul})$	396.864 MeV
$E_0$	$E_{t\ gs} - S_p$	409.973 MeV
W	width of resonance, fit	fit (around 22)
T	slope, fit	fit (around 120)

Table 4.3: Parameters used in calculating the quasi-free curve. The values of T and W are comparable to those found in other works [105, 76].

$\Delta L=0$ , while the GTR was overwhelmingly so and the IVSGDR primarily  $\Delta L=1$ . This confirms that the resonance shapes and their locations are a good match for the real resonances. The QF, G5, and G10 distributions also contain significant  $\Delta L=0$  and  $\Delta L=1$  strength.

#### 4.3.5 Extrapolation to $q=0$

These two analysis methods, resonance fitting and multipole decomposition, result in absolute cross sections for each type of multipole excitation for half-degree angular bins and 1 MeV excitation energy bins (with peak-by-peak resolution below 2 MeV). When contributions from the IAS are removed and possible contributions from the IVSGMR at high excitation energies are ignored, the  $L=0$  cross section and equation 3.24 can be used to extract the Gamow-Teller strength for a given transition. However, the cross section must first be extrapolated to zero momentum transfer ( $q=0$ ). Using

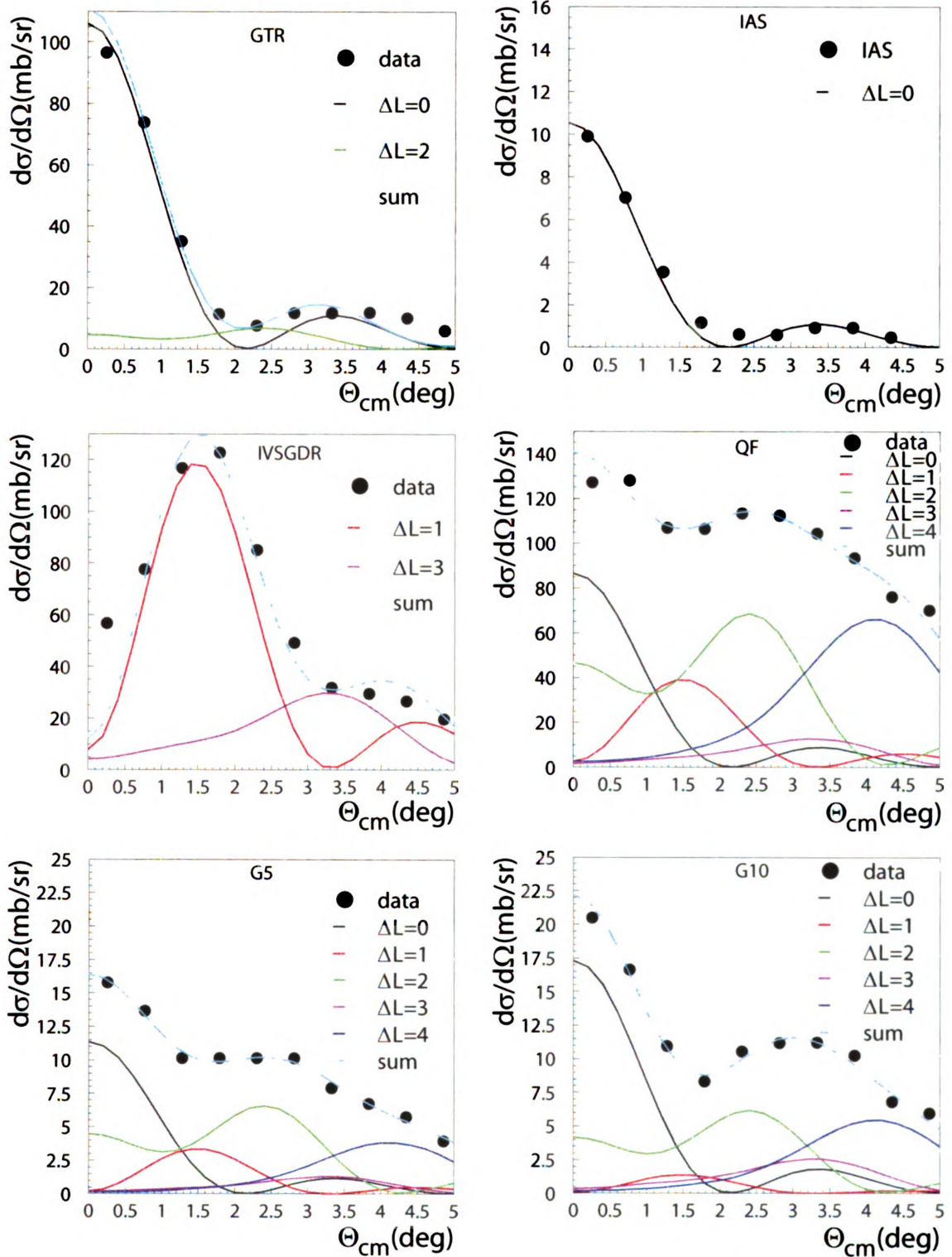


Figure 4.19: Angular distributions of the giant resonances. Components from contributing  $\Delta L$  values are included. The GTR can be reconstructed with only  $\Delta L=0$  and 2, the IAS with only  $\Delta L=0$ , and the IVSGDR with only  $\Delta L=1$  and 3, because the shapes are accurate representations of the actual resonances. The pygmy resonances and the QF are much more complex (though both have significant  $\Delta L=0,2$  contributions).

equation 4.4,

$$\left. \frac{d\sigma}{d\Omega} \right|_{q \rightarrow 0} = \left[ \frac{\frac{d\sigma}{d\Omega}(\theta = 0^\circ, Q = 0)}{\frac{d\sigma}{d\Omega}(\theta = 0^\circ, Q)} \right]_{DWBA} \times \left[ \frac{d\sigma}{d\Omega}(\theta = 0^\circ, Q) \right]_{experiment} \quad (4.4)$$

the ratio of the DWBA cross-section to that at  $0^\circ$  is calculated and multiplied by the experimental cross section. The ratio is shown in Figure 4.20 and is well-described by a polynomial:

$$Y_{ratio} = 1.00057 - 0.0236Q + 0.00185Q^2 - 4.607 \times 10^{-5}Q^3 + 1.297 \times 10^{-6}Q^4, \quad (4.5)$$

where Q is the Q value. Application of this ratio is straightforward for the individual states and the multipole decomposition analysis, since the states are well defined in their excitation energy. Giant resonance fits are spread over a much larger energy range. A convolution of the correction ratio and resonance shape was used to extract  $\left. \frac{d\sigma}{d\Omega} \right|_{q \rightarrow 0}$  for each resonance.

### 4.3.6 Calculation of the Gamow-Teller strength

After extrapolating the experimental cross sections to  $q=0$ , the unit cross section ( $\hat{\sigma}$ ) and equation 3.24 are used to calculate the B(GT). Table 4.4 shows results from the resonance fit method. The total extracted B(GT) is  $56.62 \pm 6.16$ , including both statistical and systematic errors. The IVSGDR and the IAS are excluded from this calculation, because they cannot contain any GT strength, but the QF, G5, and G10 resonance shapes are included because of the large amount of L=0 strength present and because they are composites of more than one multipole.

The MDA yields a total GT strength of  $50.01 \pm 1.69$  (combined statistical and systematic errors). Associated statistical errors from the fitting procedure are quite small, but systematic errors (including contributions from the optical potential and

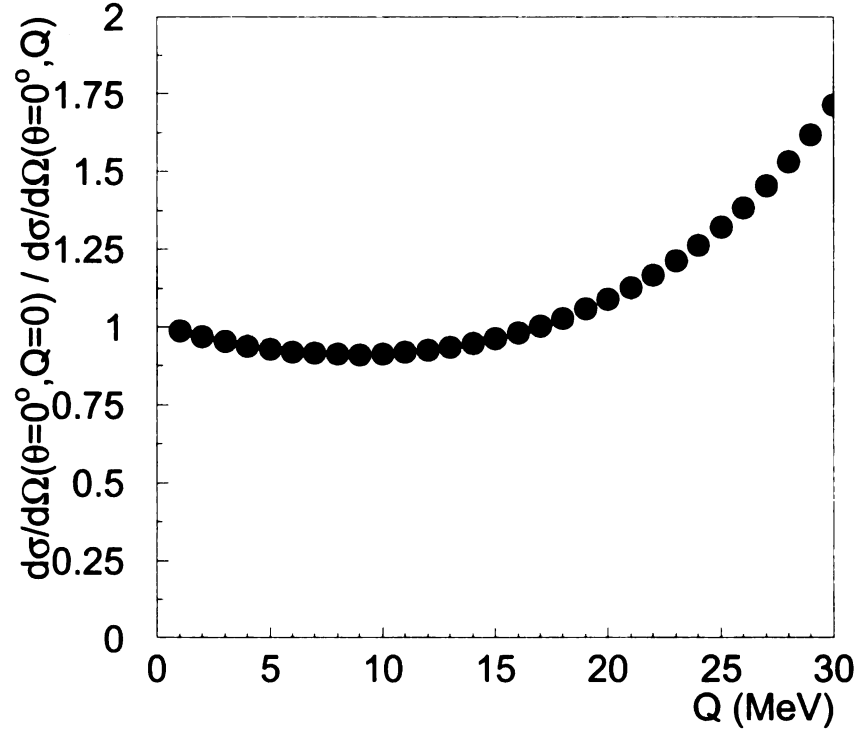


Figure 4.20: Ratio of the cross section at  $\theta=0^\circ$  and 0 linear momentum transfer to that of 0 linear momentum transfer, as calculated in DWBA. See equation 4.5.

Resonance	B(GT)	B(GT) stat. error	B(GT) syst. error	total error
G5	2.506	0.442	0.380	0.585
G10	3.812	0.656	0.574	0.872
GTR	23.072	1.170	3.484	3.676
QF	22.706	1.326	4.055	4.349
total	56.62	2.11	5.390	5.790

Table 4.4: Gamow-Teller strengths from resonance fits. Quasi-free contributions must be included because of the large amount of high-lying  $L=0$  strength. (Inclusion of the QF section also makes comparisons with the MDA method feasible.) The IVSGDR and the IAS, by definition, do not contain GT strength. Systematic errors are taken to be 15% of the GT strength, which is consistent with methods used in the MDA.

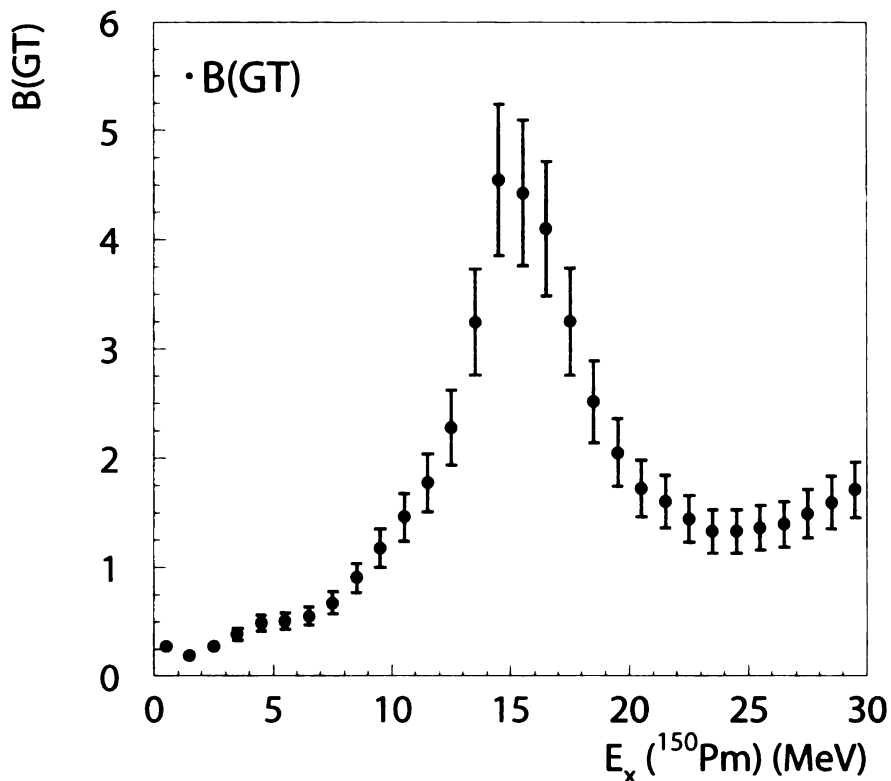


Figure 4.21: GT strength from the MDA

the nucleon-nucleon interaction) are 15% as applied to each 1-MeV fit of the angular distributions (systematic errors from different energy bins are assumed to be independent of each other). Table 4.5 and Figure 4.21 give detailed values.

Directly comparing the low-lying states, the peak-by-peak analysis sums to a total strength of  $0.370 \pm 0.023$ , while the 0-2 MeV section of the MDA sums to  $0.46 \pm 0.050$ . The two methods are barely consistent, which makes sense because the peak-by-peak analysis is ignoring everything in between what was chosen as a peak, while the full MDA takes those regions into account. Details are shown in Table 4.6 and Figure 4.22.

### 4.3.7 Other Multipole Excitations

While GT and Fermi strengths are directly proportional to the CE cross section at  $q=0$ , no such relationship is proven to exist for higher multipoles. MDA dipole and



Ex.(MeV)	B(GT)	stat. error	syst. error	total error
0.5	0.2698	0.0037	0.0405	0.0406
1.5	0.1908	0.0037	0.0286	0.0289
2.5	0.2728	0.0039	0.0409	0.0411
3.5	0.3829	0.0043	0.0574	0.0576
4.5	0.4866	0.0048	0.0730	0.0731
5.5	0.5067	0.0049	0.0760	0.0762
6.5	0.5486	0.0051	0.0823	0.0824
7.5	0.6764	0.0054	0.1015	0.1016
8.5	0.9031	0.0059	0.1355	0.1356
9.5	1.1693	0.0065	0.1754	0.1755
10.5	1.4595	0.0072	0.2189	0.2190
11.5	1.7731	0.0048	0.2660	0.2660
12.5	2.2785	0.0088	0.3418	0.3419
13.5	3.2420	0.0104	0.4863	0.4864
14.5	4.5515	0.1433	0.6827	0.6976
15.5	4.4297	0.0128	0.6645	0.6646
16.5	4.1008	0.0129	0.6151	0.6153
17.5	3.2501	0.0126	0.4875	0.4877
18.5	2.5150	0.0122	0.3773	0.3774
19.5	2.0486	0.0125	0.3073	0.3075
20.5	1.7192	0.0128	0.2579	0.2582
21.5	1.5975	0.0135	0.2396	0.2400
22.5	1.4426	0.0142	0.2164	0.2169
23.5	1.3301	0.0147	0.1995	0.2001
24.5	1.3273	0.0154	0.1991	0.1997
25.5	1.3620	0.0161	0.2043	0.2049
26.5	1.3912	0.0169	0.2087	0.2094
27.5	1.4868	0.0177	0.2230	0.2237
28.5	1.5896	0.0177	0.2384	0.2392
29.5	1.7075	0.0201	0.2561	0.2569
sum	50.01	0.1563	1.68	1.69

Table 4.5: Gamow-Teller strength distribution from the MDA. 0-30 MeV

Ex. (MeV)	B(GT)	stat. error	syst. error	total error
0.11	0.1334	0.0023	0.0202	0.0203
0.19	0.0226	0.0012	0.0034	0.0036
0.282	0.0128	0.0008	0.0019	0.0021
0.40	0.0155	0.0009	0.0023	0.0025
0.497	0.0133	0.0014	0.0020	0.0025
0.592	0.0086	0.0015	0.0013	0.0020
0.667	0.0085	0.0013	0.0013	0.0018
0.725	0.0069	0.0013	0.0010	0.0017
0.86	0.0066	0.0014	0.0010	0.0017
0.904	0.0108	0.0015	0.0016	0.0022
1.0	0.0064	0.0013	0.0010	0.0016
1.14	0.0066	0.0011	0.0010	0.0015
1.225	0.0064	0.0020	0.0010	0.0022
1.267	0.0152	0.0003	0.0023	0.0023
1.319	0.0131	0.0013	0.0020	0.0024
1.368	0.0131	0.0009	0.0020	0.0022
1.397	0.0050	0.0001	0.0008	0.0008
1.576*	0.0199	0.0021	0.0030	0.0037
1.684*	0.0181	0.0020	0.0027	0.0034
1.831	0.0219	0.0018	0.0033	0.0037
1.949	0.0041	0.0008	0.0006	0.0010
sum	0.3699	0.0065	0.0220	0.0229

Table 4.6: Gamow-Teller strength distribution from low-lying states, 0-2 MeV. Excitation energies of these states come from the fit, and may be off by  $\pm 10$  keV. The states listed with asterisks at 1.576 and 1.684 MeV are primarily dipole states.

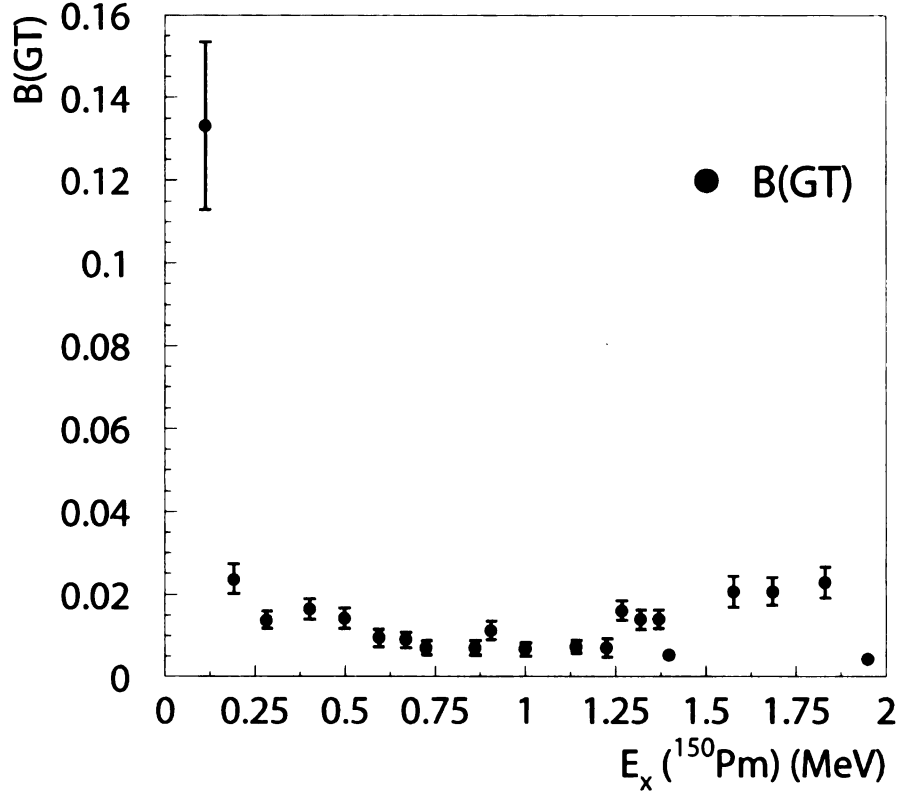


Figure 4.22: Low-lying GT strength from the MDA

quadrupole cross sections (at their peak angles), respectively, are given in Tables 4.7 and 4.8 and Figures 4.23 and 4.24. Cross sections from the resonance fit method are given in Tables 4.9 and 4.10.

Cross sections for the resonance fit method are slightly higher than for the MDA method of analysis. This discrepancy may arise for several reasons: the shape assumed for the quasi-free curve and other resonances may not be correct, and the resonance fit method assigns significant  $\Delta L=0$  and 1 strength to large regions without allowing for  $\Delta L=3$  and 4 contributions. Since the assumptions used to perform the resonance fit analysis have inherent ambiguities that are difficult to quantitatively test, the results of the MDA will be used for the remainder of the analysis.

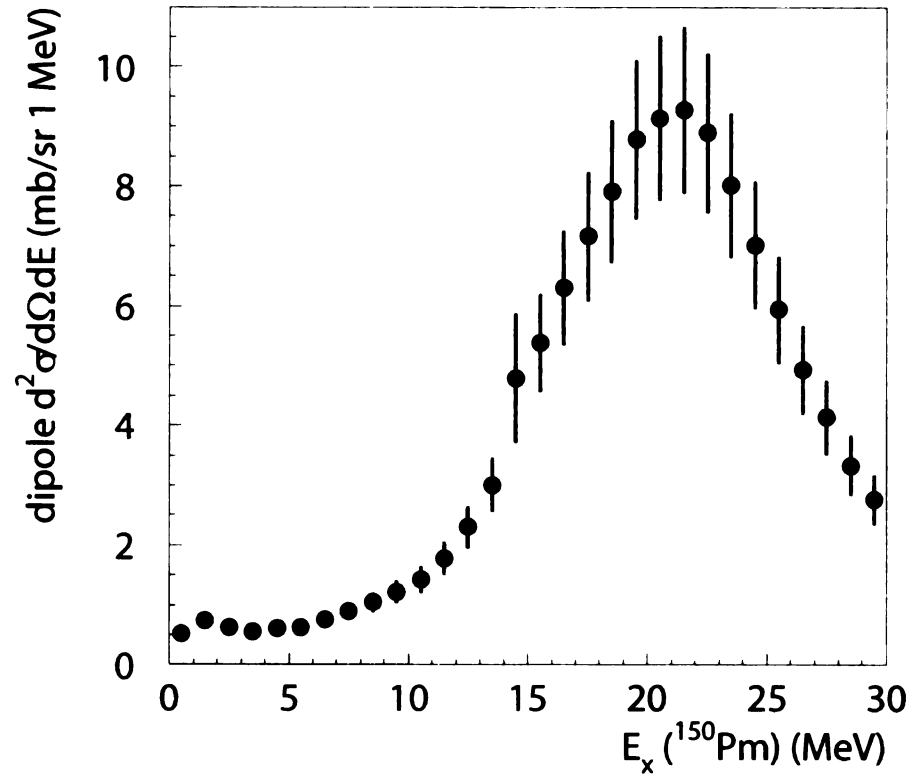


Figure 4.23: Dipole cross sections from the MDA

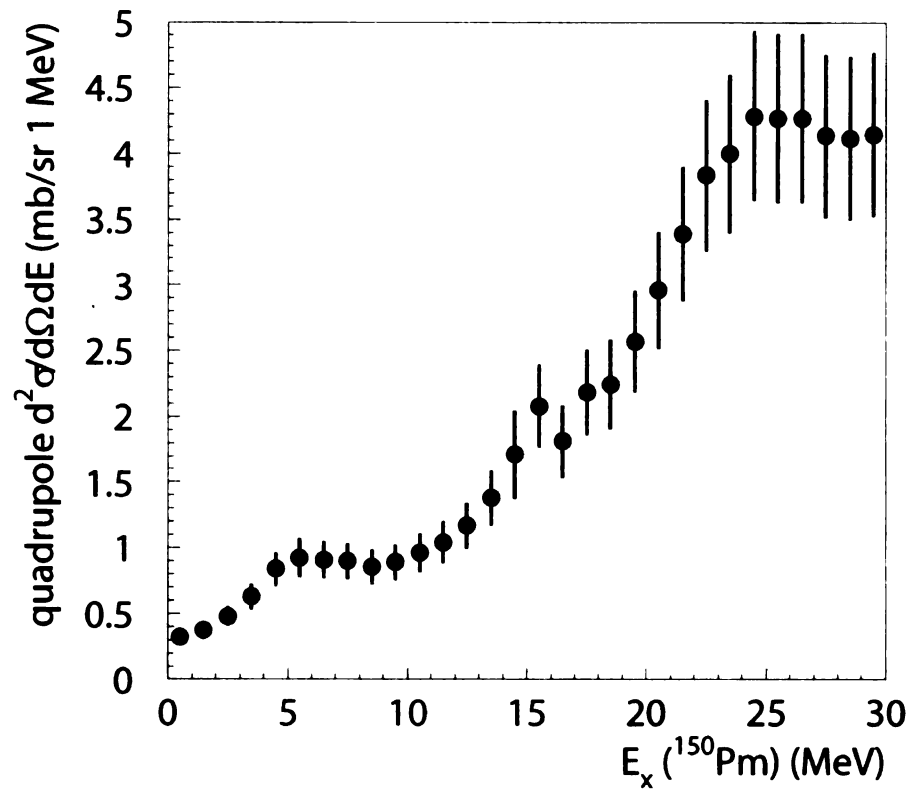


Figure 4.24: Quadrupole cross sections from the MDA

Ex. (MeV)	Cross Section (mb/sr)	stat. error	syst. error	total error
0.5	0.5270	0.0174	0.0791	0.0809
1.5	0.7445	0.0224	0.1117	0.1139
2.5	0.6236	0.0153	0.0935	0.0948
3.5	0.5599	0.0108	0.0840	0.0847
4.5	0.6033	0.0095	0.0905	0.0910
5.5	0.6122	0.0093	0.0918	0.0923
6.5	0.7589	0.0120	0.1138	0.1145
7.5	0.8910	0.0148	0.1337	0.1345
8.5	1.0410	0.0188	0.1562	0.1573
9.5	1.2193	0.0226	0.1829	0.1843
10.5	1.4205	0.0262	0.2131	0.2147
11.5	1.7795	0.0322	0.2669	0.2689
12.5	2.2994	0.0409	0.3449	0.3473
13.5	3.0044	0.0501	0.4507	0.4535
14.5	4.7925	0.8003	0.7189	1.0758
15.5	5.3794	0.0759	0.8069	0.8105
16.5	6.3067	0.1084	0.9460	0.9522
17.5	7.1589	0.1029	1.0738	1.0788
18.5	7.9162	0.1175	1.1874	1.1932
19.5	8.7827	0.1268	1.3174	1.3235
20.5	9.1426	0.1233	1.3714	1.3769
21.5	9.2700	0.1180	1.3905	1.3955
22.5	8.8952	0.1046	1.3343	1.3384
23.5	8.0133	0.0994	1.2020	1.2061
24.5	7.0217	0.0864	1.0533	1.0568
25.5	5.9347	0.0758	0.8902	0.8934
26.5	4.9326	0.0685	0.7399	0.7431
27.5	4.1357	0.0600	0.6204	0.6232
28.5	3.3305	0.0509	0.4996	0.5022
29.5	2.7587	0.0469	0.4138	0.4165
sum	119.8559	0.8850	4.1514	4.2447

Table 4.7: Dipole cross sections from the MDA, 0-30 MeV, taken at the peak of the angular distribution ( $1\text{-}1.5^\circ$ ).

Ex.(MeV)	Cross Section (mb/sr)	stat. error	syst. error	total error
0.5	0.3187	0.0116	0.0478	0.0492
1.5	0.3766	0.0105	0.0565	0.0575
2.5	0.4758	0.0163	0.0714	0.0732
3.5	0.6285	0.0257	0.0943	0.0977
4.5	0.8355	0.0350	0.1253	0.1301
5.5	0.9229	0.0399	0.1384	0.1441
6.5	0.9079	0.0329	0.1362	0.1401
7.5	0.8976	0.0293	0.1346	0.1378
8.5	0.856	0.0252	0.1284	0.1308
9.5	0.8916	0.0242	0.1337	0.1359
10.5	0.9631	0.0241	0.1445	0.1465
11.5	1.0426	0.0225	0.1564	0.1580
12.5	1.1673	0.0215	0.1751	0.1764
13.5	1.3769	0.0220	0.2065	0.2077
14.5	1.7089	0.2161	0.2563	0.3353
15.5	2.0772	0.0229	0.3116	0.3124
16.5	1.8104	0.0173	0.2716	0.2721
17.5	2.1822	0.0187	0.3273	0.3279
18.5	2.2443	0.0173	0.3366	0.3371
19.5	2.5682	0.0187	0.3852	0.3857
20.5	2.9635	0.0212	0.4445	0.4450
21.5	3.3910	0.0247	0.5087	0.5092
22.5	3.8348	0.0295	0.5752	0.5760
23.5	3.9978	0.0348	0.5997	0.6007
24.5	4.2886	0.0432	0.6433	0.6447
25.5	4.2716	0.0506	0.6407	0.6427
26.5	4.2687	0.0623	0.6403	0.6433
27.5	4.1340	0.0707	0.6201	0.6241
28.5	4.1184	0.0884	0.6178	0.6241
29.5	4.1496	0.1132	0.6224	0.6326
sum	63.37	0.3079	2.0938	2.1163

Table 4.8: Quadrupole cross sections, 0-30 MeV, taken at the peak of the angular distribution ( $2-2.5^\circ$ ).

Resonance	$\frac{d\sigma}{d\Omega}$ (mb/sr)	stat. error	syst. error	total error
IVSGDR	117	15	17.55	23.1
G5	3.5	0.5	0.525	0.725
G10	1.0	0.5	0.15	0.52
QF	38	10.0	5.7	11.51
sum	159.5	18.04	18.46	25.81

Table 4.9: Dipole cross sections from giant resonance fits.

Resonance	$\frac{d\sigma}{d\Omega}$ (mb/sr)	stat. error	syst. error	total error
G5	6.5	0.75	0.975	1.23
G10	6.25	0.5	0.94	1.06
GTR	7.0	2.0	1.05	2.26
QF	68.0	8.0	10.2	12.96
sum	87.75	8.3	10.3	13.3

Table 4.10: Quadrupole cross sections from giant resonance fits.

## 4.4 Comparison with Theory

### 4.4.1 Cross sections and Giant Resonances

The extracted cross section of the IAS at  $0^\circ$  and  $q=0$  is  $9.18 \pm 0.25$  mb/sr (see Figure 4.14 and apply Equation 4.5), and its Fermi strength is equal to  $(N-Z)=30$ . The deduced Fermi unit cross section is  $0.31 \pm .01$  mb/sr. This matches the value from the phenomenological equation [95] for  $A=150$  within 10%:

$$\hat{\sigma}_F = \frac{72}{A^{1.06}} = 0.35 \text{ (mb/sr)}. \quad (4.6)$$

This match between the phenomenological and measured  $\hat{\sigma}_F$  gives us confidence that the phenomenological  $\hat{\sigma}_{GT} = 4.19$  is also applicable. Based on reference [95], an error of 10% for  $\hat{\sigma}_{GT}$  is reasonable.

Table 3.2 gives a list of pertinent giant resonances. One way to measure the ex-

<b>GT</b>	<b>IVGMR</b>	<b>IVSGMR</b>	<b>sum</b>
0.606	22.395	0.933	0.361

Table 4.11: Exhaustion of the full normal mode strength for  $\Delta L=0$ , under the assumption that each of the resonances is the only contribution to the measured  $L=0$  strength. Data could fulfill 60% of the GT sum rule, 90% of the IVSGMR sum rule, and over 22 times the IVGMR sum rule. When combined, 36% of the possible sum rule strength from all resonances is seen; however, it is known that the IVGMR and IVSGMR peak at higher excitation energies and that the GTR thus makes up the bulk of the strength.

haustion of normal mode strength (see section 3.2.2) is to compare the measured cross section (from the MDA) with the calculated cross section in each excitation energy bin. For example, measured  $\Delta L=0$  strength can be attributed to a combination of the GTR, IVGMR, and the IVSGMR (assuming the IAS is analyzed separately), although very little strength is expected from the IVGMR. Since all three resonances have the same angular distribution, they cannot be separated. The measured strength can be compared separately to the calculated strength for each resonance and then again to the combined resonances. ( $\Delta L=0$  data is not adjusted to  $q=0$ .) Results are shown in Tables 4.11, 4.12, and 4.13. We certainly do not expect to see very much strength from the IVSGMR at low excitation energies, but it is feasible to see some of it since it peaks around 37 MeV and it is very broad.

The Fermi unit cross section calculated in DWBA is 0.2025. This difference from the experimental value of 0.31 occurs because of the large imaginary volume term in the optical potential. Since the actual unit cross section has been measured, values for the exhaustion of normal mode strength (Tables 4.11, 4.12, and 4.13) have been scaled by  $0.2025/0.31 = 0.66$  under the assumption that it applies for all transitions alike.



IVSGDR0-	IVSGDR1-	IVSGDR2-	IVGDR	sum
12.048	0.761	1.148	13.495	0.427

Table 4.12: Exhaustion of normal mode strength for  $\Delta L=1$ .

IVGQR	IVSGQR1+	IVSGQR2+	IVSGQR3+	sum
16.467	5.213	1.638	1.629	0.677

Table 4.13: Exhaustion of normal mode strength for  $\Delta L=2$ .

#### 4.4.2 QRPA calculations

The group of Vadim Rodin at the University of Tübingen has used QRPA methods to calculate the GT and dipole strengths in  $^{150}\text{Pm}$  in both the  $(^3\text{He},t)$  and  $(t,^3\text{He})$  directions [122, 55, 123]. This research group is able to incorporate nuclear deformation into their model, and will use data from this thesis to test their calculations. Table 4.14 [122, 124] gives a list of relevant parameters. Raw calculations for three different values of  $K$  (projection of angular momentum onto a deformed axis of symmetry) are shown in Figure 4.25.  $K$  is a good quantum number in deformed nuclei ( $J$  is not). GT strength is predicted around the region of the experimental GTR, and dipole strength is anticipated mostly at higher excitation energies (coinciding with the expected location of the IVSGDR).

Nucleus	$\beta_2$	$g_{pp}$	$g_{ph}$
$^{150}\text{Nd}$	0.183	1.11	1.16
$^{150}\text{Sm}$	0.114	1.11	1.16

Table 4.14: Values of the deformation parameter  $\beta_2$  for  $^{150}\text{Nd}$  and  $^{150}\text{Sm}$  as adopted in the QRPA calculations, along with the fitted values of the  $p-p$  strength parameter  $g_{pp}$ . The  $g_{ph}$  value is found by fitting the position of GT resonance [124]. Quenching of the GT strength is taken into account when  $g_{pp}$  is fitted.

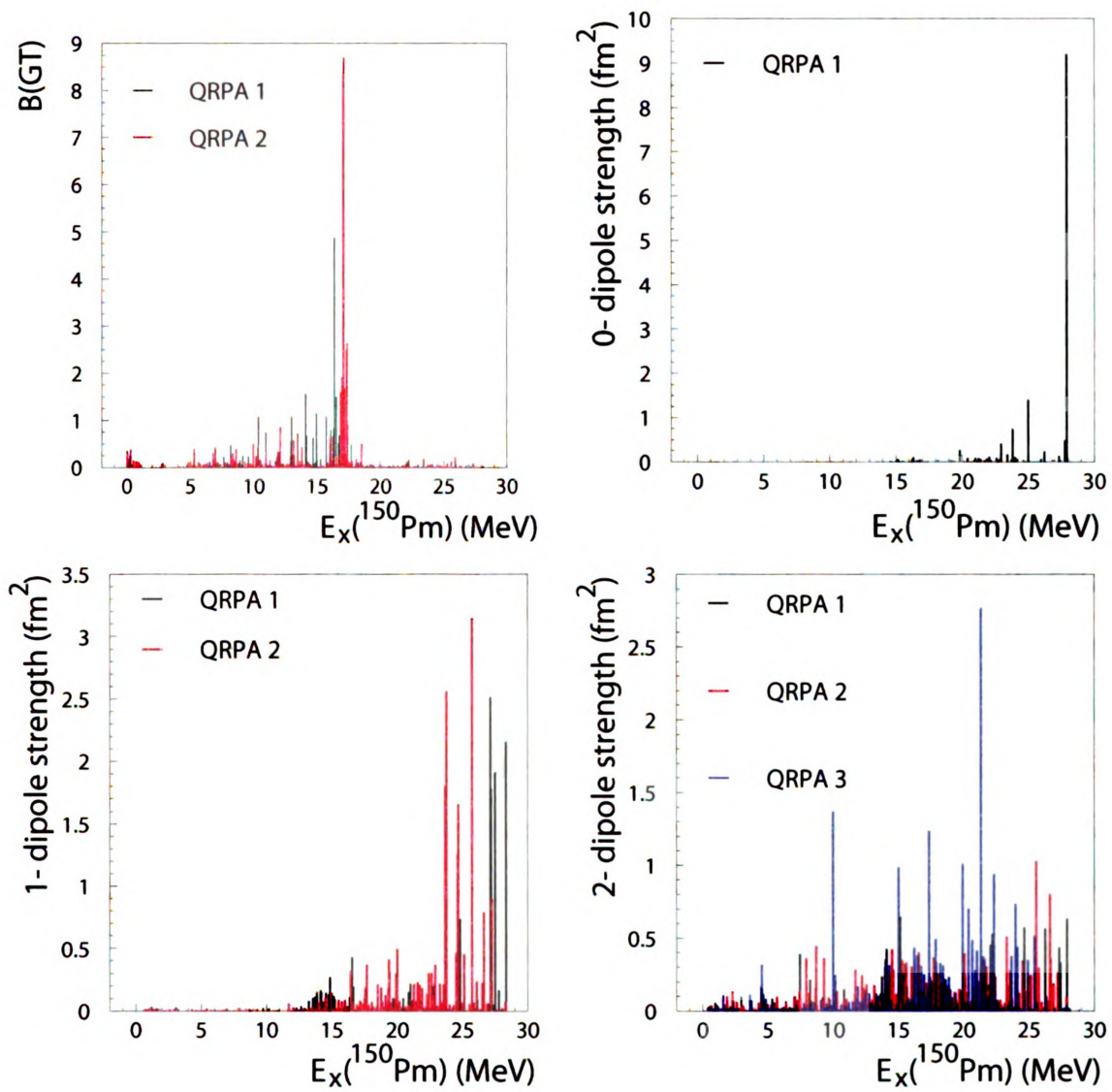


Figure 4.25: Raw QRPA calculations for  $^{150}\text{Nd}(^3\text{He},t)$ . K values are as follows: black represents K=0, red represents K=1, and blue represents K=2. Top left: unquenched GT strength, top right:  $0^-$  dipole cross sections and strength, bottom left:  $1^-$  dipole cross sections and strength, bottom right:  $2^-$  dipole cross sections and strength.

To facilitate comparison with data, these calculations are smeared with Gaussians to represent the effects of spreading not included in the calculation. For the GT strength, the smearing widths used were 0.035 MeV (FWHM) (for the region between 0-2 MeV) or 4.7 MeV (FWHM) Gaussians (for the region above 2 MeV). The dipole cross sections were smeared with widths of 3.5 MeV (FWHM). All smearing widths were tuned to the data. The calculations were then put into 1 MeV excitation energy bins. Contributions from all values of  $K$  are summed, and a GT quenching factor of 0.56 is added to the GT distribution. This GT quenching factor is the standard value of  $0.75^2$  [101] applied to all theoretical calculations of GT strength. Figure 4.26 shows a superposition of the calculation and  $^{150}\text{Nd}$  data, as well as the cumulative (running sum) Gamow-Teller strength. The experimental  $\Delta L=0$  strength does not drop off as much as predicted by theory at higher excitation energies, which may indicate the presence of high-lying GTR 2p-2h strength and/or the lower tail of the IVSGMR. The experimental GT strength in the bin between 0-1 MeV is 9 times lower than predicted.

Figure 4.27 shows the same type of comparison for dipole states. In the absence of a known unit cross section, experimental cross sections (between 1 and  $1.5^\circ$ ) and calculated dipole strengths are superimposed. The smeared calculations for dipole strength predict three distinct peaks rather than the one seen, suggesting that the placement and strength of levels could be improved. This difference results in a slight mismatch in the shape of the cumulative strength distributions.

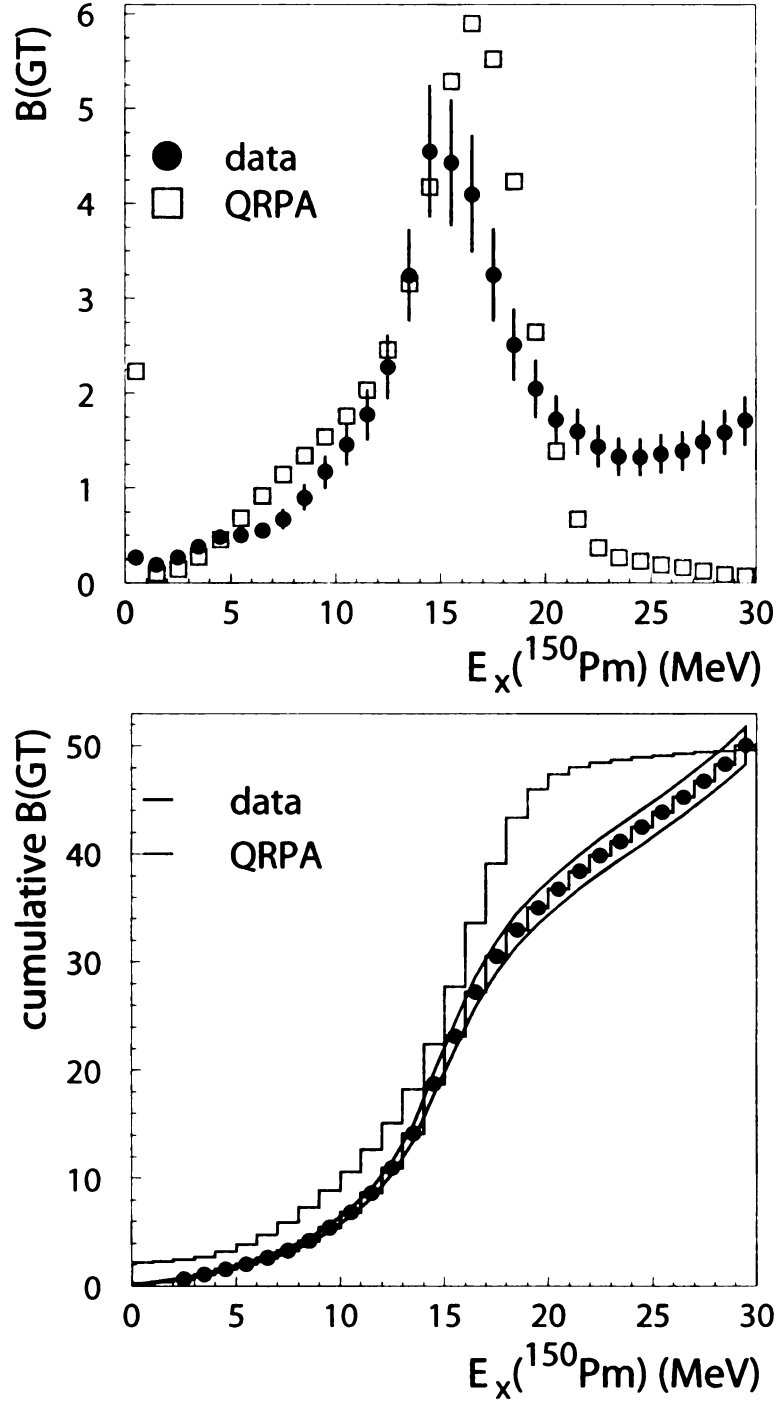


Figure 4.26: Gamow-Teller strength in  $^{150}\text{Pm}$  via  $^{150}\text{Nd}(^3\text{He},t)$ . Data is in black and QRPA is in red. The strength distribution and cumulative strength are shown. Data and theory disagree at very low excitation energy, where the QRPA predicts much more strength, and at the region between 20-30 MeV, where data sees more strength than predicted. See text.

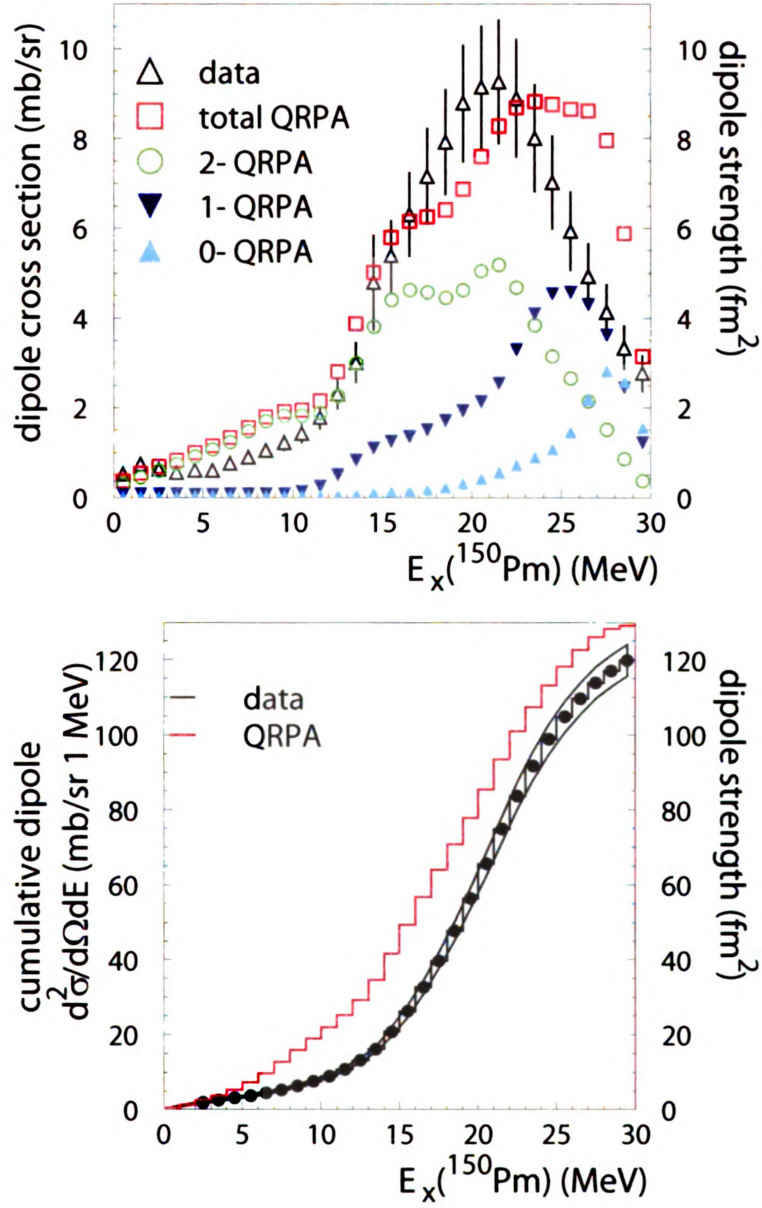


Figure 4.27: Comparisons of dipole cross sections and strength in  $^{150}\text{Pm}$  via  $^{150}\text{Nd}(^3\text{He},t)$  shown for the excitation energy distribution and for a cumulative distribution. Data is in black and QRPA calculations are in color. Data shows a cross section distribution that is smoother than predicted.

# Chapter 5

## $^{150}\text{Sm}(t, ^3\text{He})^{150}\text{Pm}^*$ at the NSCL

### 5.1 Experimental Setup and Procedure

#### 5.1.1 Production of a Triton Beam

The first triton beams at the NSCL were produced from the fragmentation of a primary alpha beam. Following the coupling of the K500 and K1200 cyclotrons [125], this was no longer the optimal method. Decoupling and recoupling the cyclotrons to produce a primary alpha beam is associated with high overhead time, and greater triton intensity can be achieved using  $^{16,18}\text{O}$  beams because less ambient neutron radiation is produced. Hitt *et al.* [126] performed a systematic study of triton production for beams of  $^{16,18}\text{O}$  impinging upon a range of primary Be targets, and found that a 345 MeV/u  $^{16}\text{O}$  beam on 3526 mg/cm<sup>2</sup> was the optimal method of triton production (for triton energies over 100 MeV) within the constraints imposed by the  $B\rho$  of the available beam lines. All subsequent triton beams have been produced this way.

Before the  $^{150}\text{Sm}(t, ^3\text{He})$  experiment, small geometric misalignments of analysis line magnets were discovered and subsequently corrected. The realignment increased triton transmission from the focal plane of the A1900 to the object of the S800 from

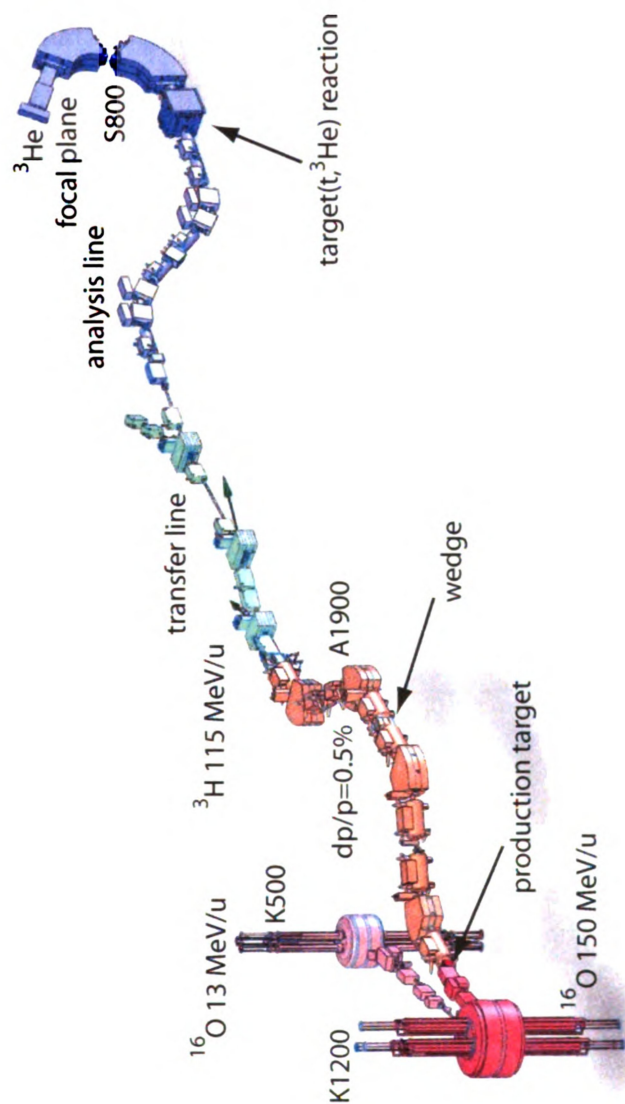


Figure 5.1: Schematic of the Coupled Cyclotron Facility and the S800 Spectrograph

around 50% to 85%. Beam purity at the beginning of the  $^{150}\text{Sm}(t, ^3\text{He})$  experiment was  $\sim 85\%$ . The contaminants were  $^6\text{He}$  and  $^9\text{Li}$ . A small, flat, background was noticed in the excitation energy spectrum, and halfway through the experiment we determined that it came from the ( $^6\text{He} \rightarrow ^3\text{He} + 3n$ ) breakup reaction on the secondary target (target directly before the S800, as compared to the triton production target). A  $195 \text{ mg/cm}^2$  wedge inserted into the A1900 removed this impurity, producing a background-free spectrum for the second half of the experiment.

Slits in the A1900 were set at a momentum bite of  $\pm 0.25\%$  (total  $0.5\%$ ). The analysis line of the S800 spectrometer [127] was operated in dispersion-matched mode (see Section 4.1.1) to achieve the best resolution. In dispersion-matched mode, the beam is dispersed over the target to match the dispersion of the spectrometer ( $11 \text{ cm}/\% \text{ dp/p}$ ). With a momentum acceptance of  $0.5\%$  in the A1900, a  $\sim 5.5 \text{ cm}$  tall beam spot is created at the target. In the non-dispersive direction, the beam spot is  $\sim 1 \text{ cm}$  wide. Figure 5.2 shows an image of the dispersion-matched beam on the viewer. The  $B\rho$  of the analysis line was set to  $4.8 \text{ Tm}$ , which is close to the maximum possible in dispersion-matched mode. The spectrometer  $B\rho$  was set to  $2.3293 \text{ Tm}$ .

Triton rates of  $10^7$  pps were achieved at the target during the experiment because of the high triton transmission. To allow for ease in target changes, the Large Scattering Chamber was installed and two remote-controlled, retractable arms placed at the target position. One arm contained a  $1 \text{ mm}$ -thick plastic scintillator for beam rate measurements, and the other held the  $18 \text{ mg/cm}^2$   $^{150}\text{Sm}$  target, a  $10 \text{ mg/cm}^2$   $^{12}\text{CH}_2$  target, and a viewer (piece of aluminum covered in  $\text{ZnO}$ , which fluoresces when hit by the beam). The thickness of the  $^{12}\text{C}$  was chosen so that the energy loss in the target would be close to that of the  $^{150}\text{Sm}$  target. Near the end of the experiment, an  $18 \text{ mg/cm}^2$   $^{13}\text{CH}_2$  target [128] was installed for further calibrations but also produced interesting physics results. Data from this  $^{13}\text{C}$  calibration target was published [129] but will not be discussed here.



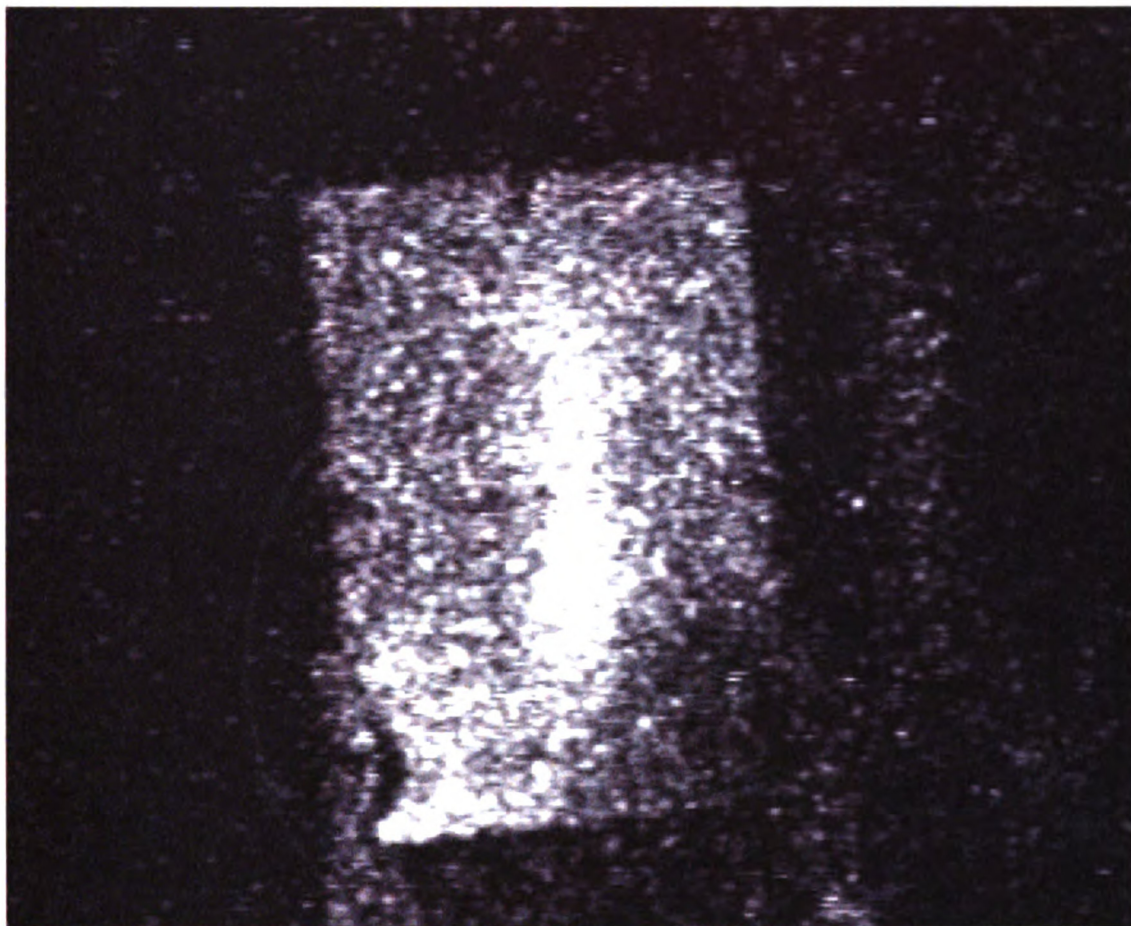


Figure 5.2: A dispersion-matched triton beam image is shown incident on a ZnO target (viewer) at the entrance to the S800 [127] spectrometer. Targets must have dimensions of about 2.5 cm by 7.5 cm to accommodate the large beam spot.

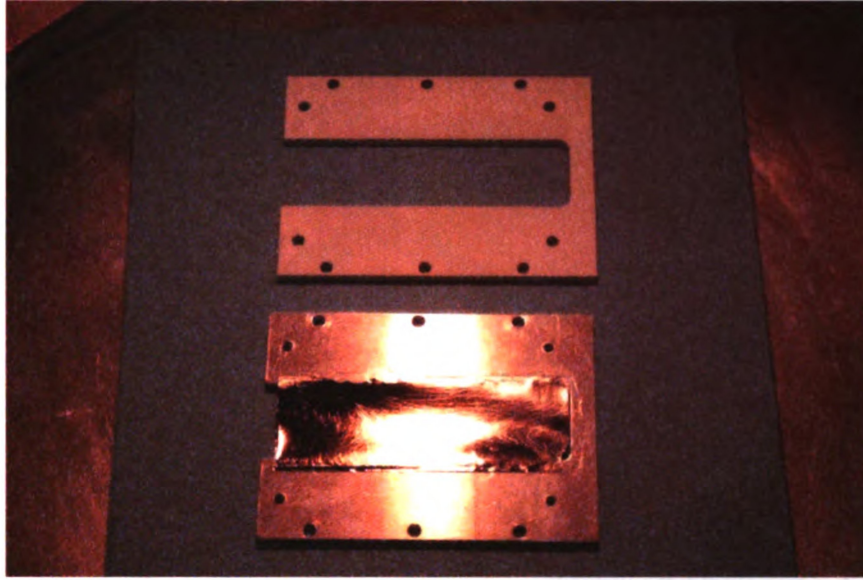


Figure 5.3: The  $^{150}\text{Sm}$  target, crafted by J. Yurkon and N. Verhanovitz. The target was sandwiched between the two halves of the frame and is shown sideways. Dimensions are 2.5 cm by 7.5 cm.

The  $^{12,13}\text{C}$  targets were a full 5 cm across, but the high cost of the  $^{150}\text{Sm}$  material provided sufficient motivation to reduce the width to 2.5 cm (2.0 cm was visible within the boundaries of the frame). Creating the  $^{150}\text{Sm}$  target was challenging. Dr. John Yurkon and Dr. Nate Verhanovitz produced the target.  $^{nat}\text{Sm}$  was used to test two methods of target production: rolling and evaporation. Samarium is a brittle metal, and an attempt to roll the target failed after reaching  $\sim 35 \text{ mg/cm}^2$ , twice the desired thickness. The evaporation procedure causes a significant fraction of the original material to be lost, but this method was successful. Several sequential evaporations produced a target of half the desired thickness and twice the desired width, so this was then folded in half to give the correct target dimensions. Figure 5.3 shows the  $^{150}\text{Sm}$  target near the end of the framing process. The position of the beam on the target was a concern, so the sides of the target frame were painted with ZnO to monitor the beam centering on the  $^{150}\text{Sm}$  metal. This proved to be a very helpful technique and was applied in a subsequent  $(t, ^3\text{He})$  experiment.



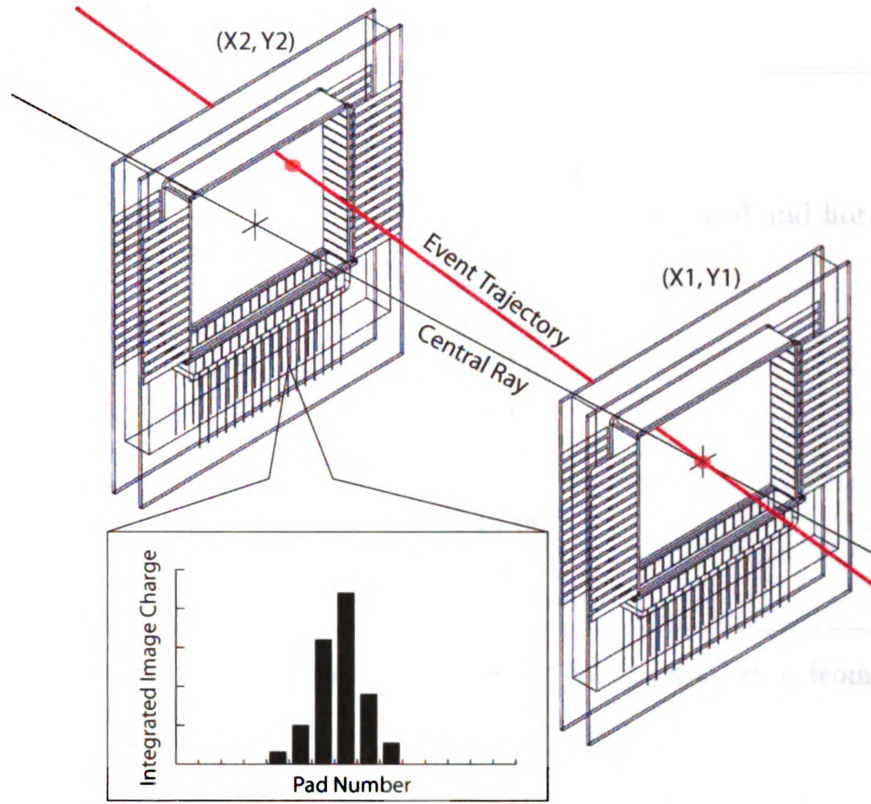


Figure 5.4: Layout of the CRDCs in the focal plane of the S800 spectrometer (shown sideways). A sample event is shown in red, relative to the central  $\rho$  of the S800. The inset shows an electron distribution from an event as it is induced on the cathode pads. This figure was created by J. Yurkon and modified by G.W. Hitt.

### 5.1.2 The S800 Focal Plane

The S800 Spectrograph contains two quadrupole and two dipole magnets, which focus and bend the  $^3\text{He}$  residuals into the focal plane of the spectrometer. Position and angle measurements are taken on an event-by-event basis with two Cathode Readout Drift Chambers (CRDCs) [130] spaced at a distance of 107.3 cm (See Figure 5.4). The x (y) coordinate is usually referred to as the dispersive (non-dispersive) coordinate. An overview of specifications for the S800 appear in Table 5.1.

In each CRDC, the ejectiles encounter field-shaping electrodes encased in a continuously-renewed 80%/20% mixture of  $\text{CF}_4$  and  $\text{C}_4\text{H}_{10}$ . This gas mixture has a high drift velocity, low avalanche electron spread and ages slowly [130]. Incoming  $^3\text{He}$  ions

Parameter	Value
momentum acceptance ( $\Delta p/p$ )	5%
energy resolution (intrinsic $\Delta E/E$ )	1/10,000
angular resolution	$\leq 2$ mrad
position resolution	0.5 mm (both vertical and horizontal)
horizontal magnification ( $x-x$ )	0.74
focal plane tilt	$28.5^\circ$
maximum $B\rho$ (analysis line)	4.8 Tm
maximum $B\rho$ (spectrograph)	4.0 Tm
maximum dipole field (spectrograph)	1.6 T
dipole bend radius	2.8 m
dipole bend angle	$75^\circ$
angular range	0 to $60^\circ$
solid angle	20 msr
weight	$\sim 250$ tons

Table 5.1: Parameters of the S800 Spectrometer. Values are taken from references [131], [132], [93], and [127].

ionize the gas, producing ion-electron pairs. Newly-created ions drift toward the Frisch grid and are not recorded, but the more quickly-moving electrons drift toward the anode wire, which is placed between two sets of cathode pads. The anode current induces charge on the cathode pads, resulting in an electron distribution over about 8-10 pads. A Gaussian fit (or center-of-gravity calculation) to this distribution provides the dispersive ( $x$ ) position signal. The non-dispersive ( $y$ ) signal is calculated from the electron drift time to the anode wire. Track angles are determined from the position differences for one event between the two CRDCs. Plastic scintillators placed behind the CRDCs measure the energy loss of the particles. The signal of one scintillator is used as the trigger for the data acquisition system and serves as the start of the time-of-flight measurement. The cyclotron RF signal provides the stop.

## 5.2 Calibrations

### 5.2.1 CRDC Mask Calibrations

The drift velocity of particles going through the CRDCs must be calibrated so that particle hit positions and angles in the non-dispersive direction can be calculated. To accomplish this, tungsten masks with a distinctive and well-known pattern of holes and lines are placed in front of each CRDC in turn. A target with a high CE event rate (such as  $\text{CH}_2$ ) is installed. The ejectiles are steered across the focal plane during the run. For most ejectiles, only sections of the CRDCs directly behind holes and lines will detect the incoming particles, reproducing the mask pattern.  $^3\text{He}$  and other very light ejectiles tend to punch through the mask. However, the particles that punch through have a different energy loss in the scintillator and can be rejected in the analysis of the run. The locations of the holes in the CRDC data in terms of channel number can be matched with their actual location on the mask, giving precise ( $\sim 1$  mm) ejectile positions. Mask runs must be taken every few days during an experiment to account for slight changes in the drift velocity, but in the  $^{150}\text{Sm}(t, ^3\text{He})$  experiment very little drift was observed. The drift can be monitored between mask runs by monitoring positions and angles in either charge states, if present, or the reconstruction of the recoil energy for a light target nucleus. Reactions on hydrogen impurities in the  $^{150}\text{Sm}$  target were used for this purpose.

### 5.2.2 Beam Rate Calibration

The number of  $^{16}\text{O}$  ions accelerated through the cyclotrons must be converted into the number of tritons at the S800 target. A retractable plastic scintillator can count particles at the target position, but it saturates at high beam rates ( $>10^5$  tritons/s). A Faraday cup at the end of the cyclotrons can measure absolute beam rates, and non-intercepting probes (NIPs) in the beam line monitor beam rate and are continu-

Parameter name	Description
afp	dispersive angle at the focal plane
bfp	nondispersive angle at the focal plane
xfp	dispersive position at the focal plane
yfp	nondispersive position at the focal plane
tof(c)	time of flight of the ejectile between the start signal (focal plane scintillator) and the stop signal (cyclotron RF)
ata(c)	dispersive angle at the target
bta(c)	nondispersive angle at the target
yta(c)	nondispersive position at the target
dta	momentum deviation from the central B $\rho$ track in the S800, related to the total energy of the ejectile by $E_{out}=(dta \cdot E_o + E_o) + m_e$ ( $m_e$ is the mass of the ejectile)
e1 <sub>up/down</sub>	energy in the top/bottom of the first scintillator
e2 <sub>up/down</sub>	energy in the top/bottom of the second scintillator
E <sub>o</sub>	central energy for a particle following the S800 B $\rho$ track
$\theta$	scattering angle as defined from the beam axis, calculated from the nondispersive and dispersive angles at the target

Table 5.2: Important S800 parameters in the analysis of the  $^{150}\text{Sm}(t, ^3\text{He})$  experiment. A c placed at the end of a parameter indicates it has been corrected for a dependency on another parameter (see section 5.2.4 for more details).

ously read during an experiment. Rate calibrations were performed every twenty-four hours during the experiment: an attenuated beam was measured at the Faraday cup, the NIPs, and the scintillator, and the relationships between the probes at different attenuator settings allowed us to calculate an absolute beam rate at the target for the entire experiment. The rate calibrations gave very consistent results and little variation was observed.

### 5.2.3 Calculation of the Excitation Energy of $^{150}\text{Pm}$

Table 5.2 defines many of the raw S800 parameters important in any experimental analysis. Using the parameters dta, ata, and bta (see Table 5.2 for further information), it is possible to calculate the total energy and scattering angles of the outgoing  $^3\text{He}$  nuclei on an event-by-event basis.

The ion-optical code COSY Infinity [133] is paired with accurate magnetic field maps of the S800 to ray-trace focal parameters (from the CRDCs) to angles, the non-dispersive position, and energy at the secondary target. COSY gives a fifth-order inversion matrix which is used in the analysis software. The use of dispersion-matching optimizes the energy resolution achievable from the S800. In this experiment, energy resolution was  $\sim 300$  keV FWHM. Around 160 keV of that was due to the difference in energy loss between  $^3\text{He}$  particles and tritons in the target. Using data from the  $^{13}\text{C}(t, ^3\text{He})$  reaction, the absolute error in the excitation energy was estimated to be 50 keV.

A CE experiment in dispersion-matched mode is very sensitive to the placement, tuning, and energy of the incoming beam, as well as changes in detector response. Small changes in any of these can produce noticeable effects in the data that must be corrected for on a run-by-run basis. The scintillator energy and time of flight were corrected for correlations with the dispersive position and angle at the focal plane. Corrections were applied to the energy loss of  $^3\text{He}$  ions in the plastic scintillator, slight changes in the beam energy or the  $B\rho$  of the S800, the placement of the beam on the target, and the time of flight. In addition, further corrections must be done to minimize the effects of an imperfect ray-tracing matrix and imperfect dispersion-matching. These corrections included making small shifts to center the dispersive and non-dispersive angles at the target, as well as correcting the excitation energy's dependence on the time of flight and both the dispersive and non-dispersive angles

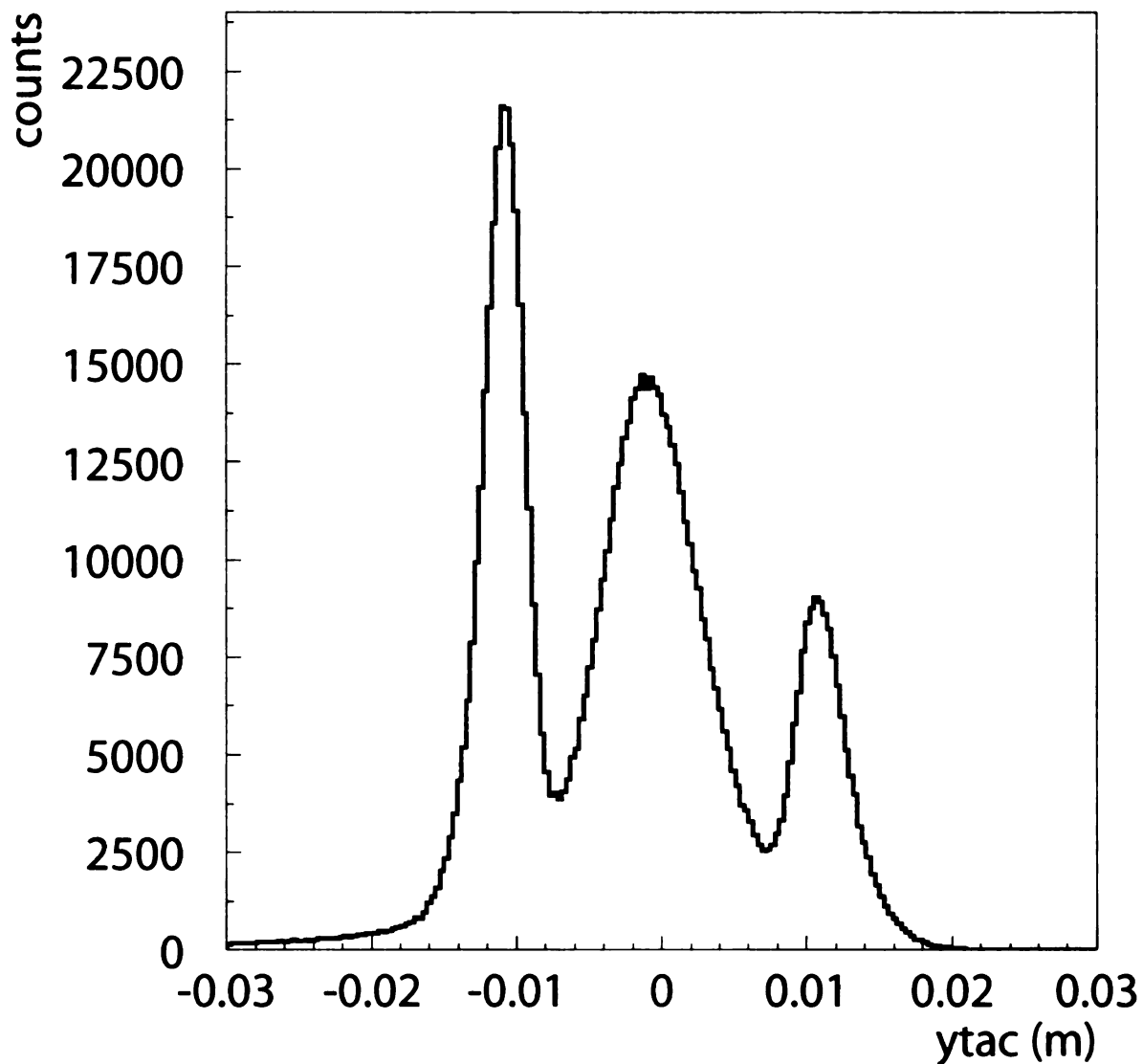


Figure 5.5: A ytac spectrum is shown for all runs on the  $^{150}\text{Sm}$  target. The two side peaks represent events from tritons incident on the aluminum target frame, while the events in the center are from the  $^{150}\text{Sm}$  metal. While the fraction of beam particles impinging upon the frame was small, the frame was very thick and therefore the yield was high. Frame events were removed from the analysis.



at the target. Once all of these corrections were done, many runs could be combined together. Figure 5.5 shows the reconstructed non-dispersive hit position at the target (ytac) spectrum for all runs on the  $^{150}\text{Sm}$  target. Events on the  $^{150}\text{Sm}$  are in the center, and events from the frame are shown on the sides. Frame events were removed with a cut on the acceptance, and the acceptance correction procedure discussed in Section 5.2.4 was used to account for real events discarded in this manner.

The particle identification spectrum for  $^3\text{He}$  nuclei in the S800 focal plane is shown in Figure 5.6. This plot shows the corrected energy loss in the second scintillator as a function of the corrected time of flight. The blob at the left (coordinates (0,500)) is  $^3\text{He}$ , and the area at the lower right may be deuterons or from a background process (such as the triton beam scattered off of the first dipole magnet chamber in the S800).

The excitation energy of the residual nucleus is found using a missing mass calculation. Parameters for this calculation are shown in Table 5.3. Using the incoming and outgoing energy and momenta of the projectile and ejectile, one can apply the conservation of energy and momentum to calculate how much momentum/energy went into exciting the residual nucleus. This is called the “missing” momentum/energy, and the excitation energy is calculated directly from these quantities and the mass of the residual nucleus (see the bottom two lines of Table 5.3).

$$E_x = \sqrt{E_{mis}^2 - P_{mis}(4)^2} - m_r \quad (5.1)$$

## 5.2.4 Acceptance Corrections

The function governing the acceptance of the S800 is complex; it depends on the momentum and scattering angle of the outgoing particle as well as the hit position on the target. Previous CE experiments were able to use only a portion of the laboratory scattering angle available (0 to  $\sim 3.5^\circ$  [134]). The CE group has created a Monte-

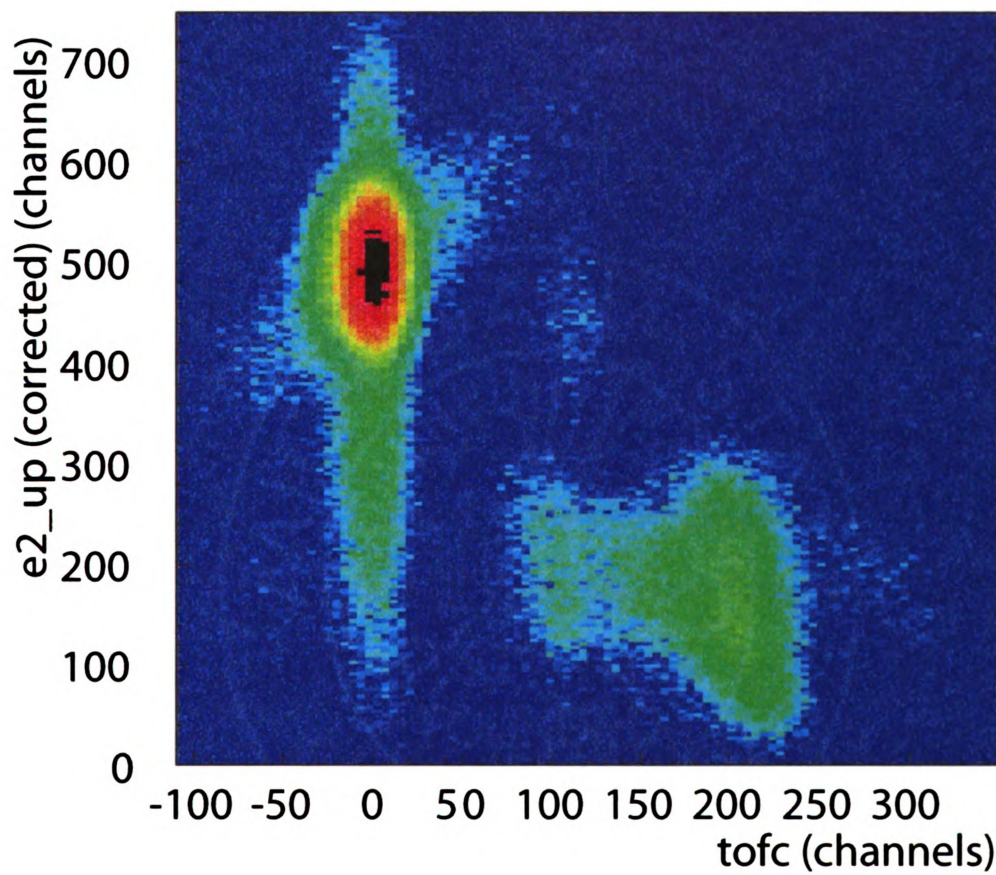


Figure 5.6: Final particle ID in the focal plane of the S800.  ${}^3\text{He}$  is in the upper left corner.

MM Parameters	Definition
$u_m$	931.5 MeV
$m_n$	mass number
$\Delta$	mass excess
$m_p$	$3*u_m + \Delta_p$ (mass of projectile (triton))
$m_e$	$3*u_m + \Delta_e$ (mass of ejectile ( ${}^3\text{He}$ ))
$m_t$	$150*u_m + \Delta_t$ mass of target
$m_r$	$150*u_m + \Delta_r$ mass of residual
$E_o$	central energy for a particle following the S800 B $\rho$ track
$E_{beam}$	Energy of the incoming beam in MeV
$E_{in}$	$E_{beam} + m_p + m_t$ (total incoming energy)
$E_{out}$	$(dta * E_o + E_o) + m_e$ (total outgoing energy)
$E_{mis}$	$E_{in} - E_{out}$ ("missing" energy)
$P_f(4)$	$\sqrt{E_{out}^2 - m_e^2}$ (total final momentum)
$P_f(1)$	$P_f(4) * \sin(atac)$ (dispersive component of final momentum)
$P_f(2)$	$P_f(4) * \sin(btac)$ (non-dispersive component of final momentum)
$P_f(3)$	$P_f(4) * \cos(\theta)$ (component of final momentum along the beam axis)
$P_i(1)$	0 (assumed) (dispersive component of initial momentum)
$P_i(2)$	0 (assumed) (non-dispersive component of initial momentum)
$P_i(3)$	1439 MeV (beam axis component of initial momentum)
$P_i(4)$	1439 MeV (total initial momentum)
$P_{mis}(1)$	$P_{in}(1) - P_f(1)$ (dispersive component of missing momentum)
$P_{mis}(2)$	$P_{in}(2) - P_f(2)$ (non-dispersive component of missing momentum)
$P_{mis}(3)$	$P_{in}(3) - P_f(3)$ (beam axis component of missing momentum)
$P_{mis}(4)$	$\sqrt{P_{mis}(1)^2 + P_{mis}(2)^2 + P_{mis}(3)^2}$ (total missing momentum)
mm	$\sqrt{E_{mis}^2 - P_{mis}(4)^2}$
$E_r$	mm-m $_r$

Table 5.3: Parameters used in the  ${}^{150}\text{Sm}(t, {}^3\text{He})$  missing mass calculation, applicable to any target used in the experiment. This calculation is done on an event-by-event basis, so all momentum and energy variables (except for  $E_{beam}$ ) refer to individual particles.

Carlo model of the S800's acceptance to allow safe use of a greater angular range. The model creates a three-dimensional acceptance matrix based on the scattering angle,  $\theta$ , and  $\phi$ . When applied to an experimental event, this matrix returns a correction factor that weights the event based on its probability of acceptance. The simulation was successfully tested for cases where the differential cross section is known ( $^{12,13}\text{C}$ ), and was then applied to  $^{150}\text{Sm}$ . Use of this acceptance weighting factor allowed us to extend our angular range to  $5^\circ$  in the laboratory frame.

### 5.2.5 Background and Hydrogen Subtraction

As mentioned in Section 5.1, a small background was evident in the data during the first half of the experiment. We eventually determined that the  $^6\text{He}$  impurity in the triton beam was breaking up on the target, forming  $^3\text{He}$  and three neutrons. This  $^3\text{He}$  momentum distribution is very broad and overlaps with  $^3\text{He}$  particles produced in the  $(t, ^3\text{He})$  reaction. A  $195 \text{ mg/cm}^2$  thick aluminum wedge was inserted into the intermediate image of the A1900 fragment separator halfway through the experiment in an attempt to purify the beam. Insertion of the wedge produced a nearly pure triton beam and removed the flat background. This background-free data set (“WW” for “with wedge”) was then used to determine the shape of and remove background from the rest of the data (“NW” for “no wedge”).

Excitation energy spectra were produced in 100 keV bins for the purpose of background subtraction. Bins of 300 keV (which corresponds to the energy resolution) and 1 MeV are used in the physics analysis. Using the number of counts in the hydrogen peak (events from the small H impurity in the  $^{150}\text{Sm}$  target), the WW data was scaled to the NW data and subtracted. The resulting background shape proved to be well-represented by a flat distribution for all angles, so the line fit was subtracted from the NW data to produce a background-free spectrum. See Fig. 5.7 for an example. While error bars are not shown in the figure to allow for maximum

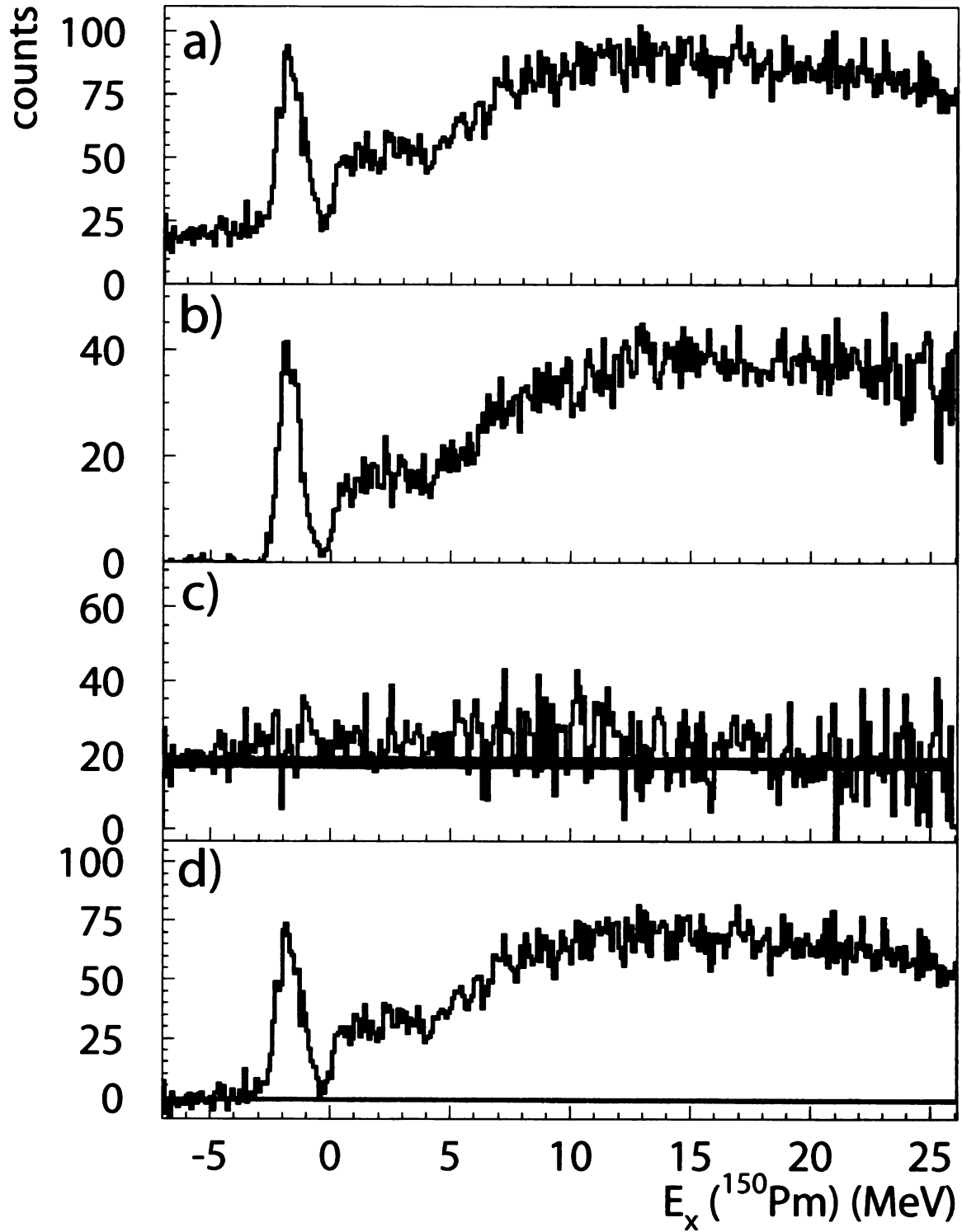


Figure 5.7: Background subtraction for the 1-2° angular bin. a) The NW excitation energy spectrum for  $^{150}\text{Pm}$  in 100 keV bins. b) The WW excitation energy spectrum for  $^{150}\text{Pm}$  in 100 keV bins c) After scaling the WW spectrum to the NW spectrum using the ratio of counts in the hydrogen peak, a line is fit to the subtracted spectrum. The WW data has slightly better resolution than the NW data, so the H peak is slightly narrower. d) The NW excitation energy spectrum after background subtraction.

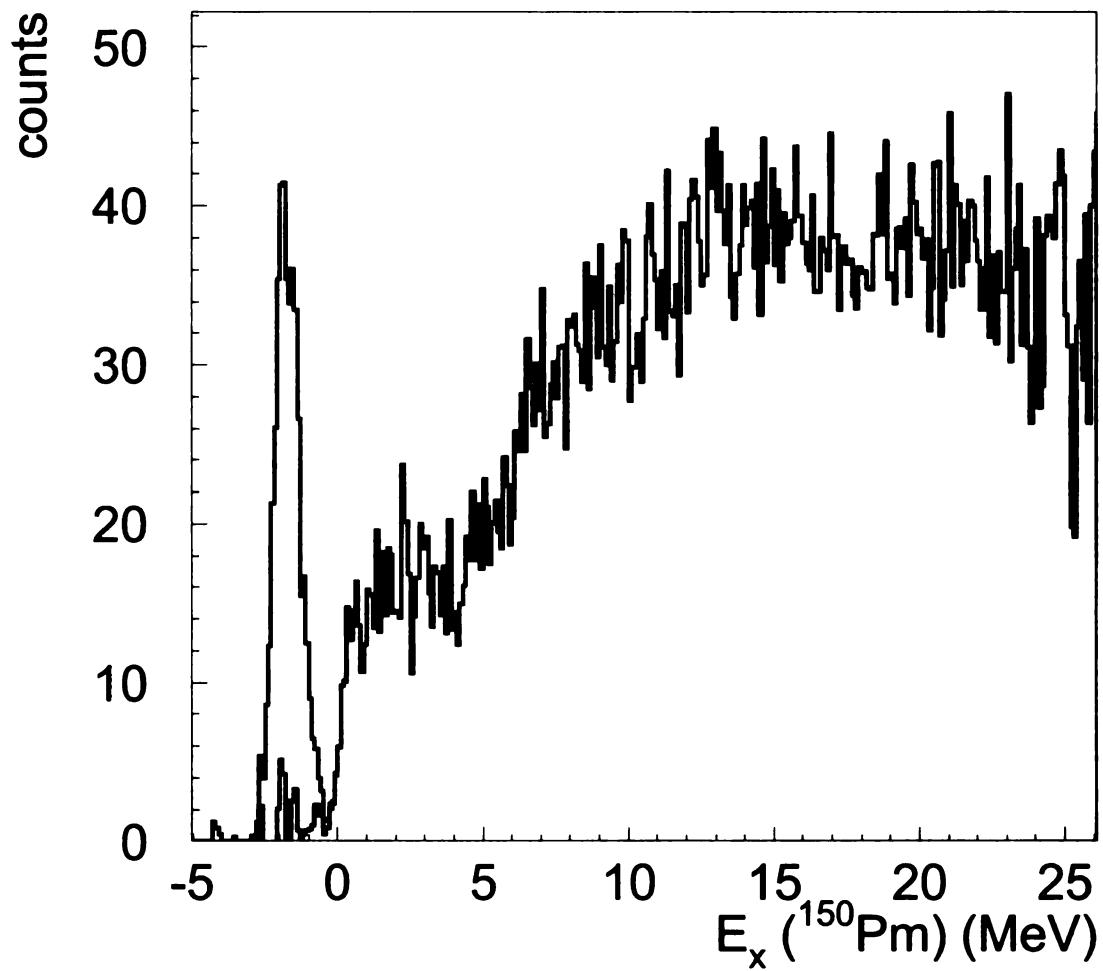


Figure 5.8: Hydrogen subtraction for the 1-2° angular bin: the WW excitation energy spectrum for  $^{150}\text{Pm}$  in 100 keV binning. The hydrogen peak is shown in blue, and the final spectrum shown in black.

clarity, they are calculated and carried through the whole analysis.

There was very little hydrogen contamination in the  $^{150}\text{Sm}$  target, but the  $^1\text{H}(t,^3\text{He})$  cross section is large and a second subtraction procedure was necessary. For a given scattering angle, the recoil energy of a neutron produced in this reaction is 150 times larger than that of the  $^{150}\text{Pm}$  produced in the  $^{150}\text{Sm}(t,^3\text{He})$  reaction. As the Q-value difference for the two reactions is only 2.67 MeV, some events from reactions on  $^1\text{H}$  begin to bleed into the  $^{150}\text{Sm}$  data at angles greater than  $2^\circ$ . The two sets of data are completely separate for scattering angles below  $2^\circ$ . Since the  $\text{CH}_2$  calibration target contained significant amounts of  $\text{H}$  and the Q-value difference between the  $^1\text{H}(t,^3\text{He})$  and  $^{12}\text{C}(t,^3\text{He})$  reactions is large (12.59 MeV), the  $^1\text{H}$  shape could be cleanly modeled from the  $\text{CH}_2$  data. This situation was predicted when the experiment was planned, and the  $\text{CH}_2$  target thickness was chosen such that the differential energy loss between  $^3\text{He}$  and tritons was the same as that of the  $^{150}\text{Sm}$  target. A double sigmoid function was found to reproduce the  $\text{H}$  shape well, and it was scaled to and subtracted from the  $^{150}\text{Sm}$  data. Figure 5.8 shows the WW 1- $2^\circ$  excitation energy spectrum before and after the hydrogen peak subtraction.

## 5.2.6 Calculation of the Cross Section

Differential cross sections were calculated using

$$\frac{d\sigma}{d\Omega} = \frac{Y}{N_b N_t d\Omega \epsilon_1 \epsilon_2}. \quad (5.2)$$

$Y$  is the total number of counts,  $N_b$  is the number of nuclei in the beam,  $N_t$  is the number of nuclei in the target,  $d\Omega$  is the opening angle,  $\epsilon_1$  corrects for the dead time in the data acquisition system (96.7% live time), and  $\epsilon_2$  corrects for the purity of the  $^{150}\text{Sm}$  target (96%).

Figures 5.9 and 5.10 show the cross sections for all five angular bins in 300 keV

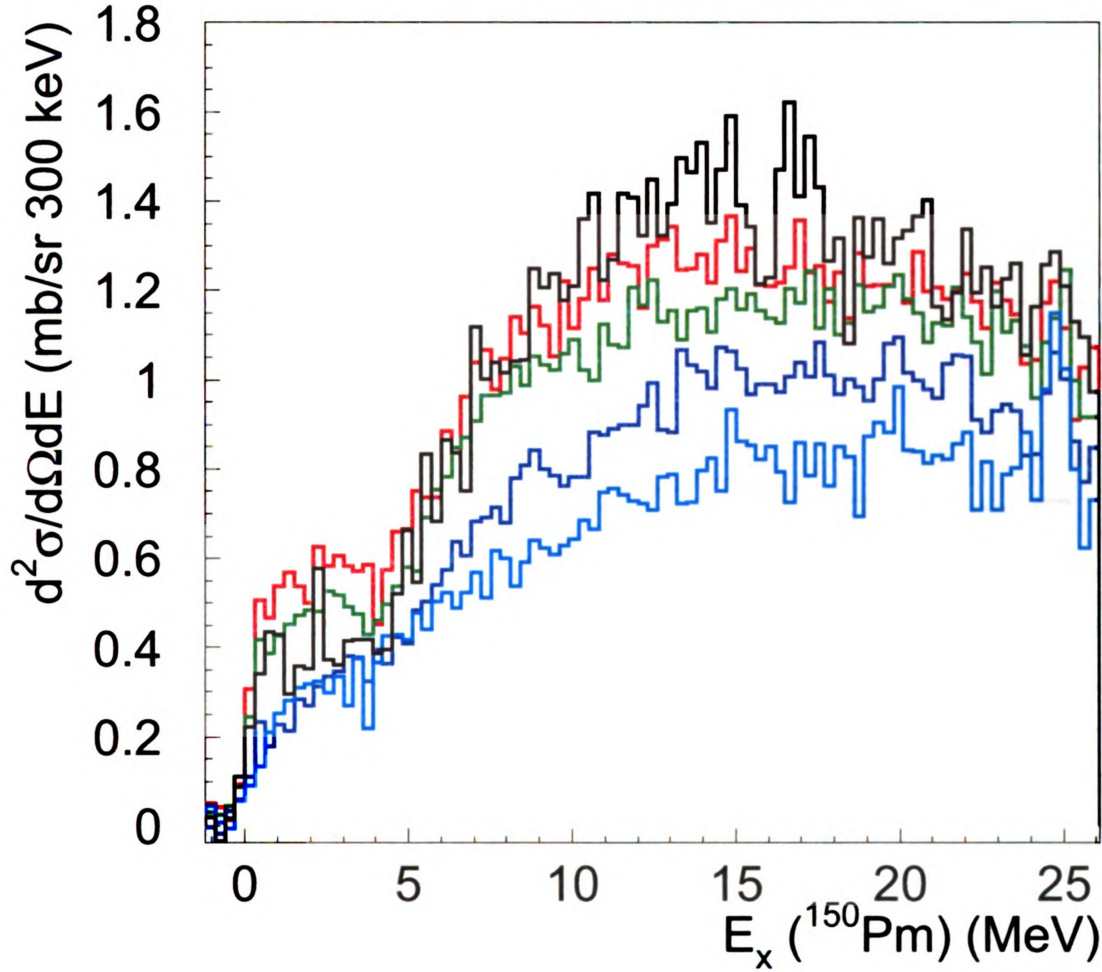


Figure 5.9: Cross sections for  $^{150}\text{Sm}(t, ^3\text{He})^{150}\text{Pm}$  from 0-26 MeV, in 300 keV bins. Data is grouped into  $1^\circ$  angular bins:  $0-1^\circ$  in black,  $1-2^\circ$  in red,  $2-3^\circ$  in green,  $3-4^\circ$  in dark blue, and  $4-5^\circ$  in light blue.

and 1 MeV excitation energy binning. Individual states are not visible. Unlike experiments in the  $(^3\text{He}, t)$  direction, experiments in the  $(t, ^3\text{He})$  direction experience strong Pauli blocking (for  $N \gg Z$ ), so much less GT strength is expected and GT transitions are not obviously present in the spectrum. Similarly, the IVSGDR strength is also reduced. The centroid of the IVSGMR is predicted to be around 15 MeV (see equation 3.29) and should contribute to the spectrum, particularly at small scattering angles. See Figure 3.8.



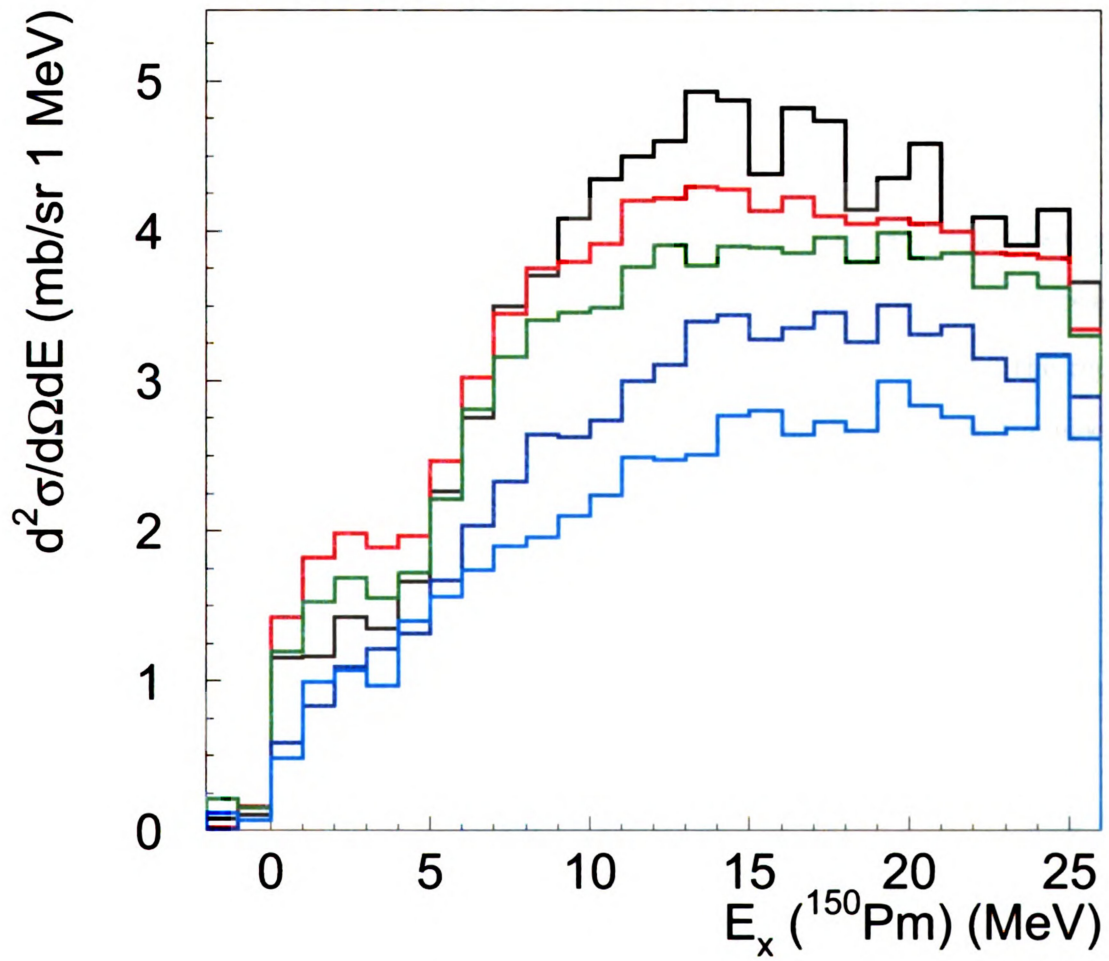


Figure 5.10: Cross sections for  $^{150}\text{Sm}(t, ^3\text{He})^{150}\text{Pm}$  from 0-26 MeV, in 1 MeV bins. Data is grouped into  $1^\circ$  angular bins:  $0-1^\circ$  in black,  $1-2^\circ$  in red,  $2-3^\circ$  in green,  $3-4^\circ$  in dark blue, and  $4-5^\circ$  in light blue.

## 5.3 Data Analysis

### 5.3.1 FOLD calculations

The FOLD code was introduced in Chapter 3. Calculated angular distributions for various multipole transitions in the  $^{150}\text{Sm}(t, ^3\text{He})$  reaction are shown in Figures 5.11 and 5.12, where an arbitrary scale factor is applied to make each function easier to see. Except for the  $\Delta L=0$  curve, shapes of the angular distributions change significantly as the excitation energy increases. This was not the case for the  $^{150}\text{Nd}(^3\text{He}, t)$  reaction. Although this phenomenon is still under investigation outside the scope of this thesis, it is believed to be due to the effects of the Coulomb force in the reaction process.

As the incoming projectile approaches the target, it is decelerated by the repulsive Coulomb force between the projectile and target. After the reaction, the ejectile is accelerated by the Coulomb force between the ejectile and target/residual. The “effective” linear momentum transfer ( $q_{eff}$ ) is defined as the difference in linear momentum between the projectile and ejectile at the interaction point, whereas the “asymptotic” linear momentum transfer ( $q_{asy}$ ) is the difference in the calculated linear momentum transfer between the projectile and ejectile far away from the interaction point. If we ignore the effect of the Coulomb force,  $q_{eff}$  equals  $q_{asy}$  and should increase with the Q-value of the reaction in a similar fashion for experiments in both the  $(t, ^3\text{He})$  and  $(^3\text{He}, t)$  directions. Accounting for the Coulomb force causes  $q_{eff} < q_{asy}$  in the  $(^3\text{He}, t)$  direction and  $q_{eff} > q_{asy}$  in the  $(t, ^3\text{He})$  direction. The larger  $q_{eff}$  for the  $(t, ^3\text{He})$  reaction results in stronger contributions from amplitudes with  $\Delta L > 0$ . This leads to significant changes in angular distributions, as shown in Figures 5.11 and 5.12.

Collection of data for the  $^{150}\text{Sm}(t, t')$  optical potential was not possible for two reasons: the S800 cannot bend 345-MeV tritons, and a measurement with the relatively low beam intensity (compared to a primary beam) would require a very long

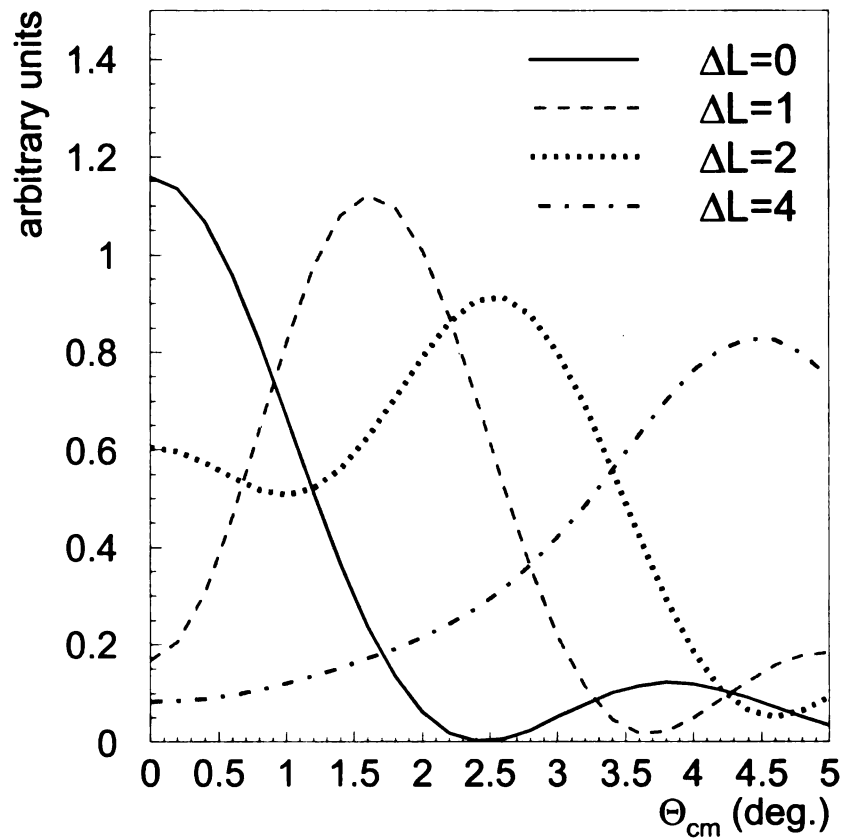


Figure 5.11: Angular distributions from  $^{150}\text{Sm}(t, {}^3\text{He})$  as calculated with FOLD, at  $Q=0$ . Relative scaling of the distributions is arbitrary and chosen solely to better display the function shape.

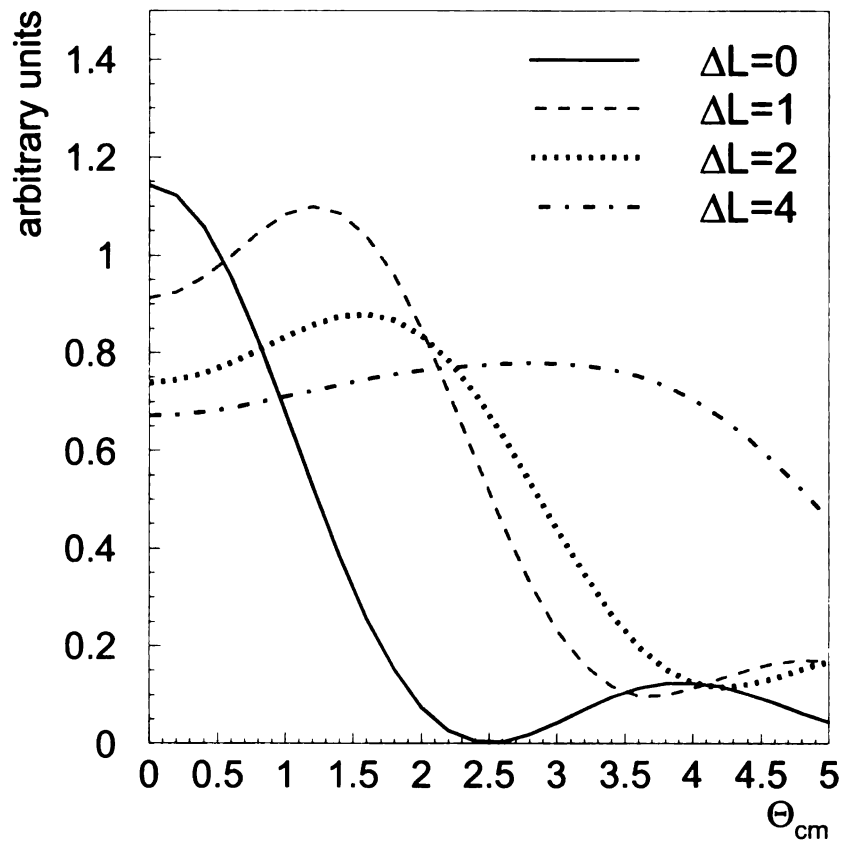


Figure 5.12: Angular distributions from  $^{150}\text{Sm}(t, {}^3\text{He})$  as calculated with FOLD, at  $Q=20$ . Relative scaling of the distributions is arbitrary and chosen solely to better display the function shape, which have changed significantly for  $\Delta L=1, 2$ , and 4 compared to Figure 5.11.

beamtime to gain enough statistics. Therefore, the optical potential parameters deduced from the  $^{150}\text{Nd}(^3\text{He},^3\text{He})$  elastic scattering measurement were adapted for the present analysis as well (see Sections 3.2.5 and 4.3.2).

### 5.3.2 Multipole Decomposition

The level density of  $^{150}\text{Pm}$  is expected to be quite high, because it is a heavy odd-odd nucleus. This was evident even in the high-resolution  $^{150}\text{Ne}(^3\text{He},t)$  data, where only some individual levels could be discerned at low excitation energy. Because of this high level density and the energy resolution of 300 keV FWHM, we cannot resolve any individual peaks in the  $^{150}\text{Sm}(t,^3\text{He})^{150}\text{Pm}$  excitation energy spectrum. Instead, the angular distributions of the data were created from each bin (0-26 MeV in excitation energy) of Figure 5.10 and the first 20 bins (0-6 MeV in excitation energy) of Figure 5.9 and multipole contributions were decomposed using the FOLD calculations. A linear combination of multipole shapes was fit to each angular distribution in each bin [116] with the equation

$$\sigma_{tot} = A * \sigma_1 + B * \sigma_2 + C * \sigma_3 + D * \sigma_4. \quad (5.3)$$

The best fit results were obtained using  $\Delta L=0,1,2$ , and 4 as shown in Figures 5.11 and 5.12.  $\Delta L=3$  was left out because the limited statistics allowed for the use of only five angular bins in this experiment. Contributions from  $\Delta L=3$  are effectively absorbed into contributions from  $\Delta L=2$  and  $\Delta L=4$ .

Figure 5.13 shows the MDA fit for the 0-1 MeV excitation energy bin.  $\Delta L=1$  strength dominates, but there is also considerable strength associated with  $\Delta L=0$  and 2. In contrast, Figure 5.14 shows the 20-21 MeV excitation energy bin.  $\Delta L=4$  strength dominates here,  $\Delta L=1$  strength is completely absent, and only small amounts of  $\Delta L=0$  and 2 strength appear. Many of the fits in this higher excitation energy

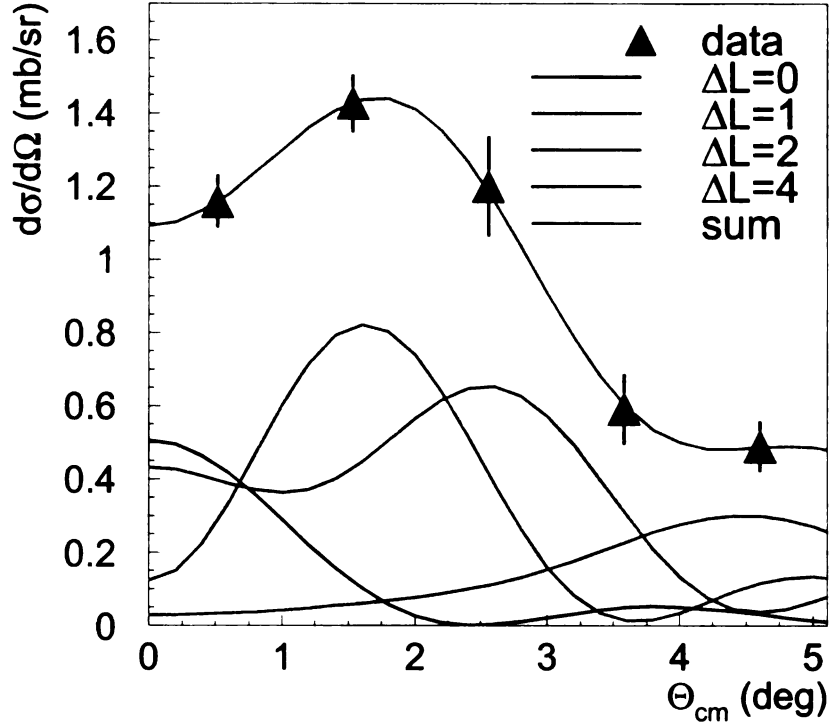


Figure 5.13: MDA for the 0-1 MeV excitation energy bin.

region are similar. Because of the previously-mentioned limitations in the MDA, it is likely that this  $\Delta L=4$  strength represents a combination of strength with  $\Delta L \geq 3$ .

Low-lying states are of particular interest for  $2\nu\beta\beta$  decay. Since a strong GT state was seen around 0.11 MeV in the  $^{150}\text{Nd}(^3\text{He},t)$  experiment, this region was closely examined for evidence of population through  $^{150}\text{Sm}(t,^3\text{He})$  as well. Figure 5.15 shows the angular distribution for the region between 0-300 keV. The  $\Delta L=0$  cross section at  $0^\circ$  is  $0.08 \text{ mb/sr} \pm 0.05 \text{ mb/sr}$ . However, this error bar can be improved upon. If the region between 100 and 200 keV (which is expected to include most of the  $1^+$  strength) is examined, the  $\Delta L=4$  component is consistent with zero. This is shown in Figure 5.16. The cross section associated with  $\Delta L=0$  in the 100-keV bin ( $0.08 \pm 0.03 \text{ mb/sr}$ ) at  $0^\circ$  is consistent with that in the 300-keV bin. Due to the limited energy resolution, some  $\Delta L=0$  strength should appear in the bins immediately below and above the 100-200 keV bin, but the extracted  $\Delta L=0$  cross sections at  $0^\circ$  are 0.018

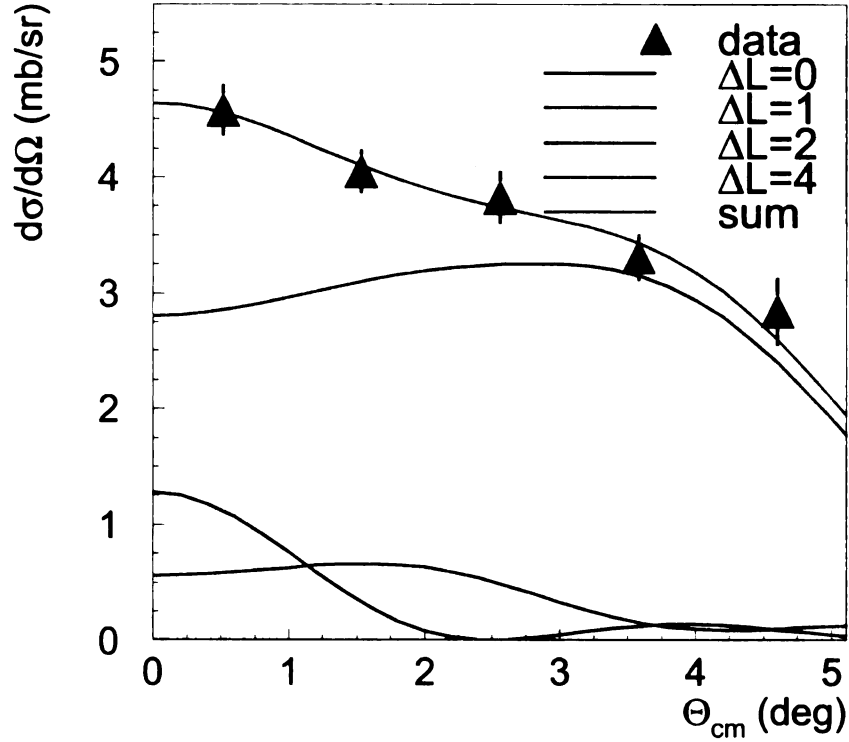


Figure 5.14: MDA for the 20-31 MeV excitation energy bin.

$+0.02$   
 $-0.018$  mb/sr (below) and  $0.012$   $+0.016$   
 $-0.012$  mb/sr (above), and both are consistent with zero. Given our uncertainty in the absolute energy calibration of 50 keV and the fact that no other  $1^+$  states appear within that error margin in the  $^{150}\text{Nd}(^3\text{He},t)$  data, we conclude that the GT strength associated with the 100-200 keV bin in the  $^{150}\text{Sm}(t,^3\text{He})$  data is likely associated with the 110 keV state in  $^{150}\text{Nd}(^3\text{He},t)$  data. However, the possibility that the two transitions do not represent the same state in  $^{150}\text{Pm}$  cannot be completely excluded.

Figures 5.17 and 5.18 show the assignment of multipole strength deduced from the MDA for the full spectrum and the lower-lying states, respectively.  $\Delta L=0$  strength is seen in several areas (0.85 MeV, 2.25 MeV, 5 MeV, and 5.5 MeV). The strength in the 100-200 keV region does not stand out with these large bin sizes. For the full spectrum, quite a bit of  $\Delta L=0$  and 2 (which may include contributions from  $\Delta L=3$ ) strength appears to peak between 10-12 MeV, and  $\Delta L=1$  strength dominates

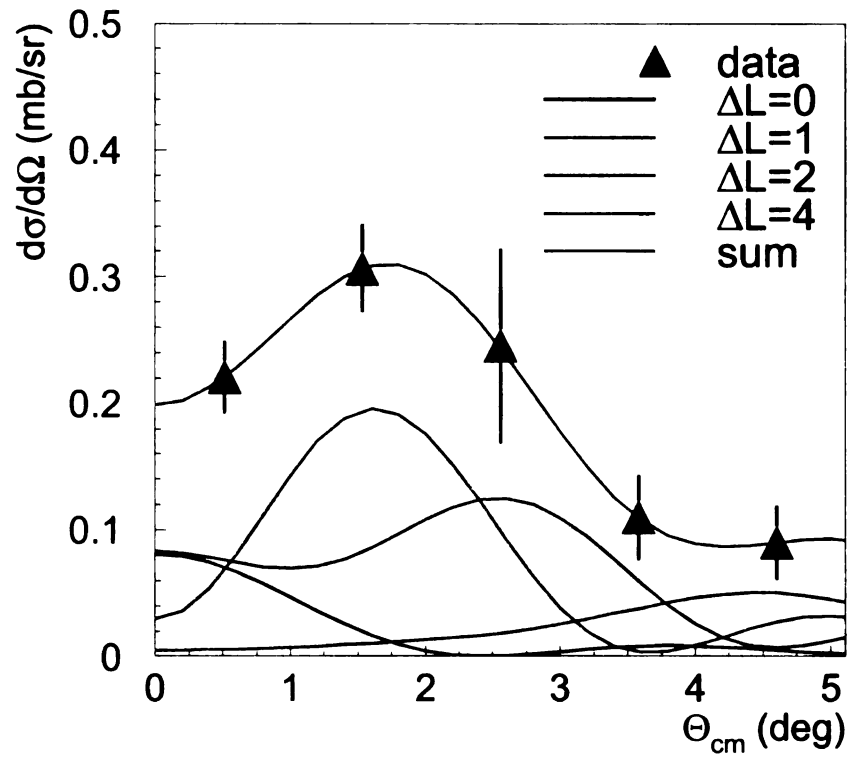


Figure 5.15: MDA for the 0-0.3 MeV excitation energy bin. The  $\Delta L=0$  angular distribution at  $0^\circ$  has a cross section of  $0.08 \text{ mb/sr} \pm 0.05 \text{ mb/sr}$ . The significant  $\Delta L=1$  cross section may correspond in part to population of the  $^{150}\text{Pm}$  ground state, which is shown to be a dipole transition in the  $^{150}\text{Nd}(^3\text{He},t)$  data.



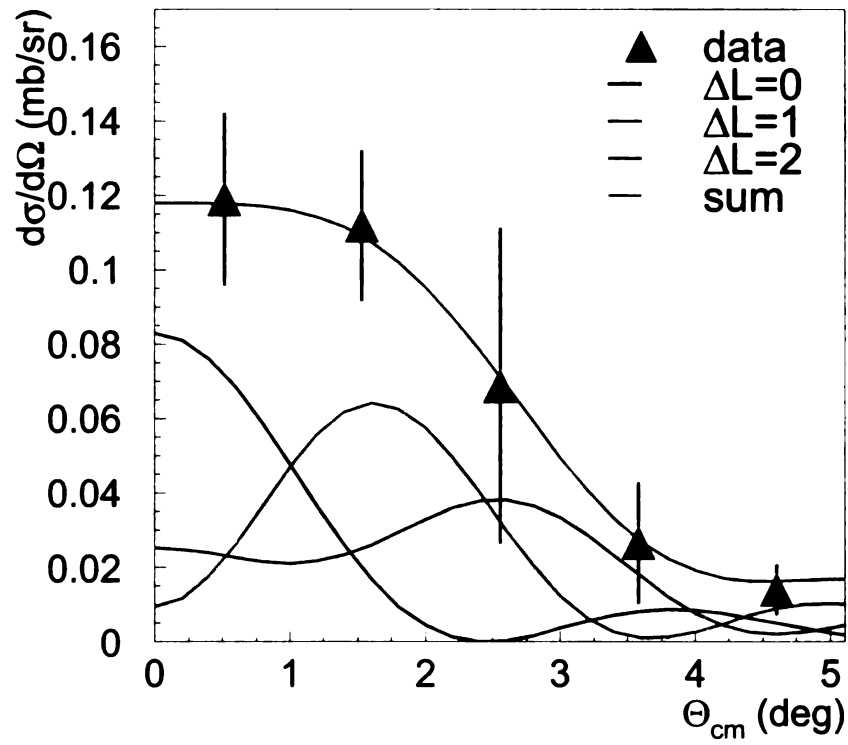


Figure 5.16: MDA for the 0.1-0.2 MeV excitation energy bin. The  $\Delta L=0$  angular distribution at  $0^\circ$  has a cross section of  $0.08 \text{ mb/sr} \pm 0.03 \text{ mb/sr}$ .  $\Delta L=0$  strength is enhanced in this bin and can be extracted with a smaller error than in a fit to the 300 keV bin.

in lower regions.  $\Delta L=4$  strength (including contributions from  $\Delta L=3, 5$ , and higher multipoles) makes up an increasing amount of the spectrum as the excitation energy increases.

### 5.3.3 Extrapolation to $q=0$

Absolute  $\Delta L=0$  cross sections from the MDA must be extrapolated to  $q=0$  (zero asymptotic linear momentum transfer) with equation 4.4 before they can be used to calculate GT strengths. A fourth-order polynomial describes this ratio, which is shown in Figure 5.19 and Equation 5.4.

$$Y_{ratio} = 1.00946 + 0.01039Q + 0.00857Q^2 - 4.082 \times 10^{-4}Q^3 + 1.843 \times 10^{-5}Q^4 \quad (5.4)$$

The effective linear momentum transfer  $q_{eff}$  is different from the asymptotic linear momentum transfer  $q_{asy}$  for the  $(t, {}^3\text{He})$  and  $({}^3\text{He}, t)$  directions, as discussed in Section 5.3.1. This difference is reflected in Figures 5.19 and 4.20.

### 5.3.4 Calculation of the Gamow-Teller strength

Once the cross section has been extrapolated to  $q=0$ , the  $B(\text{GT})$  can be extracted with Equation 3.24 using the phenomenological unit cross section [100]. Table 5.4 and Figure 5.20 show the results for 1 MeV bins up through 26 MeV in excitation energy, and Table 5.5 and Figure 5.21 show results for 300 keV bins for 0-6 MeV in excitation energy. Statistical/fitting errors are dominant in both choices of binning. Systematic errors in the extracted cross sections are estimated to be 15% and are due to uncertainties in the optical model potential and the phenomenological unit cross section. A large amount of  $\Delta L=0$  strength is seen over the region of 5-20 MeV. Between 0-6 MeV, bins centered at 0.15, 0.75, 1.0, and 2.25 MeV show evidence of GT strength. While all of the  $\Delta L=0$  strength is assumed to be GT for the purposes of this

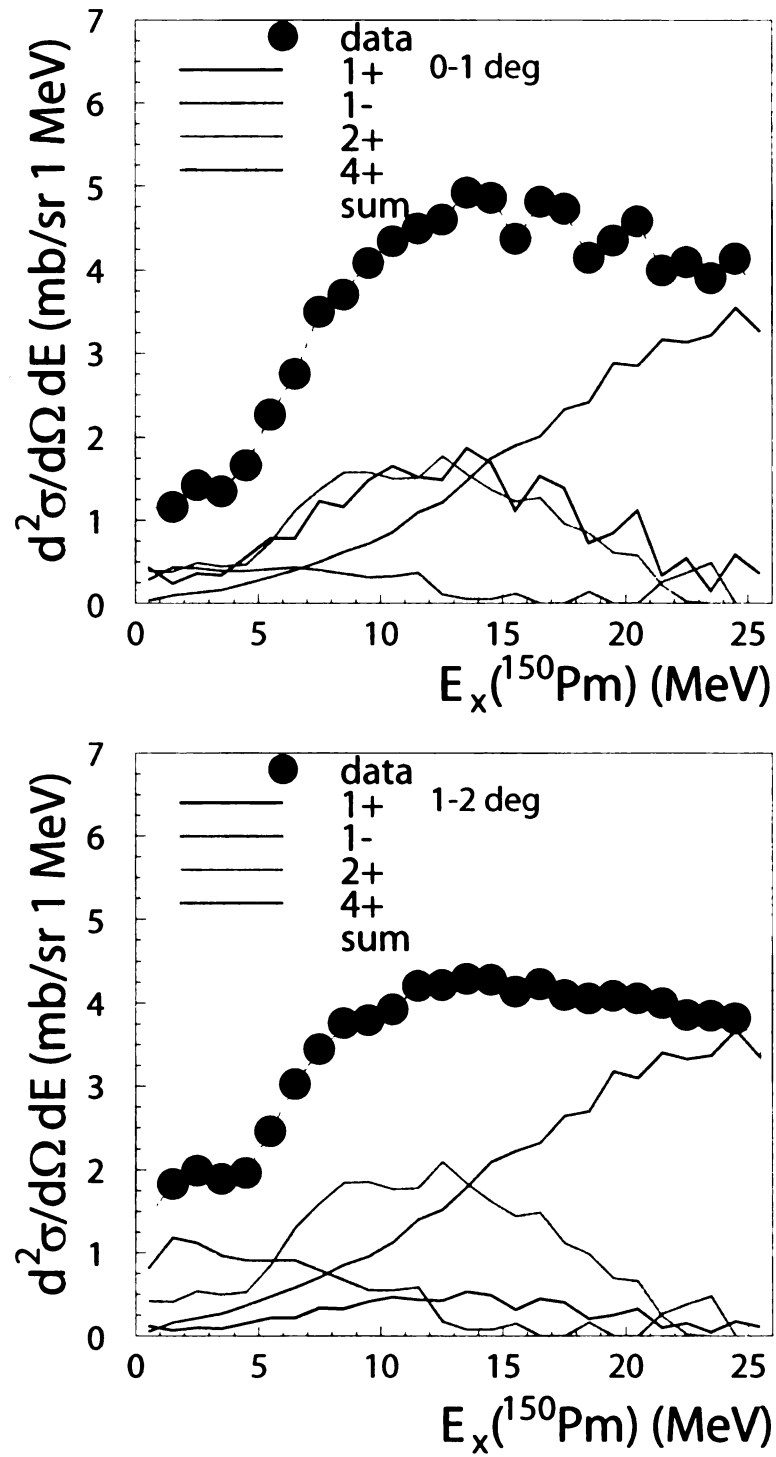


Figure 5.17: Multipole decomposition summary for each angular bin. Higher multipoles (or quasifree processes) take over at the highest excitation energies, as was discussed earlier in this section. Sizable cross sections associated with  $\Delta L=0$  and 2 are centered around 10-12 MeV, and a smaller amount of  $\Delta L=1$  cross sections are centered between 0-10 MeV.

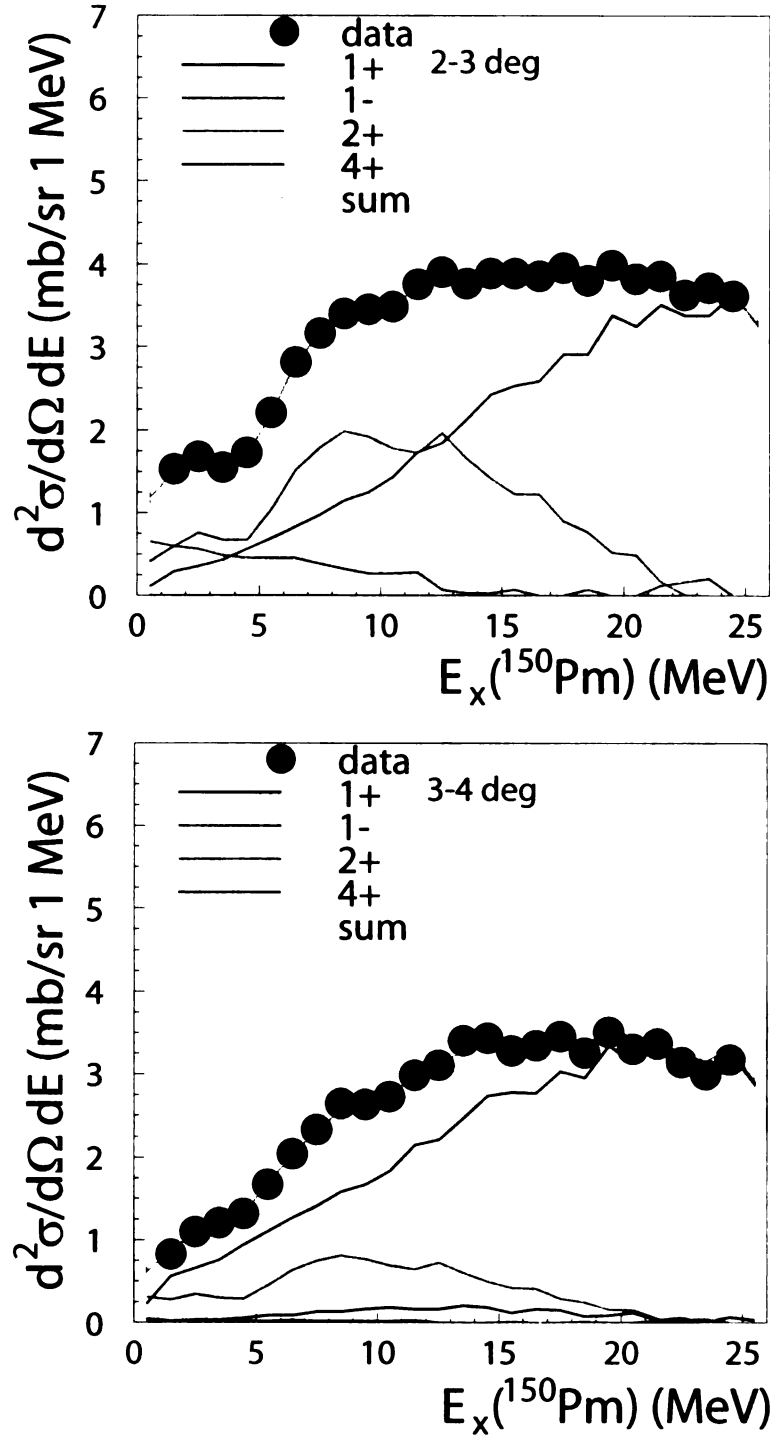


Figure 5.17: *cont.* Multipole decomposition summary for each angular bin. Higher multipoles (or quasifree processes) take over at the highest excitation energies, as was discussed earlier in this section. Sizable cross sections associated with  $\Delta L=0$  and 2 are centered around 10-12 MeV, and a smaller amount of  $\Delta L=1$  cross sections are centered between 0-10 MeV.

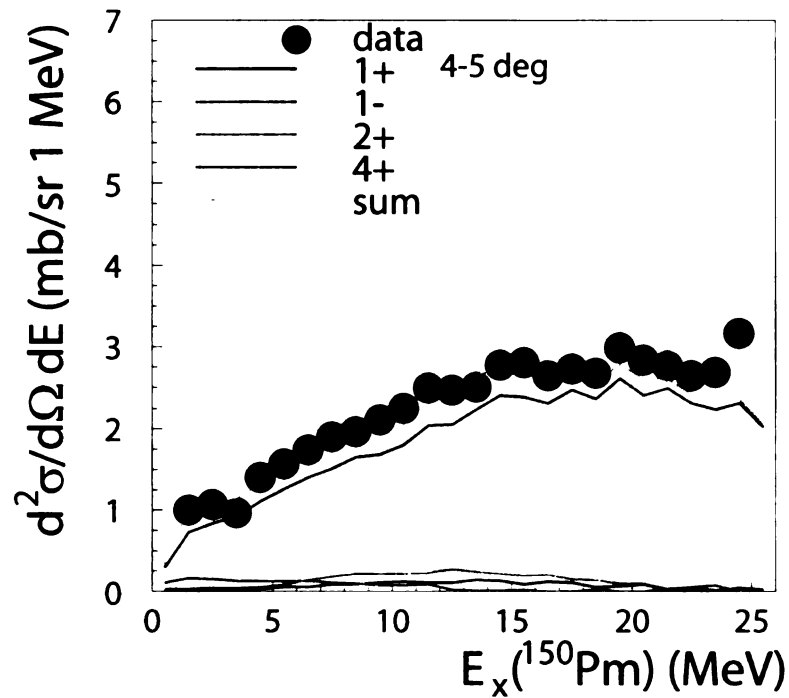


Figure 5.17: *cont.* Multipole decomposition summary for each angular bin. Higher multipoles (or quasifree processes) take over at the highest excitation energies, as was discussed earlier in this section. Sizable cross sections associated with  $\Delta L=0$  and 2 are centered around 10-12 MeV, and a smaller amount of  $\Delta L=1$  cross sections are centered between 0-10 MeV.

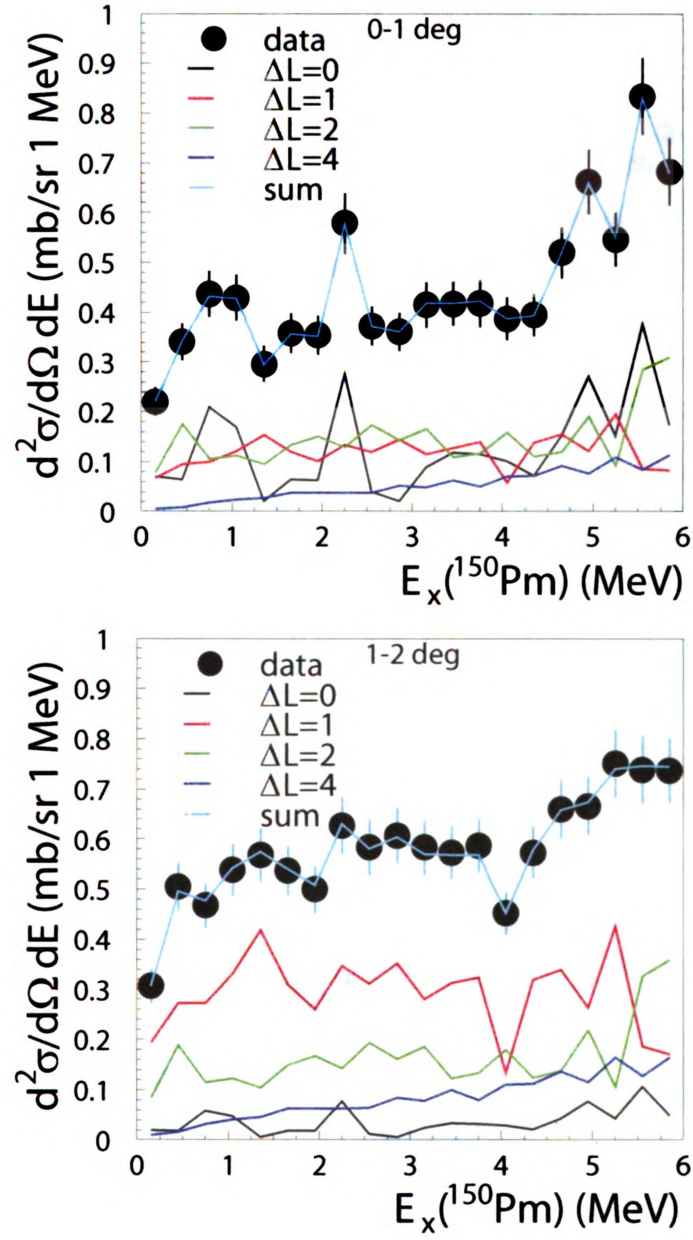


Figure 5.18: Multipole decomposition summary for each angular bin (0-6 MeV). Cross section peaks associated with  $\Delta L=0$  are visible in the  $0-1^\circ$  plot.

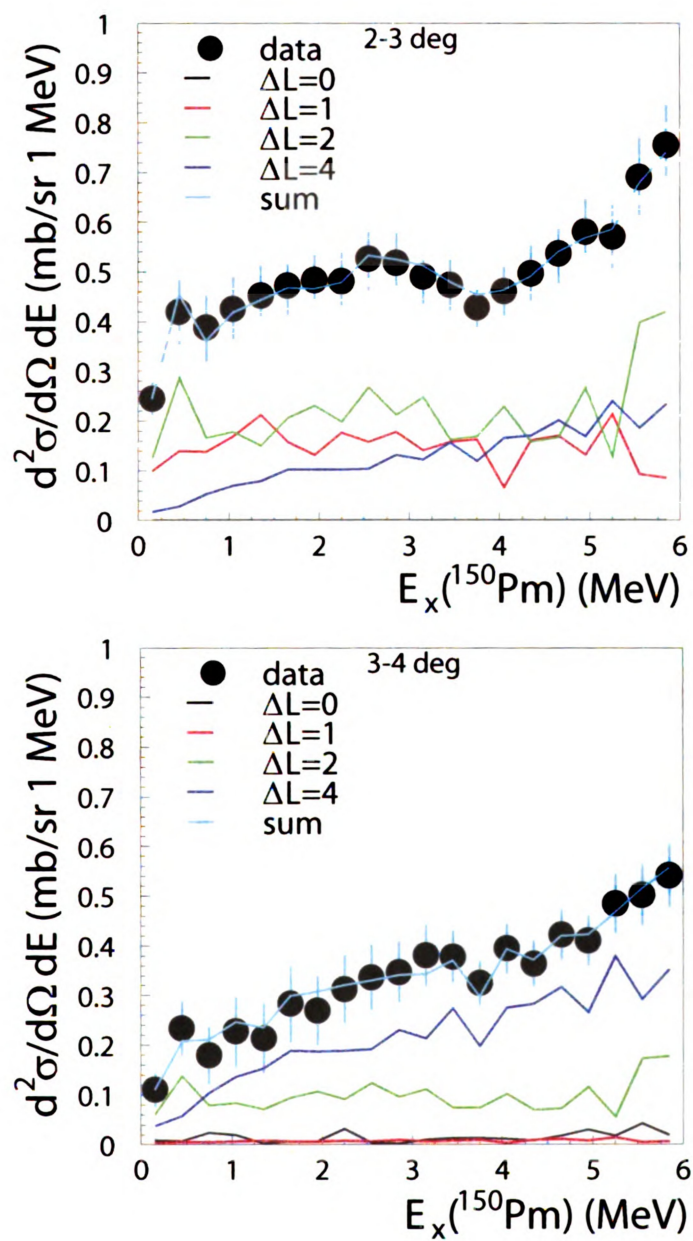


Figure 5.18: *cont.* Multipole decomposition summary for each angular bin (0-6 MeV). Cross section peaks associated with  $\Delta L=0$  are visible in the 0-1° plot.

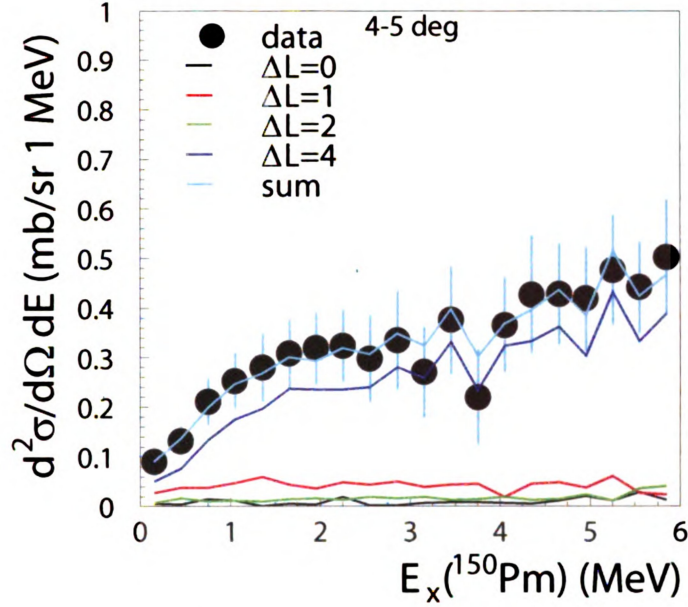


Figure 5.18: *cont.* Multipole decomposition summary for each angular bin (0-6 MeV). Cross section peaks associated with  $\Delta L=0$  are visible in the  $0-1^\circ$  plot.

calculation, the IVSGMR (which peaks around 15 MeV) is expected to contribute. The IVSGMR is expected to be very broad ( $\sim 10$  MeV) and cannot be separated from GT transitions by its angular distribution. It should be a smooth function of the excitation energy, so any isolated low-lying states likely stem from GT transitions. The magnitude of the extracted  $\Delta L=0$  cross section in terms of the IVSGMR will be further discussed in section 5.4.

### 5.3.5 Other Multipole Excitations

Since  $^{150}\text{Nd} \rightarrow ^{150}\text{Sm} \ 0\nu\beta\beta$  decays can be described as going through virtual states in  $^{150}\text{Pm}$  of any  $J^\pi$  and excitation energy, it is helpful to extract the strength distributions for dipole and quadrupole transitions. Dipole contributions, which peak at  $1-2^\circ$ , are clustered between 0-10 MeV, with the largest cross sections present between 1 and 4 MeV. Figure 5.22 and Table 5.6 contain dipole cross sections. Quadrupole cross sections (the cross sections in the  $0-1^\circ$  bin are displayed) form a diffuse area



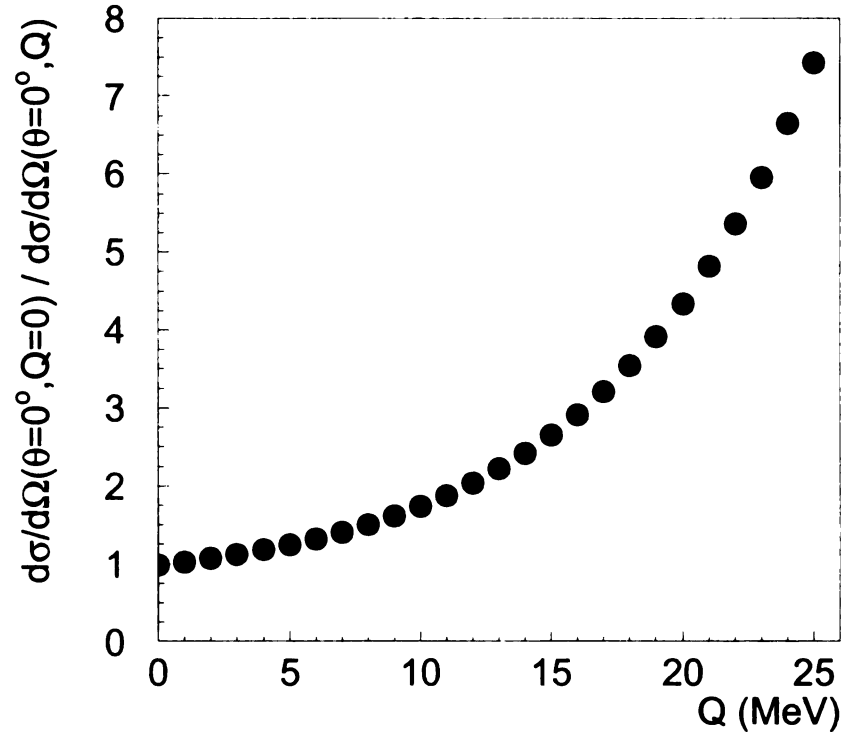


Figure 5.19: Ratio of the cross section at  $\theta=0^\circ$  and 0 linear momentum transfer to that of 0 linear momentum transfer, as calculated in DWBA. At a  $Q$  of 25 MeV, the effective momentum transfer  $q$  is 0.3.

Ex.(MeV)	B(GT)*	stat. error	syst. error	total error
0.5	0.1052	0.0278	0.0158	0.0320
1.5	0.0613	0.0282	0.0092	0.0297
2.5	0.0952	0.0334	0.0143	0.0363
3.5	0.0921	0.0334	0.0138	0.0361
4.5	0.1592	0.0404	0.0239	0.0469
5.5	0.2381	0.0541	0.0357	0.0648
6.5	0.2542	0.0702	0.0381	0.0799
7.5	0.4252	0.0864	0.0638	0.1074
8.5	0.4303	0.1014	0.0645	0.1202
9.5	0.5872	0.1182	0.0881	0.1474
10.5	0.7088	0.1293	0.1063	0.1674
11.5	0.706	0.1524	0.1059	0.1856
12.5	0.753	0.1683	0.1130	0.2027
13.5	1.0289	0.1943	0.1543	0.2481
14.5	1.0186	0.2142	0.1528	0.2631
15.5	0.7394	0.2246	0.1109	0.2505
16.5	1.1134	0.2563	0.1670	0.3059
17.5	1.1147	0.2845	0.1672	0.3300
18.5	0.645	0.4275	0.0968	0.4383
19.5	0.8295	0.3441	0.1244	0.3659
20.5	1.2223	0.4138	0.1833	0.4526
21.5	0.4127	0.6374	0.0619	0.6404
22.5	0.73	0.4694	0.1095	0.4820
23.5	0.2313	0.2377	0.0347	0.2402
24.5	0.9893	0.5002	0.1484	0.5217
25.5	0.6728	0.5167	0.1009	0.5265
sum	15.3637	1.4376	0.5275	1.5313

Table 5.4: Gamow-Teller strength distributions have been extracted for excitation energies of 0-26 MeV. See Figure 5.20. The seemingly large scatter and large error bars at higher excitation energies are due to the  $q=0$  correction factor, which sharply increases in this region and magnifies the statistical error. \*The entire  $\Delta L=0$  cross section is assumed to be GT strength here, but most of the strength is expected to actually represent IVSGMR strength.

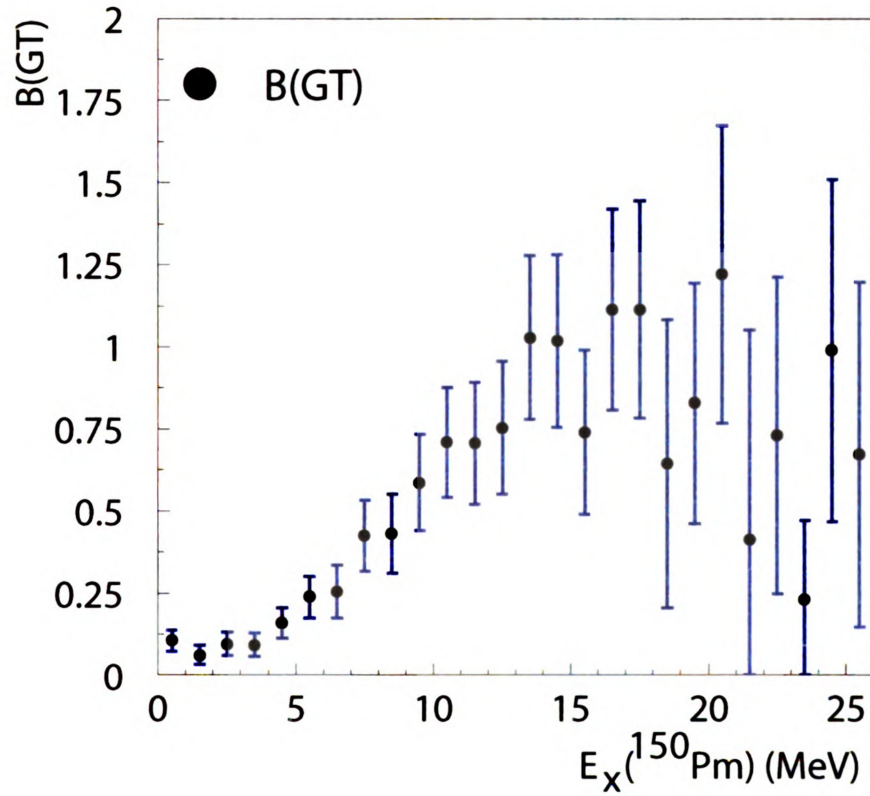


Figure 5.20: Extracted GT strength distributions are shown in the region of 0-26 MeV. Low-lying strength is seen between 0-1 MeV, and higher-lying strength is dispersed between 5 and 20 MeV. The entire  $\Delta L=0$  cross section is assumed to be GT strength here, but most may be contributions from the IVSGMR resonance. See Table 5.4 for the same information in tabular form. Some values are consistent with zero.

Ex.(MeV)	B(GT)	stat. error	syst. error	total error
0.15	0.0165	0.009	0.0025	0.0093
0.45	0.0153	0.0114	0.0023	0.0116
0.75	0.0505	0.0126	0.0076	0.0147
1.05	0.0414	0.0127	0.0062	0.0141
1.35	0.005	0.0109	0.0008	0.0109
1.65	0.0162	0.0118	0.0024	0.0120
1.95	0.0159	0.0118	0.0024	0.0120
2.25	0.0709	0.016	0.0106	0.0192
2.55	0.0102	0.0128	0.0015	0.0129
2.85	0.0057	0.0127	0.0009	0.0127
3.15	0.0238	0.0138	0.0036	0.0143
3.45	0.0323	0.0136	0.0048	0.0144
3.75	0.0318	0.0142	0.0048	0.0150
4.05	0.0284	0.0137	0.0043	0.0143
4.35	0.0208	0.0143	0.0031	0.0146
4.65	0.0443	0.0171	0.0066	0.0183
4.95	0.0801	0.0207	0.0120	0.0239
5.25	0.0457	0.0186	0.0069	0.0198
5.55	0.1152	0.025	0.0173	0.0304
5.85	0.054	0.0239	0.0081	0.0252
sum	0.724	0.0689	0.0304	0.0753

Table 5.5: Gamow-Teller strength distributions are shown for the region of 0-6 MeV (300 keV bins). See Figure 5.21. Even at these low excitation energies, the tail of the IVSGMR resonance may contribute to the extracted GT strength.

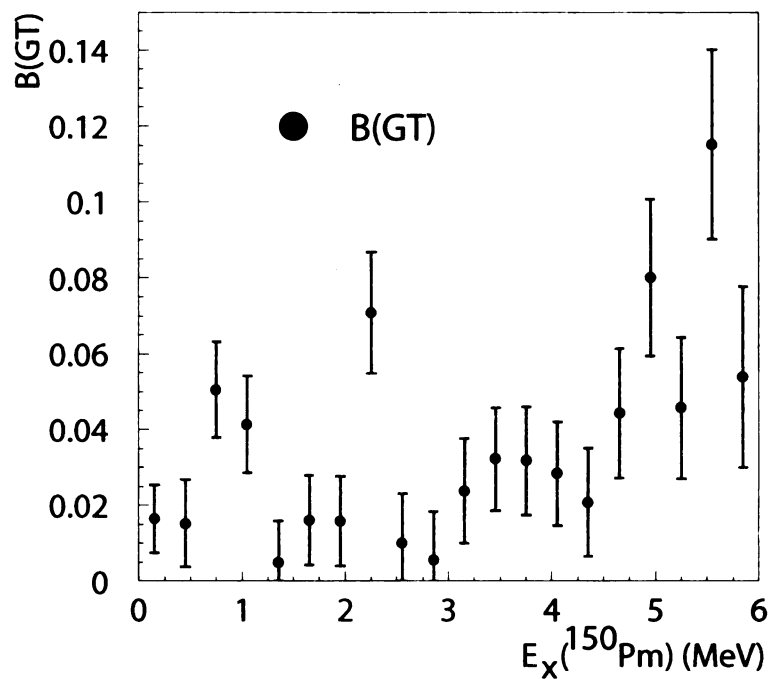


Figure 5.21: Extracted GT strength is shown for the region between 0-6 MeV. See Table 5.5 for the same information in tabular form. Some values are consistent with zero, and the tail of the IVSGMR is expected to contribute to the strength. However, isolated strength below 3 MeV is unlikely to be due to the IVSGMR.

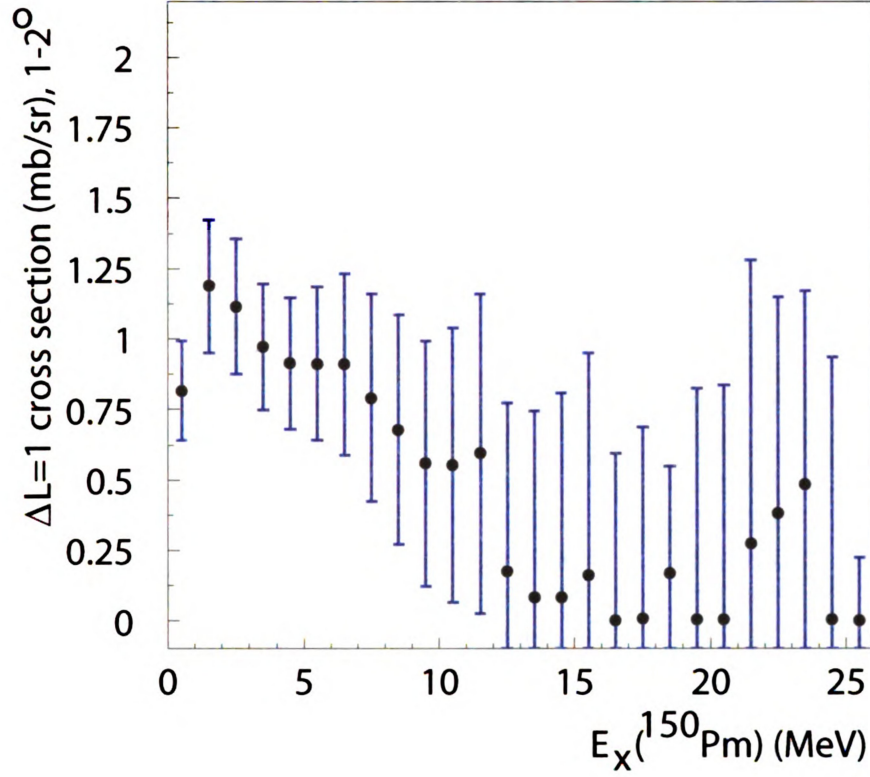


Figure 5.22: Extracted  $\Delta L=1$  cross sections are shown from 0-26 MeV (at  $1-2^\circ$ ). Some values are consistent with zero.

of strength between 5 and 17 MeV, as shown in Figure 5.23 and Table 5.7. The quadrupole distribution is similar to the  $\Delta L=0$  distribution, and could be indicative of an IVSGQR. In fact, the strength distribution of the IVSGQR and IVSGMR are expected to peak at nearly the same excitation energies and have similar widths [135]. However, the possible contributions from  $\Delta L=3$  strength in the extracted  $\Delta L=2$  cross section make it hard to draw strong conclusions on the magnitude of the IVSGQR.

Ex.(MeV)	Cross Section (mb/sr)	stat. error	syst. error	total error
0.5	0.8164	0.1253	0.1225	0.1752
1.5	1.1871	0.1550	0.1781	0.2361
2.5	1.1149	0.1714	0.1672	0.2395
3.5	0.972	0.1718	0.1458	0.2253
4.5	0.9144	0.1878	0.1372	0.2326
5.5	0.9132	0.2364	0.1370	0.2732
6.5	0.9105	0.2906	0.1366	0.3211
7.5	0.7922	0.3474	0.1188	0.3672
8.5	0.6780	0.3951	0.1017	0.4080
9.5	0.5583	0.4266	0.0837	0.4347
10.5	0.5539	0.4798	0.0831	0.4869
11.5	0.5935	0.5589	0.0890	0.5659
12.5	0.1767	0.5961	0.0265	0.5967
13.5	0.0833	0.6601	0.0125	0.6602
14.5	0.0819	0.7266	0.0123	0.7267
15.5	0.1615	0.7891	0.0242	0.7895
16.5	0.0008	0.5950	0.0001	0.5950
17.5	0.0071	0.6816	0.0011	0.6816
18.5	0.1672	0.3824	0.0251	0.3832
19.5	0.0059	0.8209	0.0009	0.8209
20.5	0.0054	0.8322	0.0008	0.8322
21.5	0.2734	1.0079	0.0410	1.0087
22.5	0.3811	0.7648	0.0572	0.7669
23.5	0.4834	0.6850	0.0725	0.6888
24.5	0.0034	0.9344	0.0005	0.9344
25.5	0.0030	0.2206	0.0005	0.2206
sum	11.8385	2.9224	0.4592	2.8582

Table 5.6:  $\Delta L=1$  cross sections are shown from 0-26 MeV (at  $1-2^\circ$ ).

Ex.(MeV)	Cross Section (mb/sr)	stat. error	syst. error	total error
0.5	0.3995	0.1533	0.0599	0.1646
1.5	0.3796	0.1662	0.0569	0.1757
2.5	0.4927	0.1848	0.0739	0.1990
3.5	0.4516	0.1886	0.0677	0.2004
4.5	0.4664	0.2140	0.0700	0.2251
5.5	0.7456	0.2611	0.1118	0.2840
6.5	1.1218	0.3146	0.1683	0.3568
7.5	1.3661	0.3699	0.2049	0.4229
8.5	1.5730	0.4035	0.2360	0.4674
9.5	1.5728	0.4403	0.2359	0.4995
10.5	1.4995	0.5018	0.2249	0.5499
11.5	1.5064	0.5874	0.2260	0.6294
12.5	1.7716	0.6251	0.2657	0.6792
13.5	1.5544	0.6808	0.2332	0.7196
14.5	1.3727	0.7700	0.2059	0.7971
15.5	1.2286	0.8376	0.1843	0.8576
16.5	1.2695	0.3209	0.1904	0.3731
17.5	0.9608	0.3267	0.1441	0.3571
18.5	0.8545	0.7063	0.1282	0.7178
19.5	0.6068	0.3972	0.0910	0.4075
20.5	0.5803	0.6267	0.0870	0.6327
21.5	0.2184	0.3726	0.0328	0.3740
22.5	0.0243	0.5938	0.0036	0.5938
23.5	0.0083	0.4641	0.0012	0.4641
24.5	0.0005	0.4770	0.0001	0.4770
25.5	0.0005	0.1972	0.0001	0.1972
sum	22.0262	2.4094	0.7806	2.5327

Table 5.7:  $\Delta L=2$  cross sections are shown from 0-26 MeV (at  $0^{-1^\circ}$ ). A portion of the cross section is likely due to  $\Delta L=3$  contributions, which were not accounted for in the MDA.



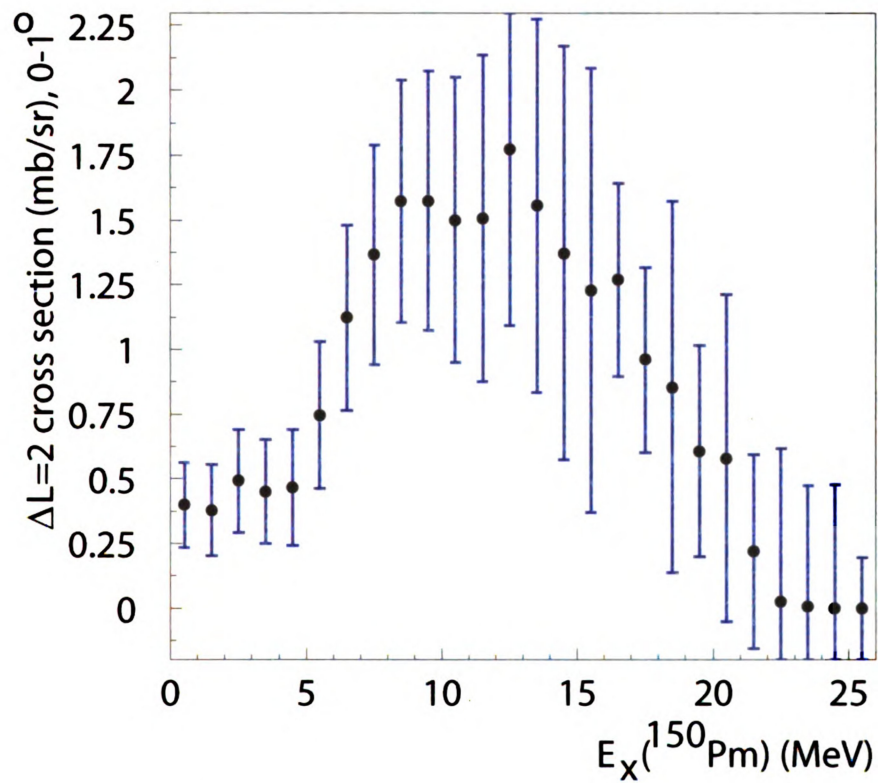


Figure 5.23: Extracted  $\Delta L=2$  cross sections are shown from 0-26 MeV (at  $0-1^\circ$ ). Some values are consistent with zero. A portion of the cross section is likely due to  $\Delta L=3$  contributions, which were not accounted for in the MDA.

## 5.4 Comparison with Theory

### 5.4.1 $\Delta L=0$ Cross sections and the IVSGMR

Very little GT strength is expected to be observed in the  $^{150}\text{Sn}(t,^3\text{He})$  reaction due to the effects of Pauli blocking. According to the QRPA calculations discussed in Section 5.4.2, the total GT strength should be 0.5. However, if we assume that all of the extracted  $\Delta L=0$  strength from the data can be attributed to GT transitions, the total strength is  $15.4 \pm 1.5$ . This is unrealistically high, especially when compared with similar (n,p)-type -experiments [82, 136, 137, 138, 139]. The largest extracted GT strength in the (n,p) direction over a comparable energy range (30 MeV) was 6 [139] for the case of  $^{116}\text{Sn}(n,p)$ , and Pauli blocking is stronger for  $^{150}\text{Sn}$  than  $^{116}\text{Sn}$ . Most references claim summed  $B(\text{GT})$  values of 1-3.

Transitions due to the IVSGMR have similar angular distributions to GT transitions and the two can't be experimentally distinguished from each other. The centroid of the IVSGMR was roughly predicted to be 15 MeV in Section 3.3, with a width of around 10 MeV [135]. Since this roughly matches the observed  $\Delta L=0$  distribution, the data strongly suggest that the bulk of the observed  $\Delta L=0$  strength is due to the excitation of the IVSGMR. To test this idea, the total IVSGMR cross section was calculated in DWBA using OBTDs from NORMOD and compared with the DWBA differential cross section per unit of  $B(\text{GT})$  for GT transitions. The extracted  $B(\text{GT})$  from the data corresponds to about 40% of the normal mode strength of the IVSGMR, assuming that all experimental  $\Delta L=0$  strength is attributed to the IVSGMR and that there is a proportionality between the IVSGMR cross section and IVSGMR strength. Although the uncertainties in this simple calculation are large, it shows that the extracted  $\Delta L=0$  strength is indeed likely due to the excitation of the IVSGMR.

### 5.4.2 QRPA calculations

QRPA calculations for the GT and dipole strength distributions in  $^{150}\text{Sm}(t, ^3\text{He})$  have been provided by Vadim Rodin's group to complement the calculations for  $^{150}\text{Nd}(^3\text{He}, t)$ . These calculations include the effect of deformation. Table 4.14 in Chapter 4 lists important parameters used in the reaction calculations.

Individual states for the B(GT) and dipole transitions ( $J^\pi=0^-, 1^-, 2^-$ ) are shown in Figure 5.24. The calculations incorporate three different values of K, which is a good quantum number in a deformed nucleus (J is not), and the three colors correspond to these three values of K. In the plot of B(GT), the GT strength has not yet been quenched.

The calculations are smeared to represent spreading in the strength distribution, which is not accounted for in the QRPA, and put into 1 MeV bins. Below 4 MeV, the GT calculations were smeared with the experimental resolution and re-binned into 1-MeV-wide bins. Above 4 MeV, the calculations were smeared with Gaussians (FWHM = 4.7 MeV) so that the width of the GTR excited via the  $^{150}\text{Nd}(^3\text{He}, t)$  reaction roughly matches the data. The dipole smearing widths (FWHM = 3.5 MeV) were chosen to match those used for the  $^{150}\text{Nd}(^3\text{He}, t)$  data. Figure 5.25 shows the distribution and cumulative B(GT) strength. Figure 5.25 compares all of the experimental  $\Delta L=0$  strength to the GT strength distribution from QRPA. Because of reasons discussed in Section 5.4.1, no conclusions can be drawn about the validity of the QRPA calculations in terms of the total GT strength found, since most of the  $\Delta L=0$  strength found is likely due to the IVSGMR. It is notable that the summed B(GT) strength predicted in the 0-1 MeV energy bin does match the data, but a single strong GT transition predicted in QRPA was not seen in the data.

Figure 5.26 compares the distribution and cumulative dipole cross section for the data and QRPA. As no proportionality between cross section and dipole strength has

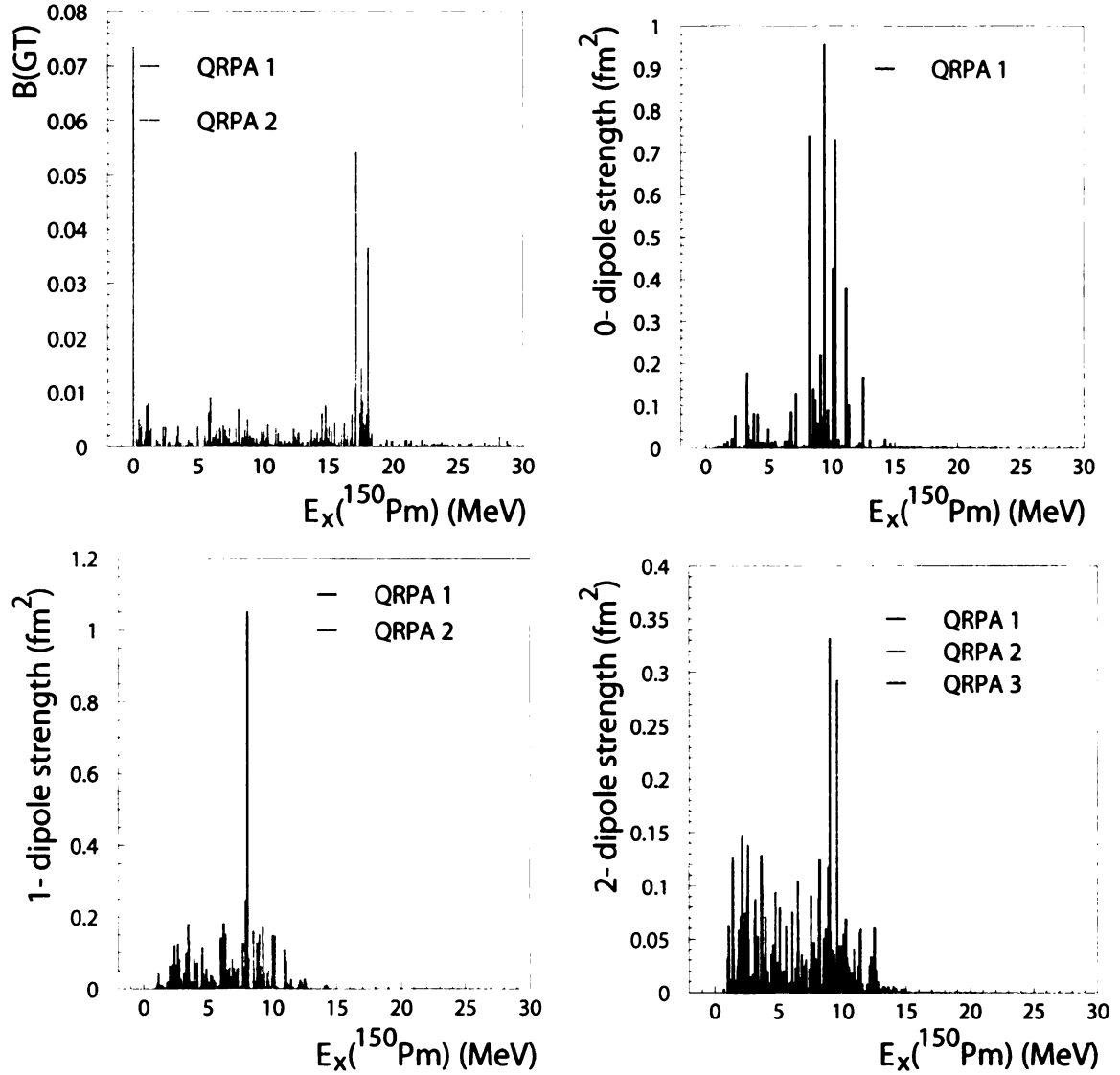


Figure 5.24: Raw QRPA calculations for  $^{150}\text{Sm}(t, {}^3\text{He})$ . Top left: GT strength, top right:  $0^-$  dipole cross sections and strength, bottom left:  $1^-$  dipole cross sections and strength, bottom right:  $2^-$  dipole cross sections and strength. The three colors represent three different values for  $K$ : black represents  $K=0$ , red represents  $K=1$ , and blue represents  $K=2$ . No quenching has (yet) been applied to the calculations of GT strength.

been established, we can only compare the shapes of cross section distribution from data with that of the calculated strength distribution.

While the dipole cross section is correctly predicted to exist entirely below 15 MeV in excitation energy, the experimental and theoretical distributions are somewhat different. The total QRPA strength distribution consists of two overlapping bumps: a small bump near 3.5 MeV and a larger one around 8.5 MeV. Dipole distributions from the data show a large bump around 2 MeV and a smaller bump around 7 MeV.

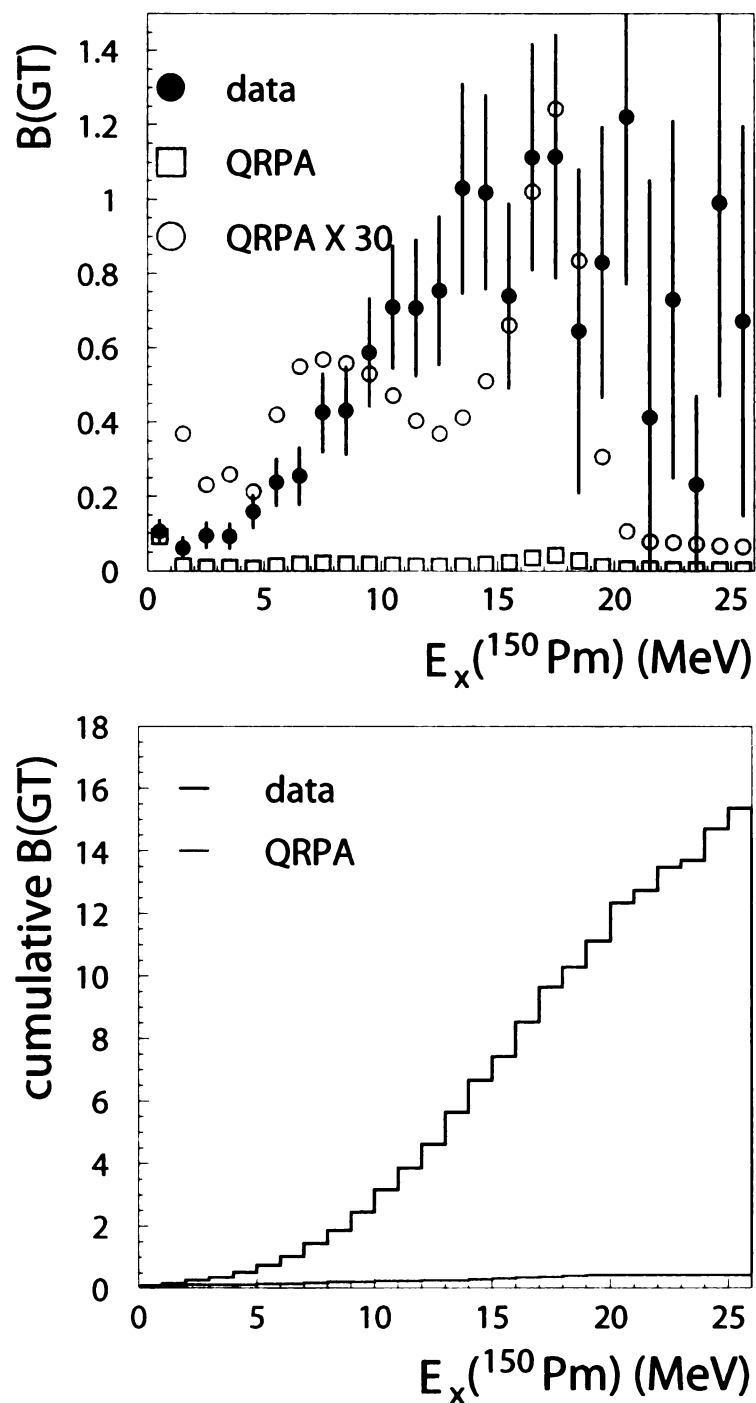


Figure 5.25: Extracted Gamow-Teller strength in  $^{150}\text{Pm}$  via  $^{150}\text{Sm}(t, ^3\text{He})$  compared with QRPA calculations. Data is shown in black, QRPA calculations in red, and in the top plot the QRPA is scaled by a factor of 30. The excess strength seen in data is attributed to the population of the IVSGMR resonance.

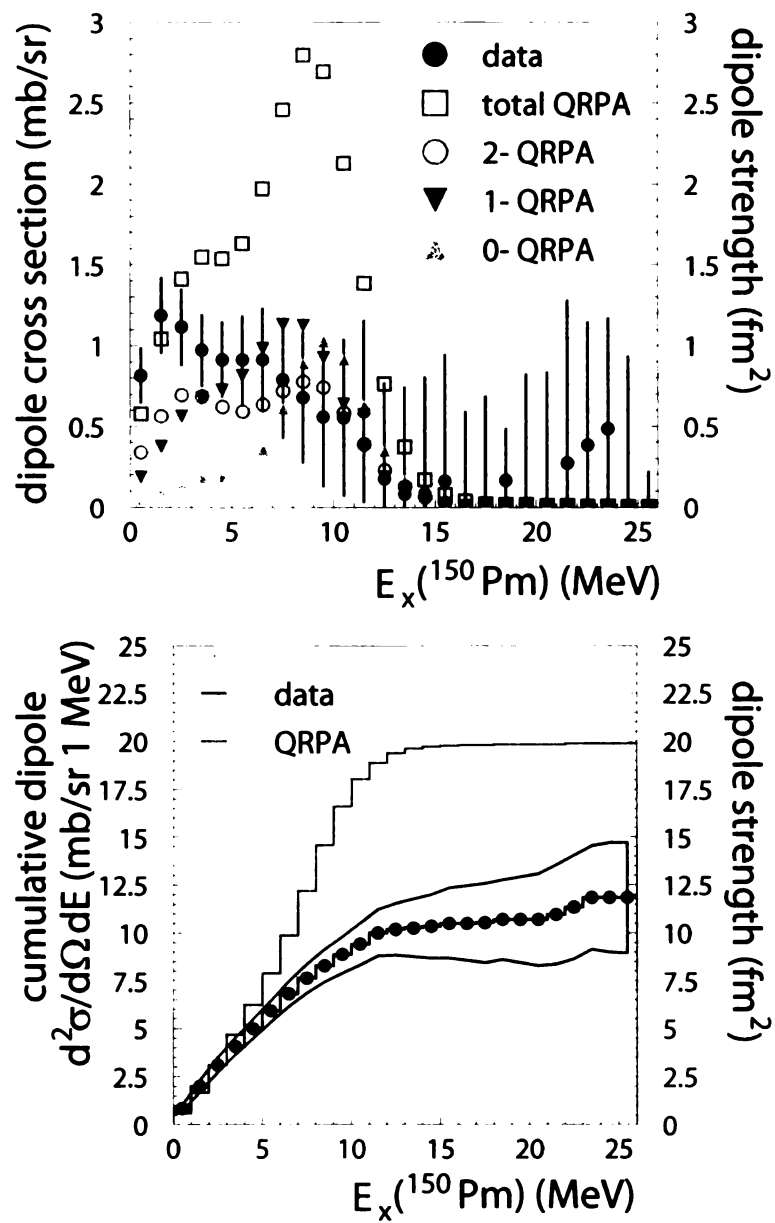


Figure 5.26: Extracted dipole cross sections in  $^{150}\text{Pm}$  via  $^{150}\text{Sm}(t, ^3\text{He})$  compared with QRPA calculations.

# Chapter 6

## Application to $2\nu\beta\beta$ decay

### 6.1 Low-lying states and the SSD hypothesis

Charge-exchange experiments can provide constraints for theory calculations aimed at modeling  $\beta\beta$  decay processes. Both experiments discussed in this thesis populated states in  $^{150}\text{Pm}$ . A  $2\nu\beta\beta$  decay transition, under the single-state dominance hypothesis (SSD) [37], is governed by a virtual two-step transition connecting the initial and final ground states through the first  $1^+$  state in the intermediate odd-odd nucleus. All of the  $2\nu\beta\beta$  decay strength is assumed to travel through this state and other intermediate states can be ignored. If the SSD hypothesis is not used, contributions from the intermediate states in Equation 2.6 can add either constructively or destructively, and these phases must be accounted for within the calculation.

The low-lying state in  $^{150}\text{Pm}$  as populated from  $^{150}\text{Nd}$  is centered at 0.11 MeV in excitation energy and has a  $B(\text{GT})$  of  $0.1334 \pm 0.0213$  associated with it. A combination of high level density and poorer resolution hindered our ability to distinguish the population of this state in the  $^{150}\text{Sm}(t, ^3\text{He})$  direction. However, a small amount of GT strength ( $0.0195 \pm 0.0071$ ) has been associated with the 0-300 keV region and appears to peak between 0.1-0.2 MeV. It is reasonable to assume that this GT strength



is due to the population of the 0.11 MeV state in  $^{150}\text{Nd}(^3\text{He},t)$  (given the 50-keV systematic error in the excitation energy in the  $^{150}\text{Sm}(t,^3\text{He})$  data). However, there is also some GT strength located at 0.19 MeV in the  $^{150}\text{Nd}$  data, and the effect of a possible overlap of this state with the  $^{150}\text{Sm}$  data must be checked with theoretical techniques. The  $2\nu\beta\beta$  decay half life will be calculated here under the SSD with the assumption that the strength between 100-200 keV in the  $^{150}\text{Sm}(t,^3\text{He})$  data matches the 0.11 MeV state in the  $^{150}\text{Nd}(^3\text{He},t)$  data.

Figure 6.1 shows low-lying GT strength in  $^{150}\text{Pm}$  from both directions. It is difficult to draw many conclusions here because of  $^{150}\text{Pm}$ 's high level density, the 50-keV uncertainty in the energy calibration for the  $^{150}\text{Sm}(t,^3\text{He})$  data, and the differences in excitation energy bins between the two experiments. In other, similar analyses [67, 138], GT strengths have been superimposed over a much larger energy range, but since much of the “GT” strength in the  $(t,^3\text{He})$  direction is likely from the IVSGMR, this would not be appropriate in this situation.

## 6.2 Calculating the $2\nu\beta\beta$ decay half life in the SSD

Four quantities are needed to calculate the  $2\nu\beta\beta$  decay half-life: the phase space factor  $G^{2\nu}$ , a sum of several energies (the denominator of Equation 2.6), and the extracted  $B(\text{GT})$ s for the 0.11 MeV state from the  $^{150}\text{Sm}(t,^3\text{He})$  and  $^{150}\text{Nd}(^3\text{He},t)$  experiments. The phase space factor of  $1.2 \times 10^{-16}$  was taken from [30]. The energy denominator includes the Q-value for  $\beta\beta$  decay, the excitation energy of the intermediate state, and the energy difference between the ground states of the initial and intermediate nuclei. These values are 3.3677 MeV, 0.11 MeV, and 0.024 MeV respectively. The double GT nuclear matrix element is then  $0.029 \pm 0.006$  and the  $2\nu\beta\beta$  decay half life is  $10.0 \pm 3.7 \times 10^{18}$  years (see Table 6.1).

The currently recommended value of  $8.2 \pm 0.9 \times 10^{18}$  years from Barabash [12]

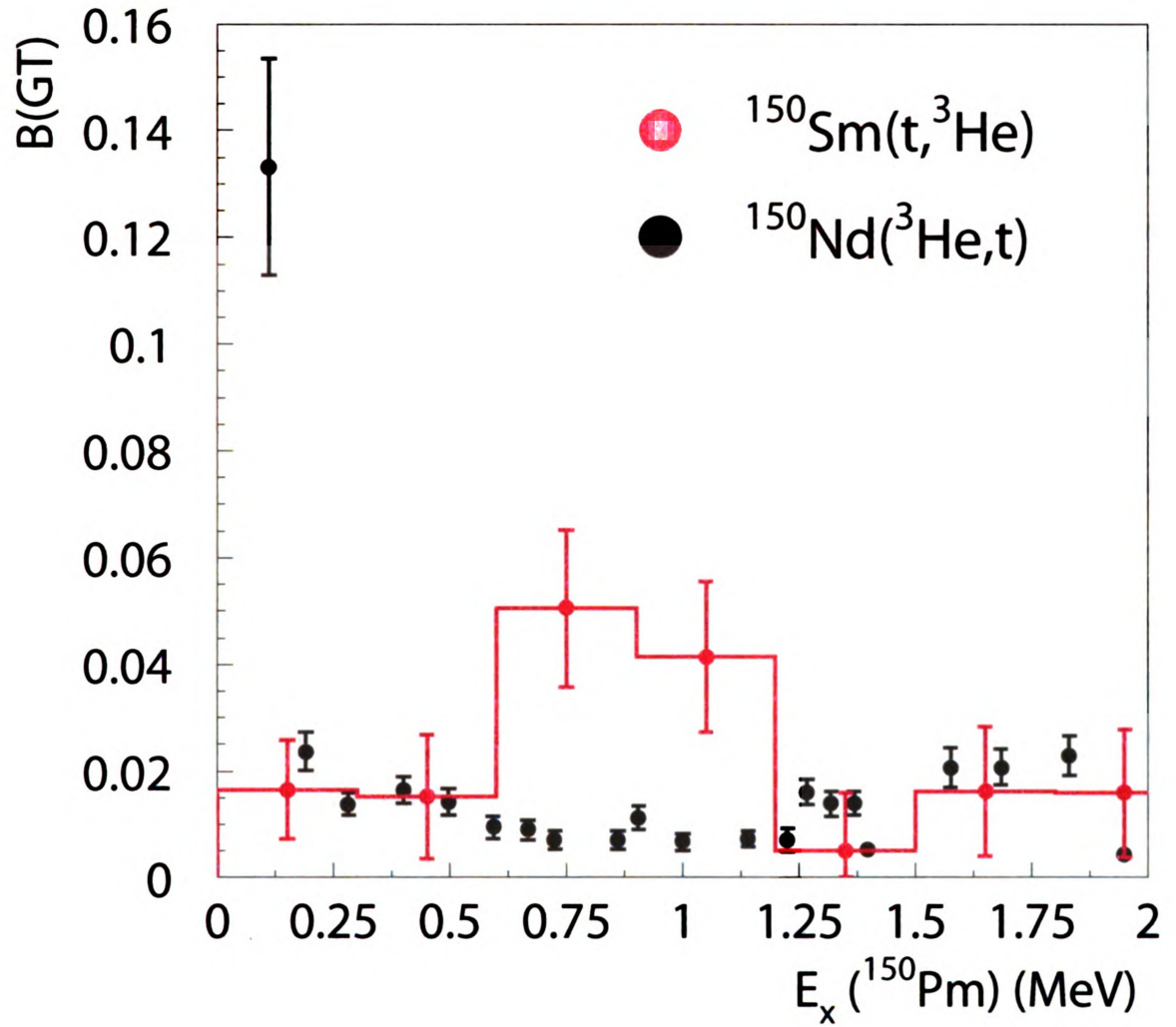


Figure 6.1: B(GT) strength in  $^{150}\text{Pm}$  at low energies from both experiments. Note that binning is different for the two experiments: the points from  $^{150}\text{Nd}$  are from a peak-by-peak analysis, while the  $^{150}\text{Sm}$  data have been put into 300 keV bins.

B(GT) from $^{150}\text{Sm}$	B(GT) from $^{150}\text{Nd}$	$M_{2\nu}$	$T^{1/2}$ (y)
$0.0194 \pm 0.0070$	$0.1344 \pm 0.0203$	$0.0289 \pm 0.0056$	$10.0 \pm 3.7 \times 10^{18}$

Table 6.1: Calculation of the  $2\nu\beta\beta$  decay matrix element assuming single-state dominance. The energy denominator of Equation 2.6 is calculated to be 1.77 MeV and is discussed in the text.

is consistent with our result, as is the recommended value from NNDC of  $7.9 \pm 0.7 \times 10^{18}$  years [140]. The error in the extracted half-life from the CE data (assuming the SSD hypothesis) would be significantly reduced if the error in the  $^{150}\text{Sm} \rightarrow ^{150}\text{Pm}$   $B(\text{GT})$  could be decreased. This would require a high-rate, high-resolution (n,p)-type CE experiment and could benefit by the addition of  $\gamma$ -ray detectors for coincidence measurements so that the excitation of the 110-keV state can be unambiguously observed.

We can conclude from our measurements that the SSD hypothesis is a plausible explanation for the  $2\nu\beta\beta$  decay half life of  $^{150}\text{Nd}$ . However, it is important to note that the transition seen in the 100-200 keV bin in the  $^{150}\text{Sm}(t, ^3\text{He})$  data may not be the 110 keV state seen in the  $^{150}\text{Nd}(^3\text{He}, t)$  data, because of the 50-keV systematic uncertainty in the  $^{150}\text{Sm}(t, ^3\text{He})$  excitation energy and the existence of a small state seen at 190 keV in the  $^{150}\text{Nd}(^3\text{He}, t)$  data. In this case the SSD hypothesis cannot be applied. Furthermore, the possibility of many higher-lying states contributing constructively or destructively to the half life cannot be ruled out. Future theoretical work, such as that by V. Rodin presented in the previous chapters, will hopefully provide further insights.

# Chapter 7

## Conclusions and Outlook

Charge-exchange reactions are an effective tool to probe the two branches of a double beta decay transition. The  $^{150}\text{Nd}(^3\text{He,t})^{150}\text{Pm}$  and  $^{150}\text{Sm}(t,^3\text{He})^{150}\text{Pm}$  reactions have been used to populate states in  $^{150}\text{Pm}$ , the intermediate nucleus in the decay of  $^{150}\text{Nd}$  to  $^{150}\text{Sm}$ . Doing the experiment at intermediate energies (over 100 MeV/u) allowed for the extraction of the GT strength distribution as well as cross sections for dipole and quadrupole transitions. Comparing the exact location of states between the two experiments is very difficult in this work because of the high level density in  $^{150}\text{Pm}$  and the differences in energy resolution, but the results are important for constraining theoretical models of both the  $2\nu\beta\beta$  and  $0\nu\beta\beta$  decays of  $^{150}\text{Nd}$ . Tables and figures of the extracted GT strength distributions and dipole and quadrupole cross section distributions in  $^{150}\text{Pm}$  have been presented for excitation energy ranges of 0-30 MeV from the  $^{150}\text{Nd}$  target and 0-26 MeV from the  $^{150}\text{Sm}$  target.

A strong GT state with low excitation energy has been identified in the  $^{150}\text{Nd}(^3\text{He,t})$  experiment, and a small amount of strength is seen in the same location in the  $^{150}\text{Sm}(t,^3\text{He})$  experiment. If the single-state dominance hypothesis is applied, the resulting  $2\nu\beta\beta$  decay half life is  $10.0 \pm 3.67 \times 10^{18}$  years, which is consistent with the accepted value from direct decay measurements. This, in conjunction with non-

zero GT strength present at several other locations in  $^{150}\text{Pm}$ , suggests that the SSD hypothesis needs to be carefully examined in this case. Reference [39] states that “[unless] there is an unknown  $1^+$  low-lying state of  $^{150}\text{Pm}$ , the experimental measurement should confirm [that the higher-state dominance (HSD) hypothesis regulates the]  $2\nu\beta\beta$  decay of  $^{150}\text{Nd}$ .” While this low-lying  $1^+$  has been shown to exist in this work and the SSD seems to adequately explain the  $2\nu\beta\beta$  decay half life, the contribution of these higher-lying GT states cannot be ruled out.

Giant resonances have been identified in regions of higher excitation energy in the  $^{150}\text{Nd}(^3\text{He},t)$  experiment, including the IAS, GTR, IVSGDR, and what may be the tail of the IVSGMR. In the  $^{150}\text{Sm}(t,^3\text{He})$  experiment, the vast majority of the  $\Delta L=0$  strength seen is very likely due to the population of the IVSGMR rather than GT excitations. Because the two types of excitations have similar angular distributions, they are not experimentally separable under current experimental configurations.

The two experiments discussed in this work provide a new basis on which to test calculations of theoretical nuclear matrix elements for both the  $2\nu\beta\beta$  and the  $0\nu\beta\beta$  decay of  $^{150}\text{Nd}$ . Those NMEs can then be used to design the next generation of  $0\nu\beta\beta$  decay direct counting experiments, such as SNO+ [141], DCBA [33], and SuperNEMO [2], and any positive signals from those will again use the NMEs to calculate the Majorana neutrino mass.

Collaborative efforts (see Section 2.3.4) to systematically measure GT transitions in  $\beta\beta$  decay nuclei are underway and have borne fruit. However, most of these crucial measurements have already been taken, so the experimental frontier for constraining the  $\beta\beta$  decay matrix elements will likely shift toward more general ways to test and improve QRPA (or Shell Model etc.) calculations. One possibility is to make a series of CE measurements on chains of stable and unstable nuclei, which should help constrain the isovector portion of the nucleon-nucleon interaction and constrain many types of theory [142]. The advent of (p,n) CE experiments in inverse kinematics should

broaden the scope of such experiments [143]. Another possibility is to investigate nuclei in the immediate region of a  $\beta\beta$  decay, such as the recent experiments in the  $^{76}\text{Ge}$  region measuring the valence proton and neutron orbits of  $^{76}\text{Ge}$  and  $^{76}\text{Se}$  [144, 145].

# BIBLIOGRAPHY

- [1] R.N. Mohapatra *et al.* Theory of neutrinos: A white paper. *Rep. Prog. Phys.*, **70**:1757, 2007.
- [2] <http://www.cenbg.in2p3.fr/spip.php?rubrique236&lang=fr>.
- [3] <http://dcba.kek.jp/>.
- [4] K. Zuber. Nd double beta decay search with SNO+. In *Workshop on Calculation of Double Beta Decay Matrix Elements (MEDEX'07)*, volume 942, page 101. AIP Conf. Proc, 2007.
- [5] E. Fermi. Versuch einer Theorie der  $\beta$ -Strahlen. I. *Zeits. f. Physik*, **88**:161, 1934.
- [6] F. Wilson. Fermi's theory of beta decay. *Amer. Journ. of Phys.*, **36**(12):1150, 1968.
- [7] M. Goeppert-Mayer. Double beta-disintegration. *Phys. Rev.*, **48**:512, 1935.
- [8] W.H. Furry. On transition probabilities in double beta-disintegration. *Phys. Rev.*, **56**:1184, 1939.
- [9] J. Bernabeu, A. De Rujula and C. Jarlskog. Neutrinoless double electron capture as a tool to measure the electron neutrino mass. *Nucl. Phys. B*, **223**(1):15, 1983.
- [10] J. Suhonen. Neutrinoless double beta decay to excited collective  $0^+$  states. *Phys. Lett. B*, **477**:99, 2000.
- [11] A.S. Barabash, Ph. Hubert, A. Nachab, and V.I. Umatov. Investigation of  $\beta\beta$  decay in  $^{150}\text{Nd}$  and  $^{148}\text{Nd}$  to the excited states of daughter nuclei. *Phys. Rev. C*, **79**:045501, 2009.
- [12] A.S. Barabash. Precise half-life values for two-neutrino double- $\beta$  decay. *Phys. Rev. C*, **81**:035501, 2010.

- [13] M. Doi, T. Kotani, and E. Takasugi. Neutrinoless double-beta decay with Majoran emission. *Phys. Rev. D*, **37**(9):2575, 1988.
- [14] K. Zuber. Double beta decay. *Contemp. Phys.*, **45**(6):491, 2004.
- [15] Y. Fukuda *et al.* Evidence for Oscillation of Atmospheric Neutrinos. *Phys. Rev. Lett.*, **81**(8):1562, 1998.
- [16] Q.R. Ahmad *et al.* Direct Evidence for Neutrino Flavor Transformation from Neutral-Current Interactions in the Sudbury Neutrino Observatory. *Phys. Rev. Lett.*, **89**:011301, 2002.
- [17] C. Aalseth *et al.* Neutrinoless double beta decay and direct searches for neutrino mass. *arXiv:hep-ph/0412300v1*, 2004.
- [18] S.R. Elliot and P. Vogel. Double beta decay. *Ann. Rev. Nucl. Part. Sci.*, **52**:115, 2002.
- [19] O. K. Manuel. Geochemical measurements of double-beta decay. *J. Phys. G: Nucl. Part. Phys.*, **17**:S221, 1991.
- [20] W.C. Haxton, G.A. Cowan, and M. Goldhaber. Radiochemical tests of double beta decay. *Phys. Rev. C*, **28**(1):467, 1983.
- [21] T. E. Economou A. L. Turkevich and G. A. Cowan. Double Beta Decay of  $^{238}\text{U}$ . *Phys. Rev. Lett.*, **67**(23):3211, 1991.
- [22] S. Yoshida *et al.* CANDLES project for double beta decay of  $^{48}\text{Ca}$ . *Nucl. Phys. B*, **138**:214, 2005.
- [23] Yu.G. Zdesenko *et al.* . CARVEL experiment with  $^{48}\text{CaWO}_4$  crystal scintillators for the double  $\beta$  decay studies of  $^{48}\text{Ca}$ . *Astroparticle Physics*, **23**:249, 2005.
- [24] M. Pedretti *et al.* CUORE experiment: the search for neutrinoless double beta decay. *Int. Jour. Mod. Phys. A*, **23**:3395, 2008.
- [25] C.E. Aalseth *et al.* The proposed Majorana  $^{76}\text{Ge}$  double-beta decay experiment. *Nucl. Phys. B (Proc. Suppl.)*, **138**, 2005.
- [26] A. Bettini *et al.* GERDA. Germanium Detector Array. search for Neutrinoless double beta decay of  $^{76}\text{Ge}$ . *Nucl. Phys. B (Proc. Suppl.)*, **168**:67, 2007.
- [27] H.V. Klapdor-Kleingrothaus *et al.* Data acquisition and analysis of the  $^{76}\text{Ge}$  double beta experiment in Gran Sasso 1990-2003. *Nucl. Instrum. Meth. Phys. Res. A*, **522**(3):371, 2004.
- [28] M. Danilov *et al.* Detection of very small neutrino masses in double beta decay using laser tagging. *Phys. Lett. B*, **480**(1-2):12, 2000.



- [29] M. Nomachi *et al.* MOON (Mo Observatory Of Neutrinos) for double beta decay. *Nucl. Phys. B. Proc. Supp.*, **138**:221, 2005.
- [30] J. Suhonen and O. Civitarese. Weak-interaction and nuclear-structure aspects of nuclear double beta decay. *Phys. Rep.*, **300**:123, 1998.
- [31] Carlos Giunti and Chung W. Kim. *Fundamentals of Neutrino Physics and Astrophysics*. Oxford University Press, New York, 2007.
- [32] C. Jackson F. Deppisch and I. Nasteva. Probing the mechanism of neutrinoless double beta decay with SuperNEMO. *Prog. Nucl. Part. Phys.*, 2010. in press.
- [33] N. Ishihara, T. Ohama, and Y. Yamada. A proposed detector DCBA for double beta decay experiments. *Nucl. Instrum. Meth. Phys. Res. A*, **373**(3):325, 1996.
- [34] C. Kraus, S.J.M. Peeters. The rich neutrino program of the SNO+ experiment. *Prog. Nucl. Part. Phys.*, 2010. in press.
- [35] J. Argyriades *et al.* Measurement of the Double Beta Decay Half-life of  $^{150}\text{Nd}$  and Search for Neutrinoless Decay Modes with the NEMO-3 Detector. *Phys. Rev. C*, **80**:032501, 2009.
- [36] A. De Silva *et al.* Double  $\beta$  decays of  $^{100}\text{Mo}$  and  $^{150}\text{Nd}$ . *Phys. Rev. C*, **56**(5):2451, 1997.
- [37] J. Abad *et al.* An estimation for the half-lives of nuclear double beta emitters. *Anales de Fisica*, **80**:9, 1984.
- [38] J. Suhonen and O. Civitarese. Testing the single-state dominance hypothesis in two-neutrino double-beta decay. *Czech. Journ. Phys*, **50**:561, 2000.
- [39] Fedor Šimkovic Rastislav Dvornický and Amand Faessler. Nuclear and particle physics aspects of the  $2\nu\beta\beta$ -decay of  $^{150}\text{Nd}$ . In *Workshop on Calculation of Double Beta Decay Matrix Elements (MEDEX'07)*, volume **942**, pages 28–32. AIP Conf. Proc, 2007.
- [40] K. Zuber. Consensus Report of a Workshop on Matrix elements for Neutrinoless Double beta decay. *arXiv:nucl-ex/0511009v1*, 2005. Summary of a Workshop on.
- [41] M. Horoi, S. Stoica, and B.A. Brown. Shell-model calculations of two-neutrino double- $\beta$  decay rates of  $^{48}\text{Ca}$  with the GXPf1 interaction. *Phys. Rev. C*, **75**:034303, 2007.
- [42] M. Horoi and S. Stoica. Shell model analysis of the neutrinoless double- $\beta$  decay of  $^{48}\text{Ca}$ . *Phys. Rev. C*, **81**:024321, 2010.
- [43] A. Poves E. Caurier, F. Nowacki and J. Retamosa. Shell model study of the neutrinoless double beta decays. *Nucl. Phys. A*, **654**(1):973c, 1999.

- [44] E. Caurier, J. Menéndez, F. Nowacki, and A. Poves. Influence of Pairing on the Nuclear Matrix Elements of the Neutrinoless  $\beta\beta$  Decays. *Phys. Rev. Lett.*, **100**:052503, 2008.
- [45] T. Tomoda. Double beta decay. *Rep. Prog. Phys.*, **54**:53, 1991.
- [46] V. A. Rodin *et al.* Assessment of uncertainties in QRPA  $0\nu\beta\beta$ -decay nuclear matrix elements. *Nucl. Phys. A*, **766**:107, 2006.
- [47] K. Muto. Neutrinoless Double Beta Decay beyond Closure Approximation. *Nucl. Phys. A*, **577**:415c, 1994.
- [48] Z.-C. Gao, Y. Sun, and Y.-S. Chen. Shell model method for Gamow-Teller transitions in heavy, deformed nuclei. *Phys. Rev. C*, **74**:054303, 2006.
- [49] J. Barea and F. Iachello. Neutrinoless double- $\beta$  decay in the microscopic interacting boson model. *Phys. Rev. C*, **79**:044301, 2009.
- [50] J. Engel, P. Vogel, and M.R. Zirnbauer. Nuclear structure effects in double-beta decay. *Phys. Rev. C*, **37**(2):731, 1988.
- [51] J. Suhonen. *From Nucleons to Nucleus*. Theoretical and Mathematical Physics. Springer, Berlin, Heidelberg, New York, 2007.
- [52] P. Ring and P. Schuck. *The Nuclear Many-Body Problem*. Theoretical and Mathematical Physics. Springer, Berlin, Heidelberg, New York, 1st edition, 1980.
- [53] J.A. Halbleib, Sr. and R.A. Sorensen. Gamow-Teller beta decay in heavy spherical nuclei and the unlike particle-hole RPA. *Nucl. Phys. A*, **98**:542, 1967.
- [54] P. Vogel and M.R. Zirnbauer. Suppression of the Two-Neutrino Double-Beta Decay by Nuclear Structure Effects. *Phys. Rev. Lett.*, **57**(25):3148, 1986.
- [55] A. Faessler M.S. Yousef, V. Rodin and F. Šimkovic. Two-neutrino double  $\beta$  decay of deformed nuclei within the quasiparticle random-phase approximation with a realistic interaction. *Phys. Rev. C*, **79**:014314, 2009.
- [56] I.N. Borzov and E.L. Trykov. *Sov. Journ. Nucl. Phys*, **52**:52, 1990.
- [57] S.A. Fayans I.N. Borzov and E.L. Trykov. *Nucl. Phys A*, **584**(2):335, 1995.
- [58] V. Rodin and M. Urin. On the Fermi and Gamow-Teller Strength Distributions in Medium-Heavy Mass Nuclei. *Phys. Atom. Nucl.*, **66**(12):2128, 2003.
- [59] J. Suhonen. Theory of double beta decay. *Nucl. Phys. A*, **752**:53c, 2005.
- [60] A.A. Raduta *et al.* Two neutrino double- $\beta$  decay in deformed nuclei with an angular momentum projected basis. *Phys. Rev. C*, **69**:064321, 2004.

- [61] O. Civitarese and J. Suhonen. Universal features of the nuclear matrix elements governing the mass sector of the  $0\nu\beta\beta$  decay. *Phys. Lett. B*, **626**:80, 2005.
- [62] J. Suhonen. Nuclear matrix elements of  $\beta\beta$  decay from  $\beta$  decay data. *Phys. Lett. B*, **607**:87, 2005.
- [63] P. Sarriguren *et al.* The Gamow-Teller Response in Deformed Nuclei. *Int. Jour. Mod. Phys. E*, **15**(7):1397, 2006.
- [64] R. Álvarez Rodríguez *et al.* Effect of deformation on two-neutrino double beta decay matrix elements. *Prog. Part. Nucl. Phys*, **57**:251, 2006.
- [65] L. Pacearescu F. Šimkovic and A. Faessler. Two-neutrino double beta decay of  $^{76}\text{Ge}$  within deformed QRPA. *Nucl. Phys. A*, **733**(3):321, 2004.
- [66] P. Sarriguren R. Álvarez Rodríguez and E. Moya de Guerra. Deformed quasi-particle random phase approximation formalism for single- and two-neutrino double  $\beta$  decay. *Phys. Rev. C*, **70**:064309, 2004.
- [67] K. Yako *et al.* Gamow-Teller Strength Distributions in  $^{48}\text{Sc}$  by the  $^{48}\text{Ca}(p,n)$  and  $^{48}\text{Ti}(n,p)$  Reactions and Two-Neutrino Double- $\beta$  Decay Nuclear Matrix Elements. *Phys. Rev. Lett.*, **103**:012503, 2009.
- [68] H. Dohmann *et al.* The  $(d,^2\text{He})$  reaction on  $^{96}\text{Mo}$  and the double- $\beta$  decay matrix elements for  $^{96}\text{Zr}$ . *Phys. Rev. C*, **78**:041602, 2008.
- [69] E.-W. Grewe *et al.* The  $(d,^2\text{He})$  reaction on  $^{76}\text{Se}$  and the double- $\beta$ -decay matrix element for  $A=76$ . *Phys. Rev. C*, **78**:044301, 2008.
- [70] E.-W. Grewe *et al.* Studies on the double- $\beta$  decay nucleus  $^{64}\text{Zn}$  using the  $(d,^2\text{He})$  reaction. *Phys. Rev. C*, **77**:064303, 2008.
- [71] H. Akimune *et al.* GT strengths studied by  $(^3\text{He}, t)$  reactions and nuclear matrix elements for double beta decays. *Phys. Lett. B*, **394**:23, 1997.
- [72] S. Rakers *et al.* Nuclear matrix elements for the  $^{48}\text{Ca}$  two-neutrino double- $\beta$  decay from high-resolution charge-exchange reactions. *Phys. Rev. C*, **70**:054302, 2004.
- [73] E.-W. Grewe *et al.* The  $(^3\text{He}, t)$  reaction on the double- $\beta$  decay nucleus  $^{48}\text{Ca}$  and the importance of nuclear matrix elements. *Phys. Rev. C*, **76**:054307, 2007.
- [74] S.D. Bloom, N.K. Glendenning, and S.A. Moszkowski. Proton-neutron interaction and the  $(p,n)$  reaction in mirror nuclei. *Phys. Rev. Lett.*, **3**(2):98, 1959.
- [75] W.P. Alford and B.M. Spicer. *Advances in Nuclear Physics, Chapter 1: Nucleon Charge-Exchange Reactions at Intermediate Energy*, volume **24**. Plenum Press, New York, 1998.

- [76] A. Erell *et al.* Measurements on isovector giant resonances in pion charge exchange. *Phys. Rev. C*, **34**(5):1822, 1986.
- [77] M. N. Harakeh and A. van der Woude. *Giant Resonances: Fundamental High-Frequency Modes of Nuclear Excitations*. Oxford University Press, New York, 2001.
- [78] K. I. Ikeda, S. Fujii, and J. I. Fujita. The (p,n) reactions and beta decays. *Phys. Lett.*, **3**:271, 1963.
- [79] B. D. Anderson *et al.* Gamow-Teller strength in the (p,n) reaction at 136 MeV on  $^{20}\text{Ne}$ ,  $^{24}\text{Mg}$ , and  $^{28}\text{Si}$ . *Phys. Rev. C*, **43**:50, 1991.
- [80] A. Arima. History of giant resonances and quenching. *Nucl. Phys. A*, **649**:260c, 1999.
- [81] H. Sakai and K. Yako. Experimental determination of Gamow-Teller quenching value, Landau-Migdal parameter  $g'_{N\Delta}$  and pion condensation. *Nucl. Phys. A*, **731**:105, 2004.
- [82] K. Yako *et al.* Determination of the Gamow-Teller quenching factor from charge exchange reactions on  $^{90}\text{Zr}$ . *Phys. Lett. B*, **615**:193, 2005.
- [83] B. D. Anderson *et al.* Gamow-Teller strength to  $^{38}\text{K}$  from the  $^{38}\text{Ar}(\text{p,n})$  reaction and  $^{38}\text{Ca}(\beta^+)$  decay. *Phys. Rev. C*, **54**:602, 1996.
- [84] J. Cook and J.A. Carr. computer program FOLD, Florida State University (unpublished), based on F. Petrovich and D. Stanley, *Nucl. Phys.* **A275**, 487 (1977), modified as described in J. Cook *et al.*, *Phys. Rev. C* **30**, 1538 (1984) and R. G. T. Zegers, S. Fracasso and G. Colò (2006), unpublished.
- [85] I.J. Thompson and F.M. Nunes. *Nuclear Reactions for Astrophysics: Principles, Calculation and Applications of Low-Energy Reactions*. Cambridge University Press, Cambridge, 2009.
- [86] B. A. Brown *et al.* NSCL report MSUCL-1289.
- [87] William D.M. Rae. Nushellx. Knoll House, Garsington, Oxford (<http://knollhouse.org/default.aspx>).
- [88] B.A. Brown. Lecture notes on nuclear structure (unpublished), 2009.
- [89] M. A. Hofstee *et al.* Localized  $1\hbar\omega$  particle-hole strength in nuclei. *Nucl. Phys. A*, **588**:729, 1995.
- [90] W. G. Love and M. A. Franey. Effective nucleon-nucleon interaction for scattering at intermediate energies. *Phys. Rev. C*, **24**:1073, 1981.

- [91] M. A. Franey and W. G. Love. Nucleon-nucleon t-matrix interaction for scattering at intermediate energies. *Phys. Rev. C*, **31**:488, 1985.
- [92] W. G. Love, K. Nakayama, and M. A. Franey. Isovector couplings for nucleon charge-exchange reactions at intermediate energies. *Phys. Rev. Lett.*, **59**:1401, 1987.
- [93] G.W Hitt. *The  $^{64}\text{Zn}(t,^3\text{He})$  Charge-Exchange Reaction at 115 MeV Per Nucleon and Application to  $^{64}\text{Zn}$  Stellar Electron-Capture*. PhD thesis, Michigan State University, 2008.
- [94] T. Udagawa, A. Schulte, and F. Osterfeld. Antisymmetric distorted wave impulse approximation calculations for composite particle scattering. *Nucl. Phys. A*, **474**:131, 1987.
- [95] R. G. T. Zegers *et al.* Extraction of Weak Transition Strengths via the ( $^3\text{He}$ , t) Reaction at 420 MeV. *Phys. Rev. Lett.*, **99**:202501, 2007.
- [96] J. Raynal. Notes on ECIS97 (unpublished), see <http://www.nea.fr/abs/html/nea-0850.html>.
- [97] I.J. Thompson. Coupled reaction channels calculations in nuclear physics. *Comput. Phys. Rep.*, **7**:167, 1988. See also <http://www.fresco.org.uk/>.
- [98] S.Y. van der Werf, S. Brandenburg, P. Grasdijk, W.A. Sterrenburg, M.N. Harakeh, M.B. Greenfield, B.A. Brown and M. Fujiwara. The effective  $^3\text{He}$ -nucleon force in a microscopic DWBA approach to the ( $^3\text{He}$ ,t) charge-exchange reaction. *Nucl. Phys. A*, **496**:305, 1989.
- [99] T. N. Taddeucci *et al.* The (p, n) reaction as a probe of beta decay strength. *Nucl. Phys. A*, **469**:125, 1987.
- [100] R. G. T. Zegers *et al.* The ( $t,^3\text{He}$ ) and ( $^3\text{He}$ , t) reactions as probes of Gamow-Teller strength. *Phys. Rev. C*, **74**:024309, 2006.
- [101] F. Osterfeld. Nuclear spin and isospin excitations. *Rev. Mod. Phys.*, **64**:491, 1992.
- [102] Y. Fujita *et al.* Gamow-Teller Strengths in Proton-Rich Exotic Nuclei Deduced in the Combined Analysis of Mirror Transitions. *Phys. Rev. Lett.*, **95**:212501, 2005.
- [103] A. L. Cole *et al.* Measurement of the Gamow-Teller strength distribution in  $^{58}\text{Co}$  via the  $^{58}\text{Ni}(t,^3\text{He})$  reaction at 115 MeV/nucleon. *Phys. Rev. C*, **74**:034333, 2006.
- [104] A. Brockstedt *et al.* The ( $^3\text{He}$ ,t) reaction at intermediate energies. *Nucl. Phys. A*, **530**:571, 1991.

- [105] R.G.T. Zegers. *Search for isovector giant monopole resonances*. PhD thesis, University of Groningen, 1999.
- [106] A. Bohr and B.R. Mottelson. *Nuclear Structure*, volume II (Nuclear Deformations). W.A. Benjamin, New York, 1975.
- [107] N. Auerbach and A. Klein. A microscopic theory of giant electric isovector resonances. *Nucl. Phys. A*, **395**:77, 1983.
- [108] H. Fujita *et al.* Better-resolution measurement of vertical scattering angle in a new ion-optical mode of spectrometer Grand Raiden. *Nucl. Instrum. Meth. Phys. Res. A*, **469**:55, 2001.
- [109] H. Fujita *et al.* Realization of matching conditions for high-resolution spectrometers. *Nucl. Instrum. Methods Phys. Res. A*, **484**:17, 2002.
- [110] T. Wakasa *et al.* High resolution beam line for the Grand Raiden Spectrometer. *Nucl. Instrum. Meth. Phys. Res. A*, **482**:79, 2002.
- [111] T. Wakasa *et al.* New Capabilities of the Grand Raiden Spectrometer. *Nucl. Phys. A*, **721**:1099c, 2003.
- [112] M. Fujiwara *et al.* Magnetic spectrometer Grand Raiden. *Nucl. Instrum. Meth. Phys. Res. A*, **422**:484, 1999.
- [113] Y. Shimbara. *High resolution study of Gamow-Teller transitions by  $^{37}\text{Cl}(^3\text{He},t)^{37}\text{Ar}$  reaction*. PhD thesis, Osaka University, 2005.
- [114] A. Matic. *High precision (p,t) reactions to determine reaction rates of explosive stellar processes*. PhD thesis, University of Groningen, 2007.
- [115] D. Bazin, M. Lewitowicz, O. Sorlin, and O. Tarasov. The program LISE: a simulation of fragment separators. *Nucl. Instrum. Meth. Phys. Res. A*, **482**:314, 2002. program LISE; <http://dnr080.jinr.ru/lise>; <http://www.nsl.msu.edu/lise>.
- [116] M.A. Moinester. Multipole decomposition of Gamow-Teller strength. *Can. Journ. of Phys.*, **65**:660, 1987.
- [117] J. Barette *et al.* Transitional nuclei. I. Decay of  $^{150}\text{Pm}$  to levels of  $^{150}\text{Sm}$ . *Can. Journ. of Phys.*, **48**:1161, 1969.
- [118] J. Jänecke *et al.* Fragmentation of Gamow-Teller strength observed in  $^{117,120}\text{Sn}(^3\text{He},t)^{117,120}\text{Sb}$  charge-exchange reactions. *Phys. Rev. C*, **48**(6):2828, 1993.
- [119] K. Pham *et al.* Fragmentation and splitting of Gamow-Teller resonances in  $\text{Sn}(^3\text{He},t)\text{Sb}$  charge-exchange reactions.  $A=112-124$ . *Phys. Rev. C*, **51**(2):526, 1995.

- [120] V.G. Guba, M.A. Nikolaev, and M.G. Urin. Gamow-Teller giant resonance (GTR) Configurational Splitting. *Phys. Lett. B*, **218**(3):283, 1989.
- [121] F. James. Minuit function minimization and error analysis reference manual. <http://hep.fi.infn.it/minuit.pdf>, March 1994. Version 94.1.
- [122] V.Rodin *et al.* to be published.
- [123] D. Fang *et al.* Running sums for  $2\nu\beta\beta$  decay matrix elements within the quasi-particle random-phase approximation with account for deformation. *Phys. Rev. C*, **81**:037303, 2010.
- [124] V. Rodin. private communication.
- [125] The K500 $\otimes$ K1200, a coupled cyclotron facility at the NSCL, NSCL Report MSUCL-939. 1988.
- [126] G. W. Hitt *et al.* Development of a secondary triton beam from primary  $^{16,18}\text{O}$  beams for (t,  $^3\text{He}$ ) experiments at intermediate energies. *Nucl. Instrum. Methods Phys. Res. A*, **566**:264, 2006.
- [127] D. Bazin, J. A. Caggiano, B. M. Sherrill, J. Yurkon, and A. Zeller. The S800 spectrograph. *Nucl. Instr. Meth. Phys. Res. B*, **204**:629, 2003.
- [128] S. Noji. Exothermic charge-exchange reaction at the S800. In *Future Prospects for Spectroscopy and Direct Reactions*, pages 8.9. 2008. <http://meetings.nsl.msui.edu/fp2008/presentations/noji.pdf>.
- [129] C.J. Guess *et al.* Spectroscopy of  $^{13}\text{B}$  via the  $^{13}\text{C}(\text{t}, ^3\text{He})$  reaction at 115A MeV. *Phys. Rev. C*, **80**:024305, 2009.
- [130] J. Yurkon, D. Bazin, W. Benenson, D. J. Morrissey, B. M. Sherrill, D. Swan, and R. Swanson. Focal plane detector for the S800 high-resolution spectrometer. *Nucl. Instr. Meth. Phys. Res. A*, **422**:291, 1999.
- [131] J.A Caggiano. *Spectroscopy of exotic nuclei with the S800 Spectrograph*. PhD thesis, Michigan State University, 1999.
- [132] M. Howard *et al.* Gamow-Teller strengths in  $^{24}\text{Na}$  using the  $^{24}\text{Mg}(\text{t}, ^3\text{He})$  reaction at 115 MeV/u. *Phys. Rev. C*, **78**:047302, 2008.
- [133] K. Makino and M. Berz. Cosy infinity version 8. *Nucl. Instrum. Meth. Phys. Res. A*, **427**:338, 1999.
- [134] G.W. Hitt *et al.* Gamow-Teller transitions to  $^{64}\text{Cu}$  measured with the  $^{64}\text{Zn}(\text{t}, ^3\text{He})$  reaction. *Phys. Rev. C*, **80**:014313, 2009.
- [135] N. Auerbach and A. Klein. Structure of isovector spin excitations in nuclei. *Phys. Rev. C*, **30**(3):1032, 1984.

- [136] R.L. Helmer *et al.* Gamow-Teller strength from the  $^{76}\text{Se}(\text{n,p})^{76}\text{As}$  reaction: Implications for double  $\beta$  decay of  $^{76}\text{Ge}$ . *Phys. Rev. C*, **55**(6):2802, 1997.
- [137] K.J. Raywood *et al.* Gamow-Teller and dipole strength in the  $^{208}\text{Pb}(\text{n,p})$  reaction. *Nucl. Phys. A*, **625**:675, 1997.
- [138] S. Rakers *et al.* Low-lying GT+ strength in  $^{116}\text{In}$  from a  $(\text{d}, ^2\text{He})$  reaction experiment and its implications for  $^{116}\text{Cd}$  double  $\beta$  decay. *Phys. Rev. C*, **71**:054313, 2005.
- [139] M. Sasano *et al.* Measurements of the  $^{116}\text{Cd}(\text{p,n})$  and  $^{116}\text{Sn}(\text{n,p})$  reactions at 300 MeV for studying Gamow-Teller transition strengths in the intermediate nucleus of the  $^{116}\text{Cd}$  double-beta decay. In *AIP Conf. Proc.*, volume 1180, page 102, 2009.
- [140] B. Pritychenko. On Double-Beta Decay Half-Life Time Systematics. *arXiv:1004.3280v1 [nucl-th]*, 2010. Brookhaven National Laboratory Report BNL-91299-2010.
- [141] L.W. Chen. A phenomenological equation of state for isospin asymmetric nuclear matter. *Science in China Ser. G: Phys., Mech., Astro.*, **52**(10):1494, 2009.
- [142] S. Fracasso and G. Colò. Fully self-consistent charge-exchange quasiparticle random-phase approximation and its application to isobaric analog resonances. *Phys. Rev. C*, **72**:064310, 2005.
- [143] G. Perdikakis *et al.* LENDA: a Low Energy Neutron Detector Array for Studies of (p,n) Reactions With Radioactive Beams. *IEEE Transactions on Nuclear Science*, **56**, 2009.
- [144] J.P. Schiffer *et al.* Nuclear Structure Relevant to Neutrinoless Double  $\beta$  Decay:  $^{76}\text{Ge}$  and  $^{76}\text{Se}$ . *Phys. Rev. Lett.*, 100:112501, 2008.
- [145] B.P. Kay *et al.* Nuclear structure relevant to neutrinoless double  $\beta$  decay: The valence protons in  $^{76}\text{Ge}$  and  $^{76}\text{Se}$ . *Phys. Rev. C*, 79:021301, 2009.



